



Universität Hamburg
DER FORSCHUNG | DER LEHRE | DER BILDUNG

EXZELLENZCLUSTER
QUANTUM UNIVERSE



Domain Walls in Extended Higgs Sectors and their Impact on the Early Universe

Dissertation

zur Erlangung des Doktorgrades an der Fakultät für Mathematik,
Informatik und Naturwissenschaften

Fachbereich Physik der Universität Hamburg

vorgelegt von

Mohamed Younes Sassi

Hamburg
2025

Domain Walls in Extended Higgs Sectors and their Impact on the Early Universe.
© Mohamed Younes Sassi 2025

GUTACHTER:INNEN DER DISSERTATION:

Prof. Gudrid Moortgat-Pick
Dr. Thomas Konstandin

ZUSAMMENSETZUNG DER PRÜFUNGSKOMMISSION:

Dr. Johannes Braathen
Dr. Thomas Konstandin
Prof. Jochen Liske
Prof. Günter Sigl
Prof. Gudrid Moortgat-Pick

VORSITZENDER DER PRÜFUNGSKOMMISSION:

Prof. Dr. Jochen Liske

DATUM DER DISPUTATION:

02. Juli 2025

VORSITZENDER DES FACH-PROMOTIONSAUSSCHUSSES PHYSIK:

Prof. Dr. Wolfgang J. Parak

LEITER DES FACHBEREICHS PHYSIK:

Prof. Dr. Markus Drescher

DEKAN DER FAKULTÄT MIN:

Prof. Dr.-Ing. Norbert Ritter

ABSTRACT

The dissertation investigates the role of domain walls in several extensions of the Standard Model (SM) Higgs sector, such as the Two-Higgs-Doublet-Models (2HDM) and the Next-to-Two-Higgs-Doublet-Models (N2HDM). Domain walls are formed after a phase transition in the early universe if a discrete symmetry is spontaneously broken. We discuss in this thesis several aspects of these domain walls in the Higgs sector, which differ significantly from the standard domain wall solution usually discussed in the literature. This includes the discussion of the several types of domain wall solutions in the 2HDM, where CP and electric charge-violating scalar field domain wall configurations can be constructed. We also discuss some aspects of the scattering of SM fermions, such as top and bottom quarks, off these different types of domain walls.

In the case of the N2HDM, we show that domain walls can be embedded in the context of electroweak baryogenesis. This is done by discussing how domain walls can lead to the electroweak symmetry restoration in a region inside and around the wall, providing a way to separate regions with unsuppressed sphaleron rates from regions where the sphaleron rate is exponentially suppressed and thus avoiding the need for first order electroweak phase transitions required in conventional models of electroweak baryogenesis. We also show that one can induce a pure gauge hypermagnetic field centered inside the domain wall that could source the needed chiral asymmetry. We provide a simplified calculation intended to demonstrate the possibility of generating a sizable and suitable amount of baryon asymmetry via this mechanism.

We finally discuss how domain walls can be used to constrain the parameter space of the N2HDM beyond the conventional cosmological domain wall problem. We demonstrate that domain walls can induce electroweak (EW) vacuum decay by showing that the large potential barrier separating long-lived EW minima from the global minimum of the potential can disappear inside the wall leading to the nucleation of the true minimum inside the wall and its subsequent expansion everywhere in the universe, leading to the decay of the electroweak vacuum to the global minimum. Since the global minimum gives different masses to the SM particles, such parameter points are ruled out.

These mechanisms show the importance of domain wall field configurations in the early universe, since they provide several new ways to alleviate some shortcomings of the SM, such as the matter-antimatter asymmetry. They also provide some new constraints on extended Higgs sectors, including EW vacuum decay induced by domain walls and the possibility to modify the early universe cosmology via new interactions, such as the electric charge breaking field configurations.

ZUSAMMENFASSUNG

Die Dissertation untersucht die Rolle von Domänenwänden in verschiedenen Erweiterungen des Higgs-Sektors des Standardmodells (SM), wie beispielsweise den Zwei-Higgs-Doublet-Modellen (2HDM) und den Nächst-zu-Zwei-Higgs-Doublet-Modellen (N2HDM). Domänenwände entstehen nach einem Phasenübergang im frühen Universum, falls eine diskrete Symmetrie spontan gebrochen wird. Wir diskutieren in dieser Arbeit verschiedene Aspekte dieser Domänenwände im Higgs-Sektor, die sich deutlich von der in der Literatur diskutierten Standardlösung für Domänenwände unterscheiden. Dies umfasst die Diskussion der verschiedenen Arten von Domänenwandlösungen im 2HDM, mit denen CP- und elektrisch ladungsverletzende Skalarfeld-Domänenwandkonfigurationen konstruiert werden können. Wir diskutieren außerdem einige Aspekte der Streuung von SM-Fermionen, wie z. B. Top- und Bottom-Quarks, an diesen verschiedenen Arten von Domänenwänden.

Im Fall des N2HDMs zeigen wir, dass Domänenwände im Kontext der elektroschwachen Baryogenese eingebettet sein können. Das geschieht durch die Art und Weise, wie Domänenwände zur Wiederherstellung der elektroschwachen Symmetrie in einem Bereich innerhalb und um die Wand herum führen können. Dadurch können Bereiche mit nicht unterdrückten Sphaleronraten von Bereichen mit exponentiell unterdrückter Sphaleronrate getrennt werden. Dadurch werden elektroschwache Phasenübergänge erster Ordnung, wie sie in konventionellen Modellen der elektroschwachen Baryogenese erforderlich sind, vermieden. Wir zeigen außerdem, dass ein reines hypermagnetisches Eichfeld mit Zentrum innerhalb der Domänenwand induziert werden kann, das die benötigte chirale Asymmetrie erzeugen könnte. Wir präsentieren eine vereinfachte Berechnung, die die Möglichkeit demonstrieren soll, über diesen Mechanismus eine beträchtliche und angemessene Baryonenasymmetrie zu erzeugen.

Abschließend diskutieren wir, wie Domänenwände genutzt werden können, um den Parameterraum des N2HDMs über das konventionelle kosmologische Domänenwandproblem hinaus einzuschränken. Wir zeigen, dass Domänenwände den Zerfall des elektroschwachen (EW) Vakuums induzieren können. Dazu zeigen wir, dass die große Potentialbarriere, die langlebige EW-Minima vom globalen Potentialminimum trennt, innerhalb der Wand verschwinden kann. Dies kann dazu führen, dass sich das wahre Minimum innerhalb der Wand bildet und sich dann anschließend im gesamten Universum ausdehnt, was zum Zerfall des elektroschwachen Vakuums auf das globale Minimum führt. Da jedoch das globale Minimum den SM-Partikeln unterschiedliche Massen zuweist, sind solche Parameterpunkte ausgeschlossen.

Diese Mechanismen verdeutlichen die Bedeutung von Domänenwand-Konfigurationen im frühen Universum, da sie neue Möglichkeiten zur Behebung einiger Schwächen des SMs, wie beispielsweise der Materie-Antimaterie-Asymmetrie, bieten. Sie liefern außerdem neue Parameter-Einschränkungen für erweiterte Higgs-Sektoren, wie beispielsweise den durch Domänenwände induzierten EW-Vakuumzerfall und die Möglichkeit, die Kosmologie des frühen Universums durch neue Wechselwirkungen zu verändern, wie beispielsweise wegen der Konfigurationen elektrischer Ladungsverletzungen.

ACKNOWLEDGMENTS

I would like to take this opportunity to thank many individuals who supported me during my PhD studies.

First, I would like to thank my PhD supervisor Gudi for giving me the opportunity to do my PhD in Hamburg, as well as for introducing me to the topic of domain walls. I'm also grateful for the Quantum Universe excellence cluster for funding my research. I'm thankful to my master's supervisor Julia Harz for recommending DESY as an amazing place to do a PhD, and you were right, the weather in Hamburg is absolutely terrible.

I would like to thank Jochen Liske for agreeing to chair my PhD defense committee. I'm also grateful to Thomas Konstandin, Günter Sigl, and Johannes Braathen for agreeing to be part of the committee.

I would like to thank Gudi and Georg for organizing the 2HDM working group seminar, which was an excellent opportunity to present and discuss my work, as well as learn more about other aspects of extended Higgs sectors.

I'm also grateful to all the colleagues I met during summer schools in Italy, Spain, France, and Brazil. We all learned a lot and had lots of fun during those brief but amazing weeks. I'm also grateful to several colleagues I met during conferences, with whom I had very insightful discussions, especially Igor Ivanov, Oleksii Matsedonskyi and Manuel Salewski.

A big thank you goes to all my fellow PhD and Postdoc colleagues at DESY and Uni Hamburg. In particular the DESY Higgsers: Romal, Panos (aka Rossmann), Kateryna, Monika, Max, Julia, Marten, Johannes, Alain, Andrii, Daniel, Jayita, Johannes, Luis, Rohan, Muriel, Cheng Li, Fran, and Felix, as well as those in the other groups: Guilherme, Jonas, Martina, Nabeen, Koschi, Sara, Enrico, Julian, Adriana and Carlo (thanks a lot Carlo for providing this amazing thesis template!). A big thank you goes also to my fellow "Domain Wallers" in the cosmo corridor; Simone and Yu. We had very nice discussions and your experience was very helpful. All of you made my PhD studies at DESY very enjoyable, and it was fun to have all those coffee and cookie breaks, those long board games nights, and those amazing christmas and karaoke parties.

I would also like to thank the colleagues and fellow students I met in München during my Bachelor's and Master's degree, in particular Amine, Andrea, Jonas, Manoram, Chandan, Emanuele, Mathias, Kåre as well as my collaborator Luca from Münster.

Going beyond DESY, I would like to thank my flatmates at the dorm in Hamburg, and in particular Ernst (thanks a lot for the TV and barbecues at the Stadtpark, and I forgive you for stealing my food), Johnny, Juliana and Marfa, as well as those of StuSta Haus 14 in München: Gigia, Armin, Marc, Julian, Manoram, Krutav, Konrad and Pavlos. We had a lot of fun together.

In particular, I'm very grateful to Lena for your enthusiasm and support, I will miss you so much!

وأخيرًا، أود أن أشكر عائلتي على كل الجهود التي بذلتها لمنحي الفرصة لمواصلة دراستي في الخارج، وكذلك على دعمكم الكامل لخياراتي في كل مرحلة من مراحل حياتي. لولاكم، لما كان كل هذا ممكنًا.

PUBLICATIONS

This thesis is based on the following publications:

- [1] M. Y. Sassi and G. Moortgat-Pick, *Domain walls in the Two-Higgs-Doublet Model and their charge and CP-violating interactions with Standard Model fermions*, *JHEP* **04** (2024) 101, [[2309.12398](#)]
- [2] M. Y. Sassi and G. Moortgat-Pick, *Electroweak Symmetry Restoration in the N2HDM via Domain Walls*, [[2407.14468](#)], Accepted for publication in JHEP.
- [3] M. Y. Sassi and G. Moortgat-Pick, “Electroweak Vacuum Decay in the N2HDM Induced by Domain Walls.” In preparation, to be published, 2025

The following publication was completed during the PhD. However, the topic is not related to the content discussed in this manuscript:

- [4] J. Harz, M. Klasen, M. Y. Sassi, and L. P. Wiggering, *Dipole formalism for massive initial-state particles and its application to dark matter calculations*, *Phys. Rev. D* **107** (2023), no. 5 056020, [[2210.03409](#)]

CONTENTS

1	Introduction	1
1.1	The standard model of particle physics	3
1.1.1	The Higgs Mechanism	5
1.1.2	Shortcomings of the Standard Model	7
1.2	Topological Defects	10
1.2.1	Types of Topological Defects	10
1.2.2	Domain Walls	13
1.2.3	Phase Transitions in the Early Universe	15
1.2.4	Formation of Domain Walls in the Early Universe	17
1.2.5	Consequences of Domain Walls on the Early Universe	20
2	Extended Higgs Sectors	25
2.1	The need for an extended Higgs sector	25
2.2	The Two-Higgs-Doublet Model	27
2.3	The Next-to-Two-Higgs-Doublet-Model	31
2.4	Theoretical and experimental constraints	34
2.4.1	Theoretical Constraints	35
2.4.2	Experimental Constraints	39
3	Domain walls in the 2HDM	43
3.1	Motivation and general idea	43
3.2	The Vacuum Manifold of the 2HDM	44
3.3	Standard Domain Wall Solution	48
3.4	Variation of a single angle across the wall	52
3.4.1	Variation of hypercharge θ	53
3.4.2	Variation of g_1	55
3.4.3	Variation of g_2	56
3.4.4	Variation of g_3	60
3.5	Variation of the hypercharge angle θ and the Goldstone modes	61
3.5.1	Variation of θ and g_1	62
3.5.2	Variation of θ and g_2	63
3.5.3	Variation of θ and g_3	66
3.5.4	Variation of $SU(2)_L$ Goldstone modes g_1, g_2 and g_3	67
3.6	General Domain Wall Solution	69
3.7	Dependence of the kink solution on the parameter points of the 2HDM	71
3.8	Non-Topological kink solutions in the 2HDM	76
3.9	Discussion	78
4	SM fermions Scattering off Domain walls in the 2HDM	81
4.1	Thin-Wall approximation	82
4.2	CP-Violating interactions of fermions with the domain walls	83
4.3	Charge violating interactions of fermions with the domain walls	90
4.4	Discussion	99
5	Electroweak Symmetry Restoration via Domain Walls	101
5.1	Motivation and general idea	101
5.2	Domain walls in the N2HDM	102
5.2.1	Symmetry restoration in the early universe	103
5.2.2	Z'_2 Domain Walls	106

5.3	Scenarios with EWSR in a large region around the wall	118
5.3.1	Scenario 1: Small CP-even Higgs masses	119
5.3.2	Scenario 2: Intermediate CP-even masses	123
5.3.3	Scenario 3: Heavy CP-even Higgs masses	124
5.3.4	Scans with fixed v_s	126
5.4	Different Goldstone modes and CP-violation in the vicinity of the wall . .	128
5.5	Electroweak Baryogenesis via Domain Walls	134
5.5.1	Standard Electroweak Baryogenesis	135
5.5.2	Domain Wall Electroweak Baryogenesis	136
5.6	Discussion	140
6	Electroweak Vacuum Decay Induced by Domain Walls	143
6.1	Motivation and general idea	143
6.2	Vacuum Instabilities in the N2HDM	144
6.3	Domain Walls in the N2HDM inducing EW vacuum decay	147
6.3.1	Several extrema inside the wall	151
6.4	Phenomenological Scenarios for Metastability	155
6.4.1	Scenario 1: a 95 GeV CP-even Higgs particle	156
6.4.2	Scan including experimental constraints	159
6.4.3	Scenario 2: SM Higgs as the lightest CP-even Higgs boson	160
6.5	Discussion	163
7	Summary and Outlook	165
A	Effects of gauge fields on the DW solution	169

1 | INTRODUCTION

For millennia, the quest to uncover the basic principles governing our universe took the effort and imagination of many scholars. The Standard Model of particle physics (SM) is our most successful theory describing the smallest subatomic structure of matter, while the theory of Λ CDM also known as the Standard Model of cosmology provides a successful description of the universe at large scales, based on the existence of a cold dark matter and dark energy content in the universe. Evidence from the Cosmic Microwave Background suggests that the universe at its early times was much smaller, dense, and very hot. Since, at high temperatures and densities the known matter in the universe would be in form of a primordial plasma of leptons, quarks, photons, gluons and other bosons, describing the early universe relies on a precise understanding of the SM in the framework of an expanding and cooling universe with the evolution of its space-time metric based on the laws of general relativity.

One central and important piece for our understanding of the early universe is the mechanism with which electroweak (EW) symmetry breaking occurred in the first nanosecond after the Big Bang, leading to the known fundamental particles acquiring their mass via the Higgs mechanism [5]. In the SM, this phase transition is a crossover, meaning that the Higgs field permeating the whole universe slowly acquired a non-zero vacuum expectation value. However, it is well-known that the SM cannot be the final description of nature at its smallest scales. Indeed, the SM suffers from several shortcomings (such as the existence of Dark Matter (DM), Neutrino masses, the matter-antimatter asymmetry of the universe, the hierarchy problem, etc). This makes it necessary to extend it with new fields that might change the nature of the EW phase transition in the early universe. Some of these so-called Beyond the Standard Model (BSM) theories rely on extending the SM with new scalar singlet/doublet fields to cure some of the problems with the SM. As an example, one can obtain a first-order phase transition when extending the SM with singlet or doublet scalar fields. This is done in order to satisfy the out-of-thermal-equilibrium condition needed to explain the matter-antimatter asymmetry of the universe.

However, these extensions of the scalar sector of the SM can also be very interesting from the point of view of allowing extra new symmetries related to an extended Higgs sector, such as discrete and continuous symmetries [6, 7]. Upon the spontaneous breaking of these new symmetries, *topological defects* could form in the early universe [8, 9], which are field configurations that act as a snapshot of the universe in its symmetric phase before the phase transition. They come in different types depending on the spontaneously broken symmetry, such as *domain walls* (DW), cosmic strings, and magnetic monopoles [9]. These topological defects can leave an imprint after their formation or annihilation in the form of gravitational waves and particle production [10, 11, 9]. They can also act as primordial seeds for large structures that are observed today [9]. The formation of DW in the early universe after the spontaneous symmetry breaking of a discrete symmetry would lead to a cosmological disaster since they would dominate the energy density of the universe at some point after their formation [12, 8]. Therefore, particle physics models that lead to their formation are largely disfavored [12, 8]. However, it was understood that this cosmological

disaster can be very easily circumvented when taking into account several mechanisms such as inflation, symmetry restoration, or the introduction of a discrete symmetry-breaking term in the Lagrangian [13, 11]. Models with approximate discrete symmetries received a renewed interest in the last few years since one can use an annihilating domain wall network as a source for gravitational waves [11, 14, 15, 16, 17] which could fit well, for instance, the data from *Pulsar Timing Array* observations [18, 19].

Several extended Higgs sectors relying on two-step phase transitions to get a first-order electroweak phase transition can also lead to the formation of domain walls during the first step phase transition [20, 21, 22]. It was shown recently that these domain walls can catalyze the EW phase transition and rescue parameter points from *vacuum trapping* [23, 21, 24, 22], where the universe gets stuck in the symmetric unbroken phase due to a barrier separating it from the minimum of the broken phase. Such a DW-induced phase transition can also alter the gravitational waves signal of usual first-order EW phase transitions [20].

In this manuscript, we look at domain walls forming after the spontaneous symmetry breaking of several extended Higgs sectors such as the *Two-Higgs-Doublet-Models* (2HDM) [25] and the *Next-To-Two-Higgs-Doublet-Models* (N2HDM) [26, 27, 28]. In contrast with the usual discussion of DW found in recent literature, which focused on the gravitational wave consequences of domain walls, we look in this manuscript at further interesting and exotic properties of domain walls, such as CP and electric charge violating field configurations in the vicinity of the walls [1], their interaction with SM fermions, the possibility of domain walls inducing EW symmetry restoration and sourcing a matter-antimatter asymmetry [2], as well as domain walls inducing EW vacuum decay [3].

Our manuscript is structured as follows: The remainder of chapter 1 is dedicated to a detailed introduction to the SM, its shortcomings, and a discussion of topological defects with an emphasis on domain walls. In chapter 2 we introduce the extended Higgs sector models studied in this manuscript, focusing on the used notation and the experimental and theoretical constraints that must be fulfilled for these models to be viable. We later describe in chapter 3 the different classes of domain wall solutions found in the 2HDM, which can have CP or electric charge violating field configurations localized inside and in the vicinity of the domain wall. In chapter 4, we describe how SM fermions such as top and bottom quarks scatter off these different types of domain walls and demonstrate the possibility of this scattering generating a chiral asymmetry in front of the wall as well as the possibility of transforming top quarks into bottom quarks upon an interaction with the domain wall. In chapter 5, we describe domain wall solutions in the N2HDM and demonstrate the possibility of inducing the *electroweak symmetry restoration* (EWSR) inside and in the vicinity of the domain wall. Such an EWSR can be useful for the mechanism of electroweak baryogenesis via domain walls, whose ingredients will be discussed in that chapter. We also provide a simplified calculation for the generated matter-antimatter asymmetry sourced by these domain walls. We later move on in chapter 6 to the discussion of EW vacuum decay induced by domain walls in the N2HDM, demonstrating a strong new source of constraints on the viable parameter region of the N2HDM. We summarize in chapter 7 and discuss some possible future directions for the topics discussed in this manuscript.

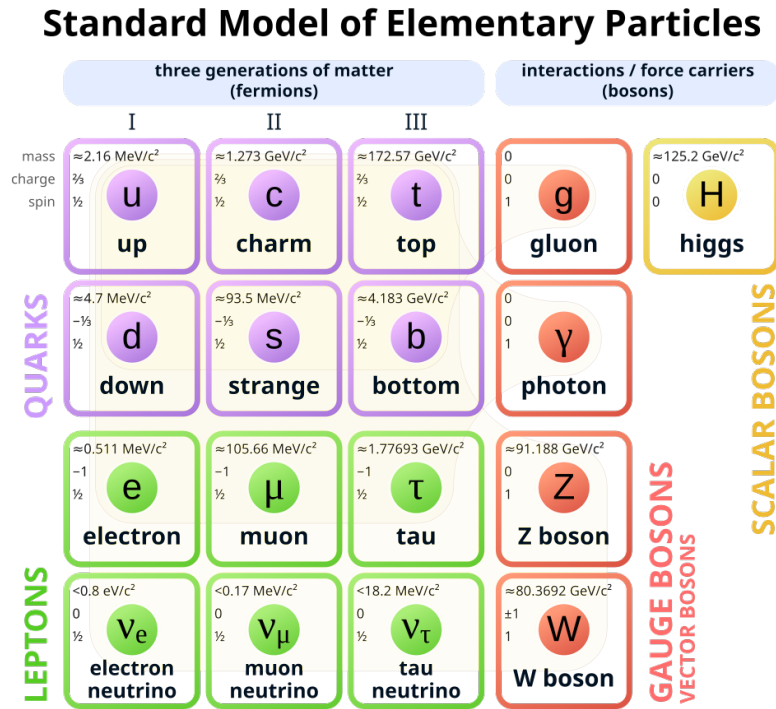


Figure 1.1: The different fundamental particles of the Standard Model of particle physics alongside their masses, gauge quantum numbers, spin, and generations. The figure was taken from [30].

1.1 THE STANDARD MODEL OF PARTICLE PHYSICS

The SM of particle physics provides a very successful description of the fundamental laws and constituents of matter at microscopic scales. Based on the theoretical framework of quantum field theory and robust, precise experimental observations [29], the SM explains the fundamental interactions of the weak, electromagnetic, and strong forces between all the observed elementary particles of nature. Using the powerful tool of symmetries, particles of the SM are classified in multiplets according to their quantum numbers, such as spin and mass for spacetime symmetries as well as charge quantum numbers for gauge symmetries. The latter play a major role in the SM since they describe the fundamental laws that govern the interactions between these fundamental particles.

We can classify the known fundamental particles in the SM according to their spin. Fermions, which constitute the visible matter observed in the universe, have spin one-half, gauge bosons, which describe the interactions between these fermions, have spin one, and a scalar particle known as the Higgs boson with spin zero, responsible for the mass of all fundamental particles of the SM. Concerning fermions, they come in two different types: six quarks with each two constituting one generation, and six leptons also made of three families as shown in Figure 1.1. Another important property of all fundamental fermions is their chirality. Quarks and Leptons can be either left-handed or right-handed, except Neutrinos, which come only with their left-handed version (and right-handed antiparticle). Each fundamental force is represented by a gauge boson: the photon γ as the fundamental particle mediating the electromagnetic force, the Z and W^\pm bosons mediating the weak force, and the gluons g mediating the strong force between the quarks. The last experimentally observed

fundamental particle, known as the Higgs boson h is a scalar boson that is responsible for giving all massive fundamental particles their mass [31, 32].

We mentioned that gauge symmetries play a fundamental role in explaining the particle content of the SM. These symmetries classify leptons and quarks into multiplets according to how they transform under the fundamental gauge symmetry of the SM, namely:

$$SU(2)_L \times U(1)_Y \times SU(3)_c.$$

The electromagnetic force, described by a $U(1)_{em}$ symmetry is a remnant symmetry of the electroweak symmetry $SU(2)_L \times U(1)_Y$ after its spontaneous symmetry breaking in the early universe.

The strong force based on *Quantum chromodynamics* (QCD) and mediated by the gluons and symmetric under $SU(3)_c$ (where c denotes the *color* quantum number) only acts on quarks, which are classified in triplet representation of $SU(3)_c$.

The weak interaction described by $SU(2)_L$ acts only on left-handed fermions and classifies them into doublets, leaving right-handed fermions as singlets. As for the hypercharge symmetry $U(1)_Y$, it acts on all the fundamental fermions of the SM and classifies them according to their hypercharge quantum number.

Since this manuscript is mostly concerned with the electroweak and scalar sectors of the SM, we describe in more detail its Lagrangian in the SM. We first start with its bosonic components encompassing the gauge fields W_μ^a with $a \in \{1, 2, 3\}$ corresponding to the three gauge fields of the weak interaction $SU(2)_L$, B_μ the hypermagnetic field of $U(1)_Y$, and the Higgs boson Φ :

$$\mathcal{L}_{EW}^b = |D_\mu \Phi|^2 + V_{SM}(\Phi) - \frac{1}{4} W_{\mu\nu}^a W_a^{\mu\nu} - \frac{1}{4} B_{\mu\nu} B^{\mu\nu}, \quad (1.1)$$

where $W_{\mu\nu}^a$ and $B_{\mu\nu}$ denote the field strength tensors:

$$W_{\mu\nu}^a = \partial_\mu W_\nu^a - \partial_\nu W_\mu^a + g f^{abc} W_\mu^b W_\nu^c, \quad (1.2)$$

$$B_{\mu\nu} = \partial_\mu B_\nu - \partial_\nu B_\mu, \quad (1.3)$$

where g is the coupling constant of the weak force and f^{abc} the Levi-Civita symbol. The covariant derivative necessary to make the Lagrangian invariant under local gauge transformations is defined as:

$$D_\mu \Phi = \partial_\mu \Phi + ig W_\mu^a \sigma^a \Phi + ig' B_\mu \Phi, \quad (1.4)$$

where g' denotes the hypermagnetic field coupling constant and σ^a the Pauli matrices.

In the SM, the Higgs field $\Phi = \begin{pmatrix} \phi_1 + i\phi_2 \\ \phi_3 + i\phi_4 \end{pmatrix}$ is a doublet of $SU(2)_L$ and therefore, the renormalizable SM Higgs potential invariant under $SU(2)_L \times U(1)_Y$ is given by:

$$V_{SM}(\Phi) = -\mu^2 \Phi^\dagger \Phi + \lambda (\Phi^\dagger \Phi)^2. \quad (1.5)$$

Note that without the coupling of the Higgs boson to the gauge bosons, the SM would suffer from unitarity problems in the scattering of longitudinally polarized W bosons $W_L^+ W_L^- \rightarrow W_L^+ W_L^-$ [33]. The scattering amplitude for such scattering (including all Feynman diagram contributions from the Z boson and photon) diverges for high values of center of mass energies s . Including a coupling of the gauge bosons with the Higgs, such as in (1.1), induces new terms in the scattering amplitude which eventually cancel the

L_l	e_r	u_l	u_r	d_l	d_r	Φ
-1	-2	1/3	4/3	1/3	-2/3	1

Table 1.1: Weak hypercharge for the SM particles. All other particles have 0 weak hypercharge.

dangerous divergent terms. This problem was one very important hint for the inevitable existence of some mechanism at the EW scale, which solves this unitarity problem, also known as the *No-Lose theorem*, acting as an "insurance" for the Large Hadron Collider finding something at that scale.

For the fermionic sector, the left-handed fermions are organized into doublets according to:

$$L_l = \begin{pmatrix} \nu_{e,l} \\ e_l \end{pmatrix} \quad \text{for leptons,} \quad \text{and} \quad Q_l = \begin{pmatrix} u_l \\ d_l \end{pmatrix} \quad \text{for quarks,} \quad (1.6)$$

where e denotes the lepton family, ν the neutrino, l denoting left-handed fermions, u up-type quarks, and d down type quarks. Right-handed fermions are singlets of $SU(2)_L$. The weak hypercharge of the particles is shown in Table 1.1. Since right-handed neutrinos are not part of the SM, they have vanishing weak hypercharge and they are singlets under $SU(2)_L$ in beyond SM models. One can now write down the Lagrangian invariant under $SU(2)_L \times U(1)_Y$ describing the interactions between the fermions, gauge bosons, and the Higgs :

$$\begin{aligned} \mathcal{L}_{EW}^f = & i\bar{L}_l\gamma^\mu D_\mu L_l + i\bar{e}_r\gamma^\mu \tilde{D}_\mu e_r + i\bar{Q}_l\gamma^\mu D_\mu Q_l + i\bar{u}_r\gamma^\mu \tilde{D}_\mu u_r + i\bar{d}_r\gamma^\mu \tilde{D}_\mu d_r \\ & y_e\bar{L}_l\Phi e_r + y_d\bar{Q}_l\Phi d_r + y_u\bar{L}_l\epsilon\Phi^* u_r + h.c, \end{aligned} \quad (1.7)$$

where γ^μ corresponds to the Gamma matrices, $y_{e,d,u}$ to the Yukawa couplings to the respective fermion and:

$$D_\mu = \partial_\mu + igW_\mu^a\sigma^a + ig'Y_w B_\mu, \quad (1.8)$$

$$\tilde{D}_\mu = \partial_\mu + ig'Y_w B_\mu, \quad (1.9)$$

$$\epsilon = i\sigma_2, \quad (1.10)$$

where Y_w corresponds to the respective weak hypercharge of each particle.

Without the interaction terms between the Higgs field and the fermions, known as the Yukawa sector, the fermions would be massless. Since mass terms of the form $m_f\bar{f}f = m_f(\bar{f}_l f_r + h.c)$ in the Lagrangian would explicitly break the $SU(2)_L \times U(1)_Y$ symmetry since f_l and f_r transform differently under $SU(2)_L$ and have different weak hypercharges, one needs to generate the masses of these fundamental particles while remaining invariant under these symmetries. A similar argument can be made for the gauge bosons, where gauge symmetries also prohibit mass terms for the Z and W^\pm gauge bosons. This shows the paramount importance of the Higgs field in the framework of the SM: the Higgs field dynamically generates a mass term for the massive fundamental particles following the well-known *Higgs Mechanism*, which we discuss in the next subsection.

1.1.1 The Higgs Mechanism

As mentioned earlier, gauge symmetries in the SM forbid mass terms for fermions and gauge bosons. This made it crucial to find a way to generate a mass term for particles while circumventing the need for preserving local gauge symmetry, which is mandatory to

describe interactions between particles in the SM. Several methods were proposed in the second half of the last century to perform this task, with the most prominent one being the *Higgs Mechanism* [5] based on a weakly coupled scalar field. Other alternative approaches include *technicolor* (experimentally ruled out after the observation of the Higgs boson) [34] and *composite Higgs models* [35].

Before electroweak symmetry breaking, the Higgs scalar field is in the symmetric phase and its vacuum expectation value is $\langle \Phi \rangle = \begin{pmatrix} 0 \\ 0 \end{pmatrix}$. In this symmetric phase the particles of the SM are massless and we have 4 massless gauge bosons $W_\mu^1, W_\mu^2, W_\mu^3$, and B_μ related to the symmetry $SU(2)_L \times U(1)_Y$ as well as four massless scalar fields corresponding to the complex Higgs doublet Φ . After the electroweak phase transition, the Higgs potential develops a new global minimum at a non-vanishing value and the Higgs field obtains a non-zero vacuum expectation value¹

$$\Phi = \frac{1}{\sqrt{2}} \begin{pmatrix} 0 \\ v_{sm} \end{pmatrix}, \quad (1.11)$$

and the $SU(2)_L \times U(1)_Y$ symmetry is spontaneously broken to $U(1)_{em}$, describing the symmetry of the electromagnetic force. Three of the four generators of $SU(2)_L \times U(1)_Y$ are broken, leading to the generation of three Goldstone bosons that are "eaten" by the W and Z bosons, which become massive. The fourth generator, which remains unbroken, is defined as:

$$Q = \frac{1}{2}\sigma_3 + \frac{1}{2}Y_\Phi = \begin{pmatrix} 1 & 0 \\ 0 & 0 \end{pmatrix}, \quad (1.12)$$

and corresponds to the electric charge. These massive states W^\pm and Z are a superposition of the previous massless gauge bosons. Using the symmetry broken phase expression of Φ in (1.1), one obtains mass terms for the following massive gauge boson degrees of freedom:

$$W_\mu^\pm = \frac{1}{2}(W_\mu^1 \mp iW_\mu^2), \quad (1.13)$$

$$Z_\mu = \cos(\theta_w)W_\mu^3 - \sin(\theta_w)B_\mu, \quad (1.14)$$

$$A_\mu = \sin(\theta)W_\mu^3 + \cos(\theta)B_\mu, \quad (1.15)$$

where $\tan(\theta_w) = \frac{g'}{g}$.

The third gauge field A_μ remains massless and corresponds to the photon field, the gauge boson of $U(1)_{em}$. The vacuum expectation value in the SM is always "neutral", meaning that the scalar potential cannot develop a minimum where all 4 generators of $SU(2)_L \times U(1)_Y$ are broken, which would then lead to the spontaneous breaking of $U(1)_{em}$ giving the photon a mass². The chosen minimum for the Higgs also provides a mass for the Higgs boson. The masses for the W and Z bosons as well as the Higgs Φ are given by:

$$m_W = \frac{gv_{sm}}{2}, \quad (1.16)$$

$$m_Z = \frac{v_{sm}}{2}\sqrt{g^2 + g'^2}, \quad (1.17)$$

¹ For an arbitrary vacuum expectation value $\Phi^T = \begin{pmatrix} a & b \end{pmatrix}$, one can always perform an $SU(2)_L \times U(1)_Y$ transformation to obtain $\Phi^T = \begin{pmatrix} 0 & c \end{pmatrix}$.

² In BSM models with several Higgs multiplets, it is possible to construct minima in the potential which also break the generator Q in (1.12) and therefore break electromagnetism.

$$m_\Phi = \sqrt{\lambda}v_{sm}. \quad (1.18)$$

For the fermions, recall that they couple to the Higgs boson via the Yukawa sector described in (1.7). The non-zero vacuum expectation value induces a mass term of the form:

$$\mathcal{L}_{EW}^f \supset y_f \frac{1}{\sqrt{2}} v_{sm} (\bar{f}_l f_r + \bar{f}_r f_l), \quad (1.19)$$

where y_f denotes the Yukawa coupling of the respective fermion f to the Higgs field. In the SM, the mass of the fermion is proportional to its coupling to the Higgs boson. This property was experimentally confirmed within the current experimental uncertainties at the LHC for the top quark, gauge bosons, and the bottom quark [29].

1.1.2 Shortcomings of the Standard Model

The Standard Model successfully describes most of the observed phenomena related to the interaction of fermions and bosons in the electroweak, strong, and scalar sectors. Despite this overwhelming success, the SM still cannot account for several theoretical and experimental shortcomings. This strongly motivates the existence of Beyond Standard Model physics, which can solve some of the theoretical problems as well as incorporate some of the experimentally observed deviations.

1.1.2.1 Theoretical issues in the SM

From a theoretical point of view, the SM based on quantum field theory does not incorporate a renormalizable theory of quantized gravity [36]. The SM, therefore, fails at describing the physics involving gravitational effects on particles at very high energy scales. This is also intertwined with the well-known *Hierarchy Problem* [37, 38, 39, 40]: why the Higgs mass is found to be at the Electroweak scale rather than at the Planck scale. In contrast to other particles found in the SM, which have their mass terms protected by gauge symmetries in the case of gauge bosons and chiral symmetries in the case of the fermions, the mass term of scalar particles is not protected from large radiative corrections by symmetry arguments and, assuming the existence of new physical phenomena at some energy scale Δ , the Higgs mass m_h^2 will receive quantum corrections proportional to Δ^2 . In order to obtain the experimentally observed value for the Higgs mass, one needs to choose the counterterms to be of the order of Δ^2 in order to cancel such a huge mass correction. This *fine-tuned* choice of the counterterm is usually called "unnatural" and needs an underlying mechanism that explains it.

Another important theoretical issue is the Strong CP-problem [41, 42]. The $SU(3)_C$ symmetry of the SM allows for a non-zero term of the form:

$$\mathcal{L} \supset \frac{\theta g_s^2}{32\pi^2} G_{\mu\nu} \tilde{G}^{\mu\nu}, \quad (1.20)$$

where g_s is the QCD coupling constant, $G^{\mu\nu}$ the gluon gauge field strength tensor, and $\tilde{G} = \frac{1}{2} \epsilon^{\mu\nu\rho\sigma} G_{\rho\sigma}$ the so-called dual tensor of $G^{\mu\nu}$. This term in the Lagrangian induces a non-zero neutron electric dipole moment $d_n \sim (10^{-16} \text{ e.cm})\theta$ [42]. However, precise experimental measurements put a large constraint on the electric dipole moment of the neutron, leading to $\theta_{exp} < 10^{-10}$ [29]. This term acts as a measure for the amount of T

and P violation in QCD [42]. It is therefore important to understand why this parameter is very small. The most promising solution for the strong CP-problem is the existence of an axion particle that dynamically leads to $\theta \rightarrow 0$ [42].

As a final example of theoretical issues within the standard model, we mention the cosmological constant problem [43, 44]. When interpreting the present acceleration rate of the universe in terms of a cosmological constant corresponding to a vacuum energy density, the value for the cosmological constant is extremely small, i.e. of the order of $\Lambda \approx 10^{-120} M_{\text{plank}}^4$. However, quantum corrections to this quantity, originating from SM fields, will lead to a larger contribution, and therefore we would expect, based on naturalness arguments, that these contributions should cancel each other in a fine-tuned way, leading to the very small value of the cosmological constant [43, 44].

1.1.2.2 Experimental problems with the SM

- *Neutrino masses*: Several experimental observations point to the existence of new physics beyond the SM. For instance, the observation of *flavor neutrino oscillations* in solar [45] and atmospheric neutrinos [46] makes it evident that neutrinos have a non-zero mass, in contrast to neutrinos being massless fermions in the SM. In order to explain this non-zero mass, several mechanisms are proposed, such as the Seesaw-mechanism [47, 48, 49]; where the SM is extended by heavier neutrinos, as well as radiative neutrino mass models [50]; where the neutrinos are massless at tree-level but acquire a mass through quantum corrections at loop level.
- *Dark Matter*: The observation, in the last century, of an anomalous rotation velocity for galaxies [51] and galaxy clusters [52] were the first hints for the existence of *dark matter*, which interacts with the usual observed matter in the universe mostly (if not exclusively) via gravitational effects. Modern evidence for the existence of dark matter includes the collisions between galaxy clusters, such as the bullet cluster [53], the role of dark matter in explaining the fluctuation in the CMB [54, 55], as well as baryon acoustic oscillations [56]. Dark matter is also a very important component in models explaining structure formation and how density fluctuations in the early universe eventually grow to produce galaxies and structures as observed today³. Since neutrinos interact feebly with other SM particles, it is natural to expect them to be a viable DM candidate. However, neutrinos have too light masses to explain the observed DM on their own since the Pauli exclusion principle will forbid fermions with masses smaller than a few keV from clumping together and inducing the gravitational force that leads to the observed rotation curves of galaxies. This constraint is also known as the Tremaine-Gunn bound on the mass of fermionic DM [59]. DM can also have a wave-like behavior when it is bosonic with a mass smaller than about 30 eV [60]. Since DM should be bound to a structure such as galaxies, the de Broglie wavelength of wave DM should be smaller than the size of dwarf galaxies. This gives a lower bound on the lightest possible candidate for DM, which should have a mass higher than $\sim 10^{-21} \text{eV}$ [60]. For a long time, a "Weakly Interacting Massive Particle" (WIMP) with masses of the order of hundreds of GeV was the leading candidate for particle DM [61, 62]. Solving the hierarchy problem using supersymmetry would also

³ The recent observations [57] by the James Webb Telescope of large galaxies at high redshift which are too large for their age is in contradiction to ΛCDM which typically predicts smaller galaxies at that redshift. In such a scenario, dark matter alone cannot explain how those galaxies became very massive at those early times. However, some authors [58] suggested that some of those galaxies are not as massive as initially thought and that they appear brighter and more massive due to black holes inside them heating the gas in the galaxy.

predict the existence of weakly interacting particles with a mass spectrum in that regime. This was then termed "*the WIMP miracle*" [61, 62] since such a particle would be a by-product of a well-motivated solution for the hierarchy problem as well as being accessible for direct searches for DM in underground DM detectors, being producible at colliders such as at the LHC and account for the correct relic abundance of Dark Matter observed in the universe. However, since WIMP DM wasn't found up to this point in any (in)direct search nor at the LHC, a paradigm shift to expand the quest for DM candidates to other lower and higher masses was followed in the last few years. This includes axion-like particles [42], primordial blackholes [63], WIMPs with very high masses, strongly interacting massive particles (SIMPs) [64], feebly interacting massive particles (FIMPs) [65], the misalignment mechanism related to axions [66], ect...

- *Matter-Antimatter Asymmetry*: Another important observational hint for the existence of physics beyond the SM is the imbalance between matter and antimatter [67, 68, 69]. Since nearby planets, solar systems, and galaxies consist of matter, one might suggest that the universe is separated into different regions where different patches might be either dominated by matter or antimatter. However, such a picture would lead to clear observational signatures in the form of large signals of gamma-rays emanating from the boundaries separating matter from antimatter. Since the observed gamma-ray background is diffuse, one can conclude that the observable universe is mostly made of matter. Other observations suggest a baryon asymmetry in the universe including the CMB background when trying to fit the multipoles in its fluctuations [54], as well as Big Bang Nucleosynthesis [70], where a matter-antimatter asymmetry is a crucial initial condition parameter for the calculation of the relic abundance of Helium, Deuterium and Lithium nuclei. From these observations, one can extract a measure for this asymmetry normalized by n_γ , the number density of photons in the universe [29]:

$$\eta_b = \frac{n_b - n_{\bar{b}}}{n_\gamma} = (6.115 \pm 0.038) \times 10^{-10}. \quad (1.21)$$

In order to obtain a matter-antimatter asymmetry in the universe, several conditions for mechanisms generating this asymmetry need to be met [71]:

- Baryon number violation,
- C, and CP violation,
- Departure from thermal equilibrium.

These conditions, also known as the *Sakharov conditions* [71], are in principle met in the SM. For instance, sphaleron processes, which are non-trivial field configurations interpolating between distinct degenerate vacua of the theory, are known to break $B + L$ quantum number [67, 68, 69], where B is the baryon number and L the lepton number. It is also known that several interactions in the SM are CP-violating due e.g. to a complex CKM matrix. One could also depart from thermal equilibrium in the early universe due to particle decoupling from the thermal plasma. However, since CP violation in the SM (which can lead to a matter-antimatter asymmetry) is too small to explain this asymmetry [69], it is very important to understand the processes that lead to this asymmetry. If one suggests that this asymmetry is one initial condition after the Big Bang, then inflation and baryon number-violating processes such as sphalerons would dilute such an asymmetry. Therefore, this puzzle constitutes one important research topic in the interface of particle physics and early universe cosmology.

In this thesis, we extend the Higgs sector of the SM with new Higgs doublets/singlets, leading to models that can alleviate some of the theoretical and experimental shortcomings of the SM. This includes, for example, proposing a mechanism to generate a matter-antimatter asymmetry using domain walls, which are a type of topological defect that can form in the early universe after the spontaneous breaking of a discrete symmetry. Before delving more into the details of the studied models, we start by introducing topological defects and, in particular, domain walls, since this thesis is centered around their properties.

1.2 TOPOLOGICAL DEFECTS

In particle physics, symmetries play a very important role. Spacetime symmetries related to the Poincaré group lead to the classification of particles into multiplets of mass and spin as the relevant quantum number. Internal symmetries, such as gauge symmetries, describe the interactions between different particles and classify the fundamental particles of the SM according to their quantum numbers (such as hypercharge, electric charge, colour, etc.). Since the SM cannot be the final description for the particle content of the whole universe, the possibility of having new particles and symmetries is worthy of a considerable investigation. Several BSM models lead to the existence of new symmetries, which might be spontaneously broken in the early universe.

In conventional scenarios describing the early universe cosmology, one assumes that in the aftermath of the electroweak spontaneous symmetry breaking, the Higgs field configuration is spatially homogeneous and that its value corresponds to one of the minima of the scalar field potential. However, in case that the vacuum manifold of the model is non-trivial and is made of several degenerate minima of the potential, one would expect that causally disconnected regions of the universe might be populated with different degenerate minima, since they cannot influence the choice of minimum in other regions of the universe. The Higgs field configuration in such a case could be inhomogeneous, and depending on the topology of the vacuum manifold, such scalar field configurations that interpolate between these minima can be stable [9, 8, 13].

In the following, we briefly describe the different types of these field configurations called *topological defects*, their formation mechanisms, as well as their potential impact on cosmology.

1.2.1 Types of Topological Defects

Topological defects are stable field configurations describing a region of space with higher energy compared with its surrounding regions. They represent a solution to the equation of motion of the scalar and gauge fields and can occur after spontaneous symmetry breaking in the early universe.

Topological defects are intrinsically related to the nature of the vacuum manifold \mathcal{M} of the theory [9, 13]. The vacuum manifold is made up of the set of all degenerate minima of the scalar potential. For instance, consider a theory invariant under a symmetry group G . After spontaneous symmetry breaking, the ground state of the theory is invariant under a

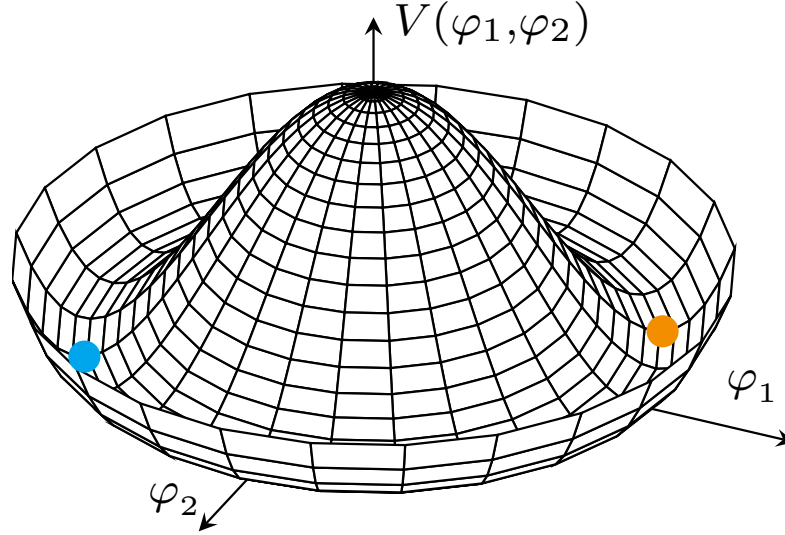


Figure 1.2: "Mexican-hat" potential showing two different but degenerate vacua $|0\rangle$ in orange, and $|0'\rangle = g|0\rangle$ in blue. This figure was generated using [72].

subgroup H , with $H \subset G$. For a vacuum state $|0\rangle$ of the potential, a group element $h \in H$ acts on $|0\rangle$ as follows:

$$h|0\rangle = |0\rangle, \quad (1.22)$$

keeping the vacuum state invariant, while a group element $g \in G$ acts on $|0\rangle$ as:

$$g|0\rangle = |0'\rangle, \quad (1.23)$$

where $|0'\rangle$ is a degenerate vacuum state of the potential and can be different than $|0\rangle$ as shown in Figure 1.2. One can therefore start with a vacuum state $|0\rangle$ and generate the set of degenerate vacua, i.e, the vacuum manifold \mathcal{M} by acting on $|0\rangle$ using elements $g \in G$ which do not keep $|0\rangle$ invariant. The vacuum manifold can then be identified with the coset space G/H [9, 13].

Depending on the topology of \mathcal{M} , one can obtain different types of topological defects. This topology can be identified according to the different homotopy groups $\pi_n(\mathcal{M})$ of \mathcal{M} . The n -th homotopy group of a manifold \mathcal{M} is the group whose elements are maps from points in the n -sphere to \mathcal{M} . Such maps that can be continuously deformed⁴ into each other are considered to be equivalent, and as such, the different maps that are equivalent to each other can be classified into equivalent classes. These equivalent classes are considered to be the elements of the group $\pi_n(\mathcal{M})$ since for every two equivalent classes of maps f_1 and f_2 , all the group identities are fulfilled [73]. For the zeroth homotopy group $\pi_0(\mathcal{M})$, the elements of the group are maps from the S_0 sphere (two points $x = \pm\infty$) to the elements of \mathcal{M} . Since such maps can be deformed into each other in the case when the vacuum manifold \mathcal{M} is connected, $\pi_0(\mathcal{M})$ is non-trivial only when \mathcal{M} is disconnected. The first homotopy group $\pi_1(\mathcal{M})$ is the group whose elements connect the 1-Sphere (a circle) to \mathcal{M} , while the second homotopy group $\pi_2(\mathcal{M})$ is the group whose elements are maps from the 2-sphere (the usual sphere in 3-dimensions) to \mathcal{M} . To illustrate the connection between these homotopy groups and the formation of topological defects, consider a scalar field configuration $\Phi(x)$, where we take the boundary condition of $\Phi(x)$ to lie on points

⁴ Two maps f_1 and f_2 can be continuously deformed into each other, if there exist a map $h(\alpha)$ where $\alpha \in [0, 1]$ such that $h(0) = f_1$ and $h(1) = f_2$.

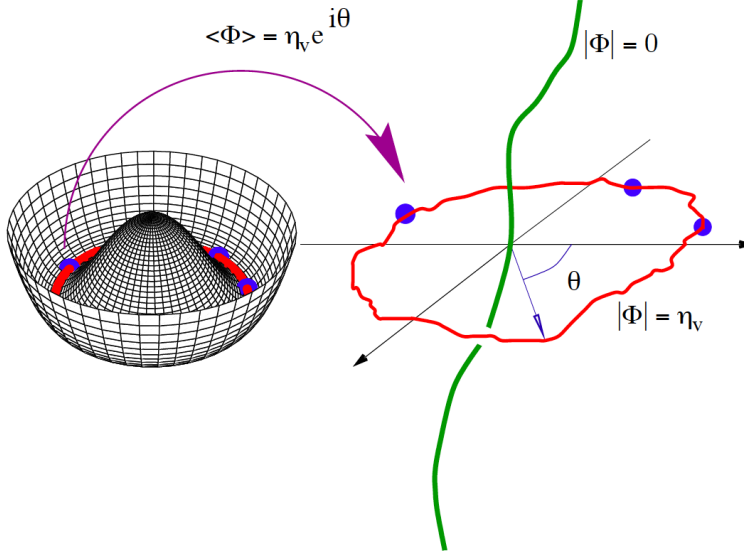


Figure 1.3: Scalar field potential of the abelian Higgs model showing a vacuum manifold S_1 on the left and the corresponding cosmic string spatial field configuration on the right. The Figure was taken from [74].

of the vacuum manifold \mathcal{M} , this means that for $x \in S_n^\infty$ (corresponding to an n -sphere with infinite radius) $\Phi(x \in S_n^\infty) \in \mathcal{M}$. Therefore, the function $\Phi_\infty := \Phi(x \in S_n^\infty)$ is an element of $\pi_n(\mathcal{M})$. If $\pi_n(\mathcal{M}) \neq I$ is non-trivial (with I denoting the identity) one says that Φ_∞ is topologically non-trivial and there must be some points in x (inside the interval bounded by S_n^∞) where the field configuration $\Phi(x)$ lies outside the vacuum manifold. To understand this argument, consider what happens to Φ_∞ as the radius R of the n -sphere is shrunk from infinity. Since $\Phi(x = R)$ will lie on the vacuum manifold and this mapping is also non-trivial, then as $R \rightarrow 0$ the field Φ will have several different values at a single point, which is unphysical. Therefore, there must be some points in the space enclosed by the boundary n -sphere, where the field configuration $\Phi(x)$ lies outside the vacuum manifold. Different topological defects can be characterized according to whether the $\pi_n(\mathcal{M})$ homotopy group is trivial or not:

- Zeroth homotopy group $\pi_0(\mathcal{M}) \neq I$: the vacuum manifold is made of disconnected points, as in the case of a Z_2 symmetry, or disconnected components. In this case, one can map the space points in S^0 such as $x = -\infty$ and $x = \infty$ to two disconnected components of \mathcal{M} . Due to the continuity of the field configuration, the scalar field $\Phi(x)$ interpolates between both vacua and will therefore lie outside of the vacuum manifold \mathcal{M} in some region of space (see Figure 1.4). This region is called a *kink*. In 3-dimensional space, this object is a 2-dimensional sheet called a *domain wall*.
- Fundamental homotopy group $\pi_1(\mathcal{M}) \neq I$: the vacuum manifold in this case is not simply connected, i.e., the manifold has non-contractible loops. The simplest model with such a vacuum manifold is the abelian Higgs model (see Figure 1.3), which is invariant under a $U(1)$ symmetry that breaks spontaneously to the identity. In such a case, the vacuum manifold $\mathcal{M} \simeq U(1)/1 \simeq S^1$ is a circle S^1 that describes the phase θ of the field $\langle \Phi \rangle = v e^{i\theta}$. Maps from S^1 in physical space to the vacuum manifold $\mathcal{M} = S^1$ cannot be continuously contracted to one point on \mathcal{M} and as we move around a closed circular path of S^1 in physical space (starting from a particular point and then back to it), one can wrap around the vacuum manifold an integer number of times $\pm 1, \pm 2, \pm 3$, ect... If we assume that for a given closed path in physical space, the vacuum manifold is wrapped one time ($\Delta\theta = 2\pi$), then by continuously

shrinking this path in physical space to a point, we cannot continuously change $\Delta\theta$ from 2π to 0 and therefore, there must be a point inside the circular path where the angle θ is undefined. Due to continuity in the field, the scalar field $\Phi(x)$ needs to vanish at that point. Obviously, at and in the vicinity of this point, the value of the scalar field is not an element of the vacuum manifold. In 3-dimensional space, this object becomes a 1-dimensional line with $\Phi = 0$ and is called a *cosmic string*.

- Second homotopy group $\pi_2(\mathcal{M}) \neq I$: in this case, the vacuum manifold has a two-dimensional hole, and the produced topological defect is one-dimensional and is called a *magnetic monopole*.

In the SM, the symmetry group G (considering only the electroweak sector) is $G = SU(2)_L \otimes U(1)_Y$, while the unbroken subgroup is $H = U(1)_{em}$. The vacuum manifold in this case is topologically equivalent to $G/H \simeq SU(2) \simeq S^3$, which is a 3-sphere. Since such an object is neither disconnected nor has holes, its zeroth as well as higher homotopy groups will be trivial, and no topological defects occur in the Standard Model [9].

1.2.2 Domain Walls

Since the focus of this thesis is on domain walls and their consequences, we shall now give a more detailed analysis of a simple model where domain walls form. As mentioned earlier, domain walls form whenever the vacuum manifold is made of disconnected components. The simplest model where this can occur is the real singlet scalar model, where a scalar field ϕ has the potential:

$$V_0(\phi) = -\frac{m_0^2}{2}\phi^2 + \frac{1}{4}\lambda\phi^4. \quad (1.24)$$

This potential is invariant under a Z_2 symmetry that acts on ϕ as:

$$\phi \xrightarrow{Z_2} -\phi. \quad (1.25)$$

When the scalar field acquires a non-zero vacuum expectation value (when $\mu < 0$), the possible minima are either $v_+ = \sqrt{\frac{m_0^2}{\lambda}}$ or $v_- = -\sqrt{\frac{m_0^2}{\lambda}}$. The vacuum manifold is then disconnected. Since both of these minima are degenerate, they have equal probability of occurring in a given region of the universe. In this case, causally disconnected regions in space can have either positive or negative vacuum expectation value, and the universe is separated into regions with different signs for the vacuum of ϕ . The different scalar field configurations need to obey the Klein-Gordon equation of motion:

$$\frac{\partial^2 \phi}{\partial t^2} - \frac{\partial^2 \phi}{\partial x^2} + \frac{\partial V_0(\phi)}{\partial \phi} = 0. \quad (1.26)$$

The homogeneous field configuration $\phi(x) = v_{\pm}$ is the lowest energy field configuration that satisfies this equation of motion. Another possibility is when two regions of the universe end with different minima v_{\pm} . Since the field configuration interpolating between two regions with minima having opposite signs needs to be continuous, the field will go out of the vacuum manifold inside the wall separating both regions. The profile of the field in that transition region needs to obey the Klein-Gordon equation (1.26). We show in Figure 1.4a the profile of $\phi(x)$:

$$\phi(x) = v_+ \tanh\left(\sqrt{\frac{\lambda}{2}}v_+x\right), \quad (1.27)$$

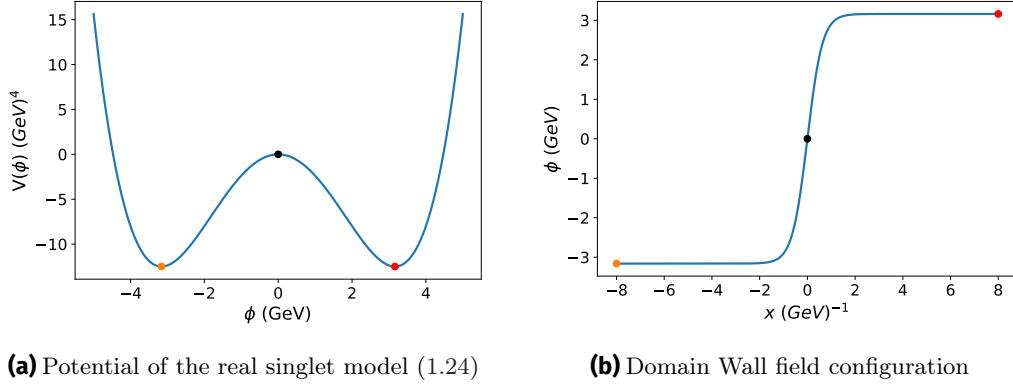


Figure 1.4: (a) Potential $V(\phi)$ of the real singlet scalar ϕ after spontaneous symmetry breaking with the minima v_- and v_+ denoted by an orange and red dot respectively. (b) Domain wall field profile with the field interpolating between the minima v_{\pm} and crossing $\phi = 0$ at $x = 0$ (denoted by a black dot in the potential).

which solves (1.26) with boundary conditions having minima with opposite signs. Inside the wall, the scalar field is zero and sits on top of the potential (see Figure 1.4b). Clearly, such a field configuration has a higher energy than the ground state field configuration, where the VEV of the scalar field is homogeneous everywhere. One would then naturally be interested in the stability of such a field configuration. However, in order to transition from this domain wall configuration to the true ground state of the vacuum (i.e. the homogeneous one), one needs to lift the scalar field in an infinite amount of space from its minimum (e.g. v_-) at one domain to the minimum v_+ . Such transformation can only be done by making the field cross the potential barrier in an infinite amount of space, which is a process that costs an infinite amount of energy and thus is not physically possible. Therefore, the domain wall field configuration (1.27) is deemed stable. Right after spontaneous symmetry breaking and assuming a non-zero temperature, the domains of space with different minima can be small enough for temperature fluctuations to lift the field to the other minimum. However, as the universe cools down below a temperature known as the Ginzburg temperature T_g [9], this process becomes suppressed, and regions of the universe are "frozen" in their respective minima.

Even though the field configuration of domain walls in this real singlet scalar Z_2 model seem very simple since the vacuum manifold in this case is made of two disconnected points, the case of realistic BSM models that also include the spontaneous breaking of a continuous symmetry (such as the electroweak symmetry [75, 76, 1] or Grand Unified Symmetries [77, 78]) alongside the discrete symmetry makes the picture considerably more challenging and phenomenologically much richer. In those more complicated models, the vacuum manifold would be made of disconnected submanifolds M_i with $i \in 1, \dots, n$. These submanifolds have a continuous structure, which gives us more freedom in choosing the vacua at both boundaries $+\infty$ and $-\infty$. These types of domain walls were already investigated in Grand Unified Theories [79, 77, 78] and Two-Higgs-Doublet-Models [76, 75, 6, 1]. One focus of this thesis is the study of these types of domain walls in extended Higgs sectors and the discussion of the different exotic phenomena that come with field configurations in such models, such as CP-violation and electric charge violation.

Having introduced topological defects and domain walls from a conceptual point of view, we delve, in the next subsection, into a more detailed description of the different formation mechanisms for domain walls after a phase transition in the early universe.

1.2.3 Phase Transitions in the Early Universe

Up to now, we have discussed how to construct the simplest field configuration that interpolates between two disconnected minima of the vacuum manifold after the spontaneous symmetry breaking of a discrete symmetry. In order to study the formation mechanisms for these defects, we first discuss how spontaneous symmetry breaking occurs in the early universe in the framework of phase transitions from a symmetry-restored phase of the scalar potential to a broken phase.

Since the universe after the Big Bang was very hot and dense, one needs to take into account the effective interaction of the scalar field with the thermal plasma. These interactions can induce large corrections to the scalar potential at high temperatures and induce a positive mass contribution in the quadratic terms, making the minimum of the potential at the origin of field space. As the temperature falls down, these positive contributions become smaller and the effective quadratic terms eventually turn negative, inducing non-zero minima in the scalar potential and leading to a spontaneous symmetry breaking.

We first start our discussion with a brief description of the effective thermal potential for the simple real singlet scalar model and demonstrate the evolution of this potential leading to a phase transition that seeds the formation of domain walls.

The full effective thermal potential of a scalar field in the thermal plasma is given by:

$$V_{tot}(\phi, T) = V_0(\phi) + V_{CW}(\phi) + V_{CT}(\phi) + V_T(\phi, T), \quad (1.28)$$

where $V_0(\phi)$ is the tree-level potential introduced in (1.24), $V_{CW}(\phi)$ denotes the Coleman-Weinberg effective potential loop corrections at zero-temperature [80], $V_{CT}(\phi)$ denotes the counterterms needed to renormalize the potential as well as keep the minima at $T = 0$ the same as the ones given by the tree-level potential. Finally, $V_T(\phi, T)$ denotes the thermal corrections at some temperature T .

Since we are only interested in applying the effective potential to obtain the evolution of the scalar potential in the early universe, leading to the phase transition, we only briefly discuss the different components of each contribution. We start with the Coleman-Weinberg potential describing the one-loop correction to the tree-level scalar potential $V_0(\phi)$. This is given in the \overline{MS} renormalization scheme by [80]:

$$V_{CW}(\phi) = \sum_j \frac{n_j}{64\pi^2} (-1)^{2s_j} m_j^4(\phi) \left(\ln \left(\frac{|m_j(\phi)|^2}{\mu^2} \right) - c_j \right), \quad (1.29)$$

where we sum over all particles j coupled to the scalar field ϕ , n_j the number of degrees of freedom for each particle species, $m_j(\phi)$ the mass for the particle species described as a function of the scalar field, μ the renormalization scale and c_j constants related to the nature of the particle and given by $c_j = 3/2$ for scalars and fermions, and $c_j = 5/6$ for gauge bosons. For our simple model of a real singlet scalar with the potential $V_0(\phi)$ (1.24), this mass term is given by $m_\phi^2 = \frac{\partial^2 V_0}{\partial \phi^2} = -m_0^2 + 3\lambda\phi^2$. The Coleman-Weinberg potential for the real singlet scalar is then given by:

$$V_{CW}(\phi) = \frac{1}{64\pi^2} (-m_0^2 + 3\lambda\phi^2)^2 \left(\ln \left(\frac{|-m_0^2 + 3\lambda\phi^2|}{\mu^2} \right) - 3/2 \right). \quad (1.30)$$

The terms in the counterterm potential are chosen in such a way that the minima of the potential $V_0(\phi) + V_{CW}(\phi)$ are the same as the tree-level potential minima:

$$V_{CT}(\phi) = \frac{\delta m_0^2}{2} \phi^2 + \frac{\delta \lambda}{4} \phi^4. \quad (1.31)$$

This condition is implemented using:

$$\frac{\partial V_{CW}}{\partial \phi} \Big|_{\phi=v_{\pm}} = \frac{\partial V_0}{\partial \phi} \Big|_{\phi=v_{\pm}}, \quad (1.32)$$

$$\frac{\partial^2 V_{CW}}{\partial \phi^2} \Big|_{\phi=v_{\pm}} = \frac{\partial^2 V_0}{\partial \phi^2} \Big|_{\phi=v_{\pm}}. \quad (1.33)$$

The thermal potential $V_T(\phi, T)$ is computed using quantum field theory methods at finite temperature. It takes into account the thermal plasma of fermions and bosons in the early universe as a thermal bath interacting with the scalar field. This contribution can be written as [81]:

$$V_T(\phi, T) = \sum_j \frac{n_j T^4}{2\pi^2} J_{\pm} \left(\frac{m_j^2(\phi)}{T^2} \right), \quad (1.34)$$

where J_{\pm} denote the thermal integrals defined by [81]:

$$J_+ \left(\frac{m_j^2(\phi)}{T^2} \right) = - \int_0^{\infty} dx x^2 \ln \left[1 + \exp \left[-(x^2 + m_j^2(\phi)/T^2)^{-1/2} \right] \right], \text{ for fermions.} \quad (1.35)$$

$$J_- \left(\frac{m_j^2(\phi)}{T^2} \right) = \int_0^{\infty} dx x^2 \ln \left[1 - \exp \left[-(x^2 + m_j^2(\phi)/T^2)^{-1/2} \right] \right], \text{ for bosons.} \quad (1.36)$$

In the high-temperature limit $m^2(\phi)/T^2 \ll 1$, we can simplify these thermal integrals as follows [81]:

$$J_+(x) = -\frac{7\pi^4}{360} + \frac{\pi^2}{24}x + \frac{1}{32}x^2 \ln \left(\frac{|x|}{a_f} \right) + \mathcal{O}(x^3), \quad (1.37)$$

$$J_-(x) = -\frac{\pi^4}{45} + \frac{\pi^2}{12}x - \frac{\pi}{6}x^{3/2} - \frac{1}{32}x^2 \ln \left(\frac{|x|}{a_b} \right) + \mathcal{O}(x^3), \quad (1.38)$$

where $a_b = \pi^2 \exp(3/2 - 2\gamma_E)$ and $a_f = 16\pi^2 \exp(3/2 - 2\gamma_E)$. For the case of the simple real singlet scalar field, the leading order in the thermal potential is given by:

$$V_T(\phi, T) = \frac{\lambda}{8} T^2 \phi^2 + T^4 \frac{\pi^2}{90}. \quad (1.39)$$

The full one-loop effective thermal potential $V_{tot}(\phi, T)$ is then:

$$\begin{aligned} V_{tot}(\phi, T) = & \left(-\frac{m_0^2}{2} + \frac{\lambda}{8} T^2 \right) \phi^2 + \frac{1}{4} \lambda \phi^4 + \frac{\delta m_0^2}{2} \phi^2 + \frac{\delta \lambda}{4} \phi^4 \\ & + \frac{1}{64\pi^2} (-m_0^2 + 3\lambda \phi^2)^2 \left(\ln \left(\frac{|-m_0^2 + 3\lambda \phi^2|}{\mu^2} \right) - 3/2 \right). \end{aligned} \quad (1.40)$$

We can now study the evolution of the real singlet scalar field potential as a function of temperature T . For sufficiently high temperatures, the effective quadratic term in (1.40) turns positive and the potential is in the symmetric phase with its minimum at $\phi = 0$ as shown in Figure 1.5, therefore, the Z_2 symmetry is restored. As the temperature falls, the effective quadratic term vanishes at a temperature $T_c = \frac{2m_0}{\sqrt{\lambda}}$. As the universe cools further down below this temperature, the effective quadratic term turns negative and the potential develops non-zero global minima. The extremum at the origin of field space is now metastable. If during this evolution a potential barrier between the extremum at $\phi = 0$ and the new minimum develops, the transition from the symmetric phase to the broken

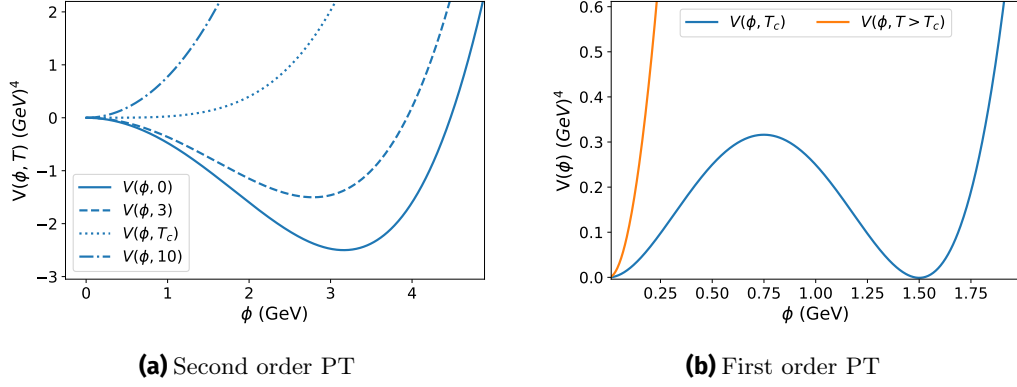


Figure 1.5: (a) Temperature evolution for a second-order phase transition. (b) Scalar potential for a first-order phase transition. At temperature $T = T_c$, the minimum at $\phi = 0$ and $\phi \approx 1.5 \text{ GeV}$ are degenerate and separated by a potential barrier.

phase requires either an external perturbation for the field to jump over the barrier (such as thermal excitations) or a quantum tunneling to the new minimum. In this case, the phase transition from the symmetric phase to the broken phase is said to be first order, since the order parameter of the phase transition (in this case, the vacuum expectation value of the scalar) as a function of temperature is discontinuous. In the absence of large perturbations and if the tunneling rate is very small, the universe can remain trapped in the symmetric phase, a phenomenon called *vacuum trapping* [23, 21, 24].

When no potential barrier develops during the thermal evolution, the scalar field rolls over to the new minimum in a classical way, and the phase transition is said to be second order since the evolution of the order parameter is continuous as a function of the temperature. In the case when the change in the order parameter occurs very smoothly as a function of temperature, the phase transition is said to be a crossover.

Now that we can describe the evolution of the scalar potential in the early universe, we discuss in the next subsection the mechanisms for the formation of domain walls upon the phase transition that leads to the spontaneous symmetry breaking of the discrete symmetry.

1.2.4 Formation of Domain Walls in the Early Universe

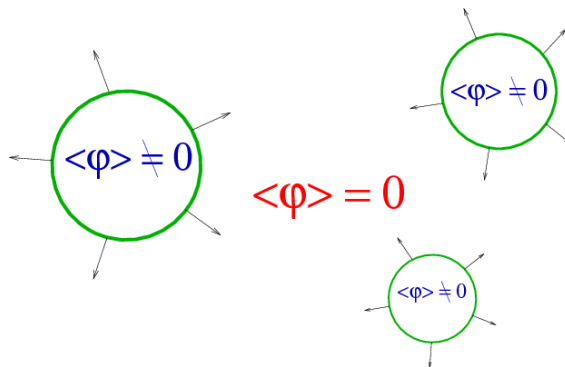


Figure 1.6: Bubbles of broken phase $\langle \phi \rangle \neq 0$ nucleating and expanding in the region of unbroken phase $\langle \phi \rangle = 0$. The figure was taken from [68].

As the universe cools down below the temperature T_c , the transition to the new minimum can be either first order, second order, or a crossover. In the case of a first-order phase transition, several bubbles of the new minimum nucleate (see Figure 1.6), with the bubble wall separating both the regions with broken and unbroken phases. These bubbles have a spatial scalar field profile $\phi(r)$ that interpolates between the new minimum at $r = 0$ and the symmetric phase minimum $\phi = 0$ at large r . Such a scalar field configuration has a non-zero energy, and the bubbles have a tension σ that tends to shrink it. When the bubbles are big enough to make the vacuum energy (the difference in the potential between $V(0)$ and $V(v_{\pm})$) large enough to overcome the bubble tension, the bubbles grow in the space of the false symmetric vacuum and after some time the universe is eventually filled with the new minimum with a non-zero VEV. Bubbles with opposite signs for the VEV will collide, and the size of domains with different VEVs will be largely determined by the dynamics of the bubbles [8, 13].

For a second-order phase transition, the VEV of the scalar field changes continuously from 0 to either $v_{\pm}(T)$. This evolution can, however, occur differently in different regions of the universe due to local thermal and quantum fluctuations. In this case, the picture for determining the size of causally disconnected regions with opposite signs for the VEV is more complicated [8, 13].

- We first start with describing the formation of domain walls in a first-order phase transition, which is also known as *the Kibble mechanism* [8]. After nucleation, the bubbles grow and expand in the region of the false vacuum. Bubbles with VEVs having different signs collide. For a phase transition with bubble nucleation rate per unit volume equal to Γ and bubble velocity v , the typical size of domains ξ when they collide is proportional to a length scale ξ [73]:

$$\xi = \left(\frac{v}{\Gamma}\right)^{1/4}. \quad (1.41)$$

Domains with different VEVs adjacent to each other will then have domain walls between them, while those with the same VEV will grow bigger, merging together. The subsequent evolution of the walls in this case is related to minimizing the tension of the walls, which we discuss later.

- In a second-order phase transition, the order parameter of the phase transition (vacuum expectation value of the scalar field) changes continuously at each point in space. This makes calculating the typical size of domains considerably more complicated. The idea which Kibble used in [8] was to find an upper bound for distances that can be in causal contact at some cosmic time τ . Since information cannot travel faster than light, two regions of the universe that are separated by a distance larger than the cosmic horizon $l > c\tau$ with c being the speed of light, cannot be in causal contact. For two regions that are separated by a distance larger than l , the choice of the vacuum cannot be correlated.

Another limit is to determine the correlation length beyond which thermal fluctuations after the phase transition cannot change the chosen vacuum, also known as the *Ginzburg length* l_G [13]. Consider, for instance, a domain with VEV v_+ and a size l_+ . If the Ginzburg length l_G is smaller than l_+ , then the domain is frozen in the minimum v_+ . If $l_G > l_+$, then thermal fluctuations caused by the thermal plasma can make the domain jump to the vacuum v_- . At some temperature T , the energy necessary to change a volume of space d^3 from v_+ to v_- is given by $\Delta E(T) = d^3 \Delta V_{tot}(T)$, while the thermal energy available from thermal fluctuation is proportional to T [73]. Therefore, in order for a domain to not be affected by thermal fluctuations, its size

needs to be bigger than $d_{min}(T) \approx (\Delta V_{tot}(T)/T)^{\frac{1}{3}}$. In our simplified toy model, this length scale is:

$$d_{min}(T) \approx (\Delta V_{tot}(T)/T)^{\frac{1}{3}} \approx \left(\frac{(2m_0^2 - \frac{1}{2}\lambda T^2)^2}{16\lambda T} \right)^{\frac{1}{3}}. \quad (1.42)$$

Domains with a smaller scale can fluctuate from one vacuum to another. An important requirement for this transition to occur is that all points of the domain fluctuate to the other vacuum at the same time. Therefore, it is needed to find the size of the correlation length for the scalar field at a given temperature T . This can be approximated by [8, 73]:

$$\bar{\xi}(T) = \frac{1}{m_\phi(T)} = \frac{1}{\sqrt{2m_0^2 - \frac{1}{2}\lambda T^2}}. \quad (1.43)$$

In case $\bar{\xi}(T) > d_{min}(T)$, domains with size smaller than $d_{min}(T)$ will have enough energy to change the sign of their vacuum. For $\bar{\xi}(T) < d_{min}(T)$, a domain with length larger than $\bar{\xi}(T)$ will remain frozen even though there is enough thermal energy to flip its sign. Therefore the Ginzburg temperature T_G corresponds to the temperature when $\bar{\xi}(T_G) = d_{min}(T_G)$ [73] and the Ginzburg length is $l_G = \bar{\xi}(T_G)$. The number density of walls in a unit volume is then proportional to $(1/l_G)^3$.

After the formation of domain walls, several domains merge together and expand. At some point, the walls percolate and we obtain domains which are infinite in size, leading to infinite walls in physical space as well as regions of space with finite walls.

The subsequent evolution of the domain walls after percolation is largely dependent on the domain wall tension $\sigma = \int_{-\infty}^{+\infty} dx \frac{1}{2} \left(\frac{\partial \phi}{\partial x} \right)^2 + V(\phi)$ as well as the friction forces acting on the domain walls due to its interaction with the thermal plasma.

The tension pressure p_t is proportional to $\frac{\sigma}{R_{wall}}$ [73, 11], where R_{wall} denotes the curvature radius of the domain. This pressure tends to stretch the wall so that the inhomogeneities and field gradients in the y and z axes are relaxed, so that the surface area of the walls gets minimized. The friction pressure p_f caused by the interaction of the wall with the thermal plasma is proportional to the momentum transfer of the particles reflecting off the wall times their number density n . To illustrate these effects, we add the interaction of the ϕ scalar field with another boson ξ and fermion Ψ via the terms in the Lagrangian:

$$\mathcal{L}_{int} \supset -\frac{1}{2} \tilde{\lambda} \phi^2 \xi^2 + y \phi \bar{\Psi} \Psi, \quad (1.44)$$

which leads to particles masses: $m_\xi = \sqrt{\tilde{\lambda}} v_+$ and $m_\Psi = y v_+$. For a particle with momentum k_z in the z -direction, the reflection probability in the thin wall limit can be approximated by [9]:

$$R(k_z) = \frac{\mu^2}{4k_z^2 + \mu^2} \text{ for bosons} \quad \text{and} \quad R(k_z) = \frac{m_\Psi^2}{k_z^2 + m_\Psi^2} \text{ for fermions}, \quad (1.45)$$

where $\mu = 2\sqrt{\frac{2}{\lambda}} \tilde{\lambda} v_+$. We start by considering the friction p_f^b caused by bosons. We distinguish two different regimes: high temperatures $T \gg \mu$ and low temperatures $T \ll \mu$. In the limit of higher temperatures $T \gg \mu$, particles have large momenta and are typically transmitted through the wall. Therefore, only particles with momenta $k_z < \mu$ exercise a friction pressure on the wall. The momentum transfer can be approximated by $\Delta p \approx \mu v$, where v is the particle's velocity. The friction pressure is then given by [9]:

$$p_f^b \propto \Delta p n_b^3 \sim v \mu^2 T^2 \quad (1.46)$$

For small temperatures $T \ll \mu$, particles have small momenta compared with μ and are therefore mostly reflected off the domain wall. The momentum transfer in this case is given by $\Delta p \approx vT$ leading to a friction pressure [9]:

$$p_f^b \propto \Delta p n_b^3 \sim vT^4, \quad (1.47)$$

where we used $n_b \propto T^3$ for the number density of relativistic particles in the plasma. Note that for non-relativistic particles, $m_\xi \gg T$ and the particles decouple from the thermal plasma and their number density in physical space as well as their interaction with the wall, is suppressed.

For fermions, after following the same analysis, we obtain:

$$p_f^f \propto \Delta p n_f^3 \sim vm_\Psi^4, \text{ for the limit } T \gg m_\Psi, \quad (1.48)$$

$$p_f^f \propto \Delta p n_f^3 \sim vT^4, \text{ for the limit } T < m_\Psi, \quad (1.49)$$

where we used the number density $n_f \propto m_\Psi^3$ for low energy fermions at high temperatures. For this simple toy model, we find that the friction pressure goes down with temperature. However, in more complicated models such as the ones studied in this manuscript, there will be non-trivial interactions between the wall and the thermal plasma, such as CP and electric charge-violating scatterings. These types of interactions could lead to a more complicated analysis of the domain wall evolution after their formation.

Assuming the simplified picture in the toy model, we find that domain walls tend to stretch under the force of their surface tension. The friction term is initially high and damps this evolution. As the universe cools down, the friction force gets smaller and the evolution of the domain walls is largely determined by the tension force [11], which grows the domain radius R_{wall} up to the horizon size. At this stage, the domain walls are known to be in the *scaling regime* and the energy density of domain walls scales with $\rho_{wall} \propto \sigma t^{-\nu}$, where $\nu \approx 1$ according to numerical simulations [9].

Having described the mechanisms by which domain walls form and evolve after a spontaneous symmetry breaking of a discrete symmetry, we discuss in the next subsection some of the consequences of domain wall formation on the early universe cosmology.

1.2.5 Consequences of Domain Walls on the Early Universe

Topological defects in the early universe present non-trivial field configurations that "trap" in their core the symmetric phase of the universe prior to the spontaneous symmetry breaking. Since the energy density of these field configurations is concentrated in a very thin one-dimensional object (in the case of cosmic strings), and thin two-dimensional layers (in the case of domain walls), one might inquire about the consequences of these objects on the early universe cosmology.

We discussed in the previous subsection that, after their formation, domains percolate and merge, creating large domain walls that subsequently stretch due to their surface tension to the horizon size when the damping pressure from the friction of the walls with the thermal plasma becomes negligible. At this point of their evolution, the domains have a volume $\propto R_{wall}^3$, therefore, assuming that the domain wall surface is of the order R_{wall}^2 , the energy density of domain walls scales as [11, 9]:

$$\rho_{wall} \propto \frac{\sigma}{R_{wall}^3} \times R_{wall}^2 = \frac{\sigma}{R_{wall}}. \quad (1.50)$$

Therefore, during this scaling regime, the energy density of the domain wall scales with $R_{wall}^{-1} \propto t^{-1}$, where t is the physical time⁵. We assume in the following that the scaling regime, based on this simple dimensional analysis, is a good approximation [83]. One can then approximate the evolution of the energy density of domain walls as a function of t [11]:

$$\rho_{wall} = \mathcal{A} \frac{\sigma}{t}, \quad (1.51)$$

where $\mathcal{A} \approx 0.8 \pm 0.1$ is a numerical factor [11]. During the radiation domination era, the scale factor is proportional to $a \propto t^{1/2}$ while $R_{wall} \propto t^{-1}$. Radiation energy density scales as $a^{-4}(t) \propto t^{-2}$, and therefore the energy density of domain walls dilutes much slower than radiation. A similar argument is also found for the scaling of domain walls during the matter domination era. Therefore, the domain walls will come to dominate the energy density of the universe at some point in time, in contradiction with present observations. This domination time t_{dom} can be approximated by [11, 9]:

$$\rho_c(t_{dom}) = \rho_{wall}(t_{dom}) = \frac{3H^2(t)M_{pl}^2}{8\pi}, \quad (1.52)$$

where M_{pl} is the Planck mass scale. This then translates into [11]:

$$t_{dom} = \frac{3M_{pl}^2}{8\pi\mathcal{A}\sigma} \approx 1,46 \times 10^{13} s \times \frac{\text{GeV}^3}{\sigma}. \quad (1.53)$$

For the simple real singlet toy model [73]: $\sigma = \frac{2\sqrt{2}}{3} \frac{m_0^3}{\lambda} = \frac{2\sqrt{2}}{3} \sqrt{\lambda} v_+^3$. Therefore, for $\lambda \approx 1$ and $v_+ \approx 100$ GeV, the domain walls dominate the energy density of the universe prior to the decoupling of CMB photons, which would considerably alter the homogeneity in the CMB spectrum. Since any inhomogeneities in the CMB fluctuations should be $\delta\rho/\rho < 10^{-5}$ to be consistent with PLANCK measurements [54], this translates into a limit on $\sigma < \mathcal{O}(\text{MeV})^3$ known as the Zel'dovich-Kobzarev-Okun bound [12].

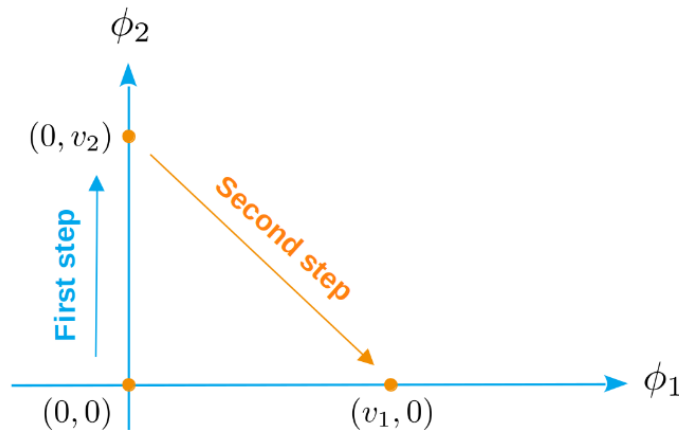


Figure 1.7: Example for a two-step phase transition in a model with two scalar fields ϕ_1 and ϕ_2 .

From this bound, as well as the bound from domain walls energy density domination, also known as the "domain wall problem", it is clear that particle physics models with discrete

⁵ This rate, however, is in slight disagreement with the results obtained from particular numerical simulations for the energy density of domain walls [82], which show a scaling $\rho_{wall} \propto t^{-\nu}$ with ν slightly different from one.

symmetries that get spontaneously broken before the MeV scale can be ruled out. However, there are several ways to circumvent this domain wall problem. This can be achieved by either proposing a mechanism to annihilate the domain walls in the early universe before they dominate the energy density of the universe (and therefore be consistent with the cosmological observations) or by dynamically lowering the energy density of domain walls in such a way as to make $\sigma(t) < \mathcal{O}(\text{MeV})^3$. This can be done in four possible ways [9, 11, 84, 13, 85, 75]:

- *Discrete symmetry restoration and non-restoration in the early universe:* We showed earlier that a phase transition in the early universe occurs from a symmetric phase to a broken phase. It can occur, however, that some parameter points do not lead to symmetry restoration at very high temperatures. In such a case, the universe would already be in the broken phase at very high temperatures, and as such, no domain walls form according to the Kibble mechanism. It is also possible that the discrete symmetry is restored again at lower temperatures. This typically can happen in several extensions of the SM, such as the real-singlet extension or the N2HDM [23]. In this phenomenon, also known as a two-step phase transition (see Figure 1.7), one scalar field develops a VEV, leading to the breaking of a discrete symmetry, and later the global minimum is at a value where the first scalar field has a zero VEV, while the other scalar field develops a non-zero VEV. In such a case, the domain wall network will be spontaneously annihilated since the global minimum for the scalar field responsible for the domain wall field configuration is at $\phi = 0$.
- *Bias in the distribution of the degenerate minima:* In this case, the population of initial domains with v_+ and those with v_- is not equal, leading to the the creation of smaller regions with one minimum inside a larger region with the other minimum. The regions having the minimum with the least population will decay quickly, and we eventually end with a single homogeneous vacuum within the Horizon radius. It is possible to obtain this behaviour if the scalar field before the symmetry breaking was initially misaligned from $\phi = 0$.
- *Bias in the potential:* if the discrete symmetry is explicitly broken by terms in the Lagrangian, such as:

$$\mathcal{L} \supset V(\phi) + a_1\phi + a_2\phi^3, \quad (1.54)$$

then the negative and positive minima in the potential (in the case of a Z_2 symmetry) are not degenerate anymore. One minimum is higher than the other, and for large symmetry-breaking terms, only one minimum survives. If the bias term is small enough to lead to the formation of domain walls, the global minimum e.g. v_+ will expand in the region of the local minimum v_- . Due to the pressure coming from the difference in the potential energy, the universe will, after some time, be mostly populated by the global minimum v_+ , leading to the decay of the domain wall network, and the domain wall energy density gets smaller. One can then approximate the evolution of the energy density of the domain walls as an exponential suppression [11, 85, 75]:

$$\rho_{wall} = \mathcal{A} \frac{\sigma}{t} e^{-at}, \quad (1.55)$$

where the coefficient a is a function of the bias terms a_1 and a_2 in the potential (1.54).

- *Inflation:* assuming that the spontaneous symmetry breaking of the discrete symmetry occurs before inflation, the domains will grow in size exponentially during inflation,

leading to one single domain populating the horizon. Therefore, the energy density of the domain wall network cannot dominate the energy density of the horizon.

Since it is relatively easy to circumvent the domain wall problem, particle physics models with (approximate) discrete symmetries are still viable and can lead to several new phenomena, as we will see in the next few chapters. This includes the possibility of electric charge-violating or CP-violating scalar field configurations as well as electroweak symmetry restoration in the early universe, leading also to the exciting prospect of using domain walls in order to generate a matter-antimatter asymmetry. One can also use domain walls in order to facilitate phase transitions which can be catalyzed inside the core of the walls, offering the possibility of rescuing parameter points from the phenomenon of *vacuum trapping* as well as constraining model parameter points where the global minimum of the potential is not the experimentally observed electroweak minimum.

In the next chapter, we introduce several well-motivated extensions of the Higgs sector, which incorporate discrete symmetries that can lead to the formation of different types of domain wall scalar field configurations.

2 | EXTENDED HIGGS SECTORS

In this chapter, we introduce several well-motivated extensions to the scalar sector of the SM, such as the Two-Higgs-Doublet Model (2HDM) and the Next-to-Two-Higgs-Doublet Model (N2HDM). We briefly discuss their particle content, current theoretical and experimental constraints on the allowed parameter space of these models, and their vacuum structure and symmetries that lead to the formation of domain walls in these models.

2.1 THE NEED FOR AN EXTENDED HIGGS SECTOR

The SM Higgs doublet is the minimal realization of the Higgs mechanism that provides the correct values of the masses for the gauge bosons and fermions in nature and is compatible with the observed phenomenology at the LHC [29]. However, the lepton and quark sectors come in several generations and flavors. This raises the question of whether the Higgs sector realized in nature is the minimal SM one or whether several additional Higgs multiplets are also waiting for discovery. Furthermore, as we discussed in the previous chapter, the SM has several shortcomings. In this section, we summarize how an extended Higgs sector can alleviate some of them.

Supersymmetry provides an elegant solution to the hierarchy problem since particles entering the loop diagrams contributing to the mass corrections will be canceled by loop diagrams from their corresponding supersymmetric partners. However, a Higgs sector containing at least two Higgs doublets is required in supersymmetric models [86]. This is the case because the superpartner of the Higgs, i.e. the Higgsinos, are fermions which enter into the triangle diagrams contributing to anomalies in the Gauge sector [86, 87]. Since this contribution from this extra fermion introduced by the supersymmetric version of the SM needs to be canceled in order for the theory to be anomaly-free and consistent, it is necessary to add a new Higgs scalar doublet whose fermionic superpartner would cancel the anomalous contribution from the first Higgsino. Another reason for the necessity of an extra Higgs doublet in supersymmetric versions of the SM is to make the superpotential holomorphic [86], a constraint that forbids the complex conjugate of the Higgs doublet from appearing in the Lagrangian. Since this complex conjugate Higgs doublet is necessary in the SM to make sure that both quarks of the $SU(2)_L$ doublet acquire a mass, one needs another Higgs doublet to give a mass to the other type of quarks.

Other dynamical solutions to the hierarchy problem, such as the relaxion model [88], also incorporate a non-minimal scalar sector [88]. In those models, the new scalar ϕ acts as a new contribution to the effective mass term of the Higgs Lagrangian, which, upon turning negative, gives a non-zero VEV to the Higgs and makes the subsequent rollover of ϕ suppressed. This then leads to the selection of a mass term for the Higgs at the electroweak scale.

Concerning the matter-antimatter asymmetry, electroweak baryogenesis [68, 89, 90] constitutes one of the most studied solutions for dynamically generating the observed asymmetry. It relies on using bubbles nucleated during a first-order electroweak phase transition in the early universe when sphaleron processes are still active. Since the SM electroweak phase transition is a crossover [68, 69], it is mandatory to extend the Higgs sector to induce a first-order phase transition. This can be done, for instance, in models where the SM Higgs doublet is extended by a real singlet scalar [91] to induce a barrier between the symmetric and the broken phase at tree level in the early universe, or by also extending it with another doublet under $SU(2)_L$ as the 2HDM, where it is possible to get a first order phase transition at the one-loop level [92]. An extra Higgs singlet/doublet extension to the SM can also be applied in order to obtain the necessary amount of CP-violation needed for electroweak baryogenesis [93, 94, 95, 96, 97, 25].

Extra Higgs multiplets can also provide dark matter candidates [28, 25, 98, 99, 100, 101, 102, 103, 104, 105], such as the real singlet extension to the SM [98] with a Z_2 symmetry that forbids the decay of this extra scalar to SM particles. In the case of the Inert-Doublet-Model [99], the model is also invariant under a Z_2 symmetry that only acts on the second Higgs doublet. This doublet does not acquire a vacuum expectation value after EWPT, and the Z_2 symmetry is therefore not spontaneously broken. One can then choose either the CP-even or CP-odd Higgs boson as the lightest inert particle that will constitute the dark matter. The 2HDM extended with a pseudoscalar a (2HDM+a) [105] also constitutes a benchmark model for DM searches at the LHC.

For the purposes of this manuscript, extending the minimal SM Higgs sector is motivated from the point of view of the extra symmetries that can be imposed on these models. An extended Higgs sector allows several possibilities for new discrete or continuous symmetries related to the Higgs multiplets. When these discrete symmetries are spontaneously broken, either alone or alongside the EW symmetry, domain walls form in the early universe, which can lead to several interesting and novel effects, such as scalar field configurations that break CP and electric charge [75, 76, 1]. This can lead to exotic phenomena like photons becoming massive in the core of the domain wall or top quark being reflected/transmitted off the wall as bottom quarks [1]. Domain walls coupled to the Higgs scalar can also induce other interesting effects: the possibility of restoring the EW symmetry inside and in the vicinity of the wall [2], induce EW vacuum decay when the EW minimum is metastable [3], source the EW phase transition in the early universe [21], and generate a matter-antimatter asymmetry in the early universe [106, 107, 108, 109].

One important constraint to take into account when extending the Higgs sector with n multiplets is to keep the ρ parameter, defined by [25]:

$$\rho = \frac{m_W^2}{m_Z^2 \sin^2(\theta_w)} = \frac{\sum_{i=1}^n [I_i(I_i + 1) - \frac{1}{4}Y_i^2]v_i}{\sum_{i=1}^n \frac{1}{2}Y_i^2 v_i}, \quad (2.1)$$

near one, where Y_i represents the hypercharge and I_i the weak isospin of the scalar. Such a requirement puts a very strict constraint on the possible extensions of the scalar sector. In the case of extra doublets or singlets, this requirement is fulfilled naturally [25] since for singlets $I_s = Y_s = 0$, and for doublets $I_d(I_d + 1) = \frac{3}{4}Y_d^2$ and $Y_d^2 = 1$.

In the following, we discuss the two extended Higgs sectors that are studied in this manuscript, namely the 2HDM and the N2HDM, and also state some of the theoretical and experimental constraints that are imposed on them.

2.2 THE TWO-HIGGS-DOUBLET MODEL

In this section, we briefly introduce the general 2HDM and the notation used in this work. In the 2HDM, the Standard Model Higgs sector is extended by an extra doublet charged under $SU(2)_L \times U(1)_Y$. The general renormalizable scalar potential invariant under the SM symmetries is given by:

$$\begin{aligned}
V_{2\text{HDM}} = & m_{11}^2 \Phi_1^\dagger \Phi_1 + m_{22}^2 \Phi_2^\dagger \Phi_2 + m_{12}^2 (\Phi_1^\dagger \Phi_2 + h.c.) \\
& + \frac{\lambda_1}{2} (\Phi_1^\dagger \Phi_1)^2 + \frac{\lambda_2}{2} (\Phi_2^\dagger \Phi_2)^2 + \lambda_3 (\Phi_1^\dagger \Phi_1) (\Phi_2^\dagger \Phi_2) + \lambda_4 (\Phi_1^\dagger \Phi_2) (\Phi_2^\dagger \Phi_1) \\
& + \left[\frac{\lambda_5}{2} (\Phi_1^\dagger \Phi_2)^2 + \lambda_6 (\Phi_1^\dagger \Phi_1) (\Phi_1^\dagger \Phi_2) + \lambda_7 (\Phi_2^\dagger \Phi_2) (\Phi_1^\dagger \Phi_2) + h.c. \right]. \quad (2.2)
\end{aligned}$$

Depending on the choice of the parameters, the potential can also be invariant under various discrete or continuous symmetries relating the Higgs doublets Φ_1 and Φ_2 [6]. The general Yukawa sector of the theory is then given by [25]:

$$\mathcal{L}_{Yukawa} = y_{ij}^1 \bar{\psi}_i \psi_j \Phi_1 + y_{ij}^2 \bar{\psi}_i \psi_j \Phi_2, \quad (2.3)$$

where ψ_i and ψ_j denote the different fermion generations. It is generally not possible to diagonalize the Yukawa couplings of fermions when having them couple to both Higgs doublets, which will then lead to the Yukawa coupling matrices y_{ij}^1 and y_{ij}^2 which are not simultaneously diagonalizable. Therefore, couplings between quarks of different flavor are then possible and this will lead to flavor-changing neutral currents (FCNCs) at tree level [25]. Such phenomena are, however, strongly constrained experimentally, which makes it necessary to forbid them in the 2HDM. To avoid this problem, one can impose that fermions with the same quantum numbers couple to the same Higgs doublet, while other fermions couple to the second one. This can be achieved by imposing a Z_2 discrete symmetry on the Yukawa sector according to which the scalar doublets transform in this way:

$$\Phi_1 \xrightarrow{Z_2} \Phi_1, \quad \Phi_2 \xrightarrow{Z_2} -\Phi_2. \quad (2.4)$$

There are therefore 4 types of 2HDMs depending on the choice of scalar doublets that fermions couple to [26, 25]:

	u-type	d-type	leptons	Q	u_R	d_R	L	l_R
Type 1	Φ_2	Φ_2	Φ_2	+	-	-	+	-
Type 2	Φ_2	Φ_1	Φ_1	+	-	+	+	+
Type 3 (lepton specific)	Φ_2	Φ_2	Φ_1	+	-	-	+	+
Type 4 (Flipped)	Φ_2	Φ_1	Φ_2	+	-	+	+	-

Table 2.1: Types of Yukawa couplings between the fermions and the scalars in the 2HDM and the charges of the fermions under the Z_2 symmetry [25]. Q and L denote left-handed quark and lepton $SU(2)_L$ doublets while u_R , d_R and l_R denote $SU(2)_L$ right-handed singlets.

The scalar potential which respects $SU(2)_L \times U(1)_Y \times Z_2$, is then given by:

$$\begin{aligned}
V_{2\text{HDM}} = & m_{11}^2 \Phi_1^\dagger \Phi_1 + m_{22}^2 \Phi_2^\dagger \Phi_2 + \frac{\lambda_1}{2} (\Phi_1^\dagger \Phi_1)^2 + \frac{\lambda_2}{2} (\Phi_2^\dagger \Phi_2)^2 + \lambda_3 (\Phi_1^\dagger \Phi_1) (\Phi_2^\dagger \Phi_2) \\
& + \lambda_4 (\Phi_1^\dagger \Phi_2) (\Phi_2^\dagger \Phi_1) + \left[\frac{\lambda_5}{2} (\Phi_1^\dagger \Phi_2)^2 + h.c. \right]. \quad (2.5)
\end{aligned}$$

After electroweak symmetry breaking, the Higgs doublets acquire a vacuum expectation value. The 2HDM includes 8 scalar degrees of freedom. In our work we adopt the non-linear representation [76, 110] to parameterize the vacua:

$$\Phi_1 = U\tilde{\Phi}_1 = U\frac{1}{\sqrt{2}}\begin{pmatrix} 0 \\ v_1 \end{pmatrix}, \quad (2.6)$$

$$\Phi_2 = U\tilde{\Phi}_2 = U\frac{1}{\sqrt{2}}\begin{pmatrix} v_+ \\ v_2 e^{i\xi} \end{pmatrix}, \quad (2.7)$$

where U is an element of the $SU(2)_L \times U(1)_Y$ group that is given by:

$$U(x) = e^{i\theta(x)} \exp\left(i\frac{\tilde{g}_i(x)\sigma_i}{2v_{sm}}\right), \quad (2.8)$$

where θ , $\tilde{g}_{1,2,3}$ are the hypercharge angle and Goldstone modes of $SU(2)_L$ respectively, σ_i denote the Pauli matrices, the generators of $SU(2)$, and v_{sm} is the vacuum expectation value of the SM Higgs doublet. Using this representation, we can separate the Goldstone modes of the $SU(2)_L$ and hypercharge symmetries from the physical vacuum parameters v_1 , v_2 , v_+ , and ξ .

There are 3 possible types of vacua in the 2HDM: charge-breaking, CP-breaking and neutral [25]:

- The most general one occurs when v_+ is non-zero and the vacuum is therefore charge-breaking:

$$\tilde{\Phi}_1 = \frac{1}{\sqrt{2}}\begin{pmatrix} 0 \\ v_1 \end{pmatrix}, \quad \tilde{\Phi}_2 = \frac{1}{\sqrt{2}}\begin{pmatrix} v_+ \\ v_2 e^{i\xi} \end{pmatrix}. \quad (2.9)$$

Such a vacuum is obviously non-physical as it will induce a mass to the photon and allow charge-breaking interactions such as the decay of electrons into neutrinos or the decay of top quarks into bottom quarks via new decay channels [111].

- The CP-breaking vacuum occurs when the phase ξ between the two doublets is non zero:

$$\tilde{\Phi}_1 = \frac{1}{\sqrt{2}}\begin{pmatrix} 0 \\ v_1 \end{pmatrix}, \quad \tilde{\Phi}_2 = \frac{1}{\sqrt{2}}\begin{pmatrix} 0 \\ v_2 e^{i\xi} \end{pmatrix}. \quad (2.10)$$

This type of vacua leads to CP-breaking Yukawa couplings and can be useful in the context of baryogenesis to generate the needed CP-violation.

- Neutral vacuum where $\xi = 0$ and $v_+ = 0$:

$$\tilde{\Phi}_1 = \frac{1}{\sqrt{2}}\begin{pmatrix} 0 \\ v_1 \end{pmatrix}, \quad \tilde{\Phi}_2 = \frac{1}{\sqrt{2}}\begin{pmatrix} 0 \\ v_2 \end{pmatrix}. \quad (2.11)$$

Such a vacuum can accommodate the SM vacuum expectation value (VEV) when $\sqrt{v_1^2 + v_2^2} = v_{sm} = 246$ GeV.

In [112, 113], it was shown that if a parameter point leads to a neutral minimum, then such a minimum of the potential will always lie above any possible charge or CP-breaking minima. Throughout this work, we will only consider that all regions of the universe ended up with a neutral vacuum after electroweak spontaneous symmetry breaking. Figure 2.1

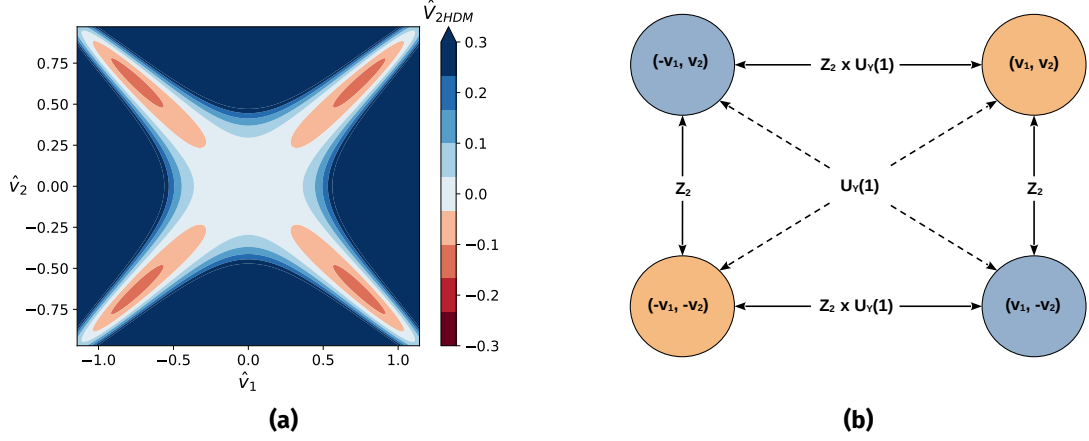


Figure 2.1: (a) Potential of the 2HDM in dimensionless units using PP I (3.31), with $\hat{v}_i = v_i/v_{sm}$. (b) Symmetry relations between the minima in the potential.

shows the dimensionless potential $\hat{V}_{2HDM} = V_{2HDM}/(m_h^2 v_{sm}^2)$ with rescaled parameters $\hat{v}_i = v_i/v_{sm}$, where $m_h = 125.09$ GeV corresponds to the SM-like Higgs boson. One distinguishes degenerate vacua that can be related by a Z_2 transformation, as for example, $(\hat{v}_1, -\hat{v}_2)$ and (\hat{v}_1, \hat{v}_2) , as well as degenerate minima that are related by a hypercharge transformation $U_Y(1)$ such as $(-\hat{v}_1, -\hat{v}_2)$ and (\hat{v}_1, \hat{v}_2) . We also have a multitude of other degenerate vacua that can be obtained from the latter ones, by using a gauge transformation of $SU(2) \times U_Y(1)$.

Taking into account a neutral minimum, the minimization conditions for the 2HDM deduced from setting the first derivative of V_{2HDM} to zero at the vacuum are given by:

$$m_{11}^2 + \frac{1}{2}(v_1^2 \lambda_1 + v_2^2 \lambda_{345}) - m_{12}^2 \frac{v_2}{v_1} = 0, \quad (2.12)$$

$$m_{22}^2 + \frac{1}{2}(v_1^2 \lambda_2 + v_1^2 \lambda_{345}) - m_{12}^2 \frac{v_1}{v_2} = 0, \quad (2.13)$$

where $\lambda_{345} = \lambda_3 + \lambda_4 + \lambda_5$.

The particle content of the CP-conserving 2HDM includes 5 physical Higgs scalars: two CP-even with masses m_h and m_H , one CP-odd with a mass m_A and two charged Higgs bosons with a degenerate mass m_C . In order to compute the mass eigenvalues present in the Higgs doublets, we parametrize the fluctuations around the EW minimum as follows:

$$\Phi_1 = \frac{1}{\sqrt{2}} \begin{pmatrix} \phi_1^+ \\ v_1 + \rho_1 + ia_1 \end{pmatrix}, \quad \Phi_2 = \frac{1}{\sqrt{2}} \begin{pmatrix} \phi_2^+ \\ v_2 + \rho_2 + ia_2 \end{pmatrix}, \quad (2.14)$$

where ϕ_1^+ , ϕ_2^+ , ρ_1 , ρ_2 , a_1 , and a_2 represent the Higgs degrees of freedom in the interaction basis. By plugging these expression for Φ_1 and Φ_2 in (2.5), we obtain the mass matrices:

$$\mathcal{M}_\rho^2 = \left[\frac{\partial^2 V_{2HDM}}{\partial \rho_i \partial \rho_j} \right] = \begin{pmatrix} m_{12}^2 \frac{v_2}{v_1} + \lambda_1 v_1^2 & -m_{12}^2 + \lambda_{345} v_1 v_2 \\ -m_{12}^2 + \lambda_{345} v_1 v_2 & m_{12}^2 \frac{v_2}{v_1} + \lambda_2 v_2^2 \end{pmatrix}, \quad (2.15)$$

$$\mathcal{M}_a^2 = \left[\frac{\partial^2 V_{2HDM}}{\partial a_i \partial a_j} \right] = \begin{pmatrix} -\lambda_5 v_2^2 m_{12}^2 \frac{v_2}{v_1} & \lambda_5 v_1 v_2 - m_{12}^2 \\ \lambda_5 v_1 v_2 - m_{12}^2 & -\lambda_5 v_1^2 + m_{12}^2 \frac{v_1}{v_2} \end{pmatrix}, \quad (2.16)$$

$$\mathcal{M}_C^2 = \left[\frac{\partial^2 V_{2HDM}}{\partial \phi_i^+ \partial \phi_j^-} \right] = \begin{pmatrix} -\frac{(\lambda_4 + \lambda_5)}{2} v_2^2 + m_{12}^2 \frac{v_2}{v_1} & \frac{(\lambda_4 + \lambda_5)}{2} v_1 v_2 - m_{12}^2 \\ \frac{(\lambda_4 + \lambda_5)}{2} v_1 v_2 - m_{12}^2 & -\frac{(\lambda_4 + \lambda_5)}{2} v_1^2 + m_{12}^2 \frac{v_1}{v_2} \end{pmatrix}. \quad (2.17)$$

To obtain the physical degrees of freedom, we diagonalize these mass matrices by using the mass eigenstates h , H for the CP-even Higgs fields, A for the CP-odd Higgs field, and C for the charged Higgs field. These mass eigenstates are related to the interaction states via the transformations:

$$\begin{pmatrix} h \\ H \end{pmatrix} = R \begin{pmatrix} \rho_1 \\ \rho_2 \end{pmatrix} = \begin{pmatrix} \cos(\alpha) & \sin(\alpha) \\ -\sin(\alpha) & \cos(\alpha) \end{pmatrix} \begin{pmatrix} \rho_1 \\ \rho_2 \end{pmatrix}, \quad (2.18)$$

where α represents the mixing angle between the CP-even Higgs bosons and R diagonalizes the mass matrix \mathcal{M}_ρ^2 . For the CP-odd and charged part, we diagonalize the mass matrices using the angle β defined by $\tan(\beta) = \frac{v_2}{v_1}$ such that the mass eigenstates are related to the interaction eigenstates by:

$$\begin{pmatrix} G_0 \\ A \end{pmatrix} = R_\beta \begin{pmatrix} a_1 \\ a_2 \end{pmatrix} = \begin{pmatrix} \cos(\beta) & \sin(\beta) \\ -\sin(\beta) & \cos(\beta) \end{pmatrix} \begin{pmatrix} a_1 \\ a_2 \end{pmatrix}, \quad (2.19)$$

$$\begin{pmatrix} G^\pm \\ C \end{pmatrix} = R_\beta \begin{pmatrix} \phi_1^\pm \\ \phi_2^\pm \end{pmatrix} = \begin{pmatrix} \cos(\beta) & \sin(\beta) \\ -\sin(\beta) & \cos(\beta) \end{pmatrix} \begin{pmatrix} \phi_1^\pm \\ \phi_2^\pm \end{pmatrix}, \quad (2.20)$$

where G_0 and G^\pm correspond to the massless Goldstone bosons that will be eaten by the gauge bosons W and Z . The mass eigenvalues for the CP-odd and charged Higgs particles are given by:

$$m_A^2 = \frac{m_{12}^2}{\sin(\beta)\cos(\beta)} - \lambda_5 v_{sm}^2, \quad (2.21)$$

$$m_C^2 = \frac{m_{12}^2}{\sin(\beta)\cos(\beta)} - \frac{(\lambda_4 + \lambda_5)}{2} v_{sm}^2, \quad (2.22)$$

Using the mass parametrization, one can trade the parameters in the scalar potential with physical parameters such as the masses of the physical scalars, the ratio between the 2 vevs of the doublets $\tan(\beta) = \frac{v_2}{v_1}$, the standard model vev $v_{sm} = 246$ GeV and the mixing angle α . The potential parameters are therefore given by:

$$\lambda_1 = \frac{1}{v_1^2} \left(-m_{12}^2 \tan(\beta) + m_h^2 \cos^2(\alpha) + m_H^2 \sin^2(\alpha) \right), \quad (2.23)$$

$$\lambda_2 = \frac{1}{v_2^2} \left(-m_{12}^2 \tan(\beta) + m_h^2 \sin^2(\alpha) + m_H^2 \cos^2(\alpha) \right), \quad (2.24)$$

$$\lambda_3 = \frac{1}{v_1 v_2} \left(m_{12}^2 + \sin(\alpha) \cos(\alpha) m_h^2 - \sin(\alpha) \cos(\alpha) m_H^2 \right) - \lambda_4 - \lambda_5, \quad (2.25)$$

$$\lambda_4 = \frac{m_{12}^2}{v_1 v_2} - 2 \frac{m_C^2}{v_{sm}^2} + \frac{m_A^2}{v_{sm}^2}, \quad (2.26)$$

$$\lambda_5 = \frac{m_{12}^2}{v_1 v_2} - \frac{m_A^2}{v_{sm}^2}, \quad (2.27)$$

$$m_{11}^2 = m_{12}^2 \tan(\beta) - \frac{\lambda_1}{2} v_1^2 - \frac{\lambda_3 + \lambda_4 + \lambda_5}{2} v_2^2, \quad (2.28)$$

$$m_{22}^2 = m_{12}^2 \tan(\beta) - \frac{\lambda_2}{2} v_1^2 - \frac{\lambda_3 + \lambda_4 + \lambda_5}{2} v_1^2. \quad (2.29)$$

The term m_{12}^2 softly breaks the Z_2 symmetry, leading the formed domain walls to be unstable and therefore to annihilate some time after their formation. When dealing with domain walls in the 2HDM, we set $m_{12}^2 = 0$ and leave the effects of a small non-vanishing value for future studies.

In the 2HDM, both the CP-even Higgs scalars can couple to the gauge bosons W^\pm and Z . One defines the coupling of a CP-even Higgs scalar to the gauge bosons g_{h_iVV} normalized by the coupling $g_{h_{SM}VV}$ in the SM by:

$$C_{hVV} = \frac{g_{hVV}}{g_{h_{SM}VV}} = \cos(\beta - \alpha), \quad C_{HVV} = \frac{g_{HVV}}{g_{h_{SM}VV}} = \sin(\beta - \alpha). \quad (2.30)$$

Note that in the limit $\beta - \alpha \approx 0$, the coupling of h to the gauge bosons is the same as in the SM. The other CP-even Higgs does not interact with the SM gauge bosons in that case, which is known as the *Alignment limit* [25].

2.3 THE NEXT-TO-TWO-HIGGS-DOUBLET-MODEL

This section briefly introduces the Next-to-Two-Higgs-Doublet model and the needed notation used in our work. For a comprehensive review of this model, the reader is referred to [26, 114, 115], which includes the phenomenology of this model, and to [23] for a detailed discussion on its thermal history.

In the N2HDM, the standard model Higgs sector is extended with an extra $SU(2)_L \times U(1)_Y$ doublet Φ_2 and an additional real singlet Φ_s . The Higgs sector potential is given by:

$$\begin{aligned} V_{N2HDM} = & m_{11}^2 \Phi_1^\dagger \Phi_1 + m_{22}^2 \Phi_2^\dagger \Phi_2 - m_{12}^2 (\Phi_1^\dagger \Phi_2 + h.c.) + \frac{\lambda_1}{2} (\Phi_1^\dagger \Phi_1)^2 + \frac{\lambda_2}{2} (\Phi_2^\dagger \Phi_2)^2 \\ & + \lambda_3 (\Phi_1^\dagger \Phi_1) (\Phi_2^\dagger \Phi_2) + \lambda_4 (\Phi_1^\dagger \Phi_2) (\Phi_2^\dagger \Phi_1) + \left[\frac{\lambda_5}{2} (\Phi_1^\dagger \Phi_2)^2 + h.c. \right] \\ & + \frac{m_s^2}{2} \Phi_s^2 + \frac{\lambda_6}{8} \Phi_s^4 + \frac{\lambda_7}{2} \Phi_s^2 (\Phi_1^\dagger \Phi_1) + \frac{\lambda_8}{2} \Phi_s^2 (\Phi_2^\dagger \Phi_2) \\ & + \left[a_1 \Phi_s + a_3 \Phi_s^3 + b_1 (\Phi_1^\dagger \Phi_1) \Phi_s + b_2 (\Phi_2^\dagger \Phi_2) \Phi_s + c_1 (\Phi_1^\dagger \Phi_2 \Phi_s + h.c.) \right]. \end{aligned} \quad (2.31)$$

Similar to the 2HDM and in order to avoid flavor-changing neutral currents [25], one imposes a Z_2 symmetry that acts on the scalar fields in the following way:

$$\Phi_1 \rightarrow \Phi_1, \quad \Phi_2 \rightarrow -\Phi_2, \quad \Phi_s \rightarrow \Phi_s. \quad (2.32)$$

This symmetry is softly broken by the terms $m_{12}^2 (\Phi_1^\dagger \Phi_2 + h.c.)$ and $c_1 (\Phi_1^\dagger \Phi_2 \Phi_s + h.c.)$. The Yukawa sector transforms under this symmetry in the same way as the 2HDM (see Table 2.1). When the parameters a_1 , a_3 , b_1 , b_2 , and c_1 are zero, the potential also allows for a discrete symmetry Z'_2 , which only acts on the singlet:

$$\Phi_s \rightarrow -\Phi_s. \quad (2.33)$$

In this work, we aim to study the influence of DW field configurations on the restoration of the EW symmetry inside the wall [2], as well as the EW vacuum decay into deeper minima of the potential in the case of the N2HDM with an exact Z'_2 symmetry [3]. We therefore assume that the Z'_2 breaking terms are enough to avoid the cosmological domain wall problem, but are still sufficiently small and therefore can be negligible in the discussion of the vacuum structure and model phenomenology. This can occur, for example, if the relevant scale of Z'_2 breaking is the Planck scale since quantum gravity effects are known to break any discrete symmetries [15]. In such a case, one can avoid the cosmological domain

wall problem while still having a similar phenomenology to the Z'_2 symmetric N2HDM potential (where $a_1, a_3, b_1, b_2,$ and c_1 are zero)¹.

After electroweak and Z'_2 spontaneous symmetry breaking, the scalar doublets and singlet acquire a vacuum expectation value. The most general vacuum can be written as:

$$\langle \Phi_1 \rangle = U \langle \tilde{\Phi}_1 \rangle = U \frac{1}{\sqrt{2}} \begin{pmatrix} 0 \\ v_1 \end{pmatrix}, \quad \langle \Phi_2 \rangle = U \langle \tilde{\Phi}_2 \rangle = U \frac{1}{\sqrt{2}} \begin{pmatrix} v_+ \\ v_2 e^{i\xi} \end{pmatrix}, \quad \langle \Phi_s \rangle = v_s, \quad (2.34)$$

where U is an element of the $SU(2)_L \times U(1)_Y$ group that is given by:

$$U = e^{i\theta} \exp \left(i \frac{\tilde{g}_i \sigma_i}{2v_{sm}} \right), \quad (2.35)$$

with θ and \tilde{g}_i denoting the Goldstone modes of the scalar doublets, σ_i the Pauli matrices and $v_{sm} \approx 246$ GeV the standard model vacuum expectation value.

Just like in the 2HDM, the scalar doublets admit three possible types of vacua, which we discussed extensively in the previous chapter. The most general one, where $v_+ \neq 0$, breaks the electromagnetism symmetry $U(1)_{em}$ and gives a mass to the photon. Consequently, such vacua are physically not allowed at present time. The second type occurs when the phase between the two scalar doublets ξ does not vanish. Such a vacuum is CP-violating as it generates an imaginary mass to the fermions via the Yukawa sector. Due to constraints from electron dipole moment experiments [116], such CP-violating vacua should have very small values for ξ to be realized in nature. The third type is the neutral vacuum, occurring when $v_+ = 0$ and $\xi = 0$. In this work, we consider the case when the singlet scalar acquires a vacuum expectation value $v_s \neq 0$, which breaks Z'_2 spontaneously and leads to the formation of domain walls in the early universe.

Taking into account a neutral minimum, the minimization conditions for the N2HDM deduced from the setting the first derivative of V_{N2HDM} to zero at the vacuum are given by:

$$m_{11}^2 + \frac{1}{2}(v_1^2 \lambda_1 + v_2^2 \lambda_{345} + v_s^2 \lambda_7) - m_{12}^2 \frac{v_2}{v_1} = 0, \quad (2.36)$$

$$m_{22}^2 + \frac{1}{2}(v_1^2 \lambda_2 + v_2^2 \lambda_{345} + v_s^2 \lambda_8) - m_{12}^2 \frac{v_1}{v_2} = 0, \quad (2.37)$$

$$m_s^2 + \frac{1}{2}(v_1^2 \lambda_7 + v_2^2 \lambda_8 + v_s^2 \lambda_6) = 0, \quad (2.38)$$

$$(2.39)$$

The particle spectrum of the N2HDM includes 3 CP-even Higgs particles with masses denoted as m_{h_1}, m_{h_2} and m_{h_3} , one CP-odd particle with mass m_A and two charged Higgs bosons m_{H^\pm} . It is more advantageous to express the potential parameters in terms of physical quantities such as the masses of the physical particles and $\tan(\beta) = v_2/v_1$. This is achieved by diagonalizing the mass matrix M_ρ^2 (see (2.40)) given in the interaction basis (ρ_1, ρ_2, ρ_3) , where $\rho_{1,2,3}$ correspond to field expansions around the neutral vacua $v_{1,2,s}$ in (2.34):

$$M_\rho^2 = \begin{pmatrix} v^2 \lambda_1 \cos(\beta)^2 + m_{12}^2 \tan(\beta) & v^2 \lambda_{345} \cos(\beta) \sin(\beta) - m_{12}^2 & v v_s \lambda_7 \cos(\beta) \\ v^2 \lambda_{345} \cos(\beta) \sin(\beta) - m_{12}^2 & v^2 \lambda_2 \sin(\beta)^2 + m_{12}^2 / \tan(\beta) & v v_s \lambda_8 \sin(\beta) \\ v v_s \lambda_7 \cos(\beta) & v v_s \lambda_8 \sin(\beta) & v_s^2 \lambda_6 \end{pmatrix},$$

¹ Note that these symmetry breaking terms lead to a bias between the two minima $\pm v_s$, which leads to the decay of the DW network at some time t_{ann} . This annihilation time is dependent on $a_1, a_3, b_1, b_2,$ and c_1 . In case the annihilation occurs at the MeV scale, the generated gravitational waves signal from DW annihilation is in the nanohertz regime, potentially explaining the PTA signals [18, 19].

$$(2.40)$$

where $v^2 = v_1^2 + v_2^2$. This mass matrix is diagonalized using a rotation matrix R which fulfills the requirement $RM_\rho^2 R^T = \text{diag}(m_{h_1}^2, m_{h_2}^2, m_{h_3}^2)$, where the masses $m_{h_{1,2,3}}$ correspond to the masses of the CP-even Higgs bosons in the physical mass basis (h_1, h_2, h_3) . The diagonalizing matrix R is parametrized using the mixing angles α_1, α_2 and α_3 as:

$$R = \begin{pmatrix} c(\alpha_1)c(\alpha_2) & s(\alpha_1)c(\alpha_2) & s(\alpha_2) \\ -(c(\alpha_1)s(\alpha_2)s(\alpha_3) + s(\alpha_1)c(\alpha_3)) & c(\alpha_1)c(\alpha_3) - s(\alpha_1)s(\alpha_2)s(\alpha_3) & c(\alpha_2)s(\alpha_3) \\ -c(\alpha_1)s(\alpha_2)c(\alpha_3) + s(\alpha_1)s(\alpha_3) & -(c(\alpha_1)s(\alpha_3) + s(\alpha_1)s(\alpha_2)c(\alpha_3)) & c(\alpha_2)c(\alpha_3) \end{pmatrix}, \quad (2.41)$$

where $c(\alpha_i)$ denotes $\cos(\alpha_i)$ and $s(\alpha_i)$ denotes $\sin(\alpha_i)$. The values of the mixing angles are constrained between $-\pi/2$ and $\pi/2$. We adopt the conventional mass hierarchy $m_{h_1} < m_{h_2} < m_{h_3}$. Note that the interaction basis (ρ_1, ρ_2, ρ_3) is related to the physical mass basis (h_1, h_2, h_3) by:

$$\begin{pmatrix} h_1 \\ h_2 \\ h_3 \end{pmatrix} = R \begin{pmatrix} \rho_1 \\ \rho_2 \\ \rho_3 \end{pmatrix}. \quad (2.42)$$

One can then relate the potential parameters and the masses of the scalars in the N2HDM using the following formulas:

$$\lambda_1 = \frac{1}{v_1^2} \left(-m_{12}^2 \tan(\beta) + \sum_i m_{h_i}^2 R_{i1}^2 \right), \quad (2.43)$$

$$\lambda_2 = \frac{1}{v_2^2} \left(-\frac{m_{12}^2}{\tan(\beta)} + \sum_i m_{h_i}^2 R_{i2}^2 \right), \quad (2.44)$$

$$\lambda_3 = \frac{1}{v_1 v_2} \left(m_{12}^2 + \sum_i R_{i2} R_{i1} m_{h_i}^2 \right) - \lambda_4 - \lambda_5, \quad (2.45)$$

$$\lambda_4 = \frac{m_{12}^2}{v_1 v_2} - 2 \frac{m_{H^\pm}^2}{v^2} + \frac{m_A^2}{v^2}, \quad (2.46)$$

$$\lambda_5 = \frac{m_{12}^2}{v_1 v_2} - \frac{m_A^2}{v^2}, \quad (2.47)$$

$$\lambda_6 = \frac{1}{v_s^2} \left(R_{i3}^2 m_{H_i}^2 \right), \quad (2.48)$$

$$\lambda_7 = \frac{1}{v_1 v_s} \left(R_{i3} R_{i1} m_{h_i}^2 \right), \quad (2.49)$$

$$\lambda_8 = \frac{1}{v_2 v_s} \left(R_{i3} R_{i2} m_{h_i}^2 \right), \quad (2.50)$$

$$m_{11}^2 = m_{12}^2 \tan(\beta) - \frac{\lambda_1}{2} v_1^2 - \left(\frac{\lambda_3 + \lambda_4 + \lambda_5}{2} \right) v_2^2 - \frac{\lambda_7}{2} v_s^2, \quad (2.51)$$

$$m_{22}^2 = \frac{m_{12}^2}{\tan(\beta)} - \frac{\lambda_2}{2} v_2^2 - \left(\frac{\lambda_3 + \lambda_4 + \lambda_5}{2} \right) v_1^2 - \frac{\lambda_8}{2} v_s^2, \quad (2.52)$$

$$m_s^2 = -\frac{\lambda_6}{2} v_s^2 - \frac{\lambda_7}{2} v_1^2 - \frac{\lambda_8}{2} v_2^2. \quad (2.53)$$

Note that the masses of the CP-odd and charged Higgs bosons are similar to the ones in the 2HDM.

	up-type	down-type	leptons
Type I	R_{i2}/s_β	R_{i2}/s_β	R_{i2}/s_β
Type II	R_{i2}/s_β	R_{i1}/c_β	R_{i1}/c_β
Type III (lepton-specific)	R_{i2}/s_β	R_{i2}/s_β	R_{i1}/c_β
Type IV (flipped)	R_{i2}/s_β	R_{i1}/c_β	R_{i2}/s_β

Table 2.2: N2HDM couplings $C_{h_i f f}$ of the CP-even Higgs mass eigenstates $h_{1,2,3}$ to the different types of fermions in (2.55) for different N2HDM model types [23]. s_β denotes $\sin(\beta)$, while c_β denotes $\cos(\beta)$.

Since ρ_3 corresponds to the singlet state, it does not interact directly with the SM fermions and gauge bosons. However, due to the mixing between $\rho_{1,2,3}$ leading to the CP-even Higgs mass eigenstates $h_{1,2,3}$, the presence of a singlet admixture in the three CP-even Higgs scalars induces a different coupling compared to the 2HDM. The coupling of $h_{1,2,3}$ to the gauge bosons V is given by [117, 23]:

$$C_{h_i V V} = \cos(\beta)R_{i1} + \sin(\beta)R_{i2}. \quad (2.54)$$

As for the interactions between the CP-even Higgs scalars with the SM fermions, we have [117, 23]:

$$\mathcal{L}_{Yukawa} \supset \frac{\sqrt{2}m_f}{v_{sm}} \left(C_{h_1 f f} h_1 + C_{h_2 f f} h_2 + C_{h_3 f f} h_3 \right) f \bar{f}, \quad (2.55)$$

where $C_{h_i f f}$ corresponds to the modification in coupling for the CP-even Higgs boson h_i to the SM fermion, compared with the SM Higgs boson. The precise formulas for these coupling modifiers are shown in Table (2.2). In the alignment limit, the SM-like Higgs boson h_{sm} has $C_{h_{sm} f f} \approx C_{h_{sm} f f} \approx 1$, while the other CP-even Higgs states have zero or negligible couplings to fermions.

Throughout our work, we use the masses of the Higgs fields in the mass eigenbasis as well as their coupling modifiers to the SM gauge bosons and fermions as input parameter to generate the parameters m_{11}^2 , m_{22}^2 , m_S^2 , and λ_i . We then use the fields in the interaction basis for our domain wall simulations. The input parameters for the package `ScannerS` [117], which we used to generate parameter points satisfying experimental and theoretical constraints, also rely on these values for the masses and coupling modifiers.

2.4 THEORETICAL AND EXPERIMENTAL CONSTRAINTS

We now briefly discuss some of the theoretical and experimental conditions used to constrain the parameter space of these two models. Some imposed constraints, such as requiring symmetry restoration of the discrete symmetries, which is necessary for the formation of domain walls in the early universe, will be discussed later in the context of EW symmetry restoration in the N2HDM (5).

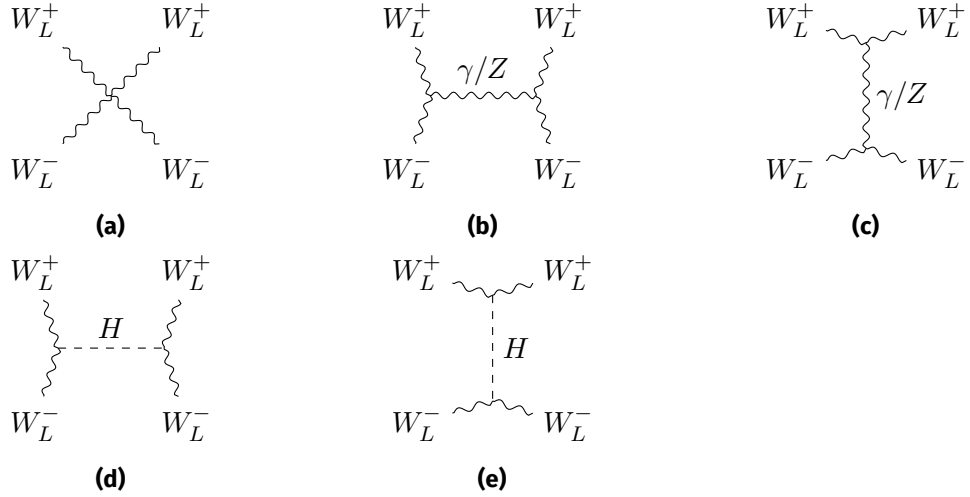


Figure 2.2: (a), (b), and (c) Feynman diagram gauge boson contributions to $W_L^+ W_L^- \rightarrow W_L^+ W_L^-$. (d) and (e) contributions from the Higgs boson.

2.4.1 Theoretical Constraints

We include constraints based on the consistency of the theory, such as unitarity, a well-behaved potential bounded from below, and the need for an EW minimum that is either stable or metastable with a lifetime larger than the age of the universe.

2.4.1.1 Perturbative unitarity

In quantum field theory, the scattering matrix S has to be unitary: $S^\dagger S = I$, in order to keep probability conserved [87]. However, before the Higgs boson was discovered, the electroweak theory suffered from an important issue related to the scattering of longitudinal W bosons (see Figure 2.2). The amplitude of this scattering process in the absence of the Higgs boson H diverges at high center-of-mass energies s . In the limit of $s \gg m_H^2, m_{W,Z}^2$, including the Higgs boson leads to the scattering amplitude [33]:

$$\mathcal{M}(W_L^+ W_L^- \rightarrow W_L^+ W_L^-) = -\sqrt{2} G_F m_H^2 \left(\frac{s}{s - m_H^2} + \frac{t}{t - m_H^2} \right). \quad (2.56)$$

Therefore, the presence of the Higgs field makes this scattering finite at high center-of-mass energies, and unitarity is satisfied.

Due to the *equivalence theorem* [33], unitarity in the $2 \rightarrow 2$ scattering of longitudinal W bosons at high energies can also be investigated using the scattering amplitudes related to Goldstone scalar bosons (see Figure 2.3) up to small corrections of order $\mathcal{O}(m_H^2/s^2)$:

$$\mathcal{M}(W_L^+ W_L^- \rightarrow W_L^+ W_L^-) = \mathcal{M}(\phi^+ \phi^- \rightarrow \phi^+ \phi^-) + \mathcal{O}(m_H^2/s^2), \quad (2.57)$$

where ϕ^\pm denote the Goldstone bosons that will be eventually eaten by the longitudinal W bosons. Even though this scattering amplitude is finite, there is an upper bound on the Higgs mass that makes the scattering amplitude unitary [33]. Above that limit, unitarity is violated [33]. Such a constraint put an upper bound on the mass of the Higgs boson before

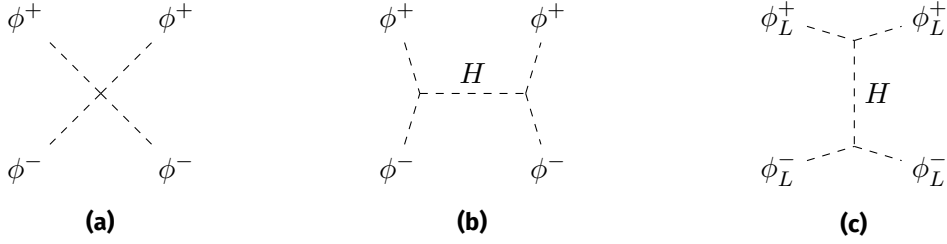


Figure 2.3: Feynman diagram of Goldstone bosons scattering $\phi^+\phi^- \rightarrow \phi^+\phi^-$.

its discovery [33]. To see this, one expresses the scattering amplitude \mathcal{M} as an expansion in partial waves according to:

$$\mathcal{M}(\theta) = 16\pi \sum_{l=0}^{\infty} a_l (2l+1) P_l(\cos(\theta)) = 16\pi a_0 + 48\pi a_1 \cos(\theta) + \dots, \quad (2.58)$$

where P_l are the well-known Legendre polynomials with degree l , θ the scattering angle, and a_l the expansion coefficients. Perturbative unitarity requires that for each partial wave, the condition:

$$|\text{Re}(a_l)| < \frac{1}{2}, \quad (2.59)$$

is met [33]. In the limit of $s \gg m_H^2$ one can extract a_0 from \mathcal{M} in (2.56) as :

$$a_0 = -\frac{G_F m_H^2}{4\pi\sqrt{2}} = \frac{m_H^2}{8\pi v_{sm}^2}. \quad (2.60)$$

Therefore, perturbative unitarity puts an upper limit on the mass of the Higgs boson $m_H < 870$ GeV [33]. Since the measured SM Higgs mass is $m_H = 125.09$ GeV, perturbative unitarity is satisfied in the SM.

When extending the Higgs sector with extra multiplets, it is crucial to make sure that the scalar contributions cancel the divergent parts in the scattering amplitude. For n extra Higgs doublets/singlets, this translates into the condition [33]:

$$\sum_i^n g_{h_i VV}^2 = g_{H_{sm} VV}^2, \quad (2.61)$$

where $g_{h_i VV}^2$ denotes the coupling of the extra Higgs bosons to the weak gauge bosons, and $g_{H_{sm} VV}$ denotes the coupling of the SM-like Higgs to the gauge bosons. One also needs to make sure that the remaining finite contributions in the scattering of the longitudinal W bosons fulfill the condition of perturbative unitarity. The same procedure can be done using the Goldstone boson scattering according to the equivalence theorem. In models with several scalar doublets, one can construct a matrix $(a_0)_{ij}$ corresponding to the different scattering amplitudes of the Goldstone bosons $(\mathcal{M}_{2 \rightarrow 2})_{ij}$ [25]. The bound on perturbative unitarity can be expressed as a bound on the eigenvalues of this matrix:

$$|\mathcal{M}_{2 \rightarrow 2}^i| < 8\pi. \quad (2.62)$$

These eigenvalues are expressed in terms of the quartic couplings of the scalar potential.

For the 2HDM, allowed parameter points need to satisfy the following conditions [25]:

$$|\lambda_3 \pm \lambda_4| < 8\pi, \quad (2.63)$$

$$|\lambda_3 \pm \lambda_5| < 8\pi, \quad (2.64)$$

$$|\lambda_3 + 2\lambda_4 \pm 3\lambda_5| < 8\pi, \quad (2.65)$$

$$\left| \frac{1}{2} \left(\lambda_1 + \lambda_2 \pm \sqrt{(\lambda_1 - \lambda_2)^2 + 4\lambda_4^2} \right) \right| < 8\pi, \quad (2.66)$$

$$\left| \frac{1}{2} \left(\lambda_1 + \lambda_2 \pm \sqrt{(\lambda_1 - \lambda_2)^2 + 4\lambda_5^2} \right) \right| < 8\pi, \quad (2.67)$$

$$\left| \frac{1}{2} \left(3\lambda_1 + 3\lambda_2 \pm \sqrt{9(\lambda_1 - \lambda_2)^2 + 4(2\lambda_3 + \lambda_4)^2} \right) \right| < 8\pi. \quad (2.68)$$

For the N2HDM, one adds the following constraints [26]:

$$|\lambda_7| < 8\pi, \quad (2.69)$$

$$|\lambda_8| < 8\pi, \quad (2.70)$$

$$\frac{1}{2}|a_{1,2,3}| < 8\pi, \quad (2.71)$$

where $a_{1,2,3}$ are the roots of the polynomial:

$$\begin{aligned} & 4(-27\lambda_1\lambda_2\lambda_6 + 12\lambda_3^2\lambda_6 + 12\lambda_3\lambda_4\lambda_6 + 3\lambda_4^2\lambda_6 + 6\lambda_2\lambda_7^2 - 8\lambda_3\lambda_7\lambda_8 - 4\lambda_4\lambda_7\lambda_8 \\ & + 6\lambda_1\lambda_8^2) + x(36\lambda_1\lambda_2 - 16\lambda_3^2 - 16\lambda_3\lambda_4 - 4\lambda_4^2 + 18\lambda_1\lambda_6 - 4\lambda_7^2 - 4\lambda_8^2) \\ & - 3x^2(\lambda_6 - 2(\lambda_1 + \lambda_2)) + x^3. \end{aligned} \quad (2.72)$$

2.4.1.2 Boundedness from below

In the SM, the condition to obtain a non-zero and finite minimum for the potential of the Higgs in (1.5) is to ensure that the quadratic term $\mu^2 > 0$ and $\lambda > 0$. This ensures that there are no directions in the field where the potential falls to $-\infty$, making it unbounded and causing an instability in the potential.

In extended Higgs sectors, several new terms are added to the scalar potential, making the potential much more complex, and therefore, it is important to make sure that no direction in the multidimensional space of the scalar fields can lead to the potential falling to $-\infty$.

In the case of the 2HDM this translates into the following conditions on the quartic terms [25]:

$$\lambda_{1,2} \geq 0, \quad (2.73)$$

$$\lambda_3 + \sqrt{\lambda_1\lambda_2} \geq 0, \quad (2.74)$$

$$\lambda_3 + \lambda_4 - |\lambda_3| + \sqrt{\lambda_1\lambda_2} \geq 0. \quad (2.75)$$

For the N2HDM, these conditions are more complicated, and the region of parameter space that is allowed is the union of the sets $\Omega_1 \cup \Omega_2$ where [26]:

$$\Omega_1 = \left\{ \lambda_{1,2,6} > 0; \sqrt{\lambda_1\lambda_6} + \lambda_7 > 0; \sqrt{\lambda_2\lambda_6} + \lambda_8; \sqrt{\lambda_1\lambda_2} + \lambda_3 + D > 0; \lambda_7 + \sqrt{\lambda_1/\lambda_2}\lambda_8 \geq 0 \right\}, \quad (2.76)$$

$$\Omega_2 = \left\{ \lambda_{1,2,6} > 0; \sqrt{\lambda_1\lambda_6} \geq \lambda_8 > -\sqrt{\lambda_2\lambda_6}; \sqrt{\lambda_1\lambda_6} > -\lambda_7 \geq \sqrt{\lambda_1/\lambda_8}; \sqrt{(\lambda_7^2 - \lambda_1\lambda_6)(\lambda_8^2 - \lambda_2\lambda_6)} > \lambda_7\lambda_8 - (D + \lambda_3)\lambda_6 \right\}, \quad (2.77)$$

where $D = \min(\lambda_4 - |\lambda_5|, 0)$.

2.4.1.3 Vacuum stability

It is known that the electroweak minimum in the framework of the SM is metastable [118]. Even though at tree-level the SM potential is stable, at very high energy scales, loop corrections cause the quartic coupling λ to turn negative and the SM potential develops another minimum which lies lower in the potential than the electroweak one. Since the potential barrier between our electroweak vacuum and such a global minimum is very large, the tunneling probability into it is very small, and the electroweak minimum is deemed to be a long-lived metastable vacuum of the theory [118].

This simple picture is completely different in beyond the SM Higgs sectors, already at tree-level. New scalar degrees of freedom can not only lead to the appearance of several new minima in the potential, both lower and higher than the electroweak, but they can also lead to the coexistence of neutral minima with ones that are CP-violating or electric charge violating [27, 113, 119, 112, 120]. This situation is illustrated in Figure 2.4, where the electroweak minimum is only a local minimum and the global minimum has VEVs that would not give us the correct values for the gauge bosons and fermion masses. Since this

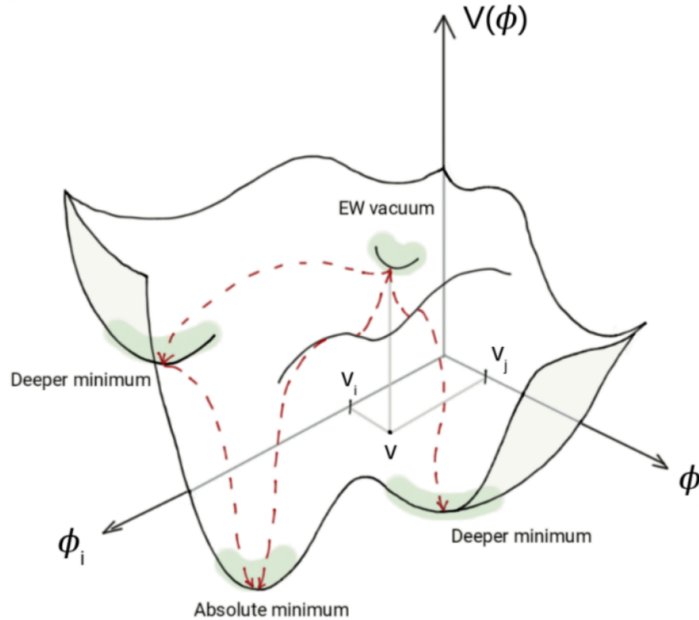


Figure 2.4: A generic illustration of the scalar potential in models with several scalar fields. The picture was created by Kateryna Radchenko [121].

constraint will be discussed later in more detail, we only give a summary of the results found in several previous studies of vacuum stability in extended Higgs sectors.

Concerning the 2HDM, several studies concentrated on studying the stability of the neutral EW vacuum with respect to CP and electric charge violating minima. It was found in [112, 120] that if a neutral EW minimum is found, then any CP or electric charge violating vacua have to be saddle points of the potential and lie higher in the potential. In case a CP or electric charge violating minimum exists, then any neutral vacuum will be a saddle point that lies higher in the potential. Therefore, by constructing a parameter point with a neutral electroweak minimum, it is certain that (at least at the tree-level), the potential is stable against tunneling to CP and electric charge violating minima.

However, it was found in [122] that in the 2HDM, the EW vacuum can coexist with other neutral minima in the potential dubbed as "*panic vacua*", and that the EW minimum can

even be a local one. This situation can be problematic since the EW vacuum can quantum tunnel to the global minimum with different vacuum expectation values and therefore catastrophically alter all masses of the fundamental particles in the SM, in a scenario dubbed as *death by vacuum* [122]. In case these other neutral minima coexist with the EW minimum, one can determine whether our EW vacuum is the global one in case the determinant $D = (m_{11}^2 - \sqrt{\frac{\lambda_1}{\lambda_2}} m_{22}^2) (\tan(\beta) - \sqrt[4]{\frac{\lambda_1}{\lambda_2}})$ is positive [122]. If $D < 0$, then one needs to calculate the tunneling rate of our EW vacuum to the global vacuum to determine the fate of our universe.

In case of the N2HDM, vacuum stability was studied in detail in [27]. One distinguishes two cases: if the EW minimum has $v_s = 0$, then CP and electric charge vacua can also exist, but they lie necessarily higher in the potential, making our neutral EW vacuum stable with respect to vacuum decay to CP and electric charge violating. While in case the electroweak minimum has $v_s \neq 0$, then it is possible to find other neutral, CP, and electric charge violating vacua that lie deeper in the potential, and therefore make the EW minimum a local minimum.

If the EW minimum is local, then one needs to calculate the transition rate to the global one. This rate per unit volume is given by [27, 123]:

$$\frac{\Gamma}{V} = K e^{-B}, \quad (2.78)$$

where K is a dimensionful constant related to the electroweak scale and B is the bounce action describing a scalar field configuration between the electroweak to the global vacuum. It was found in [27] that for $B < 390$, the EW vacuum is unstable and therefore those parameter points will be ruled out. In case $B > 440$, the electroweak vacuum is metastable with a lifetime larger than the age of the universe, making the EW vacuum phenomenologically viable.

2.4.2 Experimental Constraints

2.4.2.1 Collider Constraints

The Higgs boson was the last fundamental particle to be discovered in 2012 at the LHC. Until now, the experimental searches in colliders can only put exclusion limits on the viable parameter regions of BSM Higgs models.

There are several tools used in order to test the viability of parameter points in extended Higgs sectors with the exclusion limits provided by experiments at the LHC, such as **HiggsBounds** [124]. This tool extracts the experimental upper bounds from several BSM Higgs searches at the LHC, LEP, and the Tevatron and compares the prediction for the cross section times the branching ratio of a given parameter point with the observed upper limit at the experiment. If this ratio is larger than one, then the parameter point can be excluded since it would then lead to a larger number of events than the maximum number allowed by experiments. If the ratio is smaller than one, then the parameter point is still allowed since it leads to a prediction that is still in agreement with the experimental limits.

Another important experimental constraint is the fact that, so far, the properties of the observed Higgs boson at the LHC mostly agree with SM predictions within the experimental uncertainties. Therefore, any BSM Higgs model needs to predict a SM-like Higgs boson in its particle spectrum with properties (such as decay, production, and couplings) similar

to those of the SM. Since the LHC measurements of the 125 GeV scalar particle still allow some deviations from the SM prediction, one can compare the properties of the SM-like Higgs boson in the BSM model with the experimental measurements, including their uncertainties. One tool dedicated to this analysis is `HiggsSignals`. [125]

2.4.2.2 Flavor Constraints

Other than collider searches, one can also use flavor physics in order to constrain the BSM Higgs sector. We mentioned earlier that the Z_2 symmetry introduced in the 2HDM is necessary in order to forbid FCNC at tree level. However, loop corrections involving BSM particles can also induce FCNC. In the 2HDM and N2HDM, these contributions are mainly produced by the charged Higgs bosons H^\pm and can be relevant in low-energy B-meson decays [126]. For instance, one can place stringent limits on the allowed mass for the charged Higgs in the type two 2HDM, which requires $m_{H^\pm} > 600$ GeV and $\tan(\beta) > 1$.

2.4.2.3 Electroweak Precision Observables

We discussed earlier that the parameter ρ for any Higgs sector has to be equal to one at tree level [33]. The experimentally measured value is $\rho = (1.00031 \pm 0.00019)$ [29]. The small deviations from 1 are due to loop contributions to the gauge bosons' self-energies. If BSM Higgs models contribute to these self-energies, then one needs to make sure that the contributions do not exceed the experimentally measured value. In BSM Higgs models, these contributions can be conveniently incorporated in the framework of oblique parameters S , T , and U defined by [127]:

$$\alpha(m_Z)T = \frac{\Pi_{WW}(0)}{m_W^2} - \frac{\Pi_{ZZ}(0)}{m_Z^2}, \quad (2.79)$$

$$\frac{\alpha(m_Z)}{4 \sin^2(\theta_W) \cos^2(\theta_W)} S = \frac{\Pi_{ZZ}(m_Z^2) - \Pi_{ZZ}(0)}{m_Z^2} - \frac{\cos^2(\theta_W) - \sin^2(\theta_W)}{\sin(\theta_W) \cos(\theta_W)} \frac{\Pi_{Z\gamma}(m_Z^2)}{m_Z^2} - \frac{\Pi_{\gamma\gamma}(m_Z^2)}{m_Z^2}, \quad (2.80)$$

$$\frac{\alpha(m_Z)}{4 \sin^2(\theta_W)} (S + U) = \frac{\Pi_{WW}(m_W^2) - \Pi_{WW}(0)}{m_W^2} - \frac{\cos(\theta_W)}{\sin(\theta_W)} \frac{\Pi_{Z\gamma}(m_Z^2)}{m_Z^2} - \frac{\Pi_{\gamma\gamma}(m_Z^2)}{m_Z^2}, \quad (2.81)$$

where Π_{ij} denotes the one-loop self energies of the gauge bosons, and $\alpha(m_Z)$ denotes the weak coupling constant at the Z scale. The experimental limits for these parameters are given by [29]:

$$S = -0.04 \pm 0.1, \quad T = 0.01 \pm 0.1, \quad U = -0.01 \pm 0.09. \quad (2.82)$$

All these theoretical and experimental limits were imposed in our scans (unless claimed otherwise) using the public code `ScannerS` [117], which generates random parameter points in a given range of parameter variables that fulfill all the imposed constraints. For some particular scans, we also imposed the constraint of electroweak and discrete symmetry restoration at high temperatures, which is crucial for the formation of domain walls. This particular constraint will be discussed in more detail in the chapter 5 when we study electroweak symmetry restoration induced by domain walls in the N2HDM.

Having introduced the BSM Higgs models studied in this manuscript, as well as the constraints imposed on them, we discuss in the next chapter the possible domain wall solutions that can be obtained in the 2HDM.

This chapter is based on the following publication:

- [1] M. Y. Sassi and G. Moortgat-Pick, *Domain walls in the Two-Higgs-Doublet Model and their charge and CP-violating interactions with Standard Model fermions*, *JHEP* **04** (2024) 101, [2309.12398]

3.1 MOTIVATION AND GENERAL IDEA

In this chapter, based on the published work in [1], we investigate the domain wall solutions in the 2HDM. Such an extension allows several discrete symmetries in the model [6], whose spontaneous breaking after the electroweak symmetry breaking (EWSB) at the early universe can lead to the formation of domain walls. Recently, it was found in [110, 76] that the domain walls in the 2HDM can have non-trivial structures inside them. In particular, it was demonstrated that one-dimensional domain wall solutions (usually denoted as kink solutions in the literature) exhibit CP and electric charge-violating vacua inside the defect.

The spontaneous breaking of $SU_L(2) \times U(1)_Y$ alongside the discrete symmetry Z_2 causes the vacuum manifold of the model to consist of two disconnected 3-spheres. This leads to a degeneracy in the choice of the boundary conditions that one can impose on the vacua of different domains, in contrast to the much simpler case, where only the Z_2 symmetry is spontaneously broken and where the vacuum manifold is made of just two disconnected points. This will then lead to several classes of kink solutions with different internal structures [13]. Such effects were already investigated for domain wall solutions arising in Grand Unified Theories such as $SU(5) \times Z_2$ [77, 128, 13]. In contrast to the simple case of Z_2 domain wall solutions, the spontaneous breaking of abelian and non-abelian symmetries G alongside the discrete symmetry to a subgroup H leads to a disconnected vacuum manifold with non-trivial disconnected sectors. In such models, the symmetry group inside the wall can, in general, be smaller than the symmetry group outside the wall. This phenomenon, known as "clash-of-symmetries" [129, 130, 78], occurs when the unbroken symmetry subgroups H and H' on the two regions outside the wall are embedded differently in the spontaneously broken symmetry group G . The symmetry group inside the wall will be the intersection $H \cap H'$, which can be smaller than the group H or H' . Such a mechanism was used in [129] in order to provide a way to break symmetries using domain walls in the scenario where our 3+1-dimensional universe exists as a domain wall brane in a 4+1-dimensional spacetime with an action invariant under E_6 symmetry. In that work, the spontaneous breaking of E_6 symmetry to differently embedded unbroken $SO(10) \times U(1)$ subgroups H and H' outside the brane leads the unbroken symmetry group inside the domain wall $H \cap H'$ to be a smaller group containing $SU(5)$. In our model, we

will show that, due to this mechanism, the symmetry group of electromagnetism can be broken inside the domain wall.

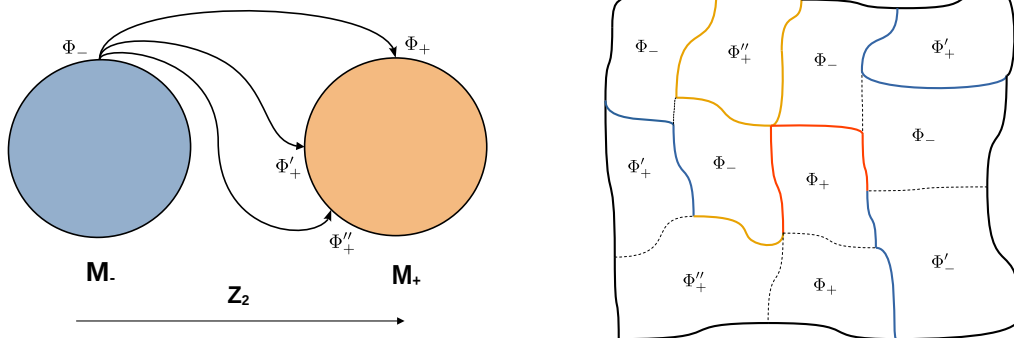
We expand the analysis done in [76] to also include the variation of all $SU(2)_L$ Goldstone and $U(1)_Y$ hypercharge modes of the $SU(2)_L \times U(1)_Y$ symmetry, as well as to study the evolution and stability of these different classes of 1D kink solution when using von Neumann boundary conditions. We then discuss the dependence of the kink solutions on the physical parameters of the 2HDM, such as the masses of the extra Higgs bosons and the parameter $\tan(\beta)$.

3.2 THE VACUUM MANIFOLD OF THE 2HDM

After electroweak symmetry breaking, the Higgs doublets acquire a neutral VEV (2.11). This vacuum breaks $SU(2)_L \times U(1)_Y \times Z_2$ into $U(1)_{em}$. In this case, the vacuum manifold of the theory is homeomorphic to the coset space:

$$M = (SU(2)_L \times U(1)_Y \times Z_2) / U(1)_{em} \simeq Z_2 \times S^3, \quad (3.1)$$

which is topologically equivalent to two disconnected 3-spheres [6] as depicted in Figure 3.1a. The vacuum manifold has then two disconnected sectors related by a Z_2 symmetry. These sectors are non-trivial (in contrast to the case when only Z_2 is broken) and consist of vacua which are related by $SU(2)_L \times U(1)_Y$ transformations. This leads to the formation of different classes of domain walls due to the multiple choices that can be taken for the electroweak matrix U inside the two regions (see Figure 3.1a), in contrast to standard Z_2 domain wall solutions where the choice of the vacua inside the two domains is fixed to be vacua that are only related by a discrete symmetry [131]. Figure 3.1b shows different



(a) Vacuum manifold M of the model.

(b) A patch of the universe after EWSB.

Figure 3.1: (a) Vacuum manifold M of the model. In this case M consists of two disconnected sectors M_- and M_+ related by the Z_2 symmetry and all the vacua in both sectors are degenerate. The elements of each sector are related by $SU(2)_L \times U(1)_Y$ transformations. Φ'_+ and Φ''_+ are related to Φ_+ by different gauge transformations of $SU(2)_L \times U(1)_Y$. (b) After EWSB, causally disconnected regions of the universe can end up in different vacua of the vacuum manifold. No topologically protected domain walls form between regions with vacua on the same spheres of M . Regions that end up with vacua in separate sectors of M can have different classes of domain walls depending on the $SU(2)_L$ and Hypercharge Goldstone modes they acquire.

possibilities for the boundary conditions after EWSB. In order to get a kink solution to

the scalar field configuration, the boundary conditions at $\pm\infty$ need to lie on disconnected sectors of the vacuum manifold. Starting at $x \rightarrow -\infty$ with a vacuum Φ_- on the vacuum manifold sector M_- corresponding to one 3-sphere:

$$\Phi_- = \left\{ \frac{1}{\sqrt{2}} \begin{pmatrix} 0 \\ v_1^* \end{pmatrix}, \frac{1}{\sqrt{2}} \begin{pmatrix} 0 \\ -v_2^* \end{pmatrix} \right\}, \quad (3.2)$$

we end up at $x \rightarrow +\infty$ with a vacuum Φ_+ on the vacuum manifold M_+ . Fixing our choice for Φ_- , we have multiple choices for the vacuum Φ_+ :

$$\Phi_+ = \left\{ \frac{1}{\sqrt{2}} U \begin{pmatrix} 0 \\ v_1^* \end{pmatrix}, \frac{1}{\sqrt{2}} U \begin{pmatrix} 0 \\ v_2^* \end{pmatrix} \right\}, \quad (3.3)$$

where U is an element of the broken electroweak symmetry group $SU(2)_L \times U(1)_Y$ and $\sqrt{(v_1^*)^2 + (v_2^*)^2} = 246$ GeV. In order to compute the kink solution of the field configuration interpolating between those two vacua, we need to minimize the energy of such a field configuration, which is equivalent to solving the time-independent Klein-Gordon equation of motion of a scalar field with the chosen boundary conditions.

In the 2HDM, a spatial field configuration has the following energy functional for the Higgs and gauge sector:

$$\mathcal{E}(x) = |D_\mu \Phi_1|^2 + |D_\mu \Phi_2|^2 + \frac{1}{4} B^{\mu\nu} B_{\mu\nu} + \frac{1}{4} W^{i\mu\nu} W_{\mu\nu}^i + V_{2\text{HDM}}(\Phi_1, \Phi_2), \quad (3.4)$$

where,

$$W_{\mu\nu}^i = \partial_\mu W_\nu^i - \partial_\nu W_\mu^i - g f^{ijk} W_\mu^j W_\nu^k, \quad (3.5)$$

$$B_{\mu\nu} = \partial_\mu B_\nu - \partial_\nu B_\mu, \quad (3.6)$$

denote the field strength tensors of the non-abelian gauge bosons of $SU(2)_L$ and the abelian gauge boson of $U(1)_Y$ respectively, with μ and ν denoting Lorentz indices. Recall that the covariant derivative D_μ is defined by:

$$D_\mu = \partial_\mu + \frac{ig}{2} W_\mu^i \sigma^i + \frac{ig'}{2} B_\mu, \quad (3.7)$$

where σ^i denotes the Pauli matrices.

The first four terms in (3.4) describe the kinetic energy of the vacuum configuration, and the fifth term denotes the potential of the scalar sector. In this work, we take $W_\mu^i(x) = 0$ and $B_\mu(x) = 0$, which is a solution that satisfies the equations of motion for the gauge fields and gives the lowest energy contribution to (3.4). We discuss in detail the validity of this solution in Appendix A.

Setting the gauge fields to zero, the energy functional (3.4) reduces to:

$$\mathcal{E}(x) = \frac{d\Phi_1^\dagger}{dx} \frac{d\Phi_1}{dx} + \frac{d\Phi_2^\dagger}{dx} \frac{d\Phi_2}{dx} + V_{2\text{HDM}}(\Phi_1, \Phi_2), \quad (3.8)$$

where we take the fields to be one-dimensional functions of x . There is an interplay between the kinetic energy that arises due to a changing profile of the field configuration as a function of x and the potential energy of this field configuration.

Using the non-linear representation for the Higgs doublets (defined in (2.6), (2.7), and (2.35)) in the expression of the energy functional (3.8) we end up with:

$$\mathcal{E}(x) = \frac{d\tilde{\Phi}_1^\dagger}{dx} \frac{d\tilde{\Phi}_1}{dx} + \frac{d\tilde{\Phi}_2^\dagger}{dx} \frac{d\tilde{\Phi}_2}{dx} + \left(\frac{d\tilde{\Phi}_{1,2}^\dagger}{dx} U^\dagger(x) \frac{dU}{dx} \tilde{\Phi}_{1,2}(x) + \text{h.c.} \right)$$

$$+ \tilde{\Phi}_{1,2}^\dagger(x) \frac{dU^\dagger}{dx} \frac{dU}{dx} \tilde{\Phi}_{1,2}(x) + V_{2HDM}(\Phi_1, \Phi_2), \quad (3.9)$$

where, in terms of the vacuum manifold parameters:

$$\begin{aligned} V_{2HDM}(v_1, v_2, v_+, \xi) &= \frac{m_{11}^2}{2} v_1^2(x) + \frac{m_{22}^2}{2} (v_2^2(x) + v_+^2(x)) + \frac{\lambda_1}{8} v_1^4(x) + \frac{\lambda_3}{4} v_1^2(x) v_+^2(x) \\ &+ \frac{\lambda_2}{8} (v_2^2(x) + v_+^2(x))^2 + \frac{\lambda_3 + \lambda_4}{4} v_1^2(x) v_2^2(x) + \frac{\lambda_5}{4} v_1^2(x) v_2^2(x) \cos(2\xi(x)). \end{aligned} \quad (3.10)$$

Writing down $U(x)$ in terms of the Pauli matrices, we get:

$$U(x) = e^{i\theta(x)} \left[\cos(G(x)) I_2 + i \frac{g_1(x)}{2} \frac{\sin(G(x))}{G(x)} \sigma_1 + i \frac{g_2(x)}{2} \frac{\sin(G(x))}{G(x)} \sigma_2 + i \frac{g_3(x)}{2} \frac{\sin(G(x))}{G(x)} \sigma_3 \right], \quad (3.11)$$

where:

$$G(x) = \sqrt{\left(\frac{g_1(x)}{2}\right)^2 + \left(\frac{g_2(x)}{2}\right)^2 + \left(\frac{g_3(x)}{2}\right)^2}, \quad g_i(x) = \tilde{g}_i(x)/v_{sm}. \quad (3.12)$$

In [76], the choice of the matrix $U(x)$ was simplified to the case where only a single Goldstone mode of $SU(2)_L$ or the hypercharge Goldstone mode θ was allowed to be non-zero and have asymmetric boundary conditions at $\pm\infty$. We will expand the results to the general case, where all modes in $U(x)$ can change. This will lead to more effects inside the domain walls compared to [76].

Since the calculation of all terms in (3.9) is straightforward but lengthy, we give the final expression of the energy functional in terms of the vacuum parametrization:

$$\begin{aligned} \mathcal{E}(x) &= \frac{1}{2} \left(\frac{dv_1}{dx}\right)^2 + \frac{1}{2} \left(\frac{dv_2}{dx}\right)^2 + \frac{1}{2} \left(\frac{dv_+}{dx}\right)^2 + \frac{1}{2} v_2^2(x) \left(\frac{d\xi}{dx}\right)^2 + \frac{1}{2} v_1^2(x) \left[\left(\frac{d\theta}{dx}\right)^2 + I_0(x)\right. \\ &+ \left. 2 \frac{d\theta}{dx} I_3(x)\right] + \frac{1}{2} v_2^2(x) \left[\left(\frac{d\theta}{dx}\right)^2 + I_0(x) + 2\left(\frac{d\theta}{dx} + \frac{d\xi}{dx}\right) I_3(x) + 2 \frac{d\theta}{dx} \frac{d\xi}{dx}\right] \\ &+ \frac{1}{2} v_+^2(x) \left[\left(\frac{d\theta}{dx}\right)^2 + I_0(x) - 2 \frac{d\theta}{dx} I_3(x)\right] + v_2(x) \left[\sin(\xi) \frac{dv_+}{dx} I_1(x) - \cos(\xi) \frac{dv_+}{dx} I_2(x)\right] \\ &+ v_+(x) \left[-\sin(\xi) \frac{dv_2}{dx} I_1(x) + \cos(\xi) \frac{dv_2}{dx} I_2(x)\right] + \frac{v_+(x)v_2(x)}{2} \left[4 \sin(\xi) I_2(x) \frac{d\theta}{dx}\right. \\ &\left. - 4 \cos(\xi) I_1(x) \frac{d\theta}{dx} - 2 \cos(\xi) \frac{d\xi}{dx} I_1(x) - 2 \sin(\xi) \frac{d\xi}{dx} I_2(x)\right] + V_{2HDM}, \end{aligned} \quad (3.13)$$

where,

$$\begin{aligned} I_0(x) &= G'^2(x) \cos^2(G(x)) + \left[(g_1'^2(x) + g_2'^2(x) + g_3'^2(x)) G^2(x) - 2(g_1 g_1' + g_2 g_2' + g_3 g_3')^2 \right. \\ &\left. + (G^2(x) + G^4(x)) G'^2(x) \right] \frac{\sin^2(G(x))}{G^4(x)}, \end{aligned} \quad (3.14)$$

$$I_1(x) = B'(x)C(x) - B(x)C'(x) - A'(x) \cos(G(x)) - A(x)G'(x) \sin(G(x)), \quad (3.15)$$

$$I_2(x) = C'(x)A(x) - A'(x)C(x) - B'(x) \cos(G(x)) - B(x)G'(x) \sin(G(x)), \quad (3.16)$$

$$I_3(x) = A'(x)B(x) - A(x)B'(x) - C'(x) \cos(G(x)) - C(x)G'(x) \sin(G(x)), \quad (3.17)$$

$$A(x) = g_1(x) \frac{\sin(G(x))}{G(x)}, \quad (3.18)$$

$$B(x) = g_2(x) \frac{\sin(G(x))}{G(x)}, \quad (3.19)$$

$$C(x) = g_3(x) \frac{\sin(G(x))}{G(x)}, \quad (3.20)$$

and the prime symbol denotes derivatives with respect to x . In order to get non-trivial vacuum configurations corresponding to different vacua at $\pm\infty$, we need to minimize the space integral of this energy functional with respect to small deviations in the fields:

$$\delta E = \delta \left(\int dx \mathcal{E}(x) \right) = 0. \quad (3.21)$$

For static solutions, this leads to a system of differential equations analogous to the time-independent Klein-Gordon equations of motion:

$$\frac{d}{dx} \left(\frac{d\mathcal{E}}{d(d\phi_i)} \right) - \frac{d\mathcal{E}}{d\phi_i} = 0, \quad (3.22)$$

where ϕ_i denotes the 8 fields in the two doublets.

Since the energy functional and the equations of motion in the general case are very complicated, it is simpler to explain the behavior of the different fields inside the domain wall by choosing some special cases that make the energy functional and equations of motion considerably simpler. In the following subsections, we will consider a few special cases for the choice of $U(x)$ at the boundaries. These simplified cases capture the interesting effects that influence the fields inside the domain wall. We will first start by considering the case of standard domain walls where the matrix $U(x) = \mathbf{I}_2$, constant everywhere in space, which means that we only consider vacua related by the Z_2 symmetry. The cases where only one mode of $U(x)$ is different in the two domains while taking all the other modes to be zero were already considered in [76]. Here we expand those results by first considering the case where more than one mode of $U(x)$ changes across the domains, and later the general case where the hypercharge and the Goldstone modes are chosen arbitrarily. We also discuss the behavior of the fields that interact with the kink solution for $v_2(x)$ inside the wall.

To solve the 8 differential equations describing the vacuum configuration as a function of x . To do this, we use the same numerical algorithm used in [110, 76, 6], namely the gradient flow method.

The gradient flow method introduces a fictitious time parameter to the field profiles $\phi_i(x, t)$. We then modify the minimization condition (3.21) to:

$$\frac{\partial \phi_i}{\partial t} = - \frac{\delta E}{\delta \phi_i} \quad (3.23)$$

Using this method, we find the solution of the system of differential equations by iteratively minimizing the energy functional at each iteration for the given boundary conditions until the vacuum configuration $\phi_i(x, t)$ leads to a minimum in the energy. As we approach such a minimal energy configuration, the derivative of $\phi_i(x, t)$ with respect to the fictitious time approaches zero, and we therefore obtain the solutions to the static equations of motion in (3.21). The solution is declared as found if, after several iterations, the vacuum configuration stays the same up to small numerical fluctuations. We also adopt the same rescaling of the dimensionful parameters that was used in [110, 76, 6]:

$$\hat{m}_i = \frac{m_i}{m_h}, \quad \hat{v}_i = \frac{v_i}{v_{sm}}, \quad \hat{x} = x \cdot m_h, \quad \hat{\mathcal{E}} = \frac{\mathcal{E}}{m_h^2 v_{sm}^2}, \quad (3.24)$$

where $m_h = 125\text{GeV}$ denotes the mass of the SM Higgs particle. Such a rescaling is useful to get dimensionless space variable \hat{x} and numerical values of the order 1.

3.3 STANDARD DOMAIN WALL SOLUTION

We start with the standard kink solution, where the two domains have the same and constant angles θ and g_i while the vacuum expectation value of v_2 changes sign. The kink solution interpolates between the following two vacua:

$$\Phi_- = \left\{ \frac{1}{\sqrt{2}} \begin{pmatrix} 0 \\ v_1^* \end{pmatrix}, \frac{1}{\sqrt{2}} \begin{pmatrix} 0 \\ -v_2^* \end{pmatrix} \right\}, \quad \Phi_+ = \left\{ \frac{1}{\sqrt{2}} \begin{pmatrix} 0 \\ v_1^* \end{pmatrix}, \frac{1}{\sqrt{2}} \begin{pmatrix} 0 \\ v_2^* \end{pmatrix} \right\}. \quad (3.25)$$

We use (3.13) and set the derivatives for θ and g_i to zero. We obtain the following energy functional that has to be minimized:

$$\begin{aligned} \mathcal{E}(x) = & \frac{1}{2} \left(\frac{dv_1}{dx} \right)^2 + \frac{1}{2} \left(\frac{dv_2}{dx} \right)^2 + \frac{1}{2} \left(\frac{dv_+}{dx} \right)^2 + \frac{1}{2} v_2^2(x) \left(\frac{d\xi}{dx} \right)^2 + \frac{1}{2} m_{11}^2 v_1^2(x) \\ & + \frac{1}{2} m_{22}^2 (v_2^2(x) + v_+^2(x)) + \frac{1}{8} \lambda_1 v_1^4(x) + \frac{1}{8} \lambda_2 (v_2^2(x) + v_+^2(x))^2 + \frac{1}{4} \lambda_3 v_1^2(x) v_+^2(x) \\ & + \frac{1}{4} \left[\lambda_3 + \lambda_4 + \lambda_5 \cos(2\xi(x)) \right] v_1^2(x) v_2^2(x), \end{aligned} \quad (3.26)$$

leading to the following equations of motion for the field profiles:

$$\begin{aligned} \frac{d}{dx} \left(\frac{d\mathcal{E}}{d(dv_1)} \right) - \frac{d\mathcal{E}}{dv_1} = & \frac{d^2 v_1}{dx^2} - \frac{1}{2} \lambda_1 v_1^3(x) + \lambda_3 v_+^2(x) - v_1(x) m_{11}^2 \\ & - \frac{1}{2} v_1(x) \left(\lambda_3 + \lambda_4 + \lambda_5 \cos(\xi(x)) \right) v_2^2(x) = 0, \end{aligned} \quad (3.27)$$

$$\begin{aligned} \frac{d}{dx} \left(\frac{d\mathcal{E}}{d(dv_2)} \right) - \frac{d\mathcal{E}}{dv_2} = & \frac{d^2 v_2}{dx^2} - \frac{1}{2} \lambda_2 v_2^3(x) - \frac{1}{2} v_2(x) \left[2(m_{22}^2 + \left(\frac{d\xi}{dx} \right)^2) + \lambda_2 v_+^2(x) \right. \\ & \left. + \left(\lambda_3 + \lambda_4 + \lambda_5 \cos(\xi(x)) \right) v_1^2(x) \right] = 0, \end{aligned} \quad (3.28)$$

$$\frac{d}{dx} \left(\frac{d\mathcal{E}}{d(dv_+)} \right) - \frac{d\mathcal{E}}{dv_+} = -\frac{1}{2} \left[2m_{22}^2 + \lambda_3 v_1^2(x) + \lambda_2 v_2^2(x) \right] v_+(x) - \frac{1}{2} \lambda_2 v_+^3 + \frac{d^2 v_+}{dx^2} = 0, \quad (3.29)$$

$$\frac{d}{dx} \left(\frac{d\mathcal{E}}{d(d\xi)} \right) - \frac{d\mathcal{E}}{d\xi} = v_2(x) \left[\lambda_5 \cos(\xi) \sin(\xi) v_1^2(x) v_2(x) + 2 \frac{dv_2}{dx} \frac{d\xi}{dx} + v_2(x) \frac{d^2 \xi}{dx^2} \right] = 0. \quad (3.30)$$

As $\mathcal{E}(x)$ is independent of θ and g_i , they therefore remain constant. The system of differential equations is solved in an interval $-10 < \hat{x} < 10$. In Figure 3.2 we plot the profile of the fields for parameter point (PP) I:

$$m_H = 800 \text{ GeV}, \quad m_A = 500 \text{ GeV}, \quad m_C = 400 \text{ GeV}, \quad \tan(\beta) = 0.85, \quad (3.31)$$

and parameter point II:

$$m_H = 200 \text{ GeV}, \quad m_A = 200 \text{ GeV}, \quad m_C = 200 \text{ GeV}, \quad \tan(\beta) = 0.85. \quad (3.32)$$

This choice of parameter points is done for pedagogical reasons to show different properties in the kink solutions. The results show that the field configuration $v_2(x)$ interpolates from a negative value in the region on the left to a positive value in the region on the right while crossing the value 0. This is the usual behavior of a kink solution. Note that also the value of $v_1(x)$ is also affected as both v_1 and v_2 are coupled via the differential equations. To understand this change in $v_1(x)$ inside the domain wall of v_2 (see Figures 3.2a and 3.2b),

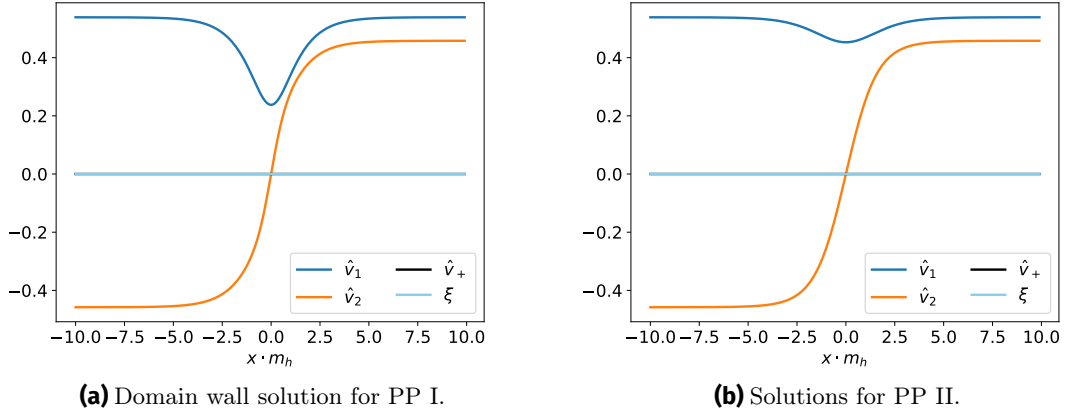


Figure 3.2: Standard domain wall solution for different parameter points I (a) and II (b). We use the rescaled dimensionless vacuum parameters $\hat{v}_i = v_i/v_{sm}$ (cf. 3.24).

we derive the standard energy functional $\mathcal{E}_{standard}(x)$ in 3.26 taking the derivatives of all fields other than v_1 and v_2 to be 0 as they all vanish at all x :

$$\begin{aligned} \mathcal{E}_{standard}(x) = & \frac{1}{2} \left(\frac{dv_1}{dx} \right)^2 + \frac{1}{2} \left(\frac{dv_2}{dx} \right)^2 + \frac{m_{11}^2}{2} v_1^2(x) + \frac{m_{22}^2}{2} v_2^2(x) + \frac{\lambda_1}{8} v_1^4(x) \\ & + \frac{\lambda_2}{8} v_2^4(x) + \frac{\lambda_3 + \lambda_4}{4} v_1^2(x) v_2^2(x) + \frac{\lambda_5}{4} v_1^2(x) v_2^2(x). \end{aligned} \quad (3.33)$$

The effective mass term for v_1 is then given by:

$$M_1(x) = \frac{m_{11}^2}{2} + \frac{(\lambda_3 + \lambda_4 + \lambda_5)}{4} v_2^2(x). \quad (3.34)$$

Inside the core of the wall ($x = 0$), $v_2 = 0$ and $M_1(0) = m_{11}^2/2$. When plotting the effective mass M_1 as function of x , we can see that the value becomes less negative inside the domain wall for both parameter points (see Figures 3.3a and 3.3b). Consequently the scalar potential $V_{2HDM}(x = 0) = V_0(v_1, v_+)$ inside the domain wall will have its minima for v_1 at a smaller value and the potential barrier between the minima will be lower. Note that for other parameter points, $(\lambda_3 + \lambda_4 + \lambda_5)$ can be positive and therefore the effective mass $M_1(0)$ inside the domain wall will be more negative than at the asymptotic values. This then corresponds to a bigger value for the minimum $v_1(0)$ of $V_0(v_1)$ and therefore v_1 inside the domain wall would be bigger than its asymptotic values at $\pm\infty$. However, a changing profile for $v_1(x)$ inside the wall will always lead to a positive contribution to the kinetic part of $\mathcal{E}(x)$. Therefore, one needs to make sure that this solution for $v_1(x)$ is stable. This is done by considering small fluctuations $\tilde{v}_1(x, t)$ around the background kink solution $v_1(x)$. The equation of motion describing such fluctuations is given by:

$$\partial_t^2 \tilde{v}_1(x, t) - \partial_x^2 \tilde{v}_1(x, t) + \frac{dV_{2HDM}}{d\tilde{v}_1} = 0. \quad (3.35)$$

Taking small fluctuations up to first order, this reduces to:

$$-\partial_x^2 \tilde{v}_1(x) + 2M_1(x) \tilde{v}_1(x) = w^2 \tilde{v}_1(x), \quad (3.36)$$

for a fluctuation of the form $\tilde{v}_1(x, t) = e^{iwt} \tilde{v}_1(x)$. If a solution with $w^2 < 0$ exists, then the fluctuation $v_1(x, t) \propto e^{\tilde{w}t}$, where $w = i\tilde{w}$, grows with time leading to the instability of the solution for $v_1(x)$. For $w^2 > 0$ the fluctuation keeps oscillating around the found

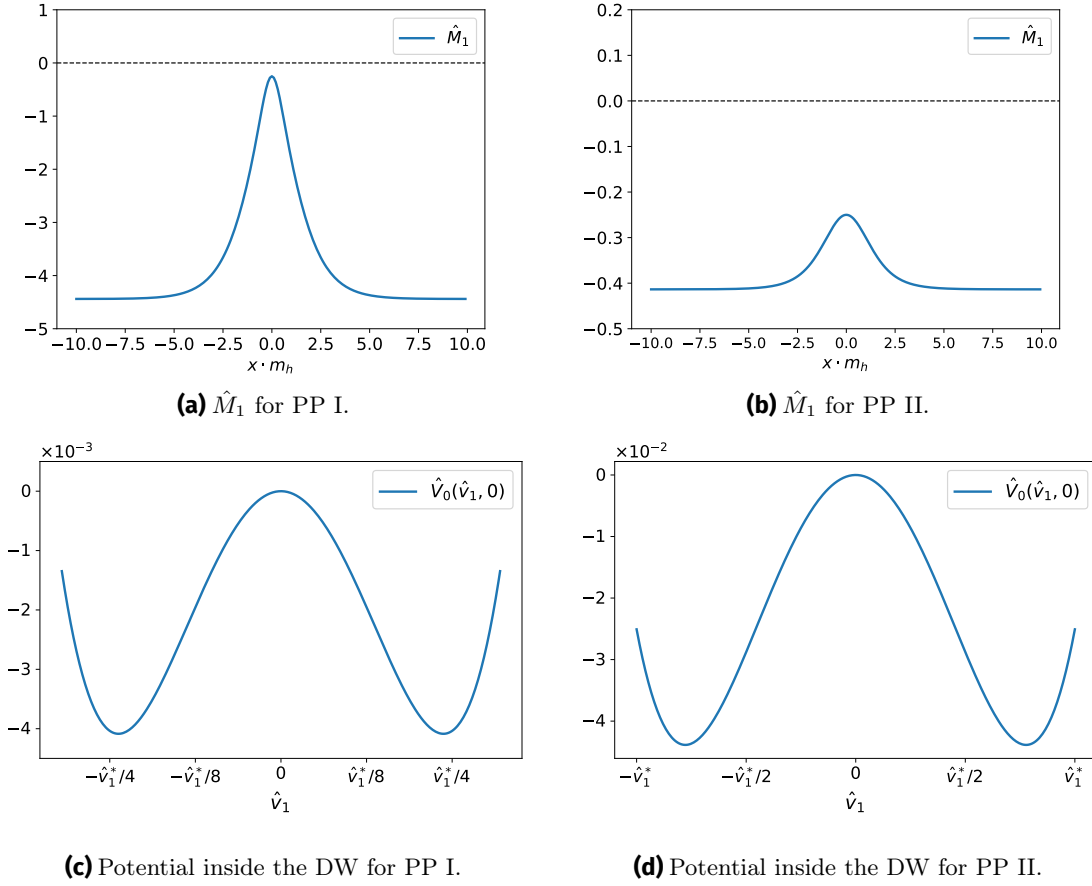


Figure 3.3: (a) and (b): Rescaled effective mass term \hat{M}_1 of v_1 as a function of x . Notice that the effective mass becomes less negative inside the domain wall. This explains why the vacuum v_1 inside the wall gets smaller. (c) and (d): Rescaled potential $\hat{V}_0(\hat{v}_1, \hat{v}_+) = \hat{V}_{2HDM}(x=0)$ inside the domain wall ($v_2(0) = 0$).

solution for $v_1(x)$. The behavior of $\tilde{v}_1(x, t)$ for PP I is shown in Figure 3.4a, showing an oscillating fluctuation around 0, which means that the solution is stable. Note that a vacuum configuration, where $v_1(x) = v_1$ is constant, will be unstable and the field $v_1(x)$ evolves to the lowest energy solution that we obtain from the numerical calculations (see Figures 3.4b and 3.2a).

For the fields $v_+(x)$ and $\xi(x)$, we observe that they stay equal to zero everywhere. A non-zero phase ξ provides a positive contribution to the energy functional (3.26) leading to a higher energy solution. In other words, $\xi(x) = 0$ presents the lowest energy solution. Concerning $v_+(x)$, the situation is more complicated: in order to study its behavior inside the wall, we consider the terms in \mathcal{E} that depend on $v_+(x)$, (cf. 3.26):

$$\mathcal{E}_+(v_+) = \frac{1}{2} \left(\frac{dv_+}{dx} \right)^2 + \frac{1}{2} m_{22}^2 v_+^2(x) + \frac{1}{8} \lambda_2 v_+^4(x) + \frac{1}{4} \lambda_2 v_+^2(x) v_2^2(x) + \frac{1}{4} \lambda_3 v_1^2(x) v_+^2(x). \quad (3.37)$$

The effective mass term for v_+ in the background of the DW is given by:

$$M_+(x) = \frac{1}{2} m_{22}^2 + \frac{1}{4} (\lambda_2 v_2^2(x) + \lambda_3 v_1^2(x)). \quad (3.38)$$

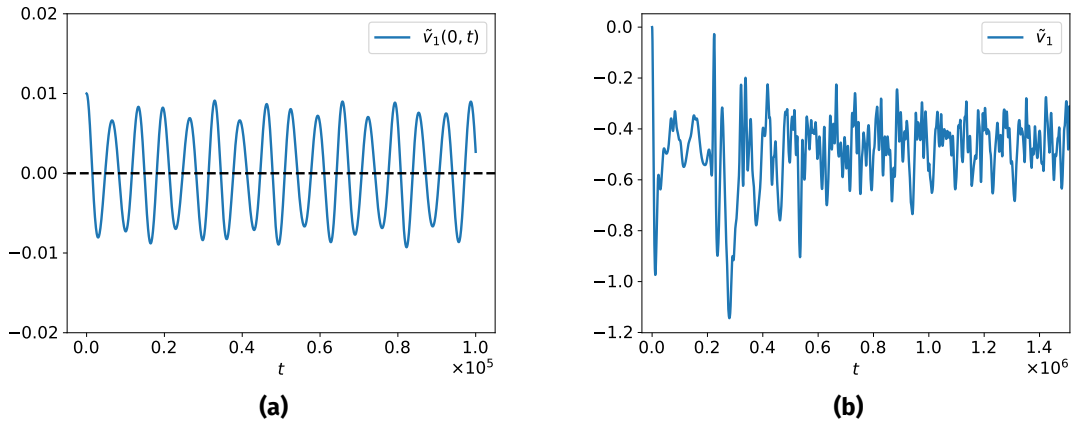


Figure 3.4: (a) The solution found in Figure 3.2a is stable as the fluctuation \tilde{v}_1 oscillates around 0. (b) The fluctuation $\tilde{v}_1(x, t)$ grows with time for the case when $v_1(x) = v_1$ indicating the instability of that solution. After some time the fluctuation oscillates around the lowest minimum corresponding to the obtained results for PP I.

Outside the domain wall, the effective mass is obviously positive and the potential minimum for v_+ is 0. Inside the wall, one gets

$$M_+(0) = \frac{1}{2}m_{22}^2 + \frac{1}{4}\lambda_3 v_1^2(0),$$

which, depending on the parameter point can also be negative (see Figures 3.5a and 3.5b). The field v_+ can develop a condensate inside the wall, i.e. when $M_+(0) < 0$. In that case the potential $V_0(v_1(0), v_+)$ will have two non zero minima for v_+ (see Figure 3.5c). If such parameter points exist, it is energetically more favorable for v_+ to get a condensate inside the wall. However, the kinetic energy part is minimized for $v_+(x) = 0$. Therefore, one should make sure that the kinetic contribution due to the spatial derivative of v_+ is not too large so that the solution for the non-zero condensate is stable inside the wall. In order to investigate the stability of the $v_+(x) = 0$ solution inside the wall, we consider the linearized time-dependent equation of motion for a small fluctuation $\tilde{v}_+(x, t)$ around $v_+(x)$ in the background of the domain wall:

$$\partial_t^2 \tilde{v}_+(x, t) - \partial_x^2 \tilde{v}_+(x, t) + \frac{dV_{2HDM}}{dv_+} = 0. \quad (3.39)$$

For a small fluctuation of the form

$$\tilde{v}_+(x, t) = e^{i\omega t} \tilde{v}_+(x), \quad (3.40)$$

the evolution of the fluctuation follows the differential equation:

$$-\partial_x^2 \tilde{v}_+(x) + 2M_+(x) \tilde{v}_+(x) = w^2 \tilde{v}_+. \quad (3.41)$$

The small fluctuation around $v_+(x) = 0$ is unstable if $w^2 < 0$, making $v_+(x, t) \propto e^{\tilde{w}t}$, where $w = i\tilde{w}$, growing with time and leading to the instability of the solution $v_+(x) = 0$. In case $w^2 > 0$, the fluctuation $\tilde{v}_+(x, t)$ oscillates around the stable solution. Figure 3.5a shows one parameter point where $M_+(0)$ is negative inside the wall. However, the lowest energy solution has $v_+(x) = 0$, meaning that the kinetic energy contribution from a $v_+(x)$ condensate inside the wall leads to a higher total energy than the solution with a vanishing $v_+(x)$ overall. We also verify numerically (see Figure 3.6) that the frequency w of a fluctuation $\tilde{v}_+(x, t)$ to the $v_+(x) = 0$ solution is real as the fluctuation oscillates around $v_+(x) = 0$.

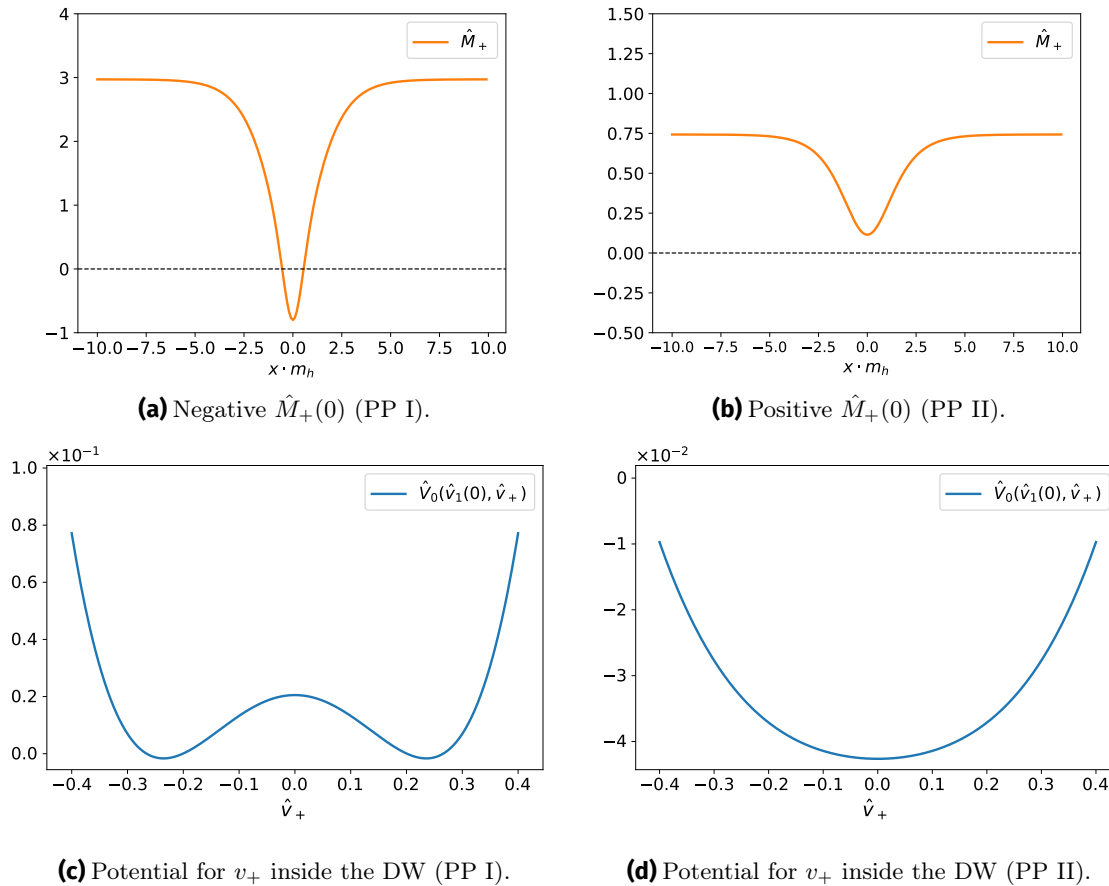


Figure 3.5: Effective mass term of v_+ as a function of x and the corresponding scalar potential $\hat{V}_0(\hat{v}_1(0), \hat{v}_+)$ inside the wall as a function of v_+ for different PP: (a) \hat{M}_+ for PP I, notice that the effective mass can become negative inside the wall, leading to the possibility of forming a condensate of v_+ localized on the wall; (b) shows \hat{M}_+ for PP II. Here the effective mass is positive everywhere and no charge violating vacua are expected inside the wall; (c) shows the potential inside the DW as a function of v_+ for PP I. In this case, the minimum is non-zero; (d) the same potential for PP II. In this case the global minimum of v_+ is zero.

3.4 VARIATION OF A SINGLE ANGLE ACROSS THE WALL

We now consider the effects of the Goldstone and hypercharge modes on the domain wall solution. We start by following the same approach in [76] and simplify $U(x)$ (2.35) by allowing the variation across the wall of either the hypercharge angle $\theta(x)$ or a single Goldstone mode $g_i(x)$ at a time. In this case, the vacua at $\pm\infty$ will be rotated relative to each other, by either a $U_Y(1)$ transformation or a transformation related to one Goldstone mode of $SU(2)_L$. For each case, we will discuss the solution of the equations of motion using either Dirichlet or von Neumann boundary conditions, where the former keeps the vacua at the boundaries fixed while the latter allows the dynamical variation of the vacua at the boundaries but keeps the spatial derivative of the vacua to be zero on the boundaries. For the following numerical solutions, we work in the alignment limit and fix the parameter point:

$$m_H = 800 \text{ GeV}, m_A = 500 \text{ GeV}, m_C = 400 \text{ GeV}, \tan(\beta) = 0.85 \text{ and } \alpha - \beta = 0. \quad (3.42)$$

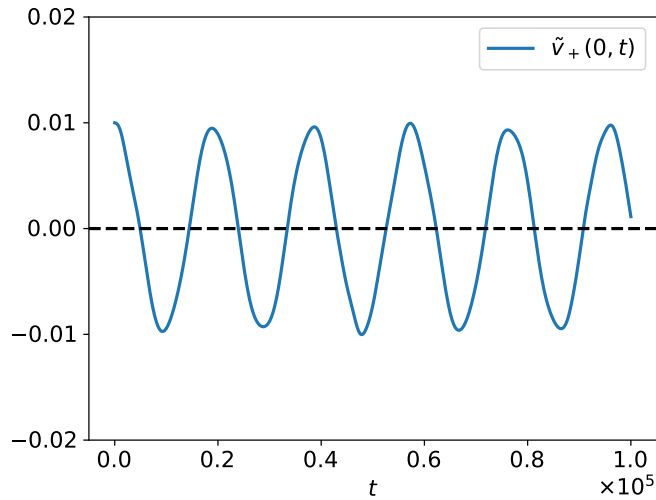


Figure 3.6: Stability of the solution $v_+(x) = 0$ under a small fluctuation $\tilde{v}_+(x, t)$, oscillating around $v_+ = 0$ with a real frequency w .

3.4.1 Variation of hypercharge θ

We first discuss the variation of the hypercharge angle $\theta(x)$ across the wall. In this case, the matrix $U(x)$ (2.35) is given by:

$$U(x) = e^{i\theta(x)} I_2,$$

which leads to the energy functional $\mathcal{E}(x)$:

$$\begin{aligned} \mathcal{E}(x) = & \frac{1}{2} \left(\frac{dv_1}{dx} \right)^2 + \frac{1}{2} \left(\frac{dv_2}{dx} \right)^2 + \frac{1}{2} \left(\frac{dv_+}{dx} \right)^2 + \frac{1}{2} v_2^2(x) \left(\frac{d\xi}{dx} \right)^2 + \frac{1}{2} v_1^2(x) \left(\frac{d\theta}{dx} \right)^2 \\ & + \frac{1}{2} v_2^2(x) \left[\left(\frac{d\theta}{dx} \right)^2 + 2 \frac{d\theta}{dx} \frac{d\xi}{dx} \right] + \frac{1}{2} v_+^2(x) \left(\frac{d\theta}{dx} \right)^2 + V_{2HDM}. \end{aligned} \quad (3.43)$$

One can immediately see from (5.41), that a change in the hypercharge across the wall cannot lead to a charge breaking solution $v_+(0) \neq 0$ inside the wall. The term $\frac{1}{2} v_+^2(x) (d\theta/dx)^2$ in (5.41) always leads to a positive contribution to the energy and therefore it only minimizes the energy of the vacuum configuration when $v_+(0) = 0$. Using the equation of motion for the hypercharge $\theta(x)$, one can derive a relation between the change in the hypercharge $\theta(x)$ and the derivative of the CP-violating phase $\xi(x)$ [76]:

$$\frac{d\theta}{dx} = \frac{-v_2^2}{v_1^2 + v_2^2 + v_+^2} \frac{d\xi}{dx}. \quad (3.44)$$

Such an equation is only valid for finite energy solutions where the spatial derivatives of the vacua at the boundaries vanish. From (3.44) one would expect that, as the hypercharge angle starts to change from the value it has in one domain to the value in the other domain, the value of the phase $\xi(x)$ will become non-zero.

Figure 3.7a shows the numerical solution of the equations of motion using Dirichlet boundary conditions with $\theta(-\infty) = 0$ and $\theta(+\infty) = \pi/2$. The initial guess for the profile of $\theta(x)$ was taken to be a hyperbolic tangent function interpolating between 0 and $\pi/2$. The

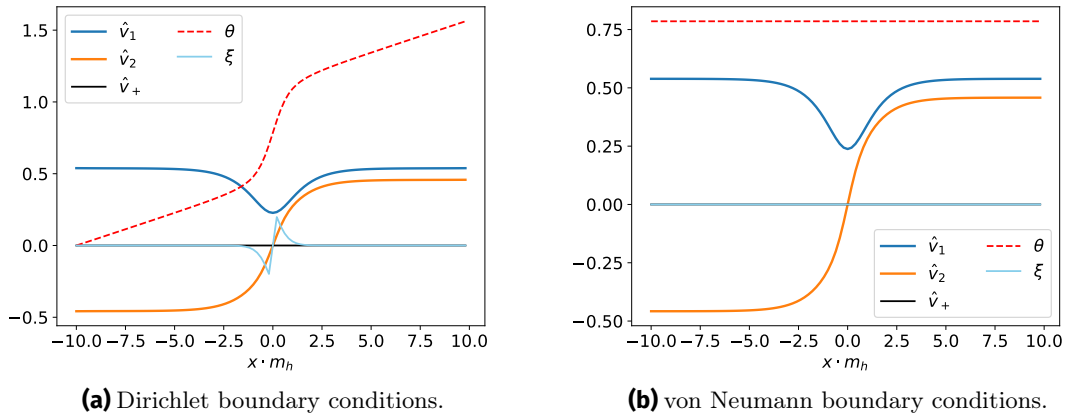


Figure 3.7: Numerical solutions of the DW equations of motion for vacua on the boundaries having different hypercharge angle θ . (a) Using Dirichlet boundary conditions. (b) Using von Neumann boundary conditions. \hat{v}_i are the rescaled vacuum parameters, cf. (3.24). We observe a non zero phase $\xi(x)$ inside the wall when using Dirichlet boundary condition. This means that the vacua inside the wall are CP-violating (see (2.10)).

numerical results point to a non-vanishing phase $\xi(x)$ localized inside the wall, where the hypercharge changes significantly. However, this vacuum configuration has a higher energy than the vacuum configuration of the standard domain walls with $\xi(x) = 0$ (see Figure 3.8b). Therefore, for these parameter points, such domain walls are unstable and should decay into the standard domain wall configuration. One can also notice that the derivative in $\theta(x)$ outside the wall are non zero due to the choice of Dirichlet boundary conditions. This shows that minimizing the energy of the wall tends to change the hypercharge angle at the boundaries. For this reason, it is more advantageous to use von Neumann boundary conditions when solving the differential equations, so that the hypercharge angle in each domain can change dynamically to minimize the energy of the wall. This can be seen in Figure 3.7b, where the hypercharge in both regions evolve to be equal to each other. This will then lead to $d\theta/dx = 0$ and therefore to a vanishing $\xi(x)$ for all x .

In Figure 3.8a we plot the profile of the solution at an intermediate time step using von Neumann boundary conditions. This shows how the hypercharge angle $\theta(x)$ at the boundaries change dynamically to minimize the energy and we see that the value of the CP-violating phase $\xi(x)$ inside the wall gets smaller. Even though the CP-violating domain wall solution is unstable, it is expected that after EWSB, the hypercharge angles on causally disconnected regions of the universe can be different. Therefore the early stages of the formation of the domain wall network would exhibit such CP-violating vacua inside the wall until the profile of the hypercharge angle $\theta(x)$ relaxes to a solution where it is constant for all x . We will also see later that in the realistic scenario, where we consider $U(x)$ to be a general $SU(2) \times U_Y(1)$ matrix, the stable domain wall solution will exhibit a non zero (albeit small) CP-violating vacua because the hypercharge angle will be different on both domains.

From the clash-of-symmetries point of view, the asymptotic vacuum Φ_- at $-\infty$ is invariant under the electromagnetism group $H = U(1)_{em}$. At $+\infty$ the asymptotic vacuum is $\Phi'_+ = g\Phi_+$ and the group keeping Φ'_+ invariant is therefore $H' = gHg^\dagger$ with $g \in U(1)_Y$. As g commutes with all elements of H , both H' and H are embedded in $SU(2)_L \times U(1)_Y$ in the same way and therefore the continuous symmetry group inside the wall will be $H \cap H' = U(1)_{em}$.

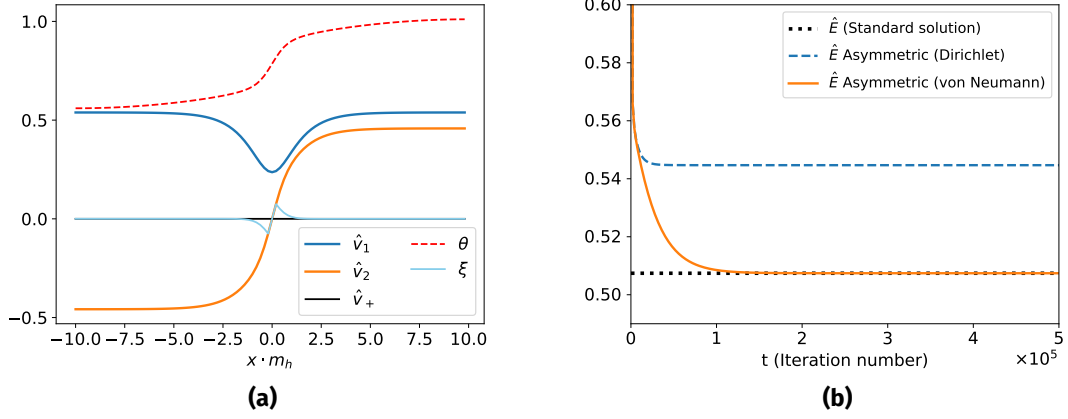


Figure 3.8: (a) Evolution of the hypercharge angle θ at an intermediate stage of the calculations. Note that the CP-violating phase ξ gets smaller as the difference in hypercharge in both domains gets smaller. (b) Evolution of the rescaled energy \hat{E} (cf. 3.24) of the vacuum configuration using Dirichlet and von Neumann boundary conditions.

3.4.2 Variation of g_1

We now discuss the case when only the Goldstone mode g_1 is non-zero and different on both domains. The matrix $U(x)$ (2.35) in such a case is given by:

$$U(x) = \cos(g_1(x)/2)I_2 + i \sin(g_1(x)/2)\sigma_1 = \begin{pmatrix} \cos(g_1(x)/2) & i \sin(g_1(x)/2) \\ i \sin(g_1(x)/2) & \cos(g_1(x)/2) \end{pmatrix}. \quad (3.45)$$

The corresponding energy functional \mathcal{E} (3.13) is simplified to:

$$\begin{aligned} \mathcal{E}(x) = & \frac{1}{2} \left(\frac{dv_1}{dx} \right)^2 + \frac{1}{2} \left(\frac{dv_2}{dx} \right)^2 + \frac{1}{2} \left(\frac{dv_+}{dx} \right)^2 + \frac{1}{2} v_2^2(x) \left(\frac{d\xi}{dx} \right)^2 + \frac{1}{8} v_+^2 \left(\frac{dg_1}{dx} \right)^2 \\ & - \frac{1}{2} v_2 \sin(\xi) \frac{dv_+}{dx} \frac{dg_1}{dx} + \frac{1}{2} v_+ \frac{dg_1}{dx} \left(\sin(\xi) \frac{dv_2}{dx} + v_2 \cos(\xi) \frac{d\xi}{dx} \right) + V_{2HDM}. \end{aligned} \quad (3.46)$$

In [76], by using the equation of motion for $g_1(x)$, an expression relating how the change in g_1 will affect v_+ and ξ was derived, namely:

$$\frac{dg_1}{dx} = \frac{2}{v_1^2 + v_2^2 + v_+^2} \left(v_2 \sin(\xi) \frac{dv_+}{dx} - v_+ \sin(\xi) \frac{dv_2}{dx} - v_2 v_+ \cos(\xi) \frac{d\xi}{dx} \right). \quad (3.47)$$

This would then imply that a change in g_1 across the wall will lead to a non-zero $v_+(x)$ and $\xi(x)$ inside the wall.

The unbroken symmetry for the asymptotic vacuum at $+\infty$ is $H' = gHg^\dagger$ with $g \in SU(2)_L$ corresponding to the first generator T^1 . As g does not commute with elements of H , this leads to both broken subgroups being embedded differently in $SU(2)_L \times U(1)_Y$ and one can expect that the domain wall solution will break $U(1)_{em}$, in case the energy of such a solution is the lowest one. In order to solve the equations of motion for the vacuum configuration, we choose $g_1(-\infty) = 0$ and $g_1(+\infty) = \pi/2$ with $g_1(x)$ having the initial profile of a hyperbolic tangent interpolating between the two asymptotic values. The numerical solution of the equations of motion using Dirichlet boundary conditions, however, points to a vanishing $v_+(x)$ and $\xi(x)$ (see Figure 3.9a), such a behavior was also found in [76]. This can be attributed to the fact that using Dirichlet boundary conditions for

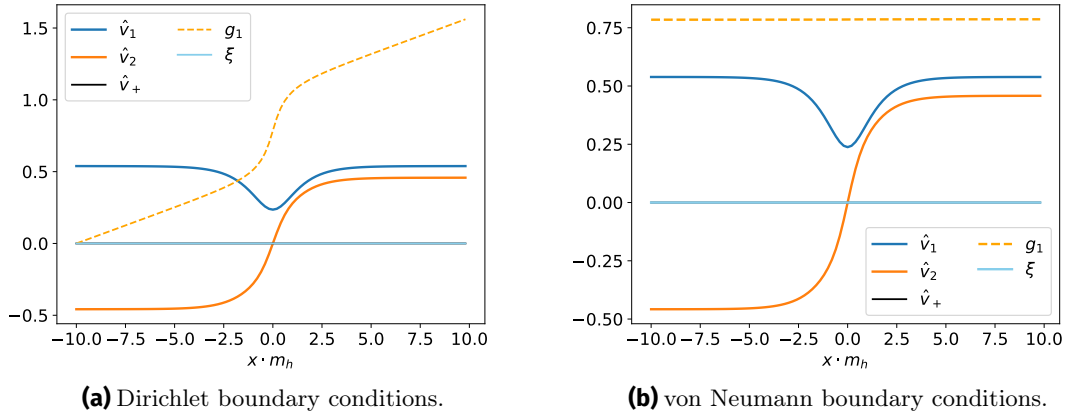


Figure 3.9: Numerical solutions of the DW equations of motion for vacua having a different Goldstone mode g_1 using: (a) Dirichlet boundary conditions and (b) von Neumann boundary conditions. The solutions do not exhibit charge or CP-violating vacua inside the wall. Only the solutions using von Neumann boundary conditions satisfy the relation (3.47). The Goldstone mode $g_1(x)$ changes dynamically from an initial asymmetric configuration to a configuration where $g_1(x)$ is the same everywhere.

this system of differential equations is not the correct approach. The equation (3.47) is valid for a static field configuration that satisfies the equations of motion, has a vanishing derivative for the Goldstone mode at the boundaries and minimizes the energy functional $\int dx \mathcal{E}(x)$. However it is clear that the condition of vanishing derivative at the boundaries is not satisfied for our solution using Dirichlet boundary conditions, even though the solution is static ($dg_1/dt = 0$).

In Figure 3.10, we compare the energies of domain wall solutions using different boundary conditions. We observe that the energy of the solution using the Dirichlet boundary conditions is only a local minimum and has a higher energy than the standard domain wall solution. When using von Neumann boundary conditions (see Figure 3.9b), the Goldstone modes g_1 in both domains change dynamically to become the same value, which eventually leads to $dg_1/dx = 0$. Such a field configuration is the correct solution: it explains the vanishing values of $v_+(x)$ and $\xi(x)$ inside the wall, satisfies the relation (3.47) and minimizes the energy.

3.4.3 Variation of g_2

We now discuss the case when only g_2 changes across the wall. The matrix $U(x)$ (2.35) is given by:

$$U(x) = \cos(g_2(x)/2)I_2 + i \sin(g_2(x)/2)\sigma_2 = \begin{pmatrix} \cos(g_2(x)/2) & \sin(g_2(x)/2) \\ -\sin(g_2(x)/2) & \cos(g_2(x)/2) \end{pmatrix}. \quad (3.48)$$

The unbroken symmetry for the asymptotic vacuum at $+\infty$ is $H' = gHg^\dagger$ with $g \in SU(2)_L$ corresponding to the second generator T^2 . In this case g does not commute with elements of H , this leads to both broken subgroups H and H' being embedded differently in $SU(2)_L \times U(1)_Y$ and one can expect that the domain wall solution will break $U(1)_{em}$ as expected by the clash-of-symmetries formalism in case the energy of such a solution is the

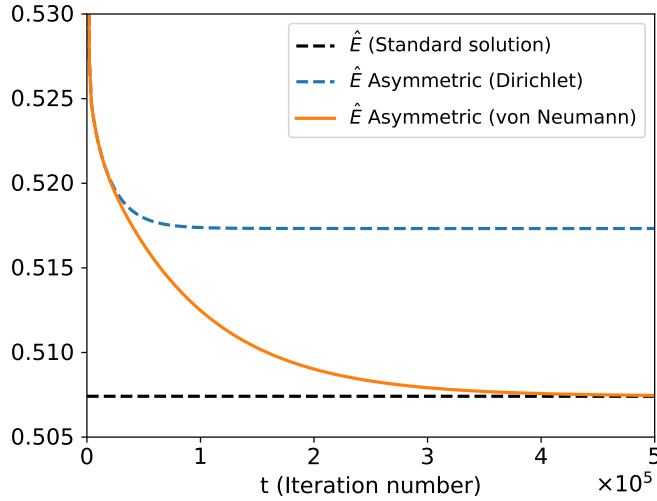


Figure 3.10: Evolution of the energy of the vacuum configuration with iteration time for Dirichlet and von Neumann boundary conditions. For g_1 having asymmetric boundaries, the energy is higher than the energy of the standard DW vacuum configuration. Therefore, the field configuration dynamically decays to the standard domain wall solution and $g_1(x)$ becomes the same value everywhere.

lowest one.

The energy functional $\mathcal{E}(x)$ (3.13) simplifies to:

$$\begin{aligned} \mathcal{E}(x) = & \frac{1}{2} \left(\frac{dv_1}{dx} \right)^2 + \frac{1}{2} \left(\frac{dv_2}{dx} \right)^2 + \frac{1}{2} \left(\frac{dv_+}{dx} \right)^2 + \frac{1}{2} v_2^2(x) \left(\frac{d\xi}{dx} \right)^2 + \frac{1}{8} (v_+^2 + v_1^2 + v_2^2) \left(\frac{dg_2}{dx} \right)^2 \\ & + \frac{1}{2} \frac{dg_2}{dx} \left(-v_+ \cos(\xi) \frac{dv_2}{dx} + v_2 \cos(\xi) \frac{dv_+}{dx} + v_2 v_+ \sin(\xi) \frac{d\xi}{dx} \right) + V_{2HDM}. \end{aligned} \quad (3.49)$$

One major difference in comparison with the analysis of the standard domain wall solution in section 3.3 is that $dg_2/dx \neq 0$ induces a linear term for $v_+(x)$ in the potential (3.49):

$$-\frac{1}{2} \frac{dg_2}{dx} v_+(x) \cos(\xi) \frac{dv_2}{dx},$$

which can give a negative contribution to the energy of the vacuum configuration depending on the sign of dg_2/dx and dv_2/dx . Using the equation of motion for $g_2(x)$, one derives an expression relating the change in $g_2(x)$ to the derivative of v_+ inside the wall [76]:

$$\frac{dg_2}{dx} = \frac{-2v_2^2 \cos^2(\xi)}{v_1^2 + v_2^2 + v_+^2} \frac{d}{dx} \left(\frac{v_+}{v_2 \cos(\xi)} \right). \quad (3.50)$$

This implies that a variation in the Goldstone mode $g_2(x)$ will lead to a non-vanishing $v_+(x)$. In this case, even if $\xi(x) = 0$, it is possible to get a negative contribution to the energy of the wall by having a non vanishing $v_+(0)$, in contrast to the previous case where the dependence was on $\sin(\xi)$. A non-zero derivative for $g_2(x)$ leads to the creation of a stable $v_+(x)$ condensate inside the wall, if the energy E of such a solution is smaller than the energy of the standard domain wall solution. Figure 3.11 shows the numerical solutions to the equations of motion using Dirichlet (Fig.3.11a) and von Neumann boundary conditions (Fig.3.11b). Like in the previous cases, we take the boundaries of the Goldstone mode to be: $g_2(-\infty) = 0$ and $g_2(+\infty) = \pi/2$. For the initial guess, we use a hyperbolic tangent interpolating between both values. We observe a non-vanishing value for $v_+(x)$

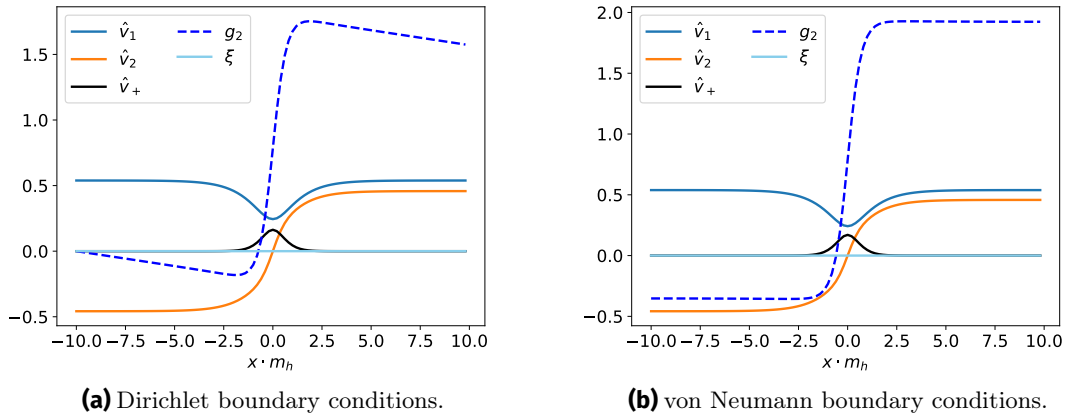


Figure 3.11: Numerical solutions of the DW equations of motion in the case of variation of g_2 . (a) Using Dirichlet boundary conditions and (b) using von Neumann boundary conditions.

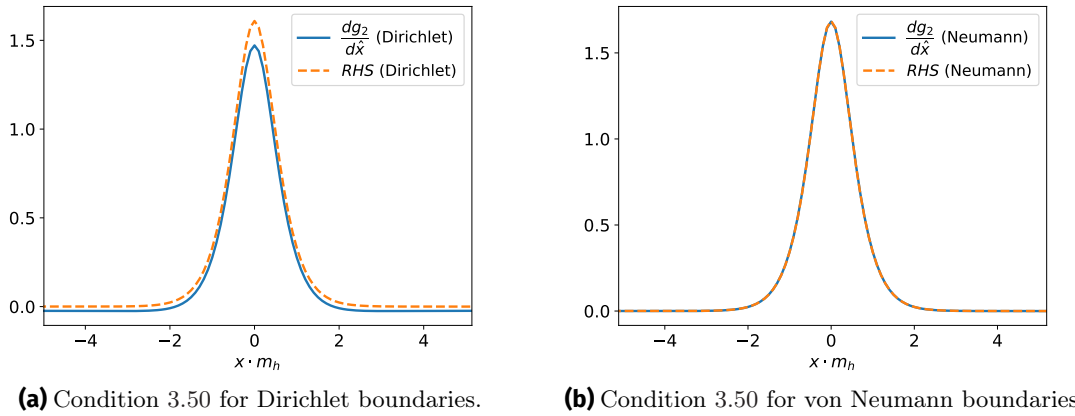


Figure 3.12: Verification of the relation (3.50) for Dirichlet and von Neumann boundary conditions. "RHS" denotes the right hand side of the equation (3.50), namely the quantity $(-2v_2^2 \cos^2(\xi))/(v_1^2 + v_2^2 + v_+^2) \frac{d}{dx} \left(\frac{v_+}{v_2 \cos(\xi)} \right)$. Using Dirichlet boundary conditions, the relation is not fulfilled because the used boundaries at $\pm\infty$ give an unstable solution. Using von Neumann boundary condition, we get a perfect agreement.

inside the wall. The $U(1)_{em}$ is therefore broken inside the wall leading to exotic phenomena such as charge breaking processes and the photon getting a mass [75, 132].

When using Dirichlet boundary conditions we observe again that the spatial derivative of $g_2(x)$ outside the domain wall is not vanishing. We can see in Figure 3.12a that the relation (3.50) is not exactly fulfilled using these boundary conditions, reflecting the instability of the solution with Dirichlet boundary conditions. Using von Neumann boundary conditions, we can verify that the non-vanishing $v_+(x)$ inside the wall is stable and that the change in $g_2(x)$ between the two regions gets enhanced, leading to a slightly higher value for $v_+(0)$ inside the wall compared with the solution using Dirichlet boundary conditions.

We also verified that the relation (3.50) is satisfied for this choice of boundary condition (see Figure 3.12b). Even though the choice of von Neumann boundary condition is the correct choice to get stable solutions for our system of differential equations, we can still use Dirichlet boundary condition in order to get an approximate solution for a fixed choice of g_2 between the two regions, as this type of boundary condition fixes those values.

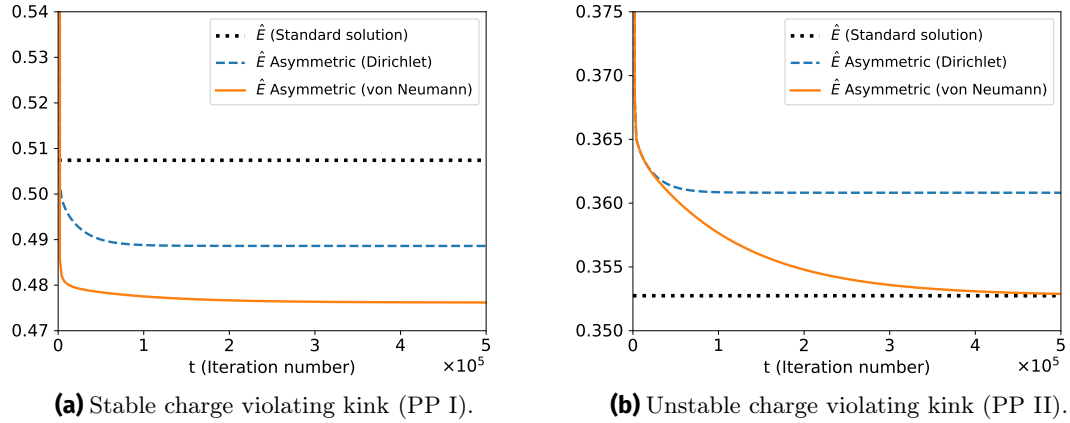


Figure 3.13: Rescaled energies of kink solutions with standard and asymmetric boundary conditions.

(a) The charged condensate $v_+(x)$ is stable because the energy of the charge violating kink solution is lower than the energy of the kink with vanishing $v_+(x)$. (b) The charge violating kink solution is unstable because the energy is higher than the solution with $v_+(x) = 0$. In this case the kink solution will decay into the standard solution. Such a solution was found for the parameter point II (cf. 3.32). This can be understood by noting that the effective mass term of M_+ for that particular parameter point is positive everywhere (see Figure 3.5b).

In the case of von Neumann boundary conditions, when choosing different initial values for g_2 on the boundaries, we always end up with a solution for $g_2(x)$ where the difference $\Delta(g_2)_{stable} = g_2(+\infty) - g_2(-\infty)$ is fixed. This means that when starting with random $\Delta(g_2)_{initial}$ between $[0, 2\pi]$, $\Delta(g_2)$ always relaxes to a fixed value $\Delta(g_2)_{stable}$ that only depends on the mass parameters and $\tan(\beta)$. For the used parameter point (3.42), the $v_+(x)$ condensate is stable and the vacuum configuration has a lower energy than the standard domain wall solution (see Figure 3.13a). There are also other parameter points where the contributions from the derivative dg_2/dx and a non-vanishing condensate $v_+(x)$ leads to a higher energy than the standard domain wall solution with $v_+(x) = 0$. In such a case, the Goldstone mode g_2 dynamically changes its values until it becomes equal in both domains leading to the charge breaking domain wall to decay into the standard domain wall solution as the latter has a lower energy (see Figure 3.13b).

For the case when $g_2(x)$ decreases when going from the region $v_2 < 0$ to the region $v_2 > 0$, for example, when taking $g_2(-\infty) = \pi/2$ and $g_2(+\infty) = 0$ (see Figure 3.14), we obtain a negative value for the condensate $v_+(x)$. This behavior can be explained by the relation 3.50 where the sign of $\frac{d}{dx}(v_+/v_2)$ is positive which can only be obtained for a negatively signed $v_+(x)$ condensate inside the wall as $v_2(x)$ goes from $-v_2$ at $-\infty$ to v_2 at $+\infty$.

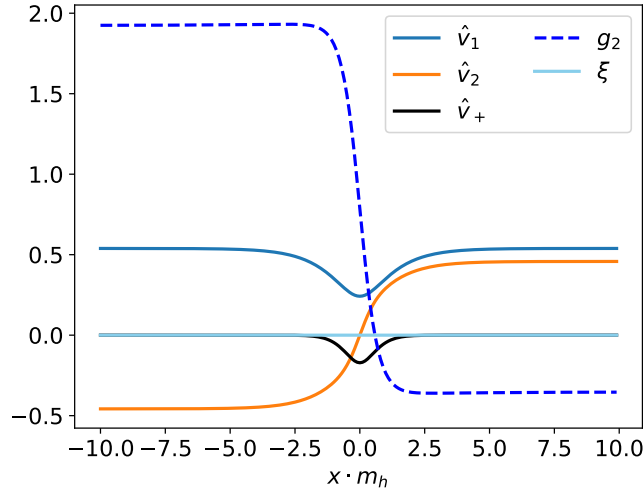


Figure 3.14: Numerical solution of the DW equations of motion in the case of variation of g_2 . In contrast to the previous case, the derivative dg_2/dx is negative, leading to a negative condensate $v_+(x)$ inside the wall.

3.4.4 Variation of g_3

We now discuss the case when we allow g_3 to have different values on the boundaries. The matrix $U(x)$ (2.35) is given by:

$$U(x) = \cos(g_3(x)/2)I_2 + i \sin(g_3(x)/2)\sigma_3 = \begin{pmatrix} e^{ig_3(x)/2} & 0 \\ 0 & e^{-ig_3(x)/2} \end{pmatrix}. \quad (3.51)$$

The energy functional \mathcal{E} (3.13) simplifies to:

$$\begin{aligned} \mathcal{E} = & \frac{1}{2} \left(\frac{dv_1}{dx} \right)^2 + \frac{1}{2} \left(\frac{dv_2}{dx} \right)^2 + \frac{1}{2} \left(\frac{dv_+}{dx} \right)^2 + \frac{1}{2} v_2^2(x) \left(\frac{d\xi}{dx} \right)^2 + \frac{1}{8} (v_+^2 + v_1^2 + v_2^2) \left(\frac{dg_3}{dx} \right)^2 \\ & - \frac{1}{2} v_2^2 \frac{d\xi}{dx} \frac{dg_3}{dx} + V_{2HDM}. \end{aligned} \quad (3.52)$$

The change in $g_3(x)$ will lead to a change in the phase $\xi(x)$ as was derived in [76] using the equation of motion for $g_3(x)$:

$$\frac{dg_3}{dx} = \frac{2v_2^2}{v_1^2 + v_2^2 + v_+^2} \frac{d\xi}{dx}. \quad (3.53)$$

Figure 3.15a shows the solution for asymmetric boundary conditions in g_3 using Dirichlet boundary conditions. We observe that the phase $\xi(x)$ is non zero inside the wall, which means that the vacuum inside the domain wall is CP-violating. Using Dirichlet boundary conditions, we see again that the derivative of the Goldstone mode $g_3(x)$ is non zero at the boundaries: such a CP-breaking solution has a higher energy than the standard domain wall solution (see Figure 3.16) and is therefore unstable for this parameter point. The gradient flow method gives us a solution where the Goldstone field tries to change its value at the boundaries, reflecting the instability of the solution. However, if we use von Neumann boundary conditions, the Goldstone mode g_3 dynamically changes its value at the boundaries in such a way that, after some time, both regions end up having the same

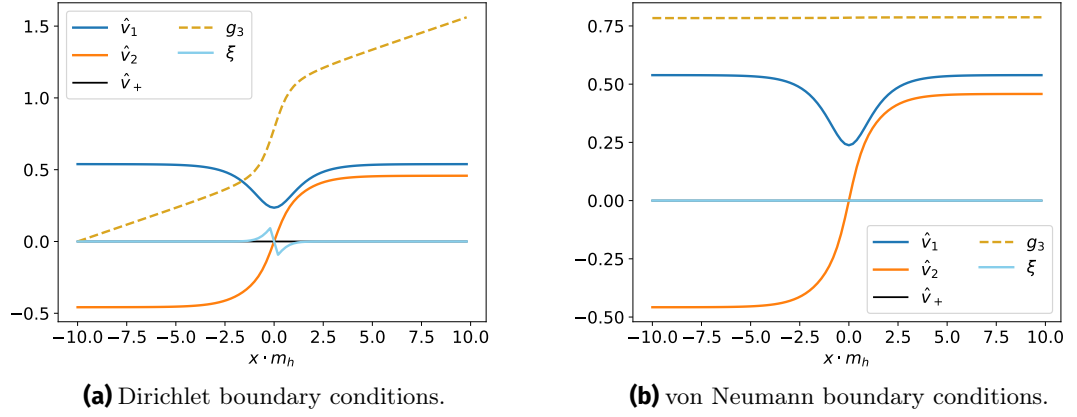


Figure 3.15: Solutions of the equations of motion for the case when g_3 is different on both domains. (a) Using Dirichlet boundary conditions. (b) Using von Neumann boundary conditions.

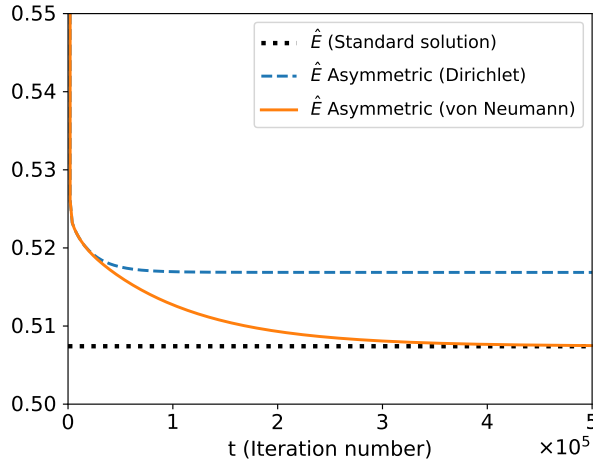


Figure 3.16: Evolution of the rescaled energy of the vacuum configuration using different boundary conditions. Notice that the energy using Dirichlet boundary conditions is higher than the energy using von Neumann boundary conditions. The class of domain walls that are CP-violating due to a variation in g_3 decays after some time to the class of standard domain walls.

g_3 (see Figure 3.15b). The CP-breaking solution at the wall will then decay and we end up with a standard domain wall. Nevertheless, the Dirichlet boundary condition provides a good approximation for determining the amount of CP-violation inside the wall just after the formation of the defect.

3.5 VARIATION OF THE HYPERCHARGE ANGLE θ AND THE GOLDSTONE MODES

We now turn to the case where we allow the hypercharge angle θ of $U(1)_Y$ to vary on both domains alongside the Goldstone modes of $SU(2)_L$. In this case, we expect the formation of domain walls which are both CP and charge violating at the same time. We first discuss the case when the hypercharge angle θ and one single Goldstone mode g_i are different on

both domains. We then discuss the case of pure $SU(2)_L$ and finish with considering the general case when $U(x)$ is a general electroweak symmetry matrix of $SU(2)_L \times U(1)_Y$. We provide the numerical solutions for the equations of motion using both Dirichlet and von Neumann boundary conditions.

3.5.1 Variation of θ and g_1

We start by considering the case when the vacua of the two domains have different hypercharge angle θ and Goldstone mode g_1 . The matrix $U(x)$ (2.35) simplifies to:

$$U(x) = e^{i\theta(x)} \begin{pmatrix} \cos(g_1(x)/2) & i \sin(g_1(x)/2) \\ i \sin(g_1(x)/2) & \cos(g_1(x)/2) \end{pmatrix}. \quad (3.54)$$

Such a case is relevant to see whether a solution $\xi(x) \neq 0$ inside the wall will lead to a non-vanishing $v_+(x)$ condensate on the wall. The energy functional (3.13) is given by:

$$\begin{aligned} \mathcal{E}(x) = & \frac{1}{2} \left(\frac{dv_1}{dx} \right)^2 + \frac{1}{2} \left(\frac{dv_2}{dx} \right)^2 + \frac{1}{2} \left(\frac{dv_+}{dx} \right)^2 + \frac{1}{2} v_2^2(x) \left(\frac{d\xi}{dx} \right)^2 \\ & + \frac{1}{2} \left(\frac{d\theta}{dx} \right)^2 \left[v_1^2(x) + v_2^2(x) + v_+^2(x) \right] + \frac{1}{8} \left(\frac{dg_1}{dx} \right)^2 \left[v_1^2(x) + v_2^2(x) + v_+^2(x) \right] \\ & + \frac{1}{2} \frac{dg_1}{dx} \left[v_+(x) \sin(\xi) \frac{dv_2}{dx} - v_2(x) \sin(\xi) \frac{dv_+}{dx} + 2v_+v_2 \cos(\xi) \frac{d\theta}{dx} + v_+v_2 \cos(\xi) \frac{d\xi}{dx} \right] \\ & + V_{2HDM}. \end{aligned} \quad (3.55)$$

Figure 3.17a shows the numerical results for the vacuum configuration using Dirichlet boundary conditions. We take the values of the hypercharge angle θ and Goldstone mode g_1 to be: $\theta(-\infty) = 0$, $g_1(-\infty) = 0$ for the vacuum Φ_- on the left and $\theta(+\infty) = \pi/2$, $g_1(+\infty) = \pi/2$ for the vacuum Φ_+ on the right. In this case we find a very small non-vanishing condensate $v_+(x)$ inside the wall. We also observe that the CP-violating phase $\xi(x)$ is slightly enhanced inside the wall compared to the case where only the hypercharge varies across the wall (cf. Figure 3.7a). However, this CP and charge breaking solution is unstable as it has a higher energy than the standard domain wall solution which leads the CP-violating phase $\xi(x)$ and the electric charge violating vacuum $v_+(x)$ to decay. When using von Neumann boundary conditions (see Figure 3.18), both the hypercharge angle θ and the Goldstone mode g_1 evolve to become equal on both domains and the solution does not exhibit CP or electric charge violating vacua.

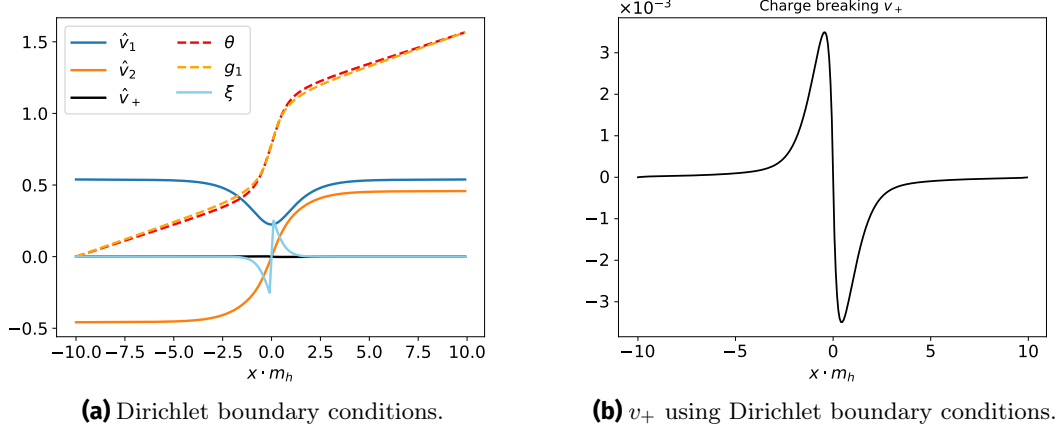


Figure 3.17: (a) Solutions of the equations of motion when varying both the hypercharge angle θ and Goldstone mode g_1 using Dirichlet boundary conditions. We observe a non-vanishing CP-violating phase $\xi(x)$ inside the domain wall. The derivatives of θ and g_1 at $\pm\infty$ are non-zero, reflecting the instability of the solution. (b) Zoom on the solution for $v_+(x)$. The solution is electric charge violating as v_+ varies inside the domain wall.

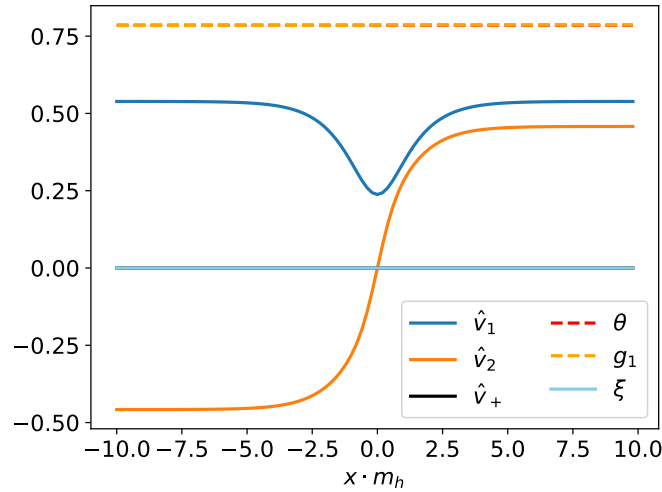


Figure 3.18: Solutions for the equations of motion using von Neumann Boundary conditions. Notice that the hypercharge angle and the Goldstone mode g_1 are the same on both domains and the domain wall solution does not exhibit CP or electric charge violation.

3.5.2 Variation of θ and g_2

We now vary both θ and g_2 . The matrix $U(x)$ (2.35) simplifies to:

$$U(x) = e^{i\theta(x)} \begin{pmatrix} \cos(g_2(x)/2) & \sin(g_2(x)/2) \\ -\sin(g_2(x)/2) & \cos(g_2(x)/2) \end{pmatrix}. \quad (3.56)$$

In this case one would expect that we get both effects of charge and CP-violation inside the wall. The energy functional (3.13) is:

$$\mathcal{E} = \frac{1}{2} \left(\frac{dv_1}{dx} \right)^2 + \frac{1}{2} \left(\frac{dv_2}{dx} \right)^2 + \frac{1}{2} \left(\frac{dv_+}{dx} \right)^2 + \frac{1}{2} v_2^2(x) \left(\frac{d\xi}{dx} \right)^2 + \frac{1}{2} \left(\frac{d\theta}{dx} \right)^2 \left[v_1^2(x) + v_2^2(x) \right]$$

$$\begin{aligned}
& + v_+^2(x) \Big] + \frac{1}{8} \left(\frac{dg_2}{dx} \right)^2 \left[v_1^2(x) + v_2^2(x) + v_+^2(x) \right] + \frac{1}{2} \frac{dg_2}{dx} \left[-v_+(x) \cos(\xi) \frac{dv_2}{dx} \right. \\
& \left. + v_2(x) \cos(\xi) \frac{dv_+}{dx} - 2v_+v_2 \sin(\xi) \frac{d\theta}{dx} + v_+v_2 \sin(\xi) \frac{d\xi}{dx} \right] + V_{2HDM}. \quad (3.57)
\end{aligned}$$

Figure 3.19 shows the solution for both Dirichlet (in Figure 3.19a) and von Neumann

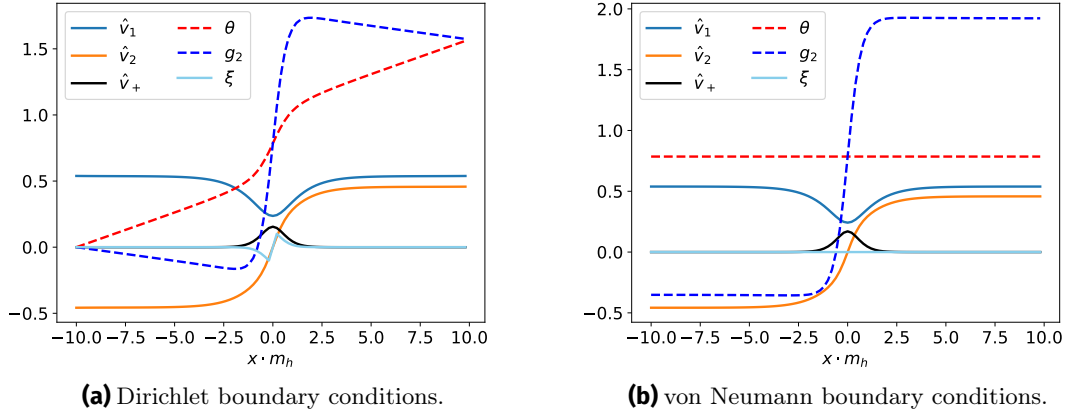


Figure 3.19: Solutions of the equations of motion in the case of different values of the hypercharge angle θ and Goldstone mode g_2 in the two regions. (a) Using Dirichlet boundary conditions. (b) Using von Neumann boundary conditions. Note that when using the von Neumann boundary condition, the CP-violating effect vanishes after some time as the hypercharge angle $\theta(x)$ becomes constant for all x , while the condensate $v_+(x) \neq 0$ stays stable.

(Figure 3.19b) boundary conditions. The initial boundary conditions for θ and g_2 ($\theta(-\infty) = g_2(-\infty) = 0$, $\theta(+\infty) = g_2(+\infty) = \pi/2$) lead to a charge and CP-breaking vacuum inside the wall when using Dirichlet boundary conditions. However, such a solution is energetically unstable since a non-zero $\xi(x)$ gives a positive contribution to the energy of the domain wall. We also observe a non-zero derivative for $\theta(x)$ and $g_2(x)$ at the boundaries. This behavior reflects the instability of this solution, since the values of θ and g_2 on both domains try to change in order to further minimize the energy of the vacuum configuration.

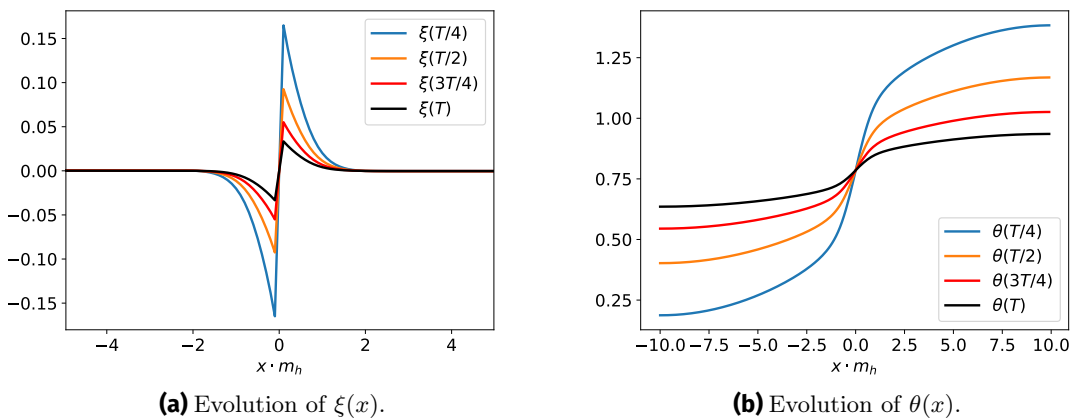


Figure 3.20: (a) Evolution of $\xi(x)$ at different iteration times with $T = 3 \times 10^5$, notice that the CP-violating phase $\xi(x)$ decreases with time. (b) Evolution of $\theta(x)$ at different iteration times with $T = 3 \times 10^5$, notice that $\theta(x)$ tend to dynamically change to become the same value on both domains.

Using von Neumann boundary conditions (Figure 3.19b), where the boundaries can change dynamically to minimize the energy of the vacuum configuration, the derivatives of $\theta(x)$ and $g_2(x)$ at the boundaries vanish. One notices that for the solution which minimizes the energy the most, the charge breaking vacuum inside the wall gets enhanced while the CP-breaking phase $\xi(x)$ inside the wall will start decreasing and eventually vanishes once the values for θ on both domains become equal to each other (as is shown in Figures 3.20b and 3.20a). This vacuum configuration is stable, since its dimensionless energy $\hat{E} = 0.476$

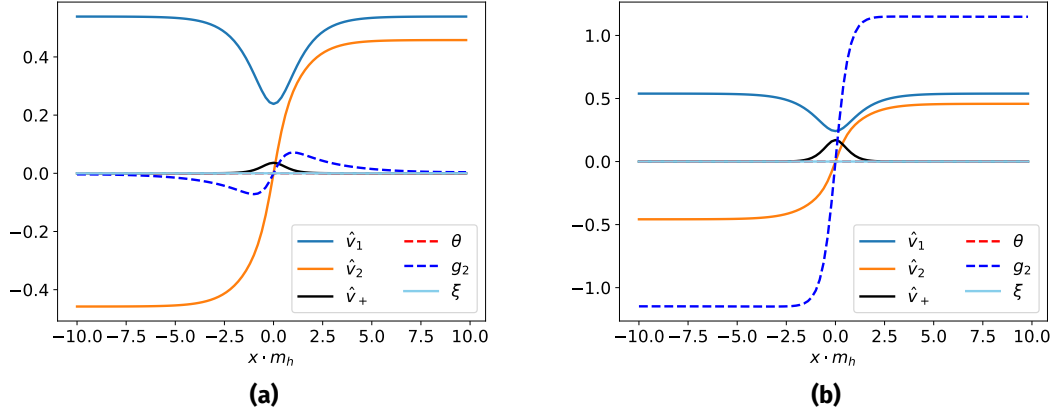


Figure 3.21: Evolution of the $v_+(x)$ condensate inside the wall. (a) Starting from a standard domain wall solution. (b) After some time the standard domain wall solution decays into a stable charge-breaking solution without CP-violation.

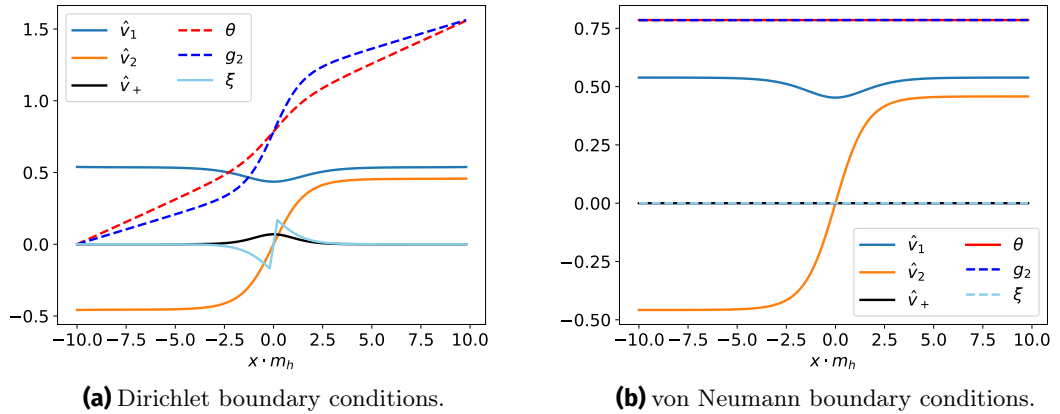


Figure 3.22: (a) Solutions of the equations of motion for PP II (3.32) using Dirichlet boundary conditions, this field configuration is unstable. (b) Solutions using von Neumann boundary conditions. The CP and charge-breaking vacua inside the wall vanish and we end with a standard domain wall solution.

is lower than the standard domain wall's energy $\hat{E}_{standard} = 0.507$. This means that the standard domain wall solution will decay into the charge-breaking domain wall solution as can be seen in Figure 3.21. The Goldstone mode g_2 changes dynamically from a vacuum configuration where it is equal on both domains to a lower energy configuration with different values for g_2 on both domains. The hypercharge angle θ , however, stays zero on both domains and a CP-violating phase $\xi(x)$ does not develop inside the wall, as such a solution would otherwise give a positive contribution to the energy of the defect.

For other parameter points, such as PP II (3.32), we observe the opposite behavior: the energy of the vacuum configuration for the CP and charge-breaking wall is higher than the energy of the standard wall. Such a scenario is shown in Figure 3.22 using Dirichlet (Figure 3.22a) and von Neumann (Figure 3.22b) boundary conditions. The Dirichlet solution exhibits a CP and charge-breaking vacuum which is energetically unstable. Using von Neumann boundary conditions, the values of $v_+(0)$ and $\xi(x)$ decrease until they vanish (both regions end up with the same value for g_2 and θ) and we recover the standard domain wall solution.

3.5.3 Variation of θ and g_3

We now discuss the variation of θ alongside g_3 . In this case one expects only a CP-violating solution and no charge violation inside the wall. The matrix $U(x)$ (2.35) simplifies to:

$$U(x) = e^{i\theta(x)} \begin{pmatrix} e^{ig_3(x)/2} & 0 \\ 0 & e^{-ig_3(x)/2} \end{pmatrix}. \quad (3.58)$$

The energy functional (3.13) is given by:

$$\begin{aligned} \mathcal{E} = & \frac{1}{2} \left(\frac{dv_1}{dx} \right)^2 + \frac{1}{2} \left(\frac{dv_2}{dx} \right)^2 + \frac{1}{2} \left(\frac{dv_+}{dx} \right)^2 + \frac{1}{2} v_2^2(x) \left(\frac{d\xi}{dx} \right)^2 + v_2^2(x) \frac{d\theta}{dx} \frac{d\xi}{dx} \\ & + \frac{1}{2} \left[v_1^2(x) + v_2^2(x) + v_+^2(x) \right] \left(\frac{d\theta}{dx} \right)^2 + \frac{1}{8} \left(\frac{dg_3}{dx} \right)^2 \left[v_1^2(x) + v_2^2(x) + v_+^2(x) \right] \\ & - \frac{1}{2} \frac{dg_3}{dx} \left[\frac{d\theta}{dx} \left(v_1^2(x) + v_2^2(x) - v_+^2(x) \right) + v_2^2(x) \frac{d\xi}{dx} \right] + V_{2HDM}. \end{aligned} \quad (3.59)$$

Using the equations of motion for $\theta(x)$ and $g_3(x)$, we can derive an equation that describes how the change in $\theta(x)$ and $g_3(x)$ causes a change in $\xi(x)$:

$$\frac{d\theta}{dx} - \frac{1}{2} \frac{dg_3}{dx} = - \frac{v_2^2}{v_1^2 + v_2^2} \frac{d\xi}{dx}. \quad (3.60)$$

From such a relation, one expects the possibility of having an interference in the contributions of θ and g_3 .

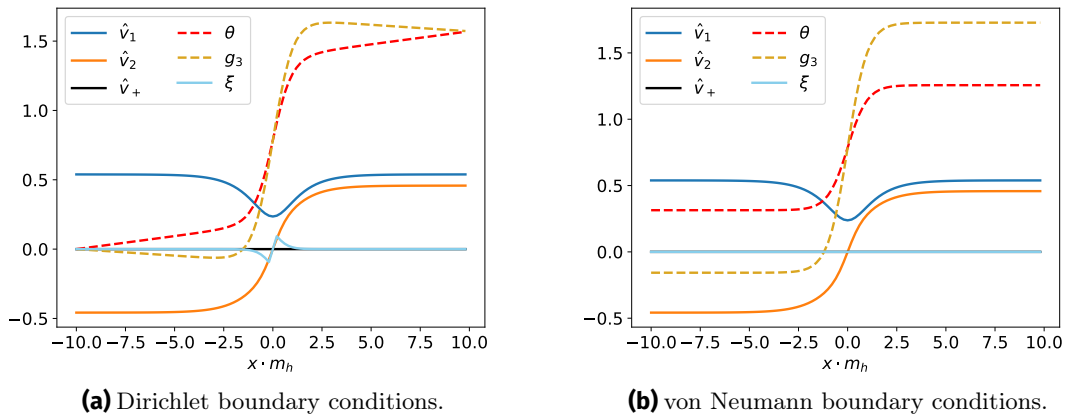


Figure 3.23: Solutions of the equations of motion in the case when θ and g_3 are different on both domains. (a) Using Dirichlet boundary conditions. (b) Using von Neumann boundary conditions. The CP-violating phase $\xi(x)$ is zero even though the Goldstone mode g_3 and hypercharge angle θ are different on both domains. This behavior is explained by the relation (3.60).

Figure 3.23 shows the numerical solution to the equations of motion. The initial condition were taken to be $\theta(-\infty) = g_3(-\infty) = 0$, $\theta(+\infty) = g_3(+\infty) = \pi/2$. In this case, we again see that the Dirichlet boundary condition leads to a localized CP-violating phase $\xi(x)$ inside the wall and that the derivatives of the Goldstone modes do not vanish at the boundaries. This vacuum field configuration is energetically unstable and decays to the standard vacuum configuration with $\xi(x) = 0$ for all x . In contrast to the results from the variation of θ and g_3 individually, the minimum vacuum configuration gets two different values for θ and g_3 in the two domains (see Figure 3.23b).

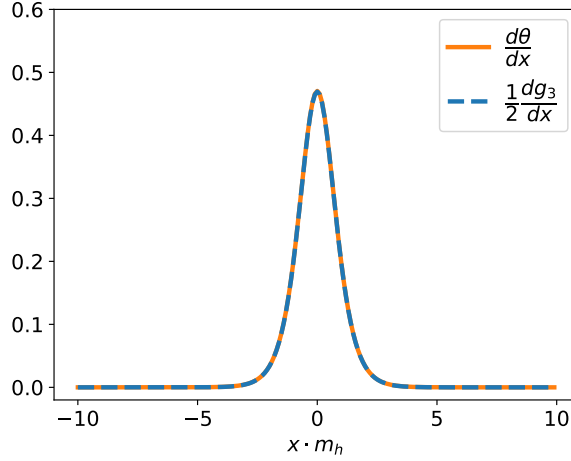


Figure 3.24: Values of the derivative of $\theta(x)$ and $g_3(x)$ using von Neumann boundary condition. The numerical solution satisfies (3.60) leading to the vanishing of the phase $\xi(x)$ inside the wall even though the Goldstone modes are different on both sides of the wall.

Using (3.60), one sees that if the derivative of $\theta(x)$ is equal to half the derivative of $g_3(x)$, one obtains $d\xi/dx = 0$. This clarifies why the values of $\xi(x)$ are vanishingly small despite the different Goldstone modes on both domains (see Figure 3.23b). This condition can be verified in Figure 3.24, where we see that both expressions agree numerically.

3.5.4 Variation of $SU(2)_L$ Goldstone modes g_1, g_2 and g_3

In this special case the vacua in both regions are related by an $SU(2)_L$ gauge transformation and we ignore the effects coming from the change in the hypercharge angle θ . The matrix $U(x)$ (2.35) simplifies to:

$$U(x) = \begin{pmatrix} \cos(G(x)) + ig_3(x) \sin(G(x))/G(x) & (g_2(x) + ig_1(x)) \sin(G(x))/G(x) \\ -(g_2(x) - ig_1(x)) \sin(G(x))/G(x) & \cos(G(x)) - ig_3(x) \sin(G(x))/G(x) \end{pmatrix}. \quad (3.61)$$

The energy functional (3.13) is given by:

$$\begin{aligned} \mathcal{E}(x) = & \frac{1}{2} \left(\frac{dv_1}{dx} \right)^2 + \frac{1}{2} \left(\frac{dv_2}{dx} \right)^2 + \frac{1}{2} \left(\frac{dv_+}{dx} \right)^2 + \frac{1}{2} v_2^2(x) \left(\frac{d\xi}{dx} \right)^2 + \frac{1}{2} v_1^2(x) I_0(x) \\ & + \frac{1}{2} v_2^2(x) \left[I_0(x) + 2 \frac{d\xi}{dx} I_3(x) \right] + v_2(x) \left[\sin(\xi) \frac{dv_+}{dx} I_1(x) - \cos(\xi) \frac{dv_+}{dx} I_2(x) \right] \\ & + v_+(x) \left[-\sin(\xi) \frac{dv_2}{dx} I_1(x) + \cos(\xi) \frac{dv_2}{dx} I_2(x) \right] - v_+(x) v_2(x) \left[\cos(\xi) \frac{d\xi}{dx} I_1(x) \right] \end{aligned}$$

$$\left. + \sin(\xi) \frac{d\xi}{dx} I_2(x) \right] + \frac{1}{2} v_+^2(x) I_0(x) + V_{2HDM}, \quad (3.62)$$

where the functions $I_{0,1,2,3}(x)$ are defined in equations (3.14)-(3.17). The numerical results

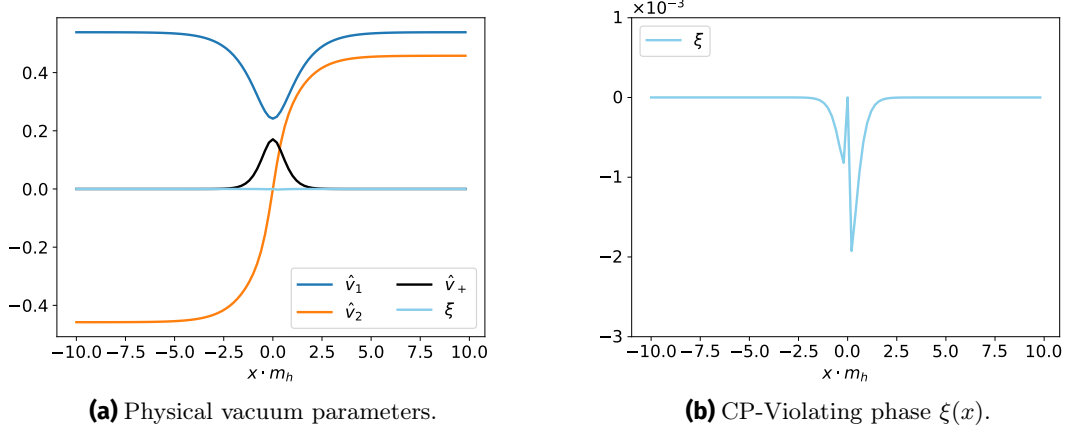


Figure 3.25: Vacuum field configuration for domains with different $SU(2)_L$ modes g_1 , g_2 and g_3 using von Neumann boundary conditions. (a) The solution for the vacuum parameters $v_i(x)$ and $\xi(x)$, we find that the DW is charge breaking ($v_+(0) \neq 0$). (b) Zoom on the CP-violating phase $\xi(x)$, we see that for this particular case $\xi(x)$ is asymmetric.

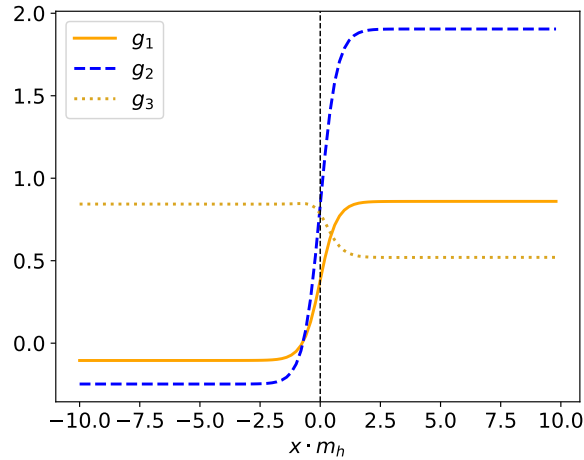


Figure 3.26: Goldstone modes $g_1(x)$, $g_2(x)$ and $g_3(x)$. Notice that the profiles of the Goldstone modes are asymmetric inside the wall. This suggests an interference between the different Goldstone modes.

using von Neumann boundary conditions are shown in Figure 3.25. The initial profile of the Goldstone modes were chosen to be $g_i(-\infty) = 0$ and $g_i(+\infty) = \pi/2$, (where i denotes 1,2,3) with a tangent hyperbolic function interpolating both boundaries. The solution has a stable charge-violating vacuum $v_+(x)$ inside the domain wall, as well as a small and stable CP-violating phase $\xi(x)$. In contrast to the previous results, $\xi(x)$ in this particular case is asymmetric. This behavior could be attributed to the fact that the profiles of the Goldstone modes $g_i(x)$ are not symmetrical (see Figure 3.26). There is also an interference between the Goldstone modes as some have negative derivatives while the others have a positive derivative inside the wall. Note that, in this case, the Goldstone modes keep having a different value on both domains.

3.6 GENERAL DOMAIN WALL SOLUTION

We finish the discussion of domain wall solutions in the 2HDM by considering the case with a general matrix $U(x)$ (2.35):

$$U(x) = e^{i\theta(x)} \exp\left(i \frac{g_i(x)}{2} \sigma_i\right), \quad (3.63)$$

We recall the general formula for the energy functional 3.13:

$$\begin{aligned} \mathcal{E}(x) = & \frac{1}{2} \left(\frac{dv_1}{dx}\right)^2 + \frac{1}{2} \left(\frac{dv_2}{dx}\right)^2 + \frac{1}{2} \left(\frac{dv_+}{dx}\right)^2 + \frac{1}{2} v_2^2(x) \left(\frac{d\xi}{dx}\right)^2 + \frac{1}{2} v_1^2(x) \left[\left(\frac{d\theta}{dx}\right)^2 + I_0(x) \right. \\ & \left. + 2 \frac{d\theta}{dx} I_3(x) \right] + \frac{1}{2} v_2^2(x) \left[\left(\frac{d\theta}{dx}\right)^2 + I_0(x) + 2 \left(\frac{d\theta}{dx} + \frac{d\xi}{dx}\right) I_3(x) + 2 \frac{d\theta}{dx} \frac{d\xi}{dx} \right] \\ & + \frac{1}{2} v_+^2(x) \left[\left(\frac{d\theta}{dx}\right)^2 + I_0(x) - 2 \frac{d\theta}{dx} I_3(x) \right] + v_2(x) \left[\sin(\xi) \frac{dv_+}{dx} I_1(x) - \cos(\xi) \frac{dv_+}{dx} I_2(x) \right] \\ & + v_+(x) \left[-\sin(\xi) \frac{dv_2}{dx} I_1(x) + \cos(\xi) \frac{dv_2}{dx} I_2(x) \right] + \frac{v_+(x)v_2(x)}{2} \left[4 \sin(\xi) I_2(x) \frac{d\theta}{dx} \right. \\ & \left. - 4 \cos(\xi) I_1(x) \frac{d\theta}{dx} - 2 \cos(\xi) \frac{d\xi}{dx} I_1(x) - 2 \sin(\xi) \frac{d\xi}{dx} I_2(x) \right] + V_{2HDM}, \quad (3.64) \end{aligned}$$

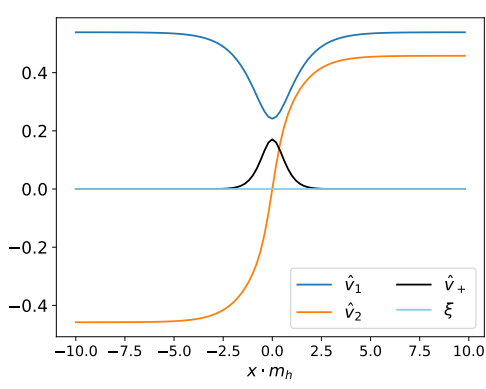
Here, the Goldstone modes g_i and hypercharge angle θ are chosen randomly and can be different on both domains.

Field	v_1	v_2	v_+	ξ	θ	g_1	g_2	g_3
Boundary at $+\infty$	positive	positive	0	0	$\pi/2$	0	$\pi/6$	0
Boundary at $-\infty$	positive	negative	0	0	0	0	$\pi/6$	0

Table 3.1: Asymptotic values of the fields at the boundaries. The initial profile for $\theta(x)$ is taken to be a tangent hyperbolic function interpolating between 0 at $-\infty$ and $\pi/2$ at $+\infty$. We use von Neumann boundary condition to get the lowest energy solution.

Table 3.1 shows an example of the initial asymptotic values for the fields at $\pm\infty$ that we use for the numerical calculations with θ having a tangent hyperbolic profile interpolating the values on the two boundaries. We use von Neumann boundary conditions to get the numerical solution of the 8 equations of motions describing the profiles of the fields.

Figure 3.27 shows the numerical solution of the vacuum configuration for this choice of hypercharge angle θ and Goldstone modes. The solution features a stable charge-violation as well as a small but stable CP-violating phase $\xi(x)$ inside the wall. In contrast to all previous cases, the behavior of the hypercharge angle $\theta(x)$ and the Goldstone modes $g_1(x)$ and $g_3(x)$ is non-trivial inside the wall. We also note that, even though we started with the Goldstone modes g_i being the same on both domains, the lowest energy solution has different values for $g_i(\pm\infty)$.



(a) Higgs vacuum parameters.

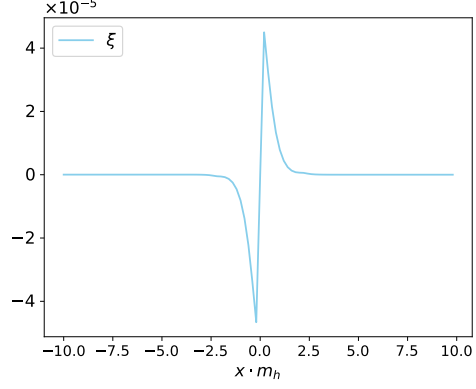
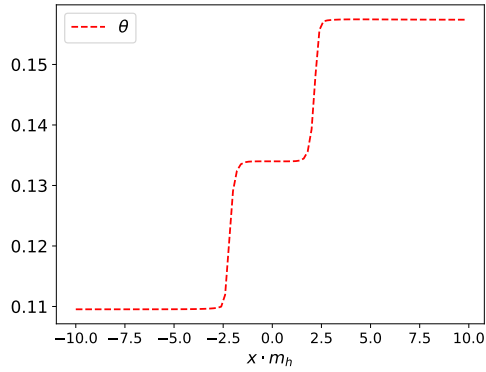
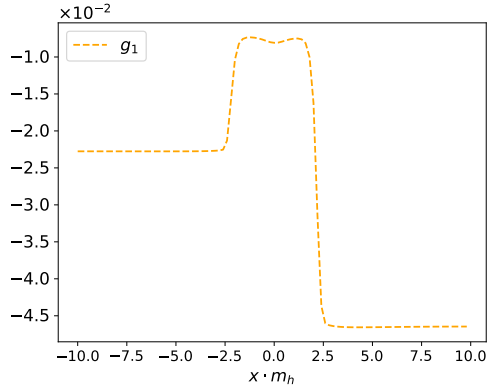
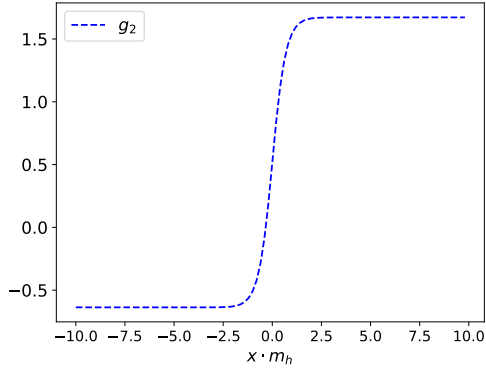
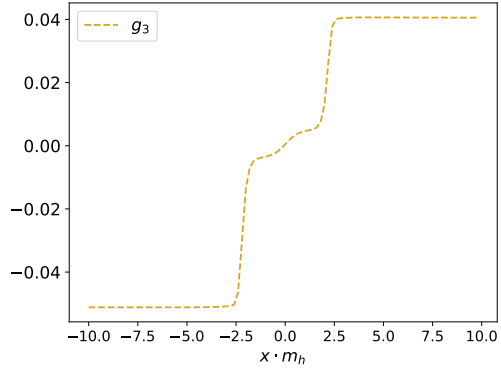
(b) CP-violating phase ξ .(c) Hypercharge angle θ .(d) Goldstone mode g_1 .(e) Goldstone mode g_2 .(f) Goldstone mode g_3 .

Figure 3.27: Domain wall solution for the vacuum parameters in the case when the hypercharge angle θ and the Goldstone modes g_i can change on both regions. (a) and (b) Vacuum parameters of the DW solution. The solution using von Neumann boundary conditions, exhibits a stable charge breaking condensate v_+ and also a small but stable CP-violating phase $\xi(x)$. (c), (d), (e) and (f) represent the DW solution for the hypercharge angle θ and Goldstone modes g_i , respectively. One notices the non-trivial behavior of the hypercharge angle and Goldstone modes $g_1(x)$ and $g_3(x)$.

3.7 DEPENDENCE OF THE KINK SOLUTION ON THE PARAMETER POINTS OF THE 2HDM

In this subsection, we briefly describe the dependence of the kink solution on the masses of the Higgs bosons of the 2HDM as well as $\tan(\beta)$. For all the discussed parameters, we use the alignment limit: $\alpha = \beta$. In this work we do not take into account experimental constraints on the 2HDM. Our choice of the parameter points discussed is done in order to give an overview of the different properties that arise for domain walls in the 2HDM.

We start by analyzing the effects of the parameter points on the standard domain wall solution. We therefore take the matrix $U(x)$ to be the identity. First, we consider varying the mass of the CP-even Higgs m_H with values between 80 GeV and 580 GeV, while the other parameters are fixed to:

$$m_A = 200 \text{ GeV}, \quad m_C = 200 \text{ GeV}, \quad \tan(\beta) = 0.85. \quad (3.65)$$

The profiles of the vacuum expectation values $v_1(x)$ and $v_2(x)$ for different m_H are shown in Figures 3.28a and 3.28b. We find that for higher m_H , the value of v_1 inside the domain wall ($v_1(x=0)$) becomes smaller. This is explained by the behavior of the effective mass $M_1(x)$ inside the domain wall (see 3.34) as shown in Figure 3.29a.

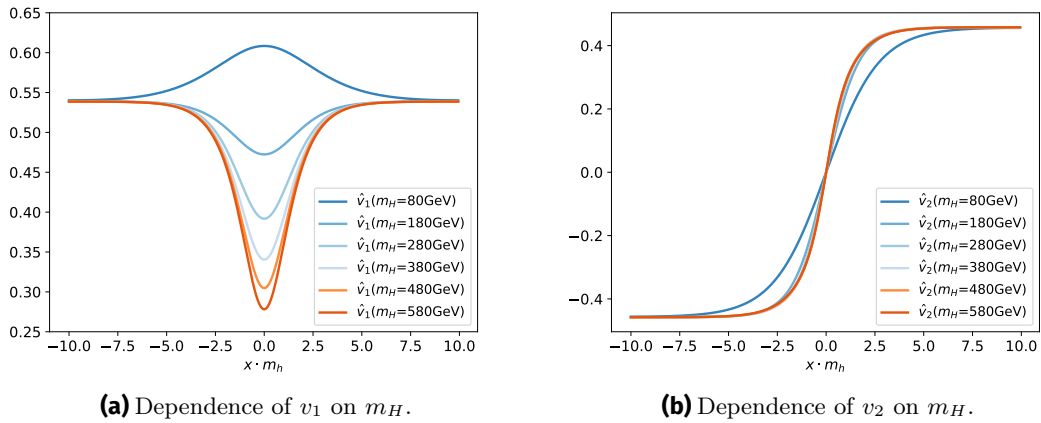


Figure 3.28: Dependence of the vacuum expectation values $v_1(x)$ and $v_2(x)$ and effective masses $M_1(x)$ and $M_+(x)$ on the variation of the CP-even Higgs mass m_H . The masses of the other Higgs scalars are fixed to be 200 GeV and $\tan(\beta) = 0.85$. (a) Profile of $v_1(x)$ inside the wall, notice that for small m_H , $v_1(x)$ becomes bigger inside the wall. (b) Profile of $v_2(x)$, we observe that a higher m_H leads to a bigger width for the wall.

In order to understand the behavior of $v_1(x)$ inside the wall and its dependence on the mass parameter m_H , we consider a potential of the form:

$$V(v_1(x), v_2(x)) = \frac{m_{22}}{2} v_2^2(x) + \frac{\lambda_2}{8} v_2^4(x) + M_1(x) v_1^2(x) + \frac{\lambda_1}{8} v_1^4(x). \quad (3.66)$$

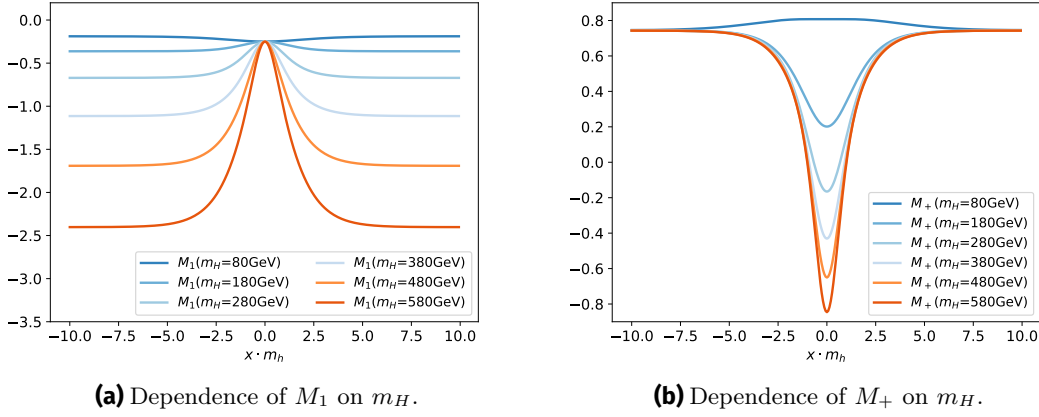


Figure 3.29: (a) Effective mass $M_1(x)$ for $v_1(x)$, notice that for higher masses, this value becomes less negative inside the wall leading to a smaller $v_1(0)$. (b) Effective mass $M_+(x)$ for $v_+(x)$. We observe that outside the wall, this quantity does not depend on m_H . However higher m_H lead to a smaller and even negative values $M_+(0)$ inside the DW.

Outside the wall and for parameter points with masses $m_H > 80$ GeV, the effective mass term M_1 is smaller (more negative) than inside the domain wall. Therefore, the minimum $v_1^{DW} = v_1(x=0)$ of the potential $V_0(v_1, v_2=0)$ inside the wall (depicted in blue) is smaller than v_1^* , the minimum of the potential $V(v_1, v_2=v_2^*)$ outside the wall (depicted in orange) as is shown in Figure 3.30a. Note that for $m_H = 80$ GeV, the opposite effect

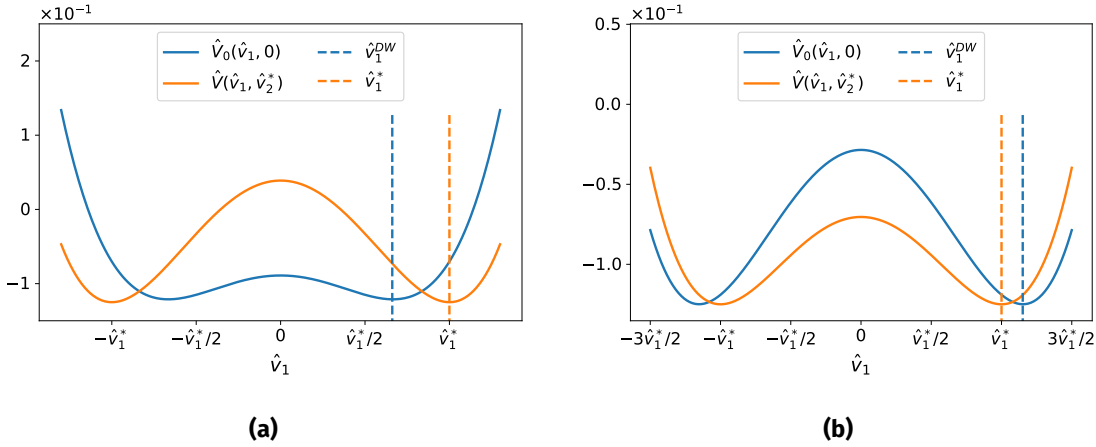


Figure 3.30: Comparison of the potential for v_1 inside (blue) and outside (orange) the domain wall. (a) For $m_H = 250$ GeV and (b) For $m_H = 80$ GeV. The other mass parameters are fixed to $m_A = m_C = 200$ GeV. The potential $\hat{V}_0(\hat{v}_1, 0)$ is shifted to have the same height as $\hat{V}(\hat{v}_1, \hat{v}_2)$.

occurs and $v_1(x=0)$ inside the wall is bigger than outside of it (see Figure 3.30b). This is due to the fact that for $m_H = 80$ GeV, $M_1(x)$ becomes more negative inside the wall than outside of it (see Figure 3.29a). This leads the minimum $v_1^{DW} = v_1(x=0)$ of the potential $V_0(v_1, v_2=0)$ inside the wall to be bigger than v_1^* , the minimum of the potential $V(v_1, v_2=v_2^*)$ outside the wall as is shown in Figure 3.30b. Notice also that the effective mass term $M_1(x=0)$ is the same for all mass parameters. This is because the parameter m_{11} does not depend on m_H . As for the dependence of the kink solution for $v_2(x)$ on m_H , we observe that increasing the mass leads to a thinner profile for the kink as can be seen in Figure 3.28b. Figure 3.29b shows $M_+(x)$ for different m_H . A negative effective mass

$M_+(0)$ inside the wall and therefore the possibility of having a charged condensate $v_+(x)$ localized on the wall is possible for higher masses of H .

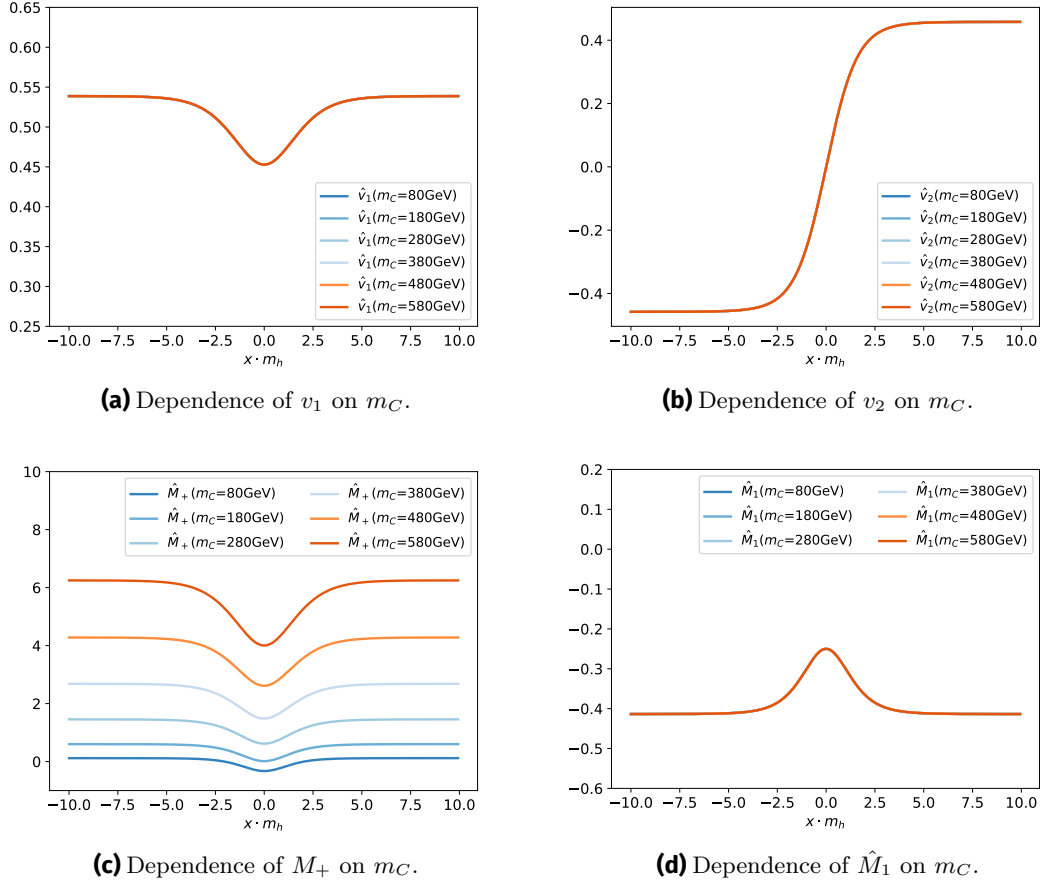


Figure 3.31: Dependence of the vacuum expectation values $v_1(x)$ (a) and $v_2(x)$ (b) and effective masses $M_+(x)$ (c) and $M_1(x)$ (d) on the change of the charged Higgs mass. These results are obtained by fixing $m_{H,A} = 200$ GeV and $\tan(\beta) = 0.85$. The profiles of the vacua $v_1(x)$ and $v_2(x)$ are independent on m_C (see (a) and (b)). The variation of m_C has an impact on the effective mass for $v_+(x)$ and lower values of m_C can lead to negative $M_+(0)$ inside the wall.

We now vary the mass of the charged Higgs m_C while keeping all other masses fixed to 200 GeV and $\tan(\beta) = 0.85$. We do not observe any change in the profiles of the vacua $v_1(x)$ and $v_2(x)$ (see Figure 3.31a and 3.31b). However, we observe a change in the effective mass $M_+(x)$ for different masses m_C and it becomes smaller inside the wall as shown in Figure 3.31c. However, the value $\hat{M}_+(x = 0)$ is only negative for small masses of the charged Higgs. Therefore, if the mass m_H of the CP-even Higgs is small, it is possible to have a stable charged condensate in the wall only if the charged Higgs masses m_C is very low.

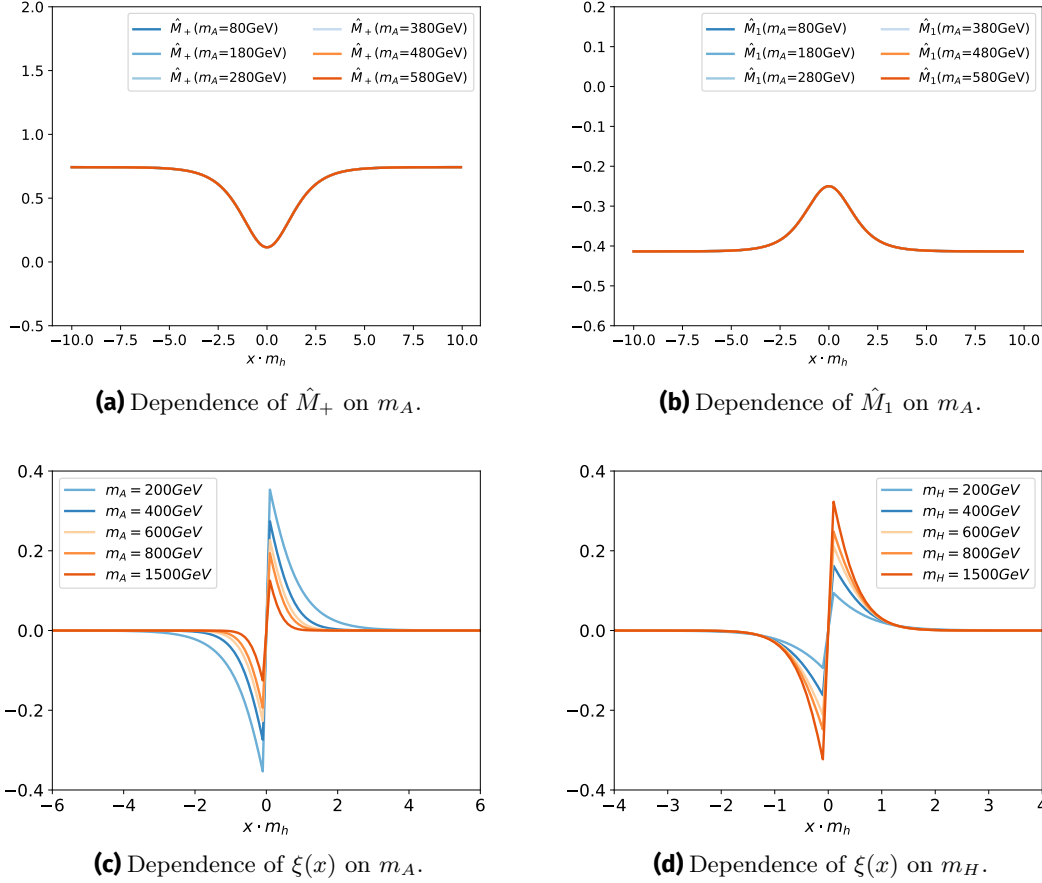


Figure 3.32: Dependence of the effective masses $M_1(x)$ and $M_+(x)$ on the variation of the CP-odd Higgs mass. We find that the properties of the domain wall solution are independent of m_A . Dependence of $\xi(x)$ on m_A and m_H . We use the Dirichlet boundary condition in order to get an estimate for the CP-violating phase $\xi(x)$ at the formation stage of the DW. (a) We fix the masses $m_H = 800$ GeV, $m_C = 400$ GeV and $\tan(\beta) = 0.85$. We observe that $\xi(x)$ gets smaller with higher m_A . (b) We fix the masses $m_A = 500$ GeV, $m_C = 400$ GeV and $\tan(\beta) = 0.85$. We observe that $\xi(x)$ gets bigger with higher m_H .

To investigate the dependence of the domain wall properties on the mass m_A of the CP-odd Higgs we vary m_A from 80 GeV to 580 GeV. We keep the masses of the other scalars to be 200 GeV and $\tan(\beta) = 0.85$. The results for $M_1(x)$ and $M_+(x)$ are shown in Figures 3.32b and 3.32a. We do not observe a variation in the properties of the domain walls for the vacuum parameters $v_1(x)$, $v_2(x)$ and $v_+(x)$. We also study the effect of m_A and m_H on the CP-violating phase $\xi(x)$. In this case we study the scenario when the two domains have different hypercharge angle θ and use the Dirichlet boundary condition with $\theta(-\infty) = 0$ and $\theta(+\infty) = \pi/2$. We first fix the masses $m_H = 800$ GeV, $m_C = 400$ GeV and $\tan(\beta) = 0.85$ and vary m_A . The results are shown in Figure 3.32c and we observe that increasing m_A leads to a smaller phase $\xi(x)$ inside the DW. However, when fixing $m_A = 500$ GeV and varying m_H , we observe the opposite behavior: increasing m_H leads to a higher CP-violating phase $\xi(x)$ (see Figure 3.32d).

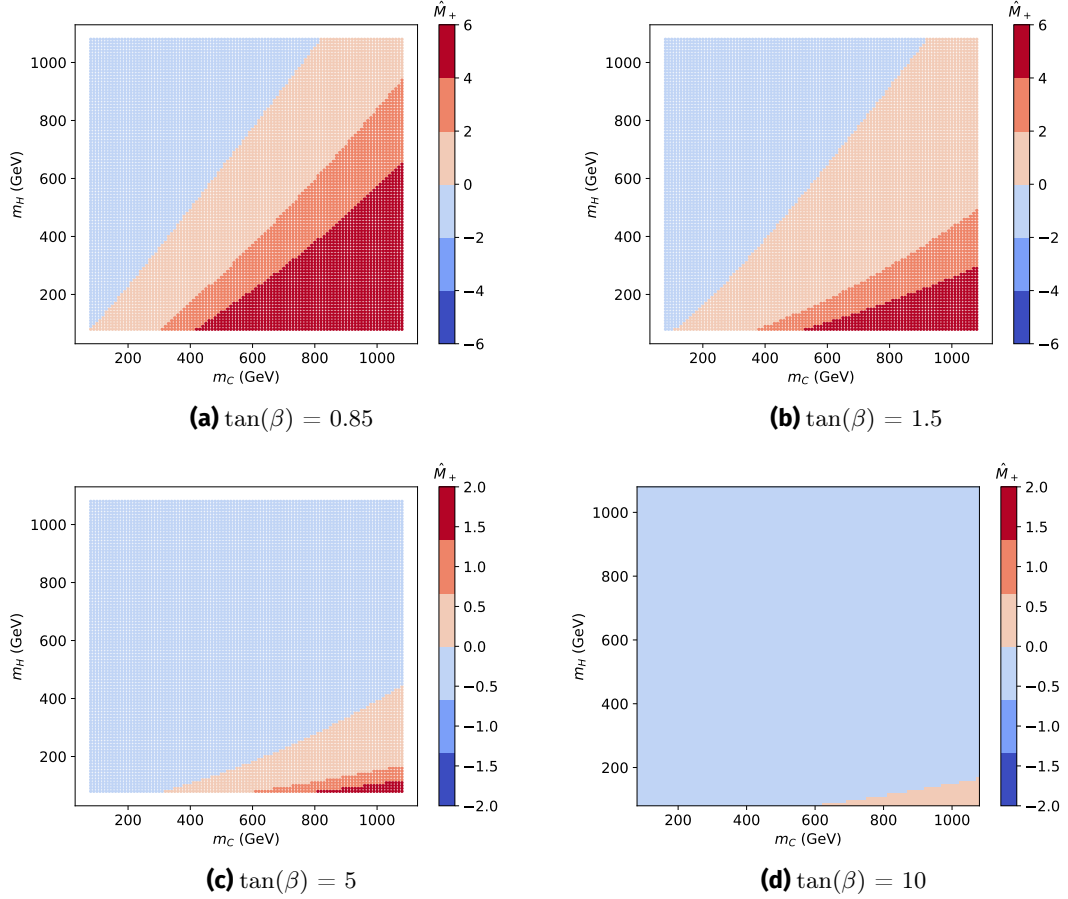


Figure 3.33: Dependence of $\hat{M}_+(0)$ inside the domain wall on the masses m_C and m_H for different values of $\tan(\beta)$. Negative values lead to the possibility of generating a charged vacuum inside the wall.

Finally, we plot in Figure 3.33 the dependence of $\hat{M}_+(0)$ on both m_H and m_C for several values of $\tan(\beta)$. $\hat{M}_+(0)$ does not depend on the mass of the CP-odd Higgs (as seen in Figure 3.32a), therefore we fixed $m_A = 300$ GeV. For low $\tan(\beta) = 0.85$, a large number of parameter points have positive $\hat{M}_+(0)$ (see Figure 3.33a). This leads the scalar potential inside the wall $V_0(v_1, v_+)$ to have its minimum at $v_+(0) = 0$ (see Figure 3.5d). This means that any charge violating solution for those domain walls is unstable. In order to get a stable $v_+(x)$ condensate inside the wall for this low value of $\tan(\beta)$, we need to choose high values for m_H . As we increase $\tan(\beta)$, the fraction of parameter points with a negative $\hat{M}_+(0)$ increases (as is shown in Figure 3.33b) and a charged condensate inside the domain wall can be stable (in case of different g_2 Goldstone mode on both domains). For high values of $\tan(\beta)$, most parameter points have a negative $\hat{M}_+(0)$ as can be seen in Figures 3.33d and 3.33c.

In the case that v_+ develops a stable condensate inside the wall, the masses m_H and m_C can have a sizable effect on the maximum value $v_+(x=0)$ of such a condensate. In order to study this, we solved the equations of motion for the case when the vacua have different values of g_2 using von Neumann boundary conditions. This was done for two scenarios:

- To study the effect of m_H , we fix $m_C = 400$ GeV, $\tan(\beta) = 0.85$ and vary m_H between 80 GeV and 1100 GeV. The results are shown in Figure 3.34a. We observe that the v_+ condensate is unstable for $m_H < 580$ GeV. The value of $v_+(0)$ inside the wall increases with the mass m_H .

- To study the effect of m_C , we fix $m_H = 800$ GeV, $\tan(\beta) = 0.85$ and vary m_C between 80 GeV and 1100 GeV. The results are shown in Figure 3.34b. In this case, $v_+(0)$ gets smaller with heavier m_C . For $m_C > 680$ GeV the condensate becomes unstable.

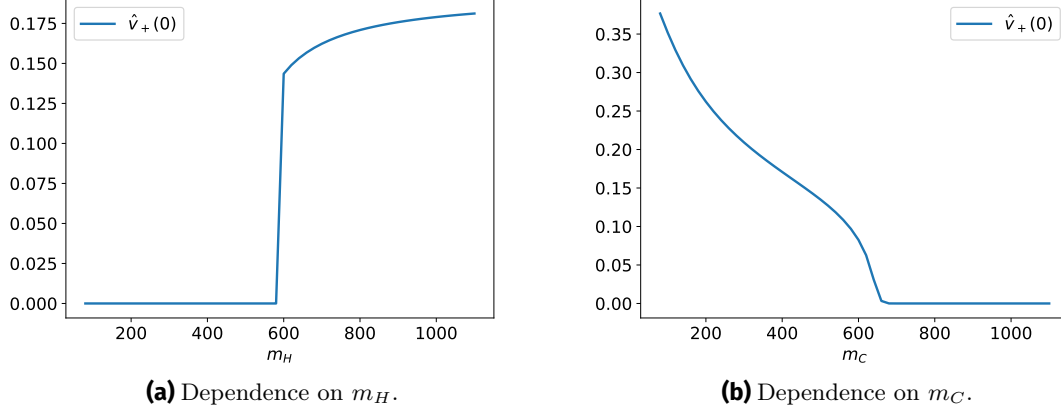


Figure 3.34: Dependence of the charged condensate $\hat{v}_+(0)$ on the mass parameters of the model. (a) We vary m_H and fix $m_C = 400$ GeV. Notice that there is no stable v_+ condensate for $m_H < 580$ GeV. This is due to the effective mass term $M_+(0) > 0$ up to $m_H \approx 500$ GeV as can be seen in Figure 3.33a. (b) We vary m_C and fix $m_H = 800$ GeV. We find that for $m_C > 680$ GeV, the condensate v_+ vanishes. This can be explained by the fact that $M_+(0)$ turns positive for masses m_C around 600 GeV (see Figure 3.33a).

3.8 NON-TOPOLOGICAL KINK SOLUTIONS IN THE 2HDM

We discussed in the previous sections the possibility of having topological kink solutions that interpolate between vacua belonging to disconnected sectors of the vacuum manifold. We now briefly discuss the scenario when both vacua at $x \rightarrow \pm\infty$ belong to the same sector (in the case of the 2HDM, the same 3-sphere M_+ or M_-) as shown in Figure 3.35. We consider the following two degenerate vacua:

$$\Phi_- = \left\{ \frac{1}{\sqrt{2}} \begin{pmatrix} 0 \\ -v_1^* \end{pmatrix}, \frac{1}{\sqrt{2}} \begin{pmatrix} 0 \\ -v_2^* \end{pmatrix} \right\}, \quad \Phi_+ = \left\{ \frac{1}{\sqrt{2}} \begin{pmatrix} 0 \\ v_1^* \end{pmatrix}, \frac{1}{\sqrt{2}} \begin{pmatrix} 0 \\ v_2^* \end{pmatrix} \right\}. \quad (3.67)$$

One can obtain Φ_- by performing a $U(1)_Y$ transformation on Φ_+ , such as for example, $\theta_- = \pi$ and $\theta_+ = 0$. Therefore, both these vacua belong to the same sector M_+ . A kink solution for such a vacuum configuration is not topologically protected against a variation in the fields and therefore any such solution should, in principle, be unstable [133]. We obtain a kink solution (see Figure 3.36a) for this configuration using von Neumann boundary conditions. However, as can be seen in Figure 3.36b, the solution is metastable and decays after some time to the lower energy solution of a homogeneous vacuum configuration. This field configuration is not topologically protected and therefore will be unstable against small field variations. This behavior is better illustrated using the linear parametrization of the Higgs doublets:

$$\Phi_1 = \frac{1}{\sqrt{2}} \begin{pmatrix} 0 \\ \phi_1 + i\phi_2 \end{pmatrix}, \quad \Phi_2 = \frac{1}{\sqrt{2}} \begin{pmatrix} 0 \\ \phi_3 + i\phi_4 \end{pmatrix}. \quad (3.68)$$

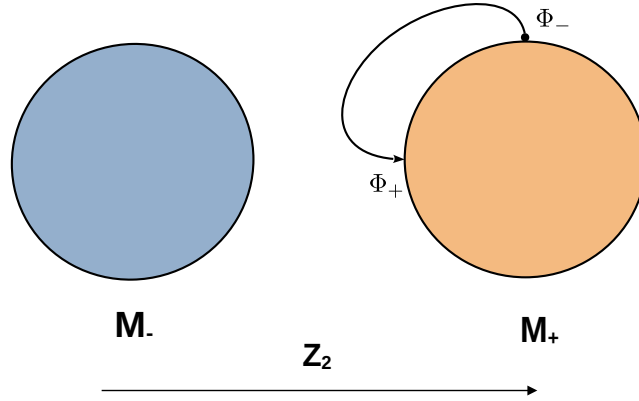


Figure 3.35: Non-topological domain wall vacuum configuration. The vacua on both regions in space lie on the same sector of the vacuum manifold.

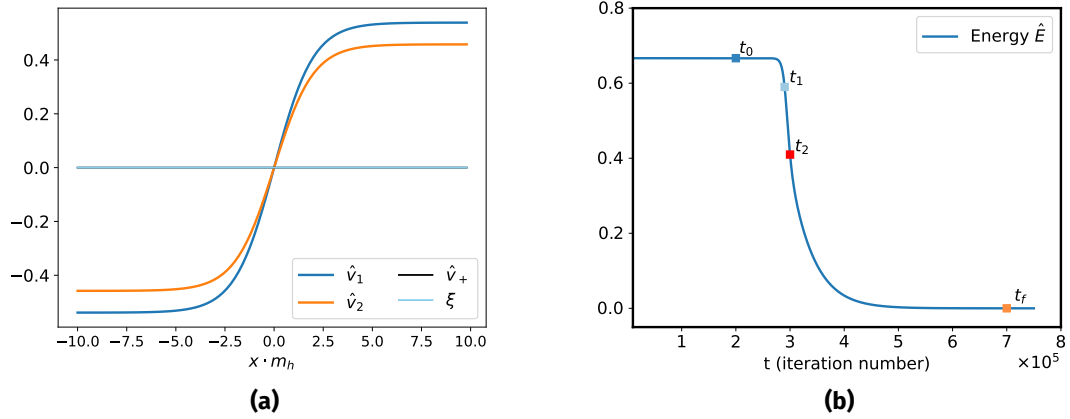


Figure 3.36: (a) Non-topological kink solution for the vacuum configuration at iteration time t_0 . (b) Energy evolution of the non-topological kink solution.

The variables of the non-linear parametrization are then obtained using:

$$v_1 = \sqrt{\phi_1^2 + \phi_2^2}, \quad v_2 = \sqrt{\phi_3^2 + \phi_4^2}, \quad \theta = \arg(\phi_1 + i\phi_2), \quad \xi = \arg(\phi_3 + i\phi_4) - \theta. \quad (3.69)$$

At t_0 , the non-topological domain wall solution interpolates between the vacuum given by $(\phi_1, \phi_2, \phi_3, \phi_4) = (-v_1, 0, -v_2, 0)$ at $x = -\infty$ and the vacuum $(\phi_1, \phi_2, \phi_3, \phi_4) = (v_1, 0, v_2, 0)$ at $x = +\infty$. At this point, the vacua of the doublets have a vanishingly small imaginary component ϕ_2 and ϕ_4 . With time, the imaginary components ϕ_2 and ϕ_4 acquire a sizable vacuum expectation value inside the wall (see Figure 3.37d), which shifts the field configuration at $x = 0$ from $v_1 = 0 = v_2$ to a non-vanishing value causing an instability to the non-topological DW solution as can be seen in Figure 3.37a. This instability grows further, and the new vacuum configuration generated inside the wall propagates into both domains until the homogeneous, trivial vacuum configuration is fulfilled. During the decay of the non-topological domain wall to the trivial vacuum configuration, the profile of $\theta(x)$ varies

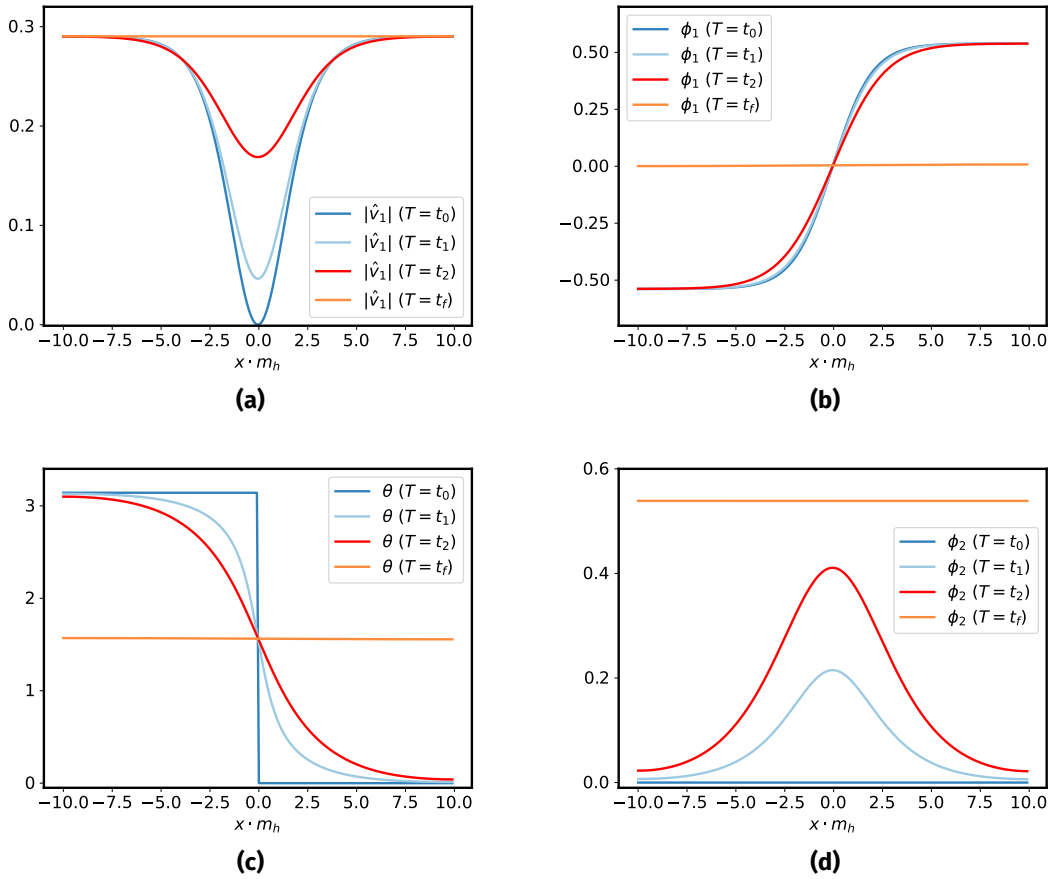


Figure 3.37: Evolution of the non-topological DW solution at different iteration times $t_0 = 2 \cdot 10^5$, $t_1 = 2.9 \cdot 10^5$, $t_2 = 3 \cdot 10^5$ and $t_f = 7 \cdot 10^5$ as shown in Figure 3.36b.

from a step-function profile to a profile interpolating smoothly between θ_- and θ_+ and in the end, we get the same value for θ on both domains.

3.9 DISCUSSION

We investigated in this chapter the different classes of domain walls arising in the 2HDM after EWSB. We extended the work done in [76] and included the variation of all the Goldstone modes of the $SU(2)_L \times U(1)_Y$ symmetry. In contrast to the standard domain wall solution, where only a discrete symmetry such as the Z_2 gets spontaneously broken, we saw that the breaking of abelian and non-abelian symmetries alongside the discrete symmetry leads to the formation of kink solutions with non-trivial effects in the core of the defect, such as CP and charge-violating field configurations. We have found that these different classes of kink solutions can be unstable and decay to the standard kink solution if their energy is higher than the energy of the standard kink solution (where no CP and electric-charge effects occur inside the wall). We demonstrated this behavior using von Neumann boundary conditions, where the Goldstone modes θ and g_i can change their boundary values dynamically in order to minimize the energy of the field configuration. The choice of von Neumann boundary conditions in these types of differential equations is necessary, since it allows higher energy domain wall scalar field configurations to relax

to lower energy domain wall configurations. When discussing the simplified cases (where only the hypercharge or/and a single $SU(2)_L$ Goldstone mode g_i were allowed to change on both domains), we found that for the CP-breaking kink solution, the CP-violating phase $\xi(x)$ inside the defect decays after some time and we recover again the standard kink solutions. Nevertheless, such CP-violating effects can be quite sizable at the time of the domain walls formation, as demonstrated when using Dirichlet boundary conditions instead of von Neumann conditions. In the case of electric charge-breaking kink solutions, we showed that the stability of the field configuration depends on the sign of the effective mass M_+ of v_+ inside the wall.

These electric charge-violating domain wall solutions demonstrate the possibility that the symmetry group inside the defect can be smaller than the one outside the wall, since $U(1)_{em}$ is broken inside the wall. This behavior can be explained in the framework of *clash-of-symmetries* mechanism. Since group elements of $SU(2)_L$ corresponding to the generator T^2 do not commute with elements of $U(1)_{em}$, both symmetry groups at the asymptotic domains have symmetry groups H and H' that are differently embedded in $SU(2)_L \times U(1)_Y$ leading to the symmetry group inside the wall being the identity $H \cap H' = I$.

When investigating the general case, where all the equations of motion of the Goldstone modes are taken into account, we saw in particular that these modes had a non-trivial profile inside the wall, in contrast to a kink-like profile that was found in all other simplified cases. We also found that the CP-violating phase $\xi(x)$ in that case is stable even though it had a small value.

In the next chapter, we discuss the interaction of SM fermions with these different types of domain walls and demonstrate the exotic effects of CP and/or electric charge breaking scattering off the walls.

This chapter is based on the following publication:

- [1] M. Y. Sassi and G. Moortgat-Pick, *Domain walls in the Two-Higgs-Doublet Model and their charge and CP-violating interactions with Standard Model fermions*, *JHEP* **04** (2024) 101, [2309.12398]

The existence of different types of domain walls in the 2HDM can have profound implications for the physics of the early universe. For instance, it was shown in [132] that photons with small frequencies, such as in the CMB, will scatter off superconducting domain walls with a large reflection coefficient. In [131], it was shown that domain walls in Grand Unified Theories arising after the spontaneous breaking of $SU(5) \times Z_2$, interact with the Higgs scalar field. This interaction induces exotic scattering phenomena of fermions off the domain wall via the Yukawa sector, such as neutrinos being reflected as down-type quarks, with the electric and color charges being absorbed by gauge fields living on the wall [131]. In this chapter, we study the interactions of SM fermions with the 2HDM domain wall solutions found in the previous chapter. This interaction occurs via the Yukawa sector and we consider the scattering solution for the Dirac equation of SM fermions within a domain wall background, which can be CP or electric charge violating. We leave the case of fermion zero modes and bound states solutions [13] on the walls, which might be relevant for baryogenesis and other interesting scenarios such as gravitational waves signals [134] in the framework of current-carrying walls, for future work.

The solution for the scattering of fermions off standard domain walls generated by the spontaneous breaking of a discrete symmetry can be found in [131, 135]. One finds that for thin walls, the rate of reflection and transmission of fermions off the walls is:

$$R(p) = \frac{m^2}{m^2 + p^2}, \quad T(p) = \frac{p^2}{m^2 + p^2} \quad (4.1)$$

In this chapter, we want to get analytical solutions for the Dirac equations within the background of different types of domain walls arising in the 2HDM. As the functions describing the spatial dependence of these vacuum configurations are non-trivial, it is appropriate to use a thin-wall approximation to simplify the form of the different vacuum configurations inside the wall. The thin-wall approximation is valid for the scattering of fermions that have wavelengths larger than the width of the wall, which is typical for particles with low momenta, such as the ones that populate the universe after EWSB. As another simplification, we do not consider the back-reaction effects of fermions on the vacuum configurations in our study, which could change the spatial kink profile of the vacuum configuration [136]. This chapter is based on the published work in [1].

4.1 THIN-WALL APPROXIMATION

In this section, we briefly discuss the validity of this approximation for domain walls in the 2HDM as well as describe the field configuration in this approximation.

From the results of the last chapter, we can infer a typical width of the domain walls to be approximately $L_w \approx 4/m_h$. The typical wavelength λ_f of a particle in the thermal plasma in the early universe is proportional to $2\pi/T$, where T is the temperature of the thermal plasma. The thin wall approximation is valid when $L_w < \lambda_f$ corresponding to particle momenta smaller than 200 GeV, which is sufficient to describe the momenta of most particles existing in the thermal plasma after EWSB.

Taking a thin-wall profile for the domain walls, we can approximate the kink solution of $v_2(x)$ to be a step-function:

$$v_2(x) = -\tilde{v}_2\Theta(x) + \tilde{v}_2\Theta(-x). \quad (4.2)$$

As for the field configurations $v_1(x)$, $v_+(x)$, and $\text{Im}(v_2(x)e^{i\xi(x)})$, it is possible to approximate them with a delta distribution:

$$v_1(x) = v_1 + \tilde{v}_1\delta(x), \quad (4.3)$$

$$v_+(x) = \tilde{v}_+\delta(x), \quad (4.4)$$

$$\tilde{v}_2(x) = \text{Im}(v_2(x)e^{i\xi(x)}) = \tilde{v}_2\delta(x-a) + \tilde{v}_2\delta(x+a), \quad (4.5)$$

where $\tilde{v}_{1,2,+}$ are dimensionless parameters defined as $\tilde{v}_{1,2,+} = \frac{v_{1,2,+}}{\text{GeV}}$. The parameter $\tilde{v}_2(x)$

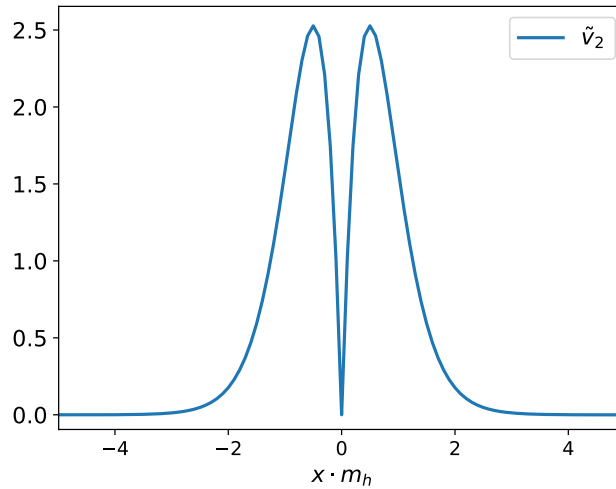


Figure 4.1: Profile of $\tilde{v}_2(x)$ using Dirichlet boundary conditions. When using von Neumann boundary conditions, \tilde{v}_2 gets smaller with time as the CP-violating phase $\xi(x)$ inside the wall vanishes.

describes the profile of the imaginary part of the CP-violating mass term that appears in the Dirac equations (see Figure 4.1). We saw in the last chapter that the phase $\xi(x)$ vanishes (in the simplified cases) when using von Neumann boundary conditions (see e.g sections [3.4.1] and [3.4.4]). However, the vanishing of $\xi(x)$ inside the wall only occurs after the dynamical evolution of the Goldstone modes or hypercharge angle θ inside the different domains, making them equal to each other. Therefore, the CP-violating phase

should still be substantial at the moment of the formation of the domain wall network and the study of CP-violating scattering of fermions off the wall is relevant for that period, when considering the simplified cases. However, as shown in sections [3.5.4] and [3.6], for domains rotated by a relative $SU(2)_L$ or an electroweak symmetry $SU(2)_L \times U_Y(1)$ the CP-violating phase $\xi(x)$ of the kink solution is small but stable. For simplicity, we consider the simplified cases in this work and leave the scattering of fermions off general domain walls in the 2HDM for future investigations.

4.2 CP-VIOLATING INTERACTIONS OF FERMIONS WITH THE DOMAIN WALLS

We start with the case of fermions scattering off CP-violating domain walls induced by a difference in the hypercharge angle θ . Recall that in this case, the Higgs doublets are given by:

$$\Phi_1(x) = \frac{U(x)}{\sqrt{2}} \begin{pmatrix} 0 \\ v_1(x) \end{pmatrix}, \quad \Phi_2(x) = \frac{U(x)}{\sqrt{2}} \begin{pmatrix} 0 \\ v_2(x)e^{i\xi(x)} \end{pmatrix}, \quad (4.6)$$

where the matrix $U(x)$ is given by:

$$U(x) = e^{i\theta(x)} I_2. \quad (4.7)$$

We can remove this matrix $U(x)$ from the Yukawa sector by performing a gauge transformation, leading to a pure gauge term for the hypercharge gauge field B^μ :

$$\Phi_1(x) \xrightarrow{U_Y(1)} U^{-1}(x)\Phi_1(x) = \tilde{\Phi}_1(x), \quad (4.8)$$

$$\Phi_2(x) \xrightarrow{U_Y(1)} U^{-1}(x)\Phi_2(x) = \tilde{\Phi}_2(x), \quad (4.9)$$

$$B_\mu \xrightarrow{U_Y(1)} \frac{i}{g} U(x) \partial_\mu (U^{-1}(x)) = \frac{1}{g} \partial_\mu \theta(x). \quad (4.10)$$

The Yukawa Lagrangian for the up-type quarks in the type-2 2HDM is then given by:

$$\begin{aligned} \mathcal{L}_{Fermion} = & i\bar{u}_L(\not{\partial} + iY_{u,L}\not{\partial}\theta(x))u_L + i\bar{u}_R(\not{\partial} + iY_{u,R}\not{\partial}\theta(x))u_R - y_u v_2(x) e^{i\xi(x)} \bar{u}_L u_R \\ & - y_u v_2(x) e^{-i\xi(x)} \bar{u}_R u_L, \end{aligned} \quad (4.11)$$

where $Y_{u,L}$ and $Y_{u,R}$ are the hypercharges of the left and right-handed up-type quarks respectively, y_u is the Yukawa coupling of the Higgs doublet to the up-type quark and u_L , u_R are the left-handed and right-handed components of the up-type quark respectively.

One can then derive the Dirac equation for up-type quarks:

$$\left(i\not{\partial} - \not{\partial}\theta(x)(Y_{u,L}P_L + Y_{u,R}P_R) - m_R(x) - im_I(x)\gamma_5 \right) u(x) = 0, \quad (4.12)$$

where P_L and P_R are the left and right-handed projector operators and $m_R(x)$, $m_I(x)$ are the real and imaginary parts of the fermion mass, respectively:

$$m_u(x) = y_u v_2(x) e^{i\xi(x)}, \quad (4.13)$$

$$m_R(x) = y_u v_2(x) \cos(\xi(x)) \approx y_u v_2(x), \quad (4.14)$$

$$m_I(x) = y_u v_2(x) \sin(\xi(x)) \approx y_u v_2(x) \xi(x) = y_u \tilde{v}_2(x), \quad (4.15)$$

where we apply a small angle approximation for the CP-violating angle $\xi(x)$, which is motivated by the simulations of the domain walls in the previous chapter. After multiplying the left hand side of (4.12) with $i\gamma_1$, we can rearrange this equation and get:

$$\begin{aligned}\partial_x u(x, t) &:= \hat{G}(x, t)u(x, t) \\ &= \left[\gamma_1 \gamma_0 \partial_t - i \partial_x \theta(x) (Y_L P_L + Y_R P_R) + i \gamma_1 m_R(x) - \gamma_1 \gamma_5 m_I(x) \right] u(x, t).\end{aligned}\quad (4.16)$$

The solution to this equation can be calculated in an analogous way to the case of fermion scattering off a CP-violating bubble wall [137]:

$$u(x, t) = \hat{P} \exp\left(\int_{x_0}^x dx' \hat{G}(x')\right) u(x_0, t), \quad (4.17)$$

where \hat{P} is an ordering operator. We consider the case of a plane wave solution of a quark scattering off the domain wall from the left ($x < 0$), that can either be reflected or transmitted to the other region ($x > 0$):

$$u(t, x) = e^{-iEt + ip_u x} u_{inc} + e^{-iEt - ip_u x} u_{ref} \text{ for } x < 0, \quad (4.18)$$

$$u(t, x) = e^{-iEt + ip_u x} u_{tra} \text{ for } x > 0, \quad (4.19)$$

where E denotes the energy of the incoming quark and u_{inc} , u_{ref} and u_{tra} are 4-component spinors describing respectively the incident, reflected and transmitted fermion.

$$u_{inc} = \begin{pmatrix} u_{1i} \\ u_{2i} \\ u_{3i} \\ u_{4i} \end{pmatrix}, \quad u_{ref} = \begin{pmatrix} u_{1m} \\ u_{2m} \\ u_{3m} \\ u_{4m} \end{pmatrix}, \quad u_{tra} = \begin{pmatrix} u_{1p} \\ u_{2p} \\ u_{3p} \\ u_{4p} \end{pmatrix}. \quad (4.20)$$

By plugging this ansatz into the Dirac equation (4.12) for the regions far away from the wall (where the field configurations $v_1(x)$ and $v_2(x)$ take on their asymptotic values and $\xi(x) = \theta(x) = 0$), we can derive relations between the different components of the spinors:

$$u_{4m} = \frac{-p_u}{E + m_u} u_{1m}, \quad u_{3m} = \frac{-p_u}{E + m_u} u_{2m}, \quad u_{4p} = \frac{p_u}{E - m_u} u_{1p}, \quad u_{3p} = \frac{p_u}{E - m_u} u_{2p}. \quad (4.21)$$

The matching condition of the solution $u(x)$ at $x = 0$ is calculated using (4.17):

$$u(+\epsilon, t) = \hat{P} \exp\left(\int_{-\epsilon}^{+\epsilon} dx' \hat{G}(x')\right) u(-\epsilon, t), \quad (4.22)$$

where ϵ is a small number taken to $\epsilon \rightarrow 0$. The final result is given by:

$$u(+\epsilon) = \exp\left(-i \frac{\Delta\theta}{2} (Y_L + Y_R)\right) \left[\cosh(a) I_4 - \frac{\sinh(a)}{a} \hat{A} \right] u(-\epsilon), \quad (4.23)$$

where:

$$\hat{A} = \begin{pmatrix} 0 & 2\tilde{v}_2 & i \frac{\Delta\theta(Y_R - Y_L)}{2} & 0 \\ 2\tilde{v}_2 & 0 & 0 & i \frac{\Delta\theta(Y_R - Y_L)}{2} \\ i \frac{\Delta\theta(Y_R - Y_L)}{2} & 0 & 0 & -2\tilde{v}_2 \\ 0 & i \frac{\Delta\theta(Y_R - Y_L)}{2} & -2\tilde{v}_2 & 0 \end{pmatrix}, \quad (4.24)$$

$$a = \sqrt{4\tilde{v}_2^2 - \frac{\Delta\theta^2(Y_R - Y_L)^2}{4}}. \quad (4.25)$$

Note that the spinor $u(x)$ is not continuous at $x = 0$. This is due to the delta-functions in $\tilde{v}_2(x)$ (see (4.5) and Figure 4.1). It is a known issue that the presence of delta distributions in the Dirac equation leads to a discontinuity of the spinor's wave function [138, 139, 140, 141] (in contrast to the discontinuity in the derivative of the wave function when dealing with delta-distribution potentials in the Schrödinger equation). In the limit of a standard domain wall, $a \rightarrow 0$ and \hat{A} is a zero matrix, therefore, we recover the continuity condition of the quark's spinor at $x = 0$ given by $u(-\epsilon) = u(+\epsilon)$.

The Dirac spinor of an incident particle moving in the positive x -direction is given by:

$$u_{inc}(x, t) = e^{(-iEt+ipx)} \begin{pmatrix} \sqrt{E + m_u} \\ 0 \\ 0 \\ p \\ \sqrt{E + m_u} \end{pmatrix}. \quad (4.26)$$

Using (4.26) alongside the equations (4.21) and (4.23), we can find the solution for the spinor components:

$$u_{1p} = e^{-ib_1} \left(\frac{1}{\sqrt{E + m_u}} \right) \frac{4a^2 p^2 E \cosh(a)}{4a^2 E^2 \cosh^2(a) - (2a_1 m_u + ib_2 p)^2 \sinh^2(a)}, \quad (4.27)$$

$$u_{2p} = e^{-ib_1} \left(\frac{1}{4a\sqrt{E + m_u}} \right) \frac{-8a^2 p^2 (2a_1 m_u + ib_2 p) \sinh(a)}{4a^2 E^2 \cosh^2(a) - (2a_1 m_u + ib_2 p)^2 \sinh^2(a)}, \quad (4.28)$$

$$u_{1m} = \left(2E\sqrt{E + m_u} \right) \frac{-2a^2 m_u \cosh^2(a) + a_1 (2a_1 m_u + ib_2 p) \sinh^2(a)}{4a^2 E^2 \cosh^2(a) - (2a_1 m_u + ib_2 p)^2 \sinh^2(a)}, \quad (4.29)$$

$$u_{2m} = \frac{-ap\sqrt{E + m_u} (2a_1 p - ib_2 m_u) \sinh(2a)}{4a^2 E^2 \cosh^2(a) - (2a_1 m_u + ib_2 p)^2 \sinh^2(a)}, \quad (4.30)$$

with:

$$a_1 = 2\tilde{v}_2, \quad b_1 = (Y_L + Y_R) \frac{\Delta\theta}{2}, \quad b_2 = (Y_R - Y_L) \Delta\theta. \quad (4.31)$$

In order to get the transmission and reflection coefficients of particles scattering off the wall, we need to calculate the fermion currents on both regions:

$$\mathcal{J}_{inc} = u_{inc}^\dagger \gamma_0 \gamma_1 u_{inc}, \quad (4.32)$$

$$\mathcal{J}_{tra} = u_{tra}^\dagger \gamma_0 \gamma_1 u_{tra}, \quad (4.33)$$

$$\mathcal{J}_{ref} = u_{ref}^\dagger \gamma_0 \gamma_1 u_{ref}. \quad (4.34)$$

Using the expression (4.26) for the incident spinor, we can derive the transmission and reflection coefficients for the up-type quark scattering off the wall:

$$\hat{R}(p) = -\frac{\mathcal{J}_{ref}}{\mathcal{J}_{inc}} = \frac{1}{E + m_u} \left(|u_{1m}|^2 + |u_{2m}|^2 \right), \quad (4.35)$$

$$\hat{T}(p) = \frac{\mathcal{J}_{tra}}{\mathcal{J}_{inc}} = \frac{1}{E - m_u} \left(|u_{1p}|^2 + |u_{2p}|^2 \right). \quad (4.36)$$

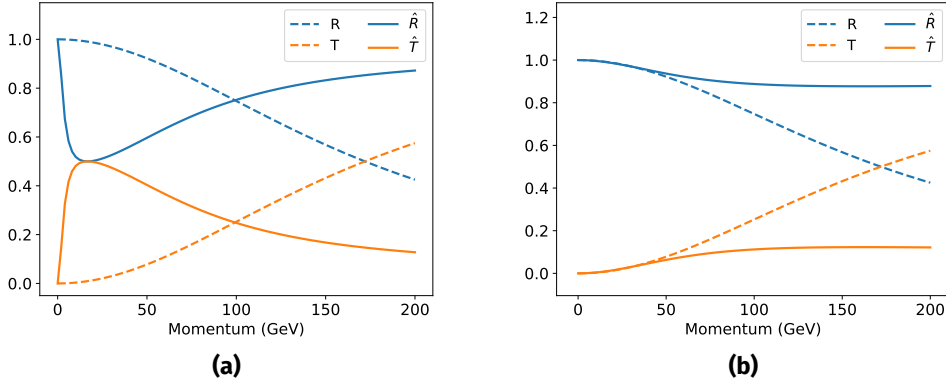


Figure 4.2: General results for the reflection \hat{R} and transmission \hat{T} coefficients of a top quark scattering off the CP-violating wall (solid lines). We also plot the reflection R and transmission coefficient T for the standard case (no CP-violation, dashed lines). (a) Reflection and transmission with $a_1 = 2.1$ and $b_2 = 1$. (b) Reflection and transmission with $a_1 = 2.1$ and $b_2 = 3$.

In Figure 4.2, we show a comparison between the reflection \hat{R} and transmission \hat{T} coefficients of quarks scattering off the CP-violating DW and the coefficients R and T for quarks scattering off standard CP-conserving DW for two different cases. The first case depicted in Figure 4.2a shows the results for $a_1 = 2.1$ and $b_2 = 1$, while for the second case (shown in Figure 4.2b) the parameters are: $a_1 = 2.1$ and $b_2 = 3$. We see that in both cases, the reflection and transmission coefficients differ a lot from the standard reflection and transmission coefficients. In particular, we see that the reflection coefficient for incident particles with higher momenta grows and stays the dominant process. Since the analytical results for the general case are quite complicated, we consider some special cases in order to understand the physical interpretation of the solution. We first consider the case where b_2 is small compared to a_1 . In such a scenario, the reflection and transmission coefficients simplify to:

$$\hat{R}(p) = \frac{4m_u^2 E^2 + p^4 (\cosh^2(2a_1) - 1)}{[(E^2 + m_u^2) + p^2 \cosh(2a_1)]^2} \quad (4.37)$$

$$\hat{T}(p) = \frac{2p^2(p^2 + (E^2 + m^2) \cosh(2a_1))}{[(E^2 + m_u^2) + p^2 \cosh(2a_1)]^2} \quad (4.38)$$

As shown in Figure 4.3a, in this case and for high values of a_1 , the reflection coefficient increases with momentum. This seems counterintuitive as particles reacting with a potential barrier should have a higher probability of crossing when they have higher energies. One can also deduce from (4.37) that for big values of CP-violation (a_1 is big), the reflection coefficient approaches 1 for all momenta, as the terms proportional to $\cosh^2(2a_1)$ will be dominant.

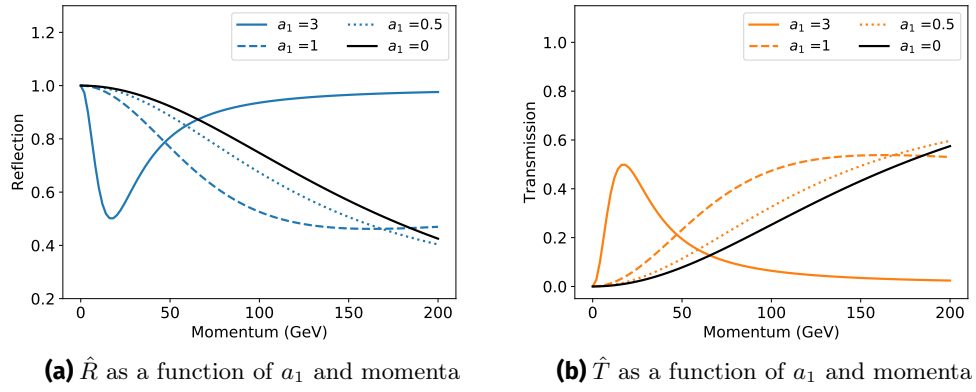


Figure 4.3: Results for the reflection (a) and transmission (b) coefficients for the case when the numerical value of the Yukawa contribution a_1 is much higher than the numerical value from the gauge field contribution b_2 . Notice that for higher values of CP-violation a_1 , the reflection coefficient increases with momentum while \hat{T} decreases.

For the opposite case $b_2 \gg 2\tilde{v}_2$, the transmission and reflection coefficients are:

$$\hat{R}(p) = \frac{2m_u^2 \cos^2(\frac{b_2}{2})}{m_u^2 + 2p^2 + m_u^2 \cos(b_2)}, \quad (4.39)$$

$$\hat{T}(p) = \frac{2p^2}{m_u^2 + 2p^2 + m_u^2 \cos(b_2)}. \quad (4.40)$$

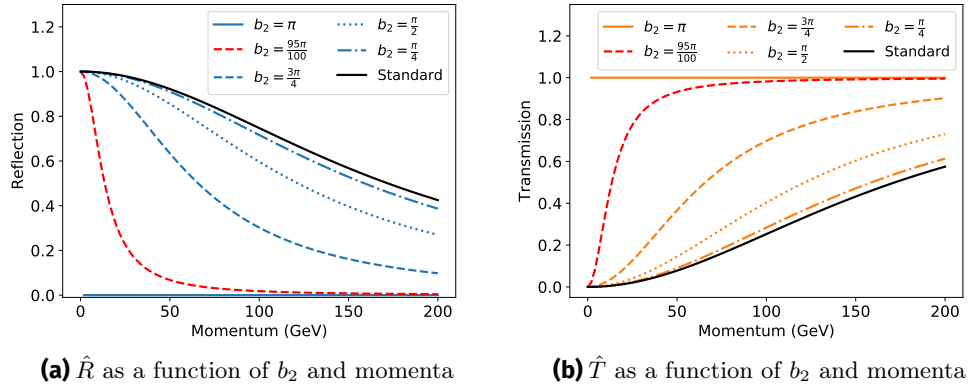


Figure 4.4: Results for the reflection (a) and transmission (b) coefficients for the case when the numerical value of the gauge contribution b_2 is much higher than the numerical value of a_1 . These rates will oscillate depending on b_2 . The standard reflection and transmission rates (black lines) refer to the scattering off standard domain walls (4.1).

For this case, the reflection and transmission coefficients will oscillate with a b_2 dependence (see Figure 4.4). Notice that for $b_2 = \pi$ all particles will be transmitted, irrespective of their incoming momentum.

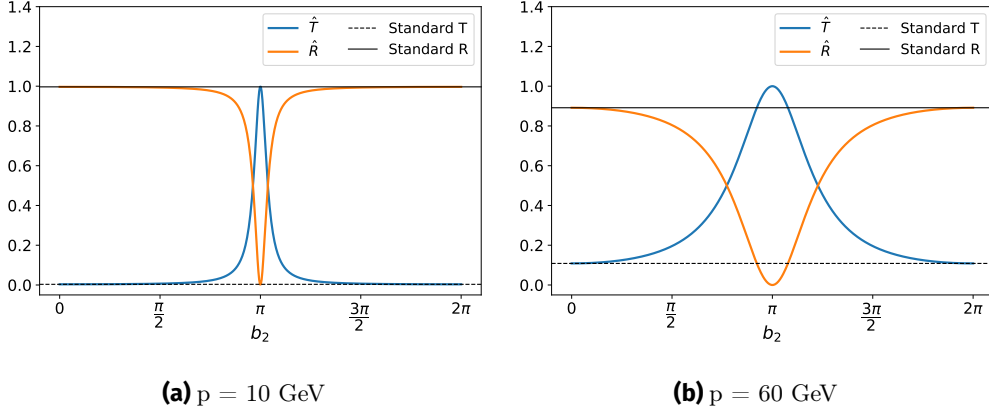


Figure 4.5: Variation of the reflection and transmission coefficient for a top quark as a function of b_2 for different fixed momenta: (a) $p = 10$ GeV and (b) $p = 60$ GeV. The standard reflection and transmission rates refer to the scattering off standard domain walls (4.1).

In Figure 4.5, we show the oscillatory behavior of the reflection and transmission coefficients for this special case as a function of b_2 for different momenta of the incident particle. We see that for small momenta (see Figure 4.5a), the deviations of the scattering rates from those of the standard DW are only relevant for b_2 in the vicinity of $b_2 = \pi$. In contrast with particles with higher momenta (see Figure 4.5b).

We now calculate the rate of reflection and transmission of the left handed (LH) and right handed (RH) components, derived from the currents of left and right-handed particles:

$$\mathcal{J}_{tra}^L = \bar{u}_{tra} \gamma_1 P_L u_{tra}, \quad (4.41)$$

$$\mathcal{J}_{tra}^R = \bar{u}_{tra} \gamma_1 P_R u_{tra}, \quad (4.42)$$

$$\mathcal{J}_{ref}^L = \bar{u}_{ref} \gamma_1 P_L u_{ref}, \quad (4.43)$$

$$\mathcal{J}_{ref}^R = \bar{u}_{ref} \gamma_1 P_R u_{ref}. \quad (4.44)$$

leading to the transmission and reflection coefficients:

$$T_L = \frac{\mathcal{J}_{tra}^L}{\mathcal{J}_{inc}} = \frac{1}{4p} \left[2d \left(|u_{1p}|^2 + |u_{2p}|^2 \right) - (1 + d^2) \left(u_{1p}^* u_{2p} + u_{1p} u_{2p}^* \right) \right], \quad (4.45)$$

$$T_R = \frac{\mathcal{J}_{tra}^R}{\mathcal{J}_{inc}} = \frac{1}{4p} \left[2d \left(|u_{1p}|^2 + |u_{2p}|^2 \right) + (1 + d^2) \left(u_{1p}^* u_{2p} + u_{1p} u_{2p}^* \right) \right], \quad (4.46)$$

$$R_L = -\frac{\mathcal{J}_{ref}^L}{\mathcal{J}_{inc}} = \frac{1}{4p} \left[2g \left(|u_{1m}|^2 + |u_{2m}|^2 \right) - (1 + g^2) \left(u_{1m}^* u_{2m} + u_{1m} u_{2m}^* \right) \right], \quad (4.47)$$

$$R_R = -\frac{\mathcal{J}_{ref}^R}{\mathcal{J}_{inc}} = \frac{1}{4p} \left[2g \left(|u_{1m}|^2 + |u_{2m}|^2 \right) + (1 + g^2) \left(u_{1m}^* u_{2m} + u_{1m} u_{2m}^* \right) \right], \quad (4.48)$$

where:

$$d = \frac{p}{E - m_u}, \quad g = \frac{p}{E + m_u}. \quad (4.49)$$

From equations (4.27)-(4.30) it is clear that for $a_1 = 0$ (as in the case of the standard domain wall), $(u_{1p}^* u_{2p})$ and $(u_{1m}^* u_{2m})$ are purely imaginary expressions leading to the vanishing of the second terms in the equations for $T_{L,R}$ and $R_{L,R}$. In such a case the reflection and transmission coefficient do not depend on the chirality of the particle.

Because analytical expressions for the general case are lengthy and complicated, we give for simplicity the analytical expressions in the limit when $b_2 \rightarrow 0$:

$$T_L = \frac{p(p^3 + p(2m^2 + p^2) \cosh(2a) + 2m(m^2 + p^2) \sinh(2a))}{(2m^2 + p^2 + p^2 \cosh(2a))^2}, \quad (4.50)$$

$$T_R = \frac{p(p^3 + p(2m^2 + p^2) \cosh(2a) - 2m(m^2 + p^2) \sinh(2a))}{(2m^2 + p^2 + p^2 \cosh(2a))^2}, \quad (4.51)$$

$$R_R = \frac{4m^2 E^2 - 8mpE^2 \cosh(a) \sinh(a) + p^4 \sinh^2(2a)}{2(2m^2 + p^2 + p^2 \cosh(2a))^2}, \quad (4.52)$$

$$R_L = \frac{4m^2 E^2 + 8mpE^2 \cosh(a) \sinh(a) + p^4 \sinh^2(2a)}{2(2m^2 + p^2 + p^2 \cosh(2a))^2}. \quad (4.53)$$

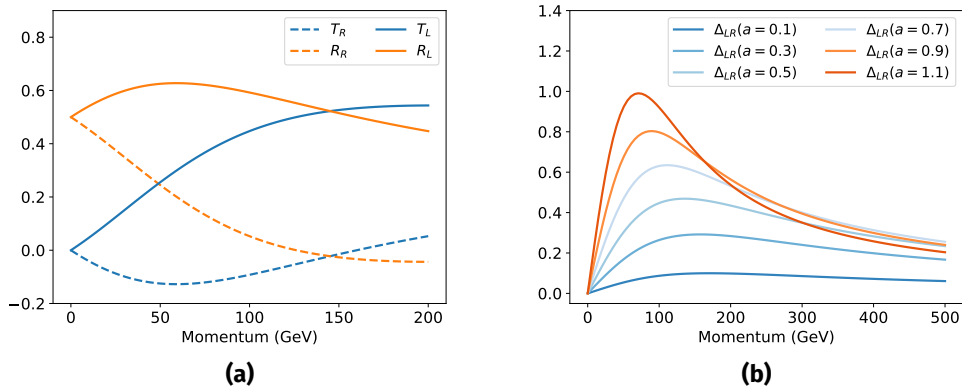


Figure 4.6: (a) Left and right-handed reflection and transmission currents normalized to the incident current. We take $a_1 = 0.5$. (b) The difference Δ_{LR} between the reflection of left and right-handed particles as a function of the CP-violating rate a_1 .

Note that for small momenta, these rates can become negative (see Figure 4.6a for $a_1 = 0.5$). This is not an issue as these rates are not describing probability amplitudes for the particles and only \hat{R} and \hat{T} should be, in principle, positive numbers between 0 and 1. This behavior might also be related to the phenomenon of Klein-Paradox [142] where negative transmission coefficients for electrons scattering off an electric potential were obtained. In that case, these negative transmission coefficients were interpreted as the formation of an electron-positron pair at the wall.

In case $a_1 \rightarrow 0$, we do not observe CP-violation in the scattering rates of the particle. In order to get a rate for the CP-violation, we calculate the difference $\Delta_{LR} = R_L - R_R$. The results are shown in Figure 4.6b. We find from (4.50)-(4.53), that when the momentum of the incoming particles gets larger, the left and right-handed rates should converge to the same value. This explains the behavior of Δ_{LR} becoming smaller at higher momenta. Since we get different rates for R_L and R_R , the motion of the wall will generate an axial asymmetry in front of it.

4.3 CHARGE VIOLATING INTERACTIONS OF FERMIONS WITH THE DOMAIN WALLS

We now discuss the case when the domain wall exhibits a non-negligible value for v_+ inside its core. In this case, the vacuum inside the domain wall is charge-breaking and the Yukawa sector inside the wall now includes couplings between fermions with different charges.

In the following, we consider the case of a Yukawa sector in the type-2 2HDM. The relevant terms are:

$$\mathcal{L}_{Yukawa} = -y_u \bar{Q}_L \Phi_2^c u_R - y_d \bar{Q}_L \Phi_1 d_R - y_l \bar{L}_L \Phi_1 e_R + h.c., \quad (4.54)$$

where $\Phi_2^c = i\sigma_2 \Phi_2$. y_u , y_d , and y_l denote the Yukawa couplings for the up-type quarks, down-type quarks, and leptons, respectively. Q_L and L_L denote the left-handed quark and lepton doublets charged under $SU_L(2)$, and finally u_R , d_R , and e_R denote the right-handed up-type, down-type quark and leptons, which are singlets under $SU_L(2)$. We take the simplification that only one of the Goldstone modes changes between the two domains. In this case, it is the second generator of $SU(2)$ which leads to charge-violating effects inside the domain wall and the CP-violating phase $\xi(x)$ vanishes (see 3.11b). The Higgs doublets are:

$$\Phi_1(x) = \frac{U(x)}{\sqrt{2}} \begin{pmatrix} 0 \\ v_1(x) \end{pmatrix}, \quad \Phi_2(x) = \frac{U(x)}{\sqrt{2}} \begin{pmatrix} v_+(x) \\ v_2(x) \end{pmatrix}. \quad (4.55)$$

The matrix $U(x)$ in this case is given by:

$$U(x) = \begin{pmatrix} \cos\left(\frac{g_2(x)}{2}\right) & \sin\left(\frac{g_2(x)}{2}\right) \\ -\sin\left(\frac{g_2(x)}{2}\right) & \cos\left(\frac{g_2(x)}{2}\right) \end{pmatrix}. \quad (4.56)$$

We can remove this matrix from the Yukawa sector by performing a gauge transformation, leading to a pure gauge term for the gauge field W_2^μ confined inside the wall:

$$\Phi_1(x) \xrightarrow{SU(2)} U^{-1}(x) \Phi_1(x) = \tilde{\Phi}_1(x), \quad (4.57)$$

$$\Phi_2(x) \xrightarrow{SU(2)} U^{-1}(x) \Phi_2(x) = \tilde{\Phi}_2(x), \quad (4.58)$$

$$W_2^\mu \xrightarrow{SU(2)} \frac{i}{g} U(x) \partial_\mu (U^{-1}(x)), \quad (4.59)$$

Writing the Lagrangian in terms of the individual quark fields, we get:

$$\begin{aligned} \mathcal{L}_F = & i\bar{u}\not{\partial}u + i\bar{d}\not{\partial}d + \frac{1}{2} \left[-i\bar{u}_L \left(\not{\partial}_x g_2(x) \right) d_L + i\bar{d}_L \left(\not{\partial}_x g_2(x) \right) u_L \right] \\ & - y_u v_2(x) \bar{u}u - y_d v_1(x) \bar{d}d + y_u v_+(x) (\bar{d}_L u_R + \bar{u}_R d_L). \end{aligned} \quad (4.60)$$

We then derive the Dirac equation for the up and down-type quarks:

$$i\not{\partial}d + \frac{i}{2} \left(\not{\partial}_x g_2(x) \right) P_L u - y_d v_1(x) d + y_u v_+(x) P_R u = 0, \quad (4.61)$$

$$i\not{\partial}u - \frac{i}{2} \left(\not{\partial}_x g_2(x) \right) P_L d - y_u v_2(x) u + y_u v_+(x) P_L d = 0. \quad (4.62)$$

To solve this system of equations, we first rewrite it in the matrix form introduced in the previous chapter, cf.(4.16):

$$\begin{pmatrix} i\not{\partial} - y_u v_2(x) & -\hat{G}_2(x) \\ -\hat{G}_1(x) & i\not{\partial} - y_d v_1(x) \end{pmatrix} \begin{pmatrix} u \\ d \end{pmatrix} = 0, \quad (4.63)$$

where:

$$\hat{G}_1(x) = -\frac{i}{2} \left(\not{\partial}_x g_2(x) \right) P_L - y_u v_+(x) P_R, \quad (4.64)$$

$$\hat{G}_2(x) = \frac{i}{2} \left(\not{\partial}_x g_2(x) \right) P_L - y_u v_+(x) P_L. \quad (4.65)$$

Notice that all terms that mix the up and down-type quark only include the left-handed component of the down-type quark. This will induce a chiral asymmetry as we will discuss later. We consider the scattering of an incident up-type quark off the domain wall. In the standard case, when $v_+ = 0$, the particle can be either reflected or transmitted as an up-type quark. However, due to the mixing between the up and down-type quarks in the Dirac equations (4.61) and (4.62), there is now the possibility that the incoming up-type quark gets also reflected or transmitted as a down-type quark after its interaction with the domain wall, inducing a charge violating interaction and the difference in charge between the up and down-type quark will be absorbed by the gauge bosons living inside the wall [13, 131]. Using a plane wave solution for the spinor fields,

$$u(t, x) = e^{-iEt} u_{inc}(x) + e^{-iEt} u_{ref}(x) \text{ for } x < 0, \quad (4.66)$$

$$u(t, x) = e^{-iEt} u_{tra}(x) \text{ for } x > 0, \quad (4.67)$$

$$d(t, x) = e^{-iEt} d_{ref}(x) \text{ for } x < 0, \quad (4.68)$$

$$d(t, x) = e^{-iEt} d_{tra}(x) \text{ for } x > 0, \quad (4.69)$$

and inserting these expressions in (4.63), we get:

$$\partial_x \begin{pmatrix} u(x) \\ d(x) \end{pmatrix} = \hat{G}(x) \begin{pmatrix} u(x) \\ d(x) \end{pmatrix} = \begin{pmatrix} iE\gamma_1\gamma_0 + i\gamma_1 m_u(x) & i\gamma_1 \hat{G}_2(x) \\ i\gamma_1 \hat{G}_1(x) & iE\gamma_1\gamma_0 + i\gamma_1 m_d(x) \end{pmatrix} \begin{pmatrix} u(x) \\ d(x) \end{pmatrix}, \quad (4.70)$$

which can be solved by taking:

$$\begin{pmatrix} u(x) \\ d(x) \end{pmatrix} = \hat{P} \exp\left(\int_{x_0}^x dx' \hat{G}(x')\right) \begin{pmatrix} u(x_0) \\ d(x_0) \end{pmatrix}, \quad (4.71)$$

where \hat{P} is, as in the previous chapter, taken to be an ordering operator.

We now derive the expressions for the spinors in the different regions $x < 0$ and $x > 0$.

Far from the wall, the Dirac equations are:

$$i\not{\partial}d - y_d v_1 d = 0, \quad (4.72)$$

$$i\not{\partial}u - y_u v_2 u = 0. \quad (4.73)$$

In the region $x < 0$, we parameterize (4.72) and (4.73) by:

$$i\gamma_0(-iE) \begin{pmatrix} d_{1m} \\ d_{2m} \\ d_{3m} \\ d_{4m} \end{pmatrix} + i\gamma_1(-ip_d) \begin{pmatrix} d_{1m} \\ d_{2m} \\ d_{3m} \\ d_{4m} \end{pmatrix} - y_d v_1 \begin{pmatrix} d_{1m} \\ d_{2m} \\ d_{3m} \\ d_{4m} \end{pmatrix} = 0, \quad (4.74)$$

$$i\gamma_0(-iE) \begin{pmatrix} u_{1m} \\ u_{2m} \\ u_{3m} \\ u_{4m} \end{pmatrix} + i\gamma_1(-ip_u) \begin{pmatrix} u_{1m} \\ u_{2m} \\ u_{3m} \\ u_{4m} \end{pmatrix} - y_u v_2 \begin{pmatrix} u_{1m} \\ u_{2m} \\ u_{3m} \\ u_{4m} \end{pmatrix} = 0, \quad (4.75)$$

leading to the following relations between the components of the spinors:

$$u_{4m} = \frac{-p_u}{E + m_u} u_{1m}, \quad u_{3m} = \frac{-p_u}{E + m_u} u_{2m}, \quad (4.76)$$

$$d_{4m} = \frac{-p_d}{E + m_d} d_{1m}, \quad d_{3m} = \frac{-p_u}{E + m_u} u_{2m}, \quad (4.77)$$

where p_u denotes the momentum of the incident up-type quark and p_d denotes the momentum of the produced down-type quark.

For the region $x > 0$, we get:

$$i\cancel{\partial}d - y_d v_1 d = 0, \quad (4.78)$$

$$i\cancel{\partial}u + y_u v_2 u = 0, \quad (4.79)$$

leading to:

$$u_{4p} = \frac{p_u}{E - m_u} u_{1p}, \quad u_{3p} = \frac{p_u}{E - m_u} u_{2p}, \quad (4.80)$$

$$d_{4p} = \frac{p_d}{E + m_d} d_{1p}, \quad d_{3p} = \frac{p_d}{E + m_d} d_{2p}. \quad (4.81)$$

We obtain for the complete spinor:

$$u(-\epsilon) = \begin{pmatrix} u_{1i} + u_{1m} \\ u_{2i} + u_{2m} \\ u_{3i} - \frac{p_u}{E+m_u} u_{2m} \\ u_{4i} - \frac{p_u}{E+m_u} u_{1m} \end{pmatrix}, \quad d(-\epsilon) = \begin{pmatrix} d_{1m} \\ d_{2m} \\ -\frac{p_d}{E+m_d} d_{2m} \\ -\frac{p_d}{E+m_d} d_{1m} \end{pmatrix}, \quad (4.82)$$

$$u(+\epsilon) = \begin{pmatrix} u_{1p} \\ u_{2p} \\ \frac{p_u}{E-m_u} u_{2p} \\ \frac{p_u}{E-m_u} u_{1p} \end{pmatrix}, \quad d(+\epsilon) = \begin{pmatrix} d_{1p} \\ d_{2p} \\ \frac{p_d}{E+m_d} d_{2p} \\ \frac{p_d}{E+m_d} d_{1p} \end{pmatrix}. \quad (4.83)$$

The results have to be matched at the boundary $x = 0$, using (4.71) where $x = +\epsilon$ and $x_0 = -\epsilon$:

$$\begin{pmatrix} u(+\epsilon) \\ d(+\epsilon) \end{pmatrix} = \hat{P} \exp\left(\int_{-\epsilon}^{+\epsilon} dx \hat{G}(x)\right) \begin{pmatrix} u(-\epsilon) \\ d(-\epsilon) \end{pmatrix}. \quad (4.84)$$

In order to get the matching conditions at $x = 0$ for the Dirac spinors, we need to calculate the exponential matrix of the integral of $\hat{G}(x)$. For simplicity, we took $v_1(x) = v_1$ as we want to isolate the effects of a non-zero v_+ . We obtain the final result:

$$\begin{pmatrix} u(+\epsilon) \\ d(+\epsilon) \end{pmatrix} = \begin{pmatrix} M_1 & M_2 \\ M_3 & M_4 \end{pmatrix} \begin{pmatrix} u(-\epsilon) \\ d(-\epsilon) \end{pmatrix}, \quad (4.85)$$

where:

$$M_1 = \cosh^2\left(\frac{1}{2}\sqrt{k^2 - m^2}\right) I_2 + \left(\frac{k^2 + m^2}{k^2 - m^2}\right) \sinh^2\left(\frac{1}{2}\sqrt{k^2 - m^2}\right) \\ + i \frac{km}{k^2 - m^2} \left[-1 + \cosh\left(\sqrt{k^2 - m^2}\right)\right] \gamma_5 \gamma_1, \quad (4.86)$$

$$M_2 = \frac{m}{\sqrt{k^2 - m^2}} \sinh\left(\sqrt{k^2 - m^2}\right) P_L - \frac{ik}{\sqrt{k^2 - m^2}} \sinh\left(\sqrt{k^2 - m^2}\right) \gamma_1 P_L, \quad (4.87)$$

$$M_3 = -\frac{m}{\sqrt{k^2 - m^2}} \sinh\left(\sqrt{k^2 - m^2}\right) P_L - \frac{ik}{\sqrt{k^2 - m^2}} \sinh\left(\sqrt{k^2 - m^2}\right) \gamma_1 P_R, \quad (4.88)$$

$$M_4 = \cosh^2\left(\frac{1}{2}\sqrt{k^2 - m^2}\right) I_2 - \sinh^2\left(\frac{1}{2}\sqrt{k^2 - m^2}\right) \gamma_5, \quad (4.89)$$

with:

$$m = \frac{\Delta g_2}{2}, \quad k = y_u \tilde{v}_+. \quad (4.90)$$

We therefore have 16 variables (4 for each spinor at $x > 0$ and $x < 0$) and 16 equations (8 from (4.85) and 8 from (4.76), (4.77), (4.80) and (4.81)). The solution of such a system of equation gives very lengthy analytical results. After finding the solution for the spinor components, we calculate the transmission and reflection coefficients of the up and down-type quarks corresponding to the scattering of an initial up-type quark scattering off the domain wall:

$$R_u(p_u) = -\frac{\mathcal{J}_u^{ref}}{\mathcal{J}_{inc}} = -\frac{u_{ref}^\dagger \gamma_0 \gamma_1 u_{ref}}{2p_u}, \quad R_d(p_u) = -\frac{\mathcal{J}_d^{ref}}{\mathcal{J}_{inc}} = -\frac{d_{ref}^\dagger \gamma_0 \gamma_1 d_{ref}}{2p_u}, \quad (4.91)$$

$$T_u(p_u) = -\frac{\mathcal{J}_u^{tra}}{\mathcal{J}_{inc}} = \frac{u_{tra}^\dagger \gamma_0 \gamma_1 u_{tra}}{2p_u}, \quad T_d(p_u) = \frac{\mathcal{J}_d^{tra}}{\mathcal{J}_{inc}} = \frac{d_{tra}^\dagger \gamma_0 \gamma_1 d_{tra}}{2p_u}, \quad (4.92)$$

where we used a plane wave solution for the incident up-type quark moving in the positive x -direction:

$$u_{inc}(x, t) = e^{(-iEt+ipx)} \begin{pmatrix} \sqrt{E + m_u} \\ 0 \\ 0 \\ \frac{p_u}{\sqrt{E + m_u}} \end{pmatrix}, \quad (4.93)$$

Since the analytical formulas in the general case are very complicated and lengthy, we present the results in Figure 4.7a for the numerical values of $m = 0.5$, $k = 10$ and a mass $m_u = 172.76$ GeV for the top quark and $m_d = 4.2$ GeV for the bottom quark. We observe that the reflection and transmission probabilities as a bottom quark are non-zero. In Figure 4.7b, we can see that as we increase the momentum of the incoming particle, the rate of top quarks being transformed into bottom quarks after the interaction with the domain wall becomes higher, while the probability of the quark staying a top quark decreases.

We also verify that all the reflected or transmitted bottom quarks are left-handed, as it can be already deduced from equations (4.61) and (4.62), where the coupling to the bottom quark includes only the left handed projector on the spinor. As can be seen in Figure 4.8 the rate of reflection and transmission coefficient as right-handed bottom quarks is zero. Concerning the chirality of the top quark after the interaction with the wall, we observe a difference in the transmission rate between the left-handed and right-handed components of the top quark, while the reflected top quarks do not show a chiral asymmetry (see Figures 4.8c and 4.8d). Therefore the scattering of top quarks on the charge breaking wall will generate a chiral asymmetry in front as well as behind the wall.

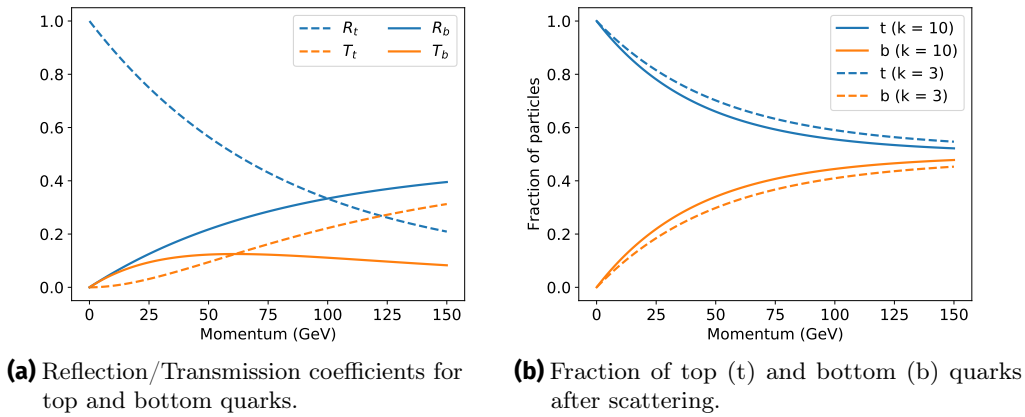


Figure 4.7: (a) Reflection and transmission coefficients for top and bottom quarks after the interaction of an initial top quark with the charge-breaking domain wall. Note that the sum of the reflection and transmission coefficients for both particles adds up to 1. The parameters used are $k = 10$ and $m = 0.5$ (b) Rate of top quarks being transformed into bottom quarks or kept as top quarks. Notice that, for high momenta, the process of reflection a bottom quark has the highest probability. The amount of produced bottom quarks gets higher with increasing k .

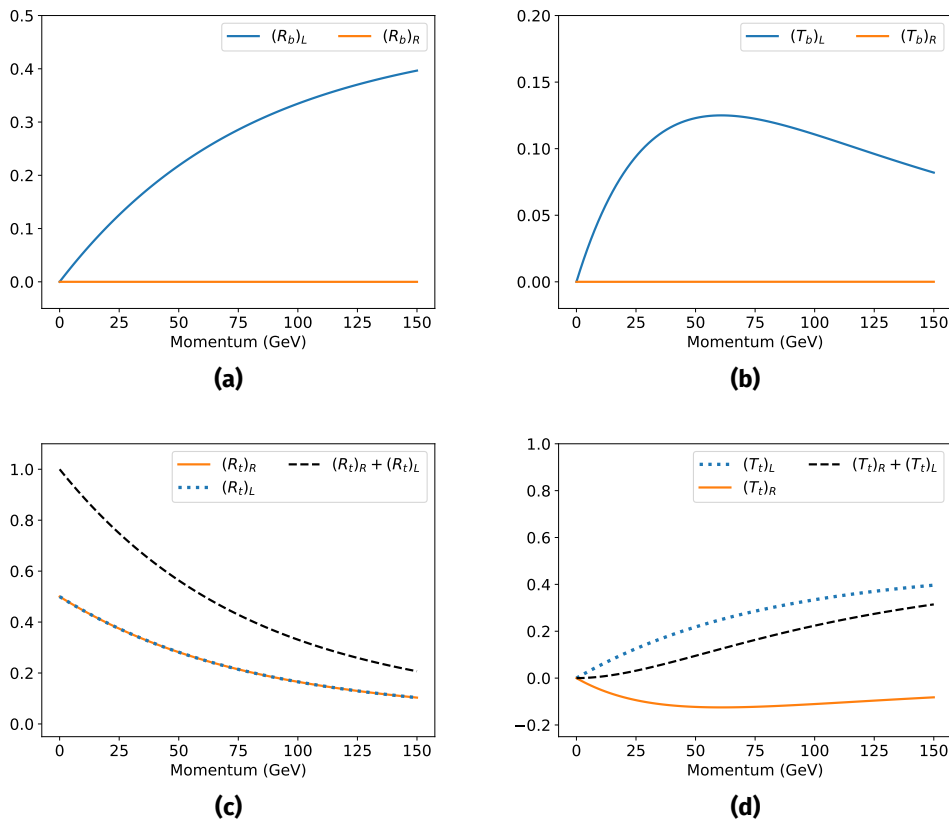


Figure 4.8: Chiralities of the reflected and transmitted particles: (a) Reflection coefficients for **LH** and **RH** bottom quarks. (b) Transmission coefficients for **LH** and **RH** bottom quarks. Notice that all the produced bottom quarks are left handed. (c) Reflection coefficients for **LH** and **RH** top quarks. (d) Transmission coefficients for **LH** and **RH** top quarks. We observe that the reflection rate as a top quark does not depend on the chirality of the particle, while the transmission for the top quark is chirality-dependent.

For the case $k \gg m$ and $m \rightarrow 0$ corresponding to having the numerical value of $v_+(0)$ inside the wall much bigger than the change in g_2 between the two domains, the formulas become considerably simpler. Using (4.26) for the spinor components of the incident top quark we get:

$$R_u(p_u) = \frac{(d_u^2 - 1)^2 g_d^2 (u_{1i})^2}{p_u d_u [g_d(1 + d_u^2) + d_u(1 + g_d^2) \tanh^2(\frac{k}{2})]^2}, \quad (4.94)$$

$$R_d(p_u) = \frac{g_d [1 + 4d_u g_d + g_d^2 + d_u^2(1 + g_d^2)] u_{1i}^2 \sinh^2(k)}{p_u [(d_u - g_d)(-1 + d_u g_d) + (d_u + g_d)(1 + d_u g_d) \cosh(k)]^2}, \quad (4.95)$$

$$T_u(p_u) = \frac{2d_u [-4(g_d^2 - 1)^2 \cosh(k) + (1 + 6g_d^2 + g_d^2)(3 + \cosh(2k))](u_{1i})^2}{p_u [4d_u(1 + g_d^2) \sinh^2(\frac{k}{2}) + 4g_d(1 + d_u^2) \cosh^2(\frac{k}{2})]^2}, \quad (4.96)$$

$$T_d(p_u) = \frac{4g_d [1 - 4d_u g_d + g_d^2 + d_u^2(1 + g_d^2)] (u_{1i})^2 \sinh^2(k)}{p_u [4d_u(1 + g_d^2) \sinh^2(\frac{k}{2}) + 4g_d(1 + d_u^2) \cosh^2(\frac{k}{2})]^2}, \quad (4.97)$$

where:

$$g_u = \frac{p_u}{E + m_u}, \quad g_d = \frac{p_d}{E + m_d}, \quad d_u = \frac{p_u}{E - m_u}, \quad d_d = \frac{p_d}{E - m_d}, \quad u_{1i}^2 = E + m_u.$$

The results for the transmission $T_{t,b}$ and reflection $R_{t,b}$ coefficients as top or bottom quarks

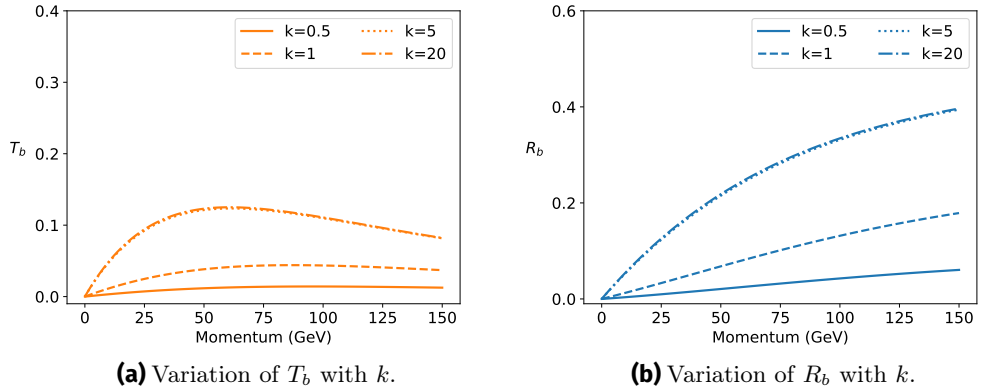


Figure 4.9: (a) Transmission rate as bottom quarks for different values of k and $m = 0$. (b) Reflection rate as a bottom quark for different values of k and $m = 0$. Notice that the reflection rate as a bottom quark is in this case higher than the transmission rate even for high momenta of the incoming incident top quark. We also observe that the rates are almost the same for $k > 5$.

are shown in Figures 4.9a and 4.9b. An interesting feature is that the rate of reflection as a bottom quark is higher than the rate of transmission as a bottom quark, even for higher momenta. Recall that we observed the same behavior in the previous section [4.2] when the numerical value of the imaginary mass \tilde{v}_2 is dominant and the reflection rate for particles becomes higher than the transmission rate.

We now look at the case when the charge-breaking term $k = y_u v_+$ is small compared with the change in the Goldstone modes between the two domains ($m > k$), cf.(4.90). The boundary condition at $x = 0$ is given by:

$$M_1 = \cos^2\left(\frac{1}{2}\sqrt{m^2 - k^2}\right) I_2 + \left(\frac{k^2 + m^2}{m^2 - k^2}\right) \sin^2\left(\frac{1}{2}\sqrt{m^2 - k^2}\right) + i \frac{2km}{m^2 - k^2} \sinh^2\left(\sqrt{k^2 - m^2}\right) \gamma_5 \gamma_1, \quad (4.98)$$

$$M_2 = \frac{m}{\sqrt{m^2 - k^2}} \sinh\left(\sqrt{m^2 - k^2}\right) P_L - \frac{ik}{\sqrt{m^2 - k^2}} \sinh\left(\sqrt{m^2 - k^2}\right) \gamma_1 P_L, \quad (4.99)$$

$$M_3 = -\frac{m}{\sqrt{m^2 - k^2}} \sin\left(\sqrt{m^2 - k^2}\right) P_L - \frac{ik}{\sqrt{m^2 - k^2}} \sin\left(\sqrt{m^2 - k^2}\right) \gamma_1 P_R, \quad (4.100)$$

$$M_4 = \cos^2\left(\frac{1}{2}\sqrt{m^2 - k^2}\right) I_2 + \sin^2\left(\frac{1}{2}\sqrt{m^2 - k^2}\right) \gamma_5. \quad (4.101)$$

Figure 4.10a gives the results for numerical values $m = 1.5$, $k = 0.1$, $m_u = 172.76$ GeV and $m_d = 4.2$ GeV.

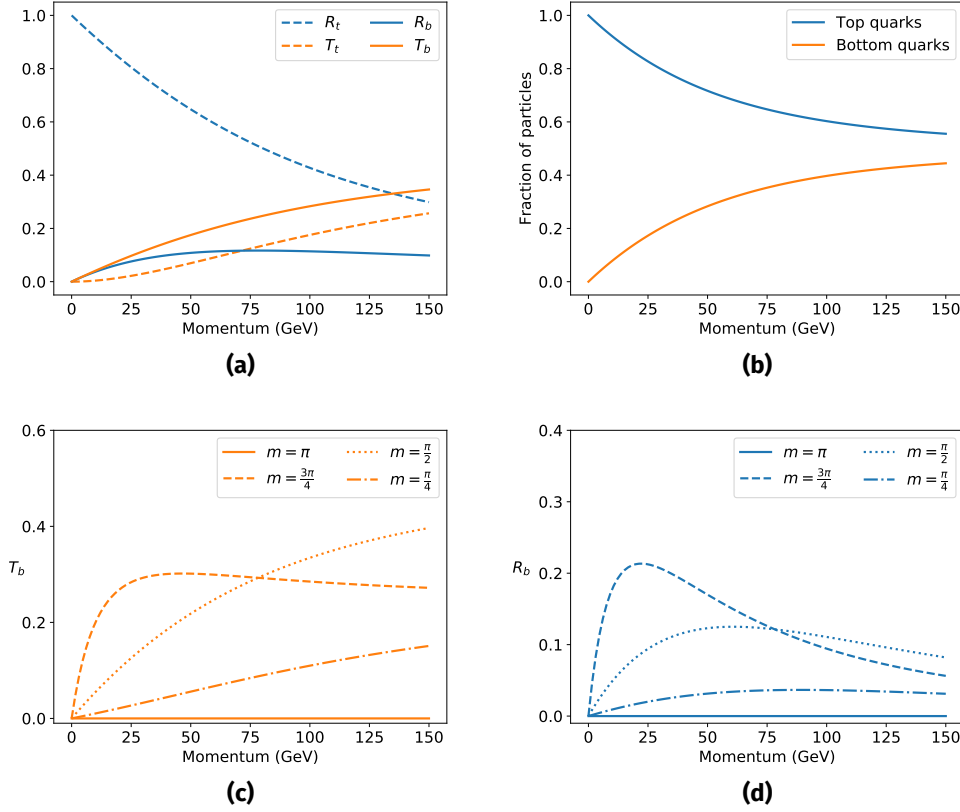


Figure 4.10: (a) Reflection and transmission coefficients for top and bottom quarks in the case of $m > k$. (b) The rate of top quarks being transformed into bottom quarks or kept as top quarks. (c) and (d) Transmission and reflection coefficients for different values of m .

One can see that, in this case, the transmission coefficient as a bottom quark gets higher as we increase the momentum of the incoming particle. The difference between this case and the one where the Yukawa term is dominant ($k \gg m$) is that there is no chirality flipping of the particle in the coupling between the gauge fields living inside the wall and the fermions (see (4.60)).

For $m \gg k$, one can get rather simple analytical expressions:

$$R_u(p_u) = \frac{g_d^2(1 - g_u^2)^2 u_{1i}^2}{p_u g_u [g_d(d_u + g_u) + (1 + g_d^2) \tan^2(\frac{m}{2})]^2}, \quad (4.102)$$

$$R_d(p_u) = \frac{g_d[1 - 4g_d g_u + g_u^2 + g_d^2(1 + g_u^2)] u_{1i}^2 \tan^2(\frac{m}{2})}{p_u [g_d(d_u + g_u) + (1 + g_d^2) \tan^2(\frac{m}{2})]^2}, \quad (4.103)$$

$$T_u(p_u) = \frac{-4 \cos(m)(-1 + g_d^2)^2 + (1 + 6g_d^2 + g_d^4)(3 + \cos(2m))}{8 \cos^4(\frac{m}{2})[g_d(d_u + g_u) + (1 + g_d^2) \tan^2(\frac{m}{2})]^2}, \quad (4.104)$$

$$T_d(p_u) = \frac{g_d u_{1i}^2 [1 + 4g_d g_u + g_u^2 + g_d^2(1 + g_u^2)] \tan^2(\frac{m}{2})}{p_u [g_d(d_u + g_u) + (1 + g_d^2) \tan^2(\frac{m}{2})]^2}. \quad (4.105)$$

In this case the rate of reflection and transmission coefficients will oscillate with increasing m . Such a behavior is shown in Figures 4.10c and 4.10d. In order to study this oscillating behavior in more detail, we fix the momentum of the incoming top quark and vary m between $[0, 2\pi]$. The results are shown in Figure 4.11. We observe that the rate of conversion of top quarks into bottom quarks also vanishes for $m = \pi$.

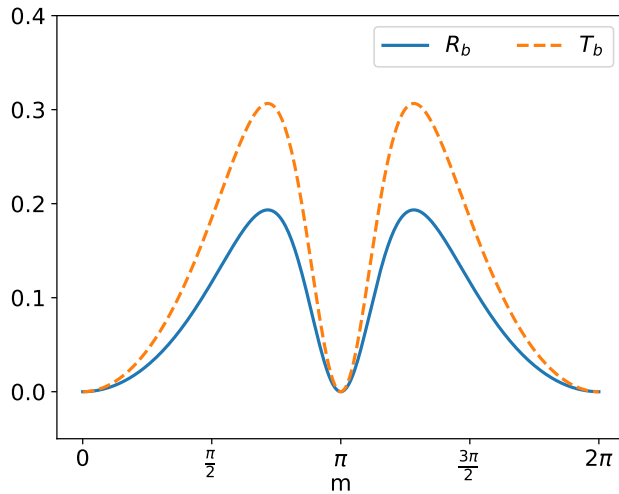


Figure 4.11: Reflection and transmission coefficients as a bottom quark for an incident top quark with momentum $p = 40$ GeV as a function of m , cf.(4.90).

We now consider the scattering of the second-generation quarks off the wall. We take, as an example, the scattering of charm quarks off the domain wall. In this case, the electric charge breaking parameter k gets smaller due to the small Yukawa coupling of the charm quark to the Higgs doublet. Figure 4.12 shows the results for $k > m$. In this case, we observe that the electric charge breaking effect is very small and most charm quarks scatter off the wall as charm quarks, even for high values of $v_+ = 65$ GeV corresponding to $k = 0.43$. However, when we consider the case $m > k$, the charge breaking effect can be quite high depending on the value of m , as is shown in Figure 4.13. This demonstrates the importance of the gauge field configurations localized on the wall in these scattering processes.

Finally, we also mention that anti up-type quarks scattering off the domain walls will lead to exactly the same rate of transformation into anti down-type quarks as the rate of the up-type quarks transformed into down-type quarks. Therefore, the interaction of fermions with these types of domain walls might only lead to *local* electric charge violation and does not lead to a net generation of electric charge in the early universe, which is a strongly constrained phenomenon [143]. However, as we saw in the previous chapter, the domain walls solution in the 2HDM can exhibit simultaneously both an electric charge and a CP violation inside the wall. This will lead to the generation of a non-zero CP-violating phase ξ inside the domain wall. This phase, along with a non-zero v_+ inside the wall, might lead to the generation of a net electric charge in the early universe, as particles and antiparticles will interact with the wall at different rates. In such a case, the domain wall network has

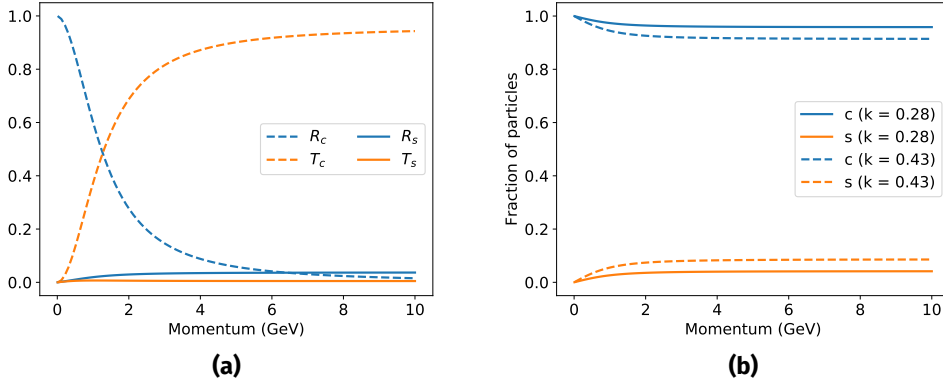


Figure 4.12: (a) Reflection and transmission coefficients for second generation quarks. We take $k = 0.28$, $m = 0.1$, $m_c = 1.27$ GeV and $m_s = 0.095$ GeV corresponding to charm (denoted c) and strange quarks (denoted s). Note that the conversion rate to strange quarks is very small even for $v_+ = 65$ GeV corresponding to $k = 0.43$. (b) Ratio of charm and strange quarks after the scattering for different values of k .

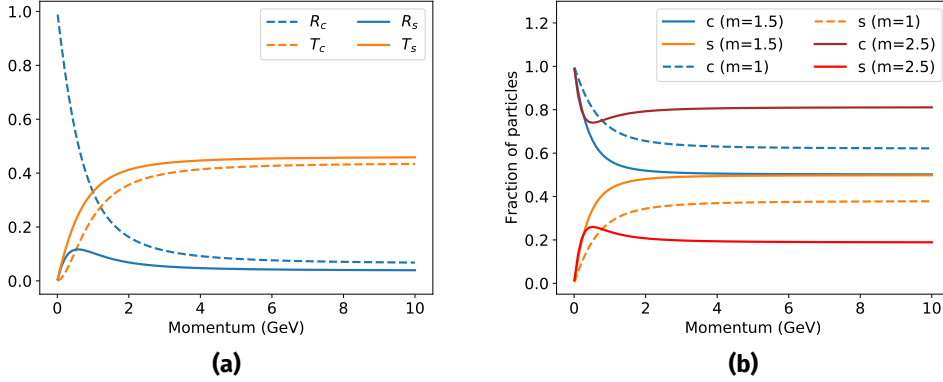


Figure 4.13: (a) Reflection and transmission coefficients for second generation quarks. We take $k = 0.43$, $m = 1.5$, $m_c = 1.27$ GeV and $m_s = 0.095$ GeV corresponding to charm (denoted c) and strange quarks (denoted s). (b) Fraction of particles after scattering with the wall for different values of m .

to annihilate very quickly in order to avoid generating an electric charge asymmetry higher than the observed cosmological constraints.

Another possible problem with these types of domain walls is that they could efficiently deplete the number of up-type quarks into down-type quarks. For example, bottom and anti-bottom quarks could be generated from the interaction of top and anti-top quarks with the wall. Due to the large difference in the masses between these two flavors, the inverse reaction would be suppressed, and we would end up with a surplus of bottom and anti-bottom quarks well before the usual annihilation time of top quarks in the thermal plasma. This phenomenon might then have consequences on Big Bang Nucleosynthesis (BBN).

4.4 DISCUSSION

We investigated in this chapter some of the possible interactions of SM fermions with the different domain wall solutions in the 2HDM. We focused on the case of the top and bottom quarks, since the interaction of the fermions with the wall via the Yukawa coupling would be negligible for the other scenarios, with the exception when the pure gauge fields localized on the wall are sizable.

We showed, in particular, that the scattering of top quarks off the CP-violating domain wall leads to a chiral asymmetry since the reflection and transmission coefficients for left and right-handed particles are different. Such a chiral asymmetry could be useful for mechanisms generating a matter-antimatter asymmetry [106, 107, 108], since it circumvents the stringent constraints on conventional sources for CP-violation put by electron dipole moment experiments [116]. One particular issue that was found is related to negative reflection coefficients for some values of the momentum, which might be associated with a Klein Paradox related to the chiral fermions. This issue warrants an in-depth investigation, possibly in the framework of quantum field theory, since it might be related to particle production and annihilation on the wall.

We also demonstrated the peculiar effect of electric charge breaking scattering, where top quarks can be transformed into bottom quarks. This effect has the same rate for antifermions, and we therefore do not expect that it leads to a net electric charge produced in the early universe¹. One interesting scenario is the inclusion of right-handed sterile neutrinos in the theory with masses in the keV scale. Since inside the electric charge-breaking wall, a non-zero coupling between these sterile neutrinos and the other SM leptons arises (which vanishes outside the wall for $v_+ = 0$), the scattering of these SM leptons off the wall could be a new mechanism for the production of sterile neutrinos in the early universe. This scenario is left for future investigations.

Another interesting possible future direction is to investigate how the domain walls could affect the number density of particles in the early universe, which might lead to a different early universe cosmology, including consequences on baryogenesis and BBN.

Having discussed the different domain wall solutions in the 2HDM and some aspects of SM particle scatterings off these walls, we study in the next chapters the domain wall solutions in the N2HDM and showcase possible new mechanisms for baryogenesis and vacuum decays induced by these domain walls.

¹ When taking the assumption that the number of fermions and antifermions is equal, otherwise this effect could turn a matter-antimatter asymmetry into an electric charge asymmetry.

This chapter is based on the following work, accepted for publication in JHEP:

- [2] M. Y. Sassi and G. Moortgat-Pick, *Electroweak Symmetry Restoration in the N2HDM via Domain Walls*, [2407.14468]

5.1 MOTIVATION AND GENERAL IDEA

As we saw in the previous chapter, domain wall field configurations in the 2HDM can be CP-violating, which leads to a chiral asymmetry when fermions scatter off the wall. For domain wall solutions in the 2HDM, $v_2(x=0) = 0$ inside the wall. However, $v_1(x)$ also changes its value considerably inside and in the vicinity of the wall. This was explained by the fact that the effective mass term $M_1(x) = m_{11}^2/2 + (\lambda_3 + \lambda_4 + \lambda_5)v_2^2(x)/4$ inside the wall reduces to $M_1(0) = m_{11}^2/2$, which can be considerably less negative than its value outside the wall and therefore, makes $v_1(0)$ smaller. Several mechanisms that generate a matter-antimatter asymmetry in the early universe rely on sphaleron processes, which break $B + L$ (the sum of baryon and lepton numbers). After electroweak symmetry breaking, the Higgs doublet(s) acquire a vacuum expectation values which leads to the exponential suppression of the sphaleron rate $\Gamma_s \propto e^{-E_{sph}/T}$, where $E_{sph} \propto v(T)$ the vacuum expectation value of the Higgs doublets. By having a region of the universe where v vanishes or becomes small, such as inside or in the vicinity of the domain wall, one can have an efficient source for baryon number-violating processes necessary for a successful baryogenesis.

Motivated by these results, we consider in this chapter another interesting phenomenon induced by the domain wall of the real singlet scalar in the N2HDM, namely the possibility of electroweak symmetry restoration (EWSR) inside and in the vicinity of the domain wall. In such a case, the sphaleron rate is much less suppressed inside and in the vicinity of the wall than in the regions outside of it. Therefore, this effect combined with a source for CP-violation, can lead, a priori, to the generation of a matter-antimatter asymmetry in the early universe induced by domain walls. Such a mechanism was examined in previous works [144, 145, 106, 146, 107, 66, 147, 148] in the framework of general topological defects such as cosmic strings and domain walls. One significant advantage of such a mechanism compared to conventional electroweak baryogenesis is that the need for a first-order phase transition can be avoided, given that the topological defect will provide the separation in the regions with drastically different sphaleron rates, ensuring the out-of-thermal-equilibrium condition. For the case of cosmic strings, it was shown in [66] that any matter-antimatter asymmetry produced by this mechanism is orders of magnitude smaller than the observed asymmetry.

This is mainly due to cosmic strings being one-dimensional defects, which renders the volume in space where the mechanism is active very small [66]. Such volume suppression is, however, not present in the case of moving domain walls as they are two-dimensional objects and therefore this mechanism can be effective in a large volume spanned by the moving walls [146, 107].

The outline of this chapter is as follows: we first discuss the phenomenology of domain wall solutions in the N2HDM, which are related to the breaking of the Z'_2 discrete symmetry. We later discuss the possibility of inducing electroweak symmetry restoration inside and in the vicinity of the wall, which is one requirement for electroweak baryogenesis induced by domain walls. We also study some phenomenological scenarios to pinpoint parameter regions where one achieves electroweak symmetry restoration in a large area around the wall. Finally, we discuss possibilities for generating an axial asymmetry inside the wall, such as inducing a pure gauge hypermagnetic field centered on the wall, and show, in a simplified calculation, that one can indeed obtain a significant amount of baryon asymmetry using this mechanism.

5.2 DOMAIN WALLS IN THE N2HDM

In our model, different types of domain wall solutions can be found depending on which discrete symmetry gets broken in the early universe. Recall that the scalar potential of the N2HDM:

$$\begin{aligned}
V_{N2HDM} = & m_{11}^2 \Phi_1^\dagger \Phi_1 + m_{22}^2 \Phi_2^\dagger \Phi_2 - m_{12}^2 (\Phi_1^\dagger \Phi_2 + h.c.) + \frac{\lambda_1}{2} (\Phi_1^\dagger \Phi_1)^2 + \frac{\lambda_2}{2} (\Phi_2^\dagger \Phi_2)^2 \\
& + \lambda_3 (\Phi_1^\dagger \Phi_1) (\Phi_2^\dagger \Phi_2) + \lambda_4 (\Phi_1^\dagger \Phi_2) (\Phi_2^\dagger \Phi_1) + \left[\frac{\lambda_5}{2} (\Phi_1^\dagger \Phi_2)^2 + h.c. \right] \\
& + \frac{m_s^2}{2} \Phi_s^2 + \frac{\lambda_6}{8} \Phi_s^4 + \frac{\lambda_7}{2} \Phi_s^2 (\Phi_1^\dagger \Phi_1) + \frac{\lambda_8}{2} \Phi_s^2 (\Phi_2^\dagger \Phi_2) \\
& + \left[a_1 \Phi_s + a_3 \Phi_s^3 + b_1 (\Phi_1^\dagger \Phi_1) \Phi_s + b_2 (\Phi_2^\dagger \Phi_2) \Phi_s + c_1 (\Phi_1^\dagger \Phi_2 \Phi_s + h.c.) \right], \quad (5.1)
\end{aligned}$$

is invariant under the discrete symmetry Z_2 :

$$\Phi_1 \rightarrow \Phi_1, \quad \Phi_2 \rightarrow -\Phi_2, \quad \Phi_s \rightarrow \Phi_s, \quad (5.2)$$

when $m_{12}^2 = 0$, and invariant under a Z'_2 discrete symmetry:

$$\Phi_s \rightarrow -\Phi_s, \quad (5.3)$$

When the parameters a_1, a_3, b_1, b_2 and c_1 are zero.

Domain wall solutions are constructed by imposing vacua related by a discrete symmetry at the boundaries $\pm\infty$. In the case of a spontaneously broken Z'_2 symmetry, DW solutions interpolate between regions with vacua $\langle \Phi_s \rangle = -v_s$ and $\langle \Phi_s \rangle = v_s$ and therefore, necessarily cross $\langle \Phi_s \rangle = 0$ inside the core of the wall.

In the case when the Z_2 -discrete symmetry gets spontaneously broken (alongside the electroweak symmetry), possible domain wall solutions interpolate between the vacua located on two disconnected 3-spheres of the vacuum manifold:

$$\langle \Phi_1 \rangle = \frac{1}{\sqrt{2}} \begin{pmatrix} 0 \\ v_1 \end{pmatrix}, \quad \langle \Phi_2 \rangle = \frac{-1}{\sqrt{2}} \begin{pmatrix} 0 \\ v_2 \end{pmatrix}, \quad \langle \Phi_s \rangle = v_s, \quad U = U_1 \quad \text{at } -\infty, \quad (5.4)$$

$$\langle \Phi_1 \rangle = \frac{1}{\sqrt{2}} \begin{pmatrix} 0 \\ v_1 \end{pmatrix}, \quad \langle \Phi_2 \rangle = \frac{1}{\sqrt{2}} \begin{pmatrix} 0 \\ v_2 \end{pmatrix}, \quad \langle \Phi_s \rangle = v_s, \quad U = U_2 \quad \text{at } +\infty, \quad (5.5)$$

with U_1 and U_2 corresponding to different Goldstone modes θ and g_i of $SU(2)_L \times U(1)_Y$, leading to the creation of different classes of DW solutions as was recently found in [1, 76].

In the following sections, we focus on the domain wall solutions obtained in the N2HDM after the spontaneous symmetry breaking of Z'_2 leading to a non-zero v_s as well as describing the effects of the domain wall solution for $\Phi_s(x)$ on the field configurations of $\Phi_1(x)$ and $\Phi_2(x)$, demonstrating the possibility of restoring the EW symmetry inside the wall.

5.2.1 Symmetry restoration in the early universe

Before we start discussing the domain wall solutions in the N2HDM, we first briefly consider the thermal evolution of the N2HDM scalar potential in the early universe. One crucial condition for the validity of our analysis is the restoration of the Z'_2 symmetry in the early universe at high temperatures. This requirement is important because in the case of non-restoration of the Z'_2 symmetry, domain walls wouldn't have formed in the first place, and the singlet would be in the broken phase already at very high temperatures.

To check whether a parameter point features electroweak and/or Z'_2 symmetry restoration in the early universe, one needs to follow the evolution of the effective thermal potential of the N2HDM at high temperatures given by [23]:

$$V_{N2HDM}(T, \Phi_1, \Phi_2, \Phi_s) = V_{N2HDM}^{tree} + V_{CW} + V_{N2HDM}^T + V_{CT}, \quad (5.6)$$

where V_{N2HDM}^{tree} denotes the tree-level potential defined in (5.1). The second and third terms correspond to one-loop corrections known as the Coleman-Weinberg potential one-loop correction at zero temperature V_{CW} , and a finite temperature correction V_{N2HDM}^T . The last term V_{CT} is a counterterm used to renormalize the one-loop corrections and cure the UV divergences. V_{CW} and V_{N2HDM}^T are obtained from the effective one-loop scalar potential V_{eff}^1 [81, 149, 69]:

$$\begin{aligned} V_{eff}^1(\phi_i) &= \sum_j \frac{n_j T}{2} \sum_{-\infty}^{+\infty} \int \frac{d^3 p}{(2\pi)^3} \log(w_n + |\vec{p}|^2 + m_j^2(\phi_i)) \\ &= \sum_j \frac{n_j}{2} \left[\int \frac{d^3 p}{(2\pi)^3} \sqrt{|\vec{p}|^2 + m_j^2(\phi_i)} \mp \frac{T^4}{\pi^4} \int_0^{+\infty} dx x^2 \log\left(1 \pm e^{-\sqrt{x^2 + \frac{m_j^2(\phi_i)}{T^2}}}\right) \right] \\ &= V_{CW}(\phi_i) + V_{N2HDM}^T(\phi_i), \end{aligned} \quad (5.7)$$

with Matsubara frequencies $w_n = 2n\pi T$ for bosons, and $w_n = (2n + 1)\pi T$ for fermions. The first term is temperature independent and corresponds to the Coleman-Weinberg [81, 149, 69]:

$$V_{CW}(\phi_i) = \sum_j \frac{n_j}{64\pi^2} (-1)^{2s_i} m_j^4(\phi_i) \left[\ln\left(\frac{|m_j^2(\phi_i)|}{\mu^2}\right) - c_j \right], \quad (5.8)$$

where n_j denotes the multiplicities of the thermal bath particles given by index j , $m_j(\phi_i)$ the mass formulas of the particle as a function of the scalar field ϕ_i and c_j the $\overline{\text{MS}}$ renormalization constants with $c_j = 3/2$ for fermions and scalars and $c_j = 5/6$ for gauge

bosons [23]. This Coleman-Weinberg potential is renormalized using the counterterms potential V_{CT} by keeping the zero-temperature VEVs at one-loop level the same as the VEVs at the tree level [23, 150, 151]. This is done using the conditions (1.32) and (1.33).

The second term V_{N2HDM}^T in (5.7) corresponds to the one-loop thermal correction to the scalar potential generated by the interaction of the scalar sector with the thermal bath in the early universe and can be re-written as [152, 81, 149, 69]:

$$V_{N2HDM}^T = \sum_j \frac{n_j T^4}{(2\pi)^2} J_{\pm} \left(\frac{m_j^2(\phi_i)}{T^2} \right), \quad (5.9)$$

$$J_{\pm} \left(\frac{m_j^2(\phi_i)}{T^2} \right) = \mp \int_0^{+\infty} dx x^2 \log \left[1 \pm \exp \left(-\sqrt{x^2 + \frac{m_j^2(\phi_i)}{T^2}} \right) \right], \quad (5.10)$$

where n_j denotes, again, the multiplicities of the thermal bath particles given by index j , $m_j(\phi_i)$ the mass formulas of the particle as a function of the scalar field ϕ_i and J_{\pm} the thermal functions for fermions (+) and bosons (-).

In the high temperature limit (m^2/T^2 small), the thermal functions reduce to [152]:

$$J_{-}(y) \approx -\frac{\pi^4}{45} + \frac{\pi^2}{12}y - \frac{\pi}{6}y^{\frac{3}{2}} - \frac{1}{32}y^2 \log\left(\frac{|y|}{a_b}\right) + O(y^3), \quad (5.11)$$

$$J_{+}(y) \approx -\frac{7\pi^4}{360} + \frac{\pi^2}{24}y + \frac{1}{32}y^2 \log\left(\frac{|y|}{a_f}\right) + O(y^3), \quad (5.12)$$

where $a_b = \pi^2 \exp(3/2 - 2\gamma_E)$ and $a_f = 16\pi^2 \exp(3/2 - 2\gamma_E)$.

One final contribution that needs to be taken into account is the daisy contribution to the thermal potential [81, 153, 154, 155]. This is done due to the breakdown of perturbation theory caused by zero Matsubara frequencies for bosons [69, 81], which behave as massless particles at the high temperature limit and causing infrared divergencies in the propagator poles of the effective potential (see (5.7)) [69, 81]. To cure these divergencies, one needs to perform a resummation of the multi-loop diagrams causing the divergencies also known as the Daisy diagrams [81, 69, 149].

We do not discuss the details of these resummation procedures and only follow the treatment used in [23] where the authors used the Arnold-Espinosa resummation scheme [153] where one cures these IR divergencies by giving a thermal mass $\Pi_j^2(\phi_j, T)$ to the bosons for the part with zero Matsubara frequency:

$$m_j^2(\phi) \rightarrow m_j^2(\phi) + \Pi_j^2(\phi_j, T). \quad (5.13)$$

After plugging these new mass terms in (5.7) for the contribution with zero Matsubara frequency ($n=0$), this translates into an additional term V_{daisy}^T in the thermal potential which can be written as [23]:

$$V_{daisy}^T(\phi_j, T) = - \sum_j \frac{T}{12\pi} \text{Tr} \left[\left(m_j^2(\phi_j) + \Pi_j^2(\phi_j, T) \right)^{3/2} - \left(m_j^2(\phi_j) \right)^{3/2} \right]. \quad (5.14)$$

As a summary, the thermal effective potential has the effect of rendering the effective mass terms to be temperature-dependent:

$$V_{N2HDM}(T, \Phi_1, \Phi_2, \Phi_s) = m_{11}^2(T)|\Phi_1|^2 + m_{22}^2(T)|\Phi_2|^2 + m_S^2(T)\Phi_s^2 + m_{12}^2\Phi_1\Phi_2 + \dots \quad (5.15)$$

It is therefore possible that for a non-zero temperature T , the effective mass terms turn positive, leading the minimum of the potential to be at the origin of field space $(\Phi_1, \Phi_2, \Phi_s)_T = (0, 0, 0)$ and therefore to the restoration of the symmetry. To investigate this, one can use an analytical or numerical approach. The analytical approach discussed in [23] calculates the Hessian matrix of the potential at its origin $(0,0,0)$ at high temperatures T , which gives us information about the curvature of the potential around the origin. This involves calculating the principal minors of the Hessian matrix $H_{i,j}^0 = \partial^2 V / \partial \phi_i \partial \phi_j |_{(0,0,0)}$. One can then define the quantities¹ $c_{ii} \equiv \lim_{T \rightarrow \infty} H_{ii}^0 / T^2$ [23]:

$$c_{11} \simeq -0.025 + c_1 - \frac{1}{2\pi} \left(\frac{3}{2} \lambda_1 \sqrt{c_1} + \lambda_3 \sqrt{c_2} + \frac{1}{2} \lambda_4 \sqrt{c_2} + \frac{1}{4} \lambda_7 \sqrt{c_3} \right), \quad (5.16)$$

$$c_{22} \simeq -0.025 + c_2 - \frac{1}{2\pi} \left(\frac{3}{2} \lambda_2 \sqrt{c_2} + \lambda_3 \sqrt{c_1} + \frac{1}{2} \lambda_4 \sqrt{c_1} + \frac{1}{4} \lambda_8 \sqrt{c_3} \right), \quad (5.17)$$

$$c_{33} = c_3 - \frac{1}{2\pi} \left(\lambda_7 \sqrt{c_1} + \lambda_8 \sqrt{c_2} + \frac{3}{4} \lambda_6 \sqrt{c_3} \right), \quad (5.18)$$

where the coefficients c_i are defined as [23]:

$$c_1 = \frac{1}{16}(g'^2 + 3g^2) + \frac{\lambda_1}{4} + \frac{\lambda_3}{6} + \frac{\lambda_4}{12} + \frac{\lambda_7}{24}, \quad (5.19)$$

$$c_2 = \frac{1}{16}(g'^2 + 3g^2) + \frac{\lambda_2}{4} + \frac{\lambda_3}{6} + \frac{\lambda_4}{12} + \frac{\lambda_8}{24} + \frac{1}{4}y_t^2, \quad (5.20)$$

$$c_3 = \frac{1}{6}(\lambda_7 + \lambda_8) + \frac{1}{8}\lambda_6, \quad (5.21)$$

with g and g' denoting the weak gauge couplings and y_t the Yukawa coupling to the top quark. For positive c_{11} and c_{22} , the electroweak symmetry is restored at high T and in case $c_{33} > 0$, the Z'_2 symmetry is restored. In this work, we focus on the restoration of the Z'_2 symmetry at higher temperatures to ensure the formation of the singlet domain walls. In case when $c_{11,22} < 0$, the doublets have a temperature-dependent VEV, and the required Hessian matrix has to be evaluated at $(v_1(T), v_2(T), 0)$ to reliably determine whether the Z'_2 symmetry is restored. Such a calculation is more complicated and can only be done numerically for the N2HDM. However, we observed that for several parameter points satisfying only the condition $c_{33} > 0$, it is possible to restore the Z'_2 . Considering the leading order in T^2 for the thermal potential, the effective mass term for the singlet field at a given temperature T can be approximated by

$$M_S(T) \approx m_s^2 + c_{33}T^2 + \frac{\lambda_7}{4}v_1^2(T) + \frac{\lambda_8}{4}v_2^2(T).$$

In case $M_S(T)$ is positive, $v_s(T) = 0$ minimizes the thermal potential. Such a scenario can be obtained for $\lambda_{7,8} > 0$ or small negative $\lambda_{7,8}$. It is also possible to obtain a thermal history where the EW and/or the Z'_2 symmetry are restored for an intermediate temperature interval as was found in [23]. Such a scenario can only be examined by a full numerical approach and therefore we limit ourselves to the more conservative scenario where c_{11} , c_{22} and c_{33} are positive (unless otherwise specified for some parameter scans) ensuring that all symmetries get restored at some high temperature T . This constraint was included in our implementation of `ScannerS` [156, 157, 26, 158, 117] in order to only generate parameter points for our scans where the EW and Z'_2 symmetries get restored at some stage in the

¹ These coefficients also incorporate terms from the daisy resummation of infrared-divergent contributions in the thermal potential. The authors of [23] use the Arnold-Espinosa method [153] for the derivation of the coefficients c_{ii} .

early universe. Note that the expressions for c_{11} , c_{22} and c_{33} derived in [23] use the Arnold-Espinosa resummation scheme [153]. It is known that different resummation schemes can lead to different outcomes for the thermal evolution of the scalar fields in the early universe (see e.g. page 23 in [23]). A detailed discussion of these aspects is beyond the scope of this work and therefore, we use these formulas in the framework of the Arnold-Espinosa method only as an attempt to verify the restoration of the Z'_2 and EW symmetries in the early universe.

5.2.2 Z'_2 Domain Walls

We discuss the singlet domain wall solution in the N2HDM and its effects on the VEVs of the doublets v_1 and v_2 . Here, we only consider the zero-temperature potential for the calculation of the field configuration. We therefore assume that the change in the scalar potential at small temperatures after EWSB is negligible. This choice was made in order to simplify obtaining results for large sets of parameter scans, as otherwise, one would need to calculate the exact VEVs at a particular temperature $T < T_{ew}$ for every parameter point, with T_{ew} the temperature at which the EW symmetry gets spontaneously broken, making the computation lengthy and more complicated.

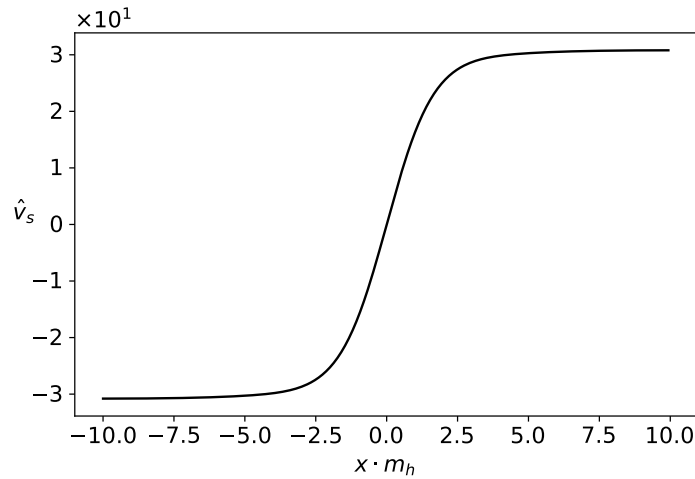


Figure 5.1: Domain wall solution for the singlet scalar field ϕ_s . The result is shown in terms of the rescaled VEV $\hat{v}_s = v_s/v_{sm}$.

In order to get domain wall solutions, we require the singlet vacua v_s to have a different sign at both spatial boundaries $\pm\infty$ depicting two regions of the universe with different signs for v_s . Outside the wall, the electroweak symmetry is broken and the doublets Φ_1 and Φ_2 acquire VEVs $(v_1(\pm\infty), v_2(\pm\infty)) \neq (0, 0)$. In this work, we only consider neutral CP-conserving vacua, therefore: $v_+(\pm\infty) = 0$ and $\xi(\pm\infty) = 0$.

The spatially varying field configuration is then obtained by solving the equations of motion for the scalar fields using the latter boundary conditions:

$$\frac{\partial^2 v_i}{\partial t^2} - \frac{\partial^2 v_i}{\partial x^2} + \frac{\partial V_{N2HDM}}{\partial v_i} = 0, \quad (5.22)$$

where i denotes the different scalar fields. Due to the complicated nature of these non-linear differential equations, we find the solutions numerically using the gradient flow method [76] which minimizes the total energy per unit area of the static field configuration given by:

$$\sigma_{dw} = \int_{-\infty}^{+\infty} dx \frac{d\Phi_i}{dx} \frac{d\Phi_i^\dagger}{dx} + V_{N2HDM}(x), \quad (5.23)$$

where the first term denotes the kinetic energy contribution from each scalar field and the second term gives the potential energy of the field configuration.

The spatial profile for the rescaled VEV $\hat{v}_s(x) = v_s(x)/v_{sm}$ is shown in Figure 5.1. In the simpler case of a model with only a real singlet scalar field, the width of the wall can be well approximated by $\delta_s = (\sqrt{\frac{\lambda_6}{4}} v_s)^{-1}$ [11]. This expression is, however, only applicable to our domain wall solution when the coupling terms between the doublets and the singlet are very small or zero ($\lambda_{7,8} \approx 0$). For non-vanishing values of $\lambda_{7,8}$ the back-reaction of the doublet fields will lead to a deviation of the wall's width from δ_s .

In the background of the domain wall of the singlet $v_s(x)$, the potential for (v_1, v_2) is x -dependent. We rewrite the potential V_{N2HDM} (5.1) as:

$$\begin{aligned} V_{N2HDM}(x) = & \left(\frac{m_{11}^2}{2} + \frac{\lambda_7}{4} v_s^2(x) \right) v_1^2(x) + \left(\frac{m_{22}^2}{2} + \frac{\lambda_8}{4} v_s^2(x) \right) v_2^2(x) + M_+(x) v_+^2(x) \\ & + \frac{m_s^2}{2} v_s^2(x) + \left(\frac{\lambda_3 + \lambda_4 + \lambda_5 \cos(2\xi(x))}{4} \right) v_1^2(x) v_2^2(x) + \frac{\lambda_1}{8} v_1^4(x) \\ & + \frac{\lambda_2}{8} v_2^4(x) + \frac{\lambda_2}{8} v_+^4(x) + \frac{\lambda_6}{8} v_s^4(x) - m_{12}^2 v_1(x) v_2(x) \cos \xi(x), \end{aligned} \quad (5.24)$$

where,

$$M_+(x) = \frac{m_{22}^2}{2} + \frac{\lambda_2}{4} v_2^2(x) + \frac{\lambda_3}{4} v_1^2(x) + \frac{\lambda_8}{4} v_s^2(x). \quad (5.25)$$

Due to the coupling terms between the doublet scalar fields Φ_1 and Φ_2 with the singlet scalar field Φ_s , the profile of the field configuration for the doublets in the background of the singlet domain wall will not be homogeneous in space. In the vicinity of the domain wall's core, $v_1(x)$ and $v_2(x)$ can depart considerably from their asymptotic values. The behavior of $v_1(x)$ and $v_2(x)$ inside the wall is largely influenced by the effective mass of the doublets, which we define as:

$$M_1(x) = \frac{m_{11}^2}{2} + \frac{\lambda_{345}}{4} v_2^2(x) + \frac{\lambda_7}{4} v_s^2(x), \quad (5.26)$$

$$M_2(x) = \frac{m_{22}^2}{2} + \frac{\lambda_{345}}{4} v_1^2(x) + \frac{\lambda_8}{4} v_s^2(x), \quad (5.27)$$

where $\lambda_{345} = \lambda_3 + \lambda_4 + \lambda_5$. In the case when m_{12}^2 is small or vanishing, the effective masses $M_{1,2}$ far from the wall are negative (see Figure 5.2a). This is required for the potential to develop non-vanishing vacuum expectation values. For $\lambda_{7,8} < 0$, it is possible to get $M_{1,2}(\pm\infty) < 0$ even if m_{11}^2 and m_{22}^2 are positive. The effective mass terms inside the wall are reduced to:

$$M_{1,2}(0) = \frac{m_{11,22}^2}{2} + \frac{\lambda_{345}}{4} v_{2,1}^2(0). \quad (5.28)$$

It is therefore possible to turn the effective mass terms inside the wall positive, which leads the potential $V_{N2HDM}(\Phi_1, \Phi_2, 0)$, effectively describing a 2HDM model, to be in the symmetric phase where the minima of the scalar doublets are zero.

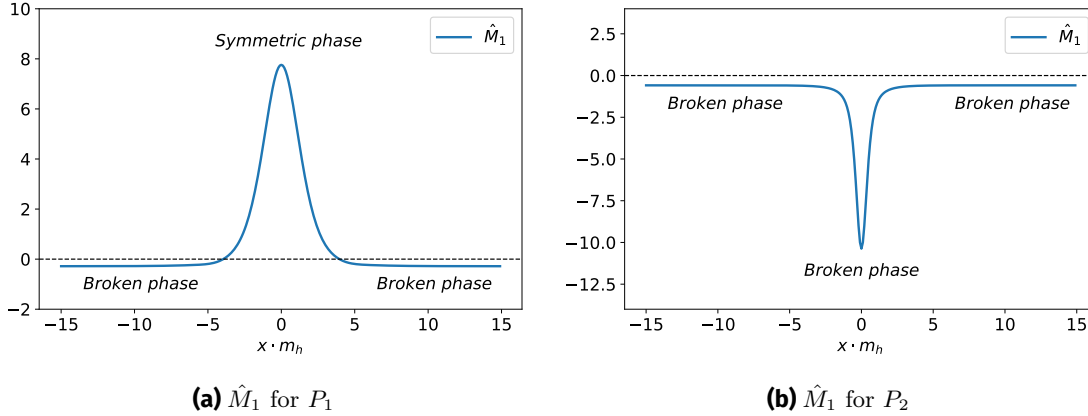


Figure 5.2: Rescaled spatial profile of the effective mass term $\hat{M}_1 = M_1(x)/m_h^2$ (with $m_h = 125.09$ GeV) for different parameter points P_1 and P_2 . (a) Spatial profile of \hat{M}_1 for P_1 . Far from the wall, \hat{M}_1 is negative and the potential of the doublet is in the broken phase. Inside the wall, \hat{M}_1 turns positive due to the term $\lambda_7 v_s^2$ vanishing, and the potential of the doublet has a minimum at the origin. (b) Spatial profile of \hat{M}_1 for P_2 . Inside of the wall, \hat{M}_1 is even more negative and we remain in the broken phase.

	m_{h_1}	m_{h_2}	m_{h_3}	$\tan(\beta)$	v_s	α_1	α_2	α_3	m_{12}^2
P_1	95.81	125.09	420.18	1	7599.26	0.88	1.01	0.47	0
P_2	125.09	248.80	828.88	1	1755.75	0.70	-0.07	-0.001	0
P_3	125.09	242.27	1698.10	1	1041.23	0.797	-0.049	-0.176	0
P_4	125.09	392.9	1141.1	1	1009.4	0.77	0.11	-0.14	0
P_5	125.09	391.31	693.66	1	2868.37	0.73	0.33	1.39	198916
P_6	125.09	242.59	622.04	1	798.66	0.877	-0.55	-1.48	179776

Table 5.1: Benchmark parameter points demonstrating different behavior for the doublet VEVs inside the singlet domain wall. The mass parameters m_{h_1} , m_{h_2} , m_{h_3} as well as v_s are given in GeV while m_{12}^2 is given in GeV^2 .

We show the behavior of the doublets inside the domain wall of the singlets for 2 different parameter points P_1 and P_2 (see Table 6.2). In case $M_{1,2}(0)$ are positive inside the wall (e.g. for $\lambda_{7,8} < 0$), the doublet scalar fields can have a vanishingly small vacuum expectation values $v_{1,2}(0) = 0$ (see Figure 5.3a).

Even when the doublets scalar potential for $v_s = 0$ has its global minimum at $v_1 = 0$ and $v_2 = 0$ (as is the case when the effective mass terms are positive and $m_{12} = 0$), one does not always achieve $v_{1,2}(0) = 0$ inside the wall whenever the effective masses are positive. This is due to the interplay between the kinetic and potential energy contributions of the domain wall's field configuration. When the energy barrier between the asymptotic vacua $(v_1, v_2, \pm v_s)$ and the extremum at $(v_1 = 0, v_2 = 0, v_s = 0)$ is large, the contribution of the potential energy to the total energy of the solution will be large. According to the Bogomolnyi method for static kink solutions [13], the minimal energy solution of the kink field configuration requires the contribution to the total energy of the domain wall from the potential part and the kinetic part to be equal. This leads the field configuration to have a high contribution from the kinetic energy and therefore the fields inside the wall will have a rapidly changing profile without having to pass through $v_{1,2} = 0$.

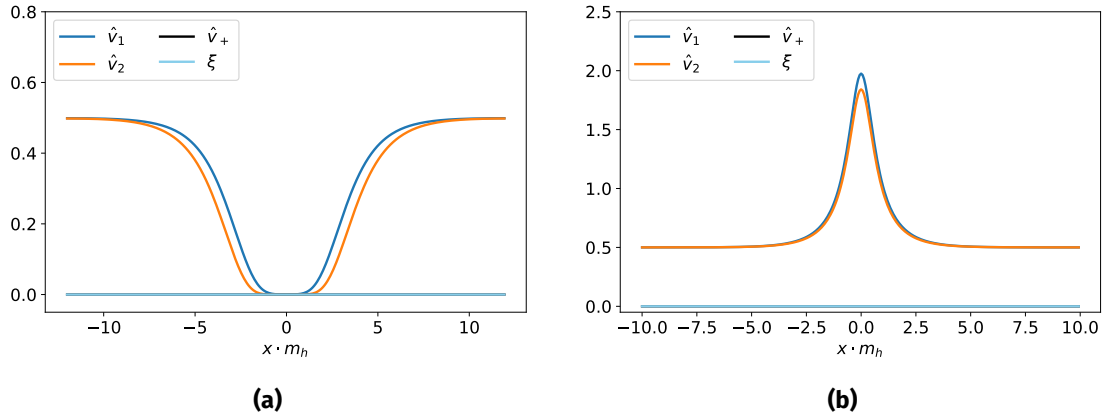


Figure 5.3: Rescaled VEV profiles for the doublet fields $\hat{v}_{1,2}(x) = v_{1,2}/v_{sm}$ for different parameter points. (a) For parameter point P_1 , $\hat{v}_{1,2}(x)$ inside the wall are much smaller than outside the wall. (b) For parameter point P_2 , $\hat{v}_{1,2}(x)$ inside the wall gets higher than outside the wall, due to the effective mass term being more negative in the DW.

In the case of a small potential barrier, the potential energy and therefore also the kinetic energy will be both small leading to a thicker wall, and therefore the VEVs of the doublets can have enough space to converge to the actual minimum of the potential at $x = 0$.

The opposite effect can happen when $\lambda_{7,8} > 0$ (e.g. parameter point P_2). In this case the effective mass terms in (5.26) and (5.27) receive a negative contribution inside the wall (see Figure 5.2b) and $v_{1,2}$ grow bigger (see Figure 5.3b).

In order to explain these two distinct behaviors, we show in Figure 5.4 the potential of the Higgs doublets Φ_1 and Φ_2 inside and outside the singlet domain wall. For P_2 , due to the quadratic effective masses being smaller inside the wall, the potential gets "stretched" and the minima of the potential have a higher value than those outside of the wall (depicted as a white cross sign in Figure 5.4d). For P_1 , the effective mass terms are higher and positive inside the wall. This leads to the 2HDM potential being in the symmetric phase just like the potential before EWSB. We observe in Figure 5.4b that the minimum of the potential in this case is zero for both fields Φ_1 and Φ_2 . Therefore, the vacuum expectation values for v_1 and v_2 inside the domain wall become very small in order to minimize the energy of the scalar fields configuration.

In the following, we perform scans of random N2HDM parameter points to determine the different behaviors that can occur for the doublet fields inside the wall. The samples of parameter points were obtained using `Scanners` [156, 157, 26, 158, 117]. We impose the theoretical constraints of boundedness from below, perturbative unitarity and vacuum stability, as well as experimental constraints from flavor physics and precision observables S, T and U. The boundedness from below condition is used to make sure that the potential does not tend to minus infinity at some direction. Perturbative unitarity ensures that the eigenvalues of the tree level S-matrix for $2 \rightarrow 2$ scattering processes are smaller than 8π [26]. We also impose the constraint of Z'_2 symmetry restoration at higher temperatures to ensure that all used parameter points lead to the formation of domain walls after the spontaneous breaking of that discrete symmetry at some point in the early universe.

We solve the differential equations describing the scalar field configuration for each generated parameter point satisfying the constraints. The results are quantified using the quantities:

$$r_1 = \frac{v_1(0)}{v_1(\pm\infty)}, \quad r_2 = \frac{v_2(0)}{v_2(\pm\infty)}, \quad \hat{v}_{ew}(0) = \frac{\sqrt{v_1^2(0) + v_2^2(0)}}{v_{sm}}, \quad (5.29)$$

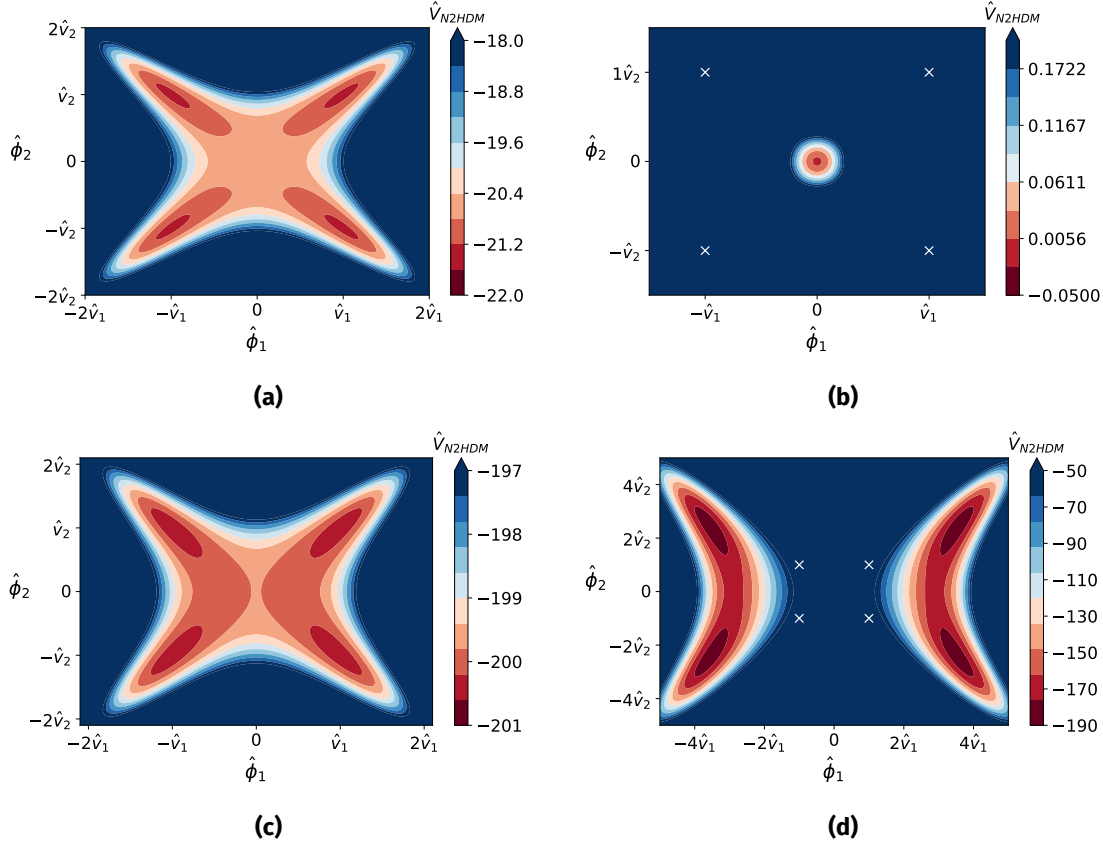


Figure 5.4: The potential of the N2HDM: (b) inside ($\phi_s = 0$) and (a) outside ($\phi_s = v_s$) the domain wall for 2 parameter points P_1 (a,b) and P_2 (c,d).

which gives a measure for the restoration of the electroweak symmetry inside the wall. We analyze the correlations between the results of the parameter scans and the difference in the effective mass inside and outside the wall $\Delta_{1,2}$:

$$\Delta_{1,2} = M_{1,2}(0) - M_{1,2}(\pm\infty) = \frac{1}{4} \lambda_{345} (v_{2,1}^2(0) - v_{2,1}^2(\pm\infty)) - \frac{1}{4} \lambda_{7,8} v_s^2. \quad (5.30)$$

Using the quantities $\Delta_{1,2}$ is motivated by the observation in the results of P_1 and P_2 that when the effective masses become less negative inside the wall ($\Delta_{1,2} > 0$) we obtain $r_{1,2} < 1$ and when the effective masses inside the wall become more negative than outside of it ($\Delta_{1,2} < 0$) we obtain $r_{1,2} > 1$.

5.2.2.1 General parameter scan with $m_{12}^2 = 0$

m_{h_a}	m_{h_b}	m_{h_c}	m_A	m_{H^\pm}	$\tan\beta$
125.09	[125.09, 700]	[125.09, 1400]	[400, 700]	[650, 700]	1
$C_{h_a t \bar{t}}^2$	$C_{h_a V V}^2$	R_{b3}	m_{12}^2	v_s	type
[0.6, 1]	[0.8, 1.2]	[-1, 1]	0	[200, 1500]	2

Table 5.2: Set of input parameters for our ScannerS scan. We focus first on parameter points with $m_{12}^2 = 0$. $C_{h_a t \bar{t}}$ and $C_{h_a V V}$ are defined respectively as the coupling factors of the CP-even Higgs boson h_a to the SM gauge bosons and the top quark and are defined as $C_{h_a V V} = \cos(\beta)R_{a1} + \sin(\beta)R_{a2}$ and $C_{h_a t \bar{t}} = R_{a2}/\sin(\beta)$ (see 2.2 and [117]).

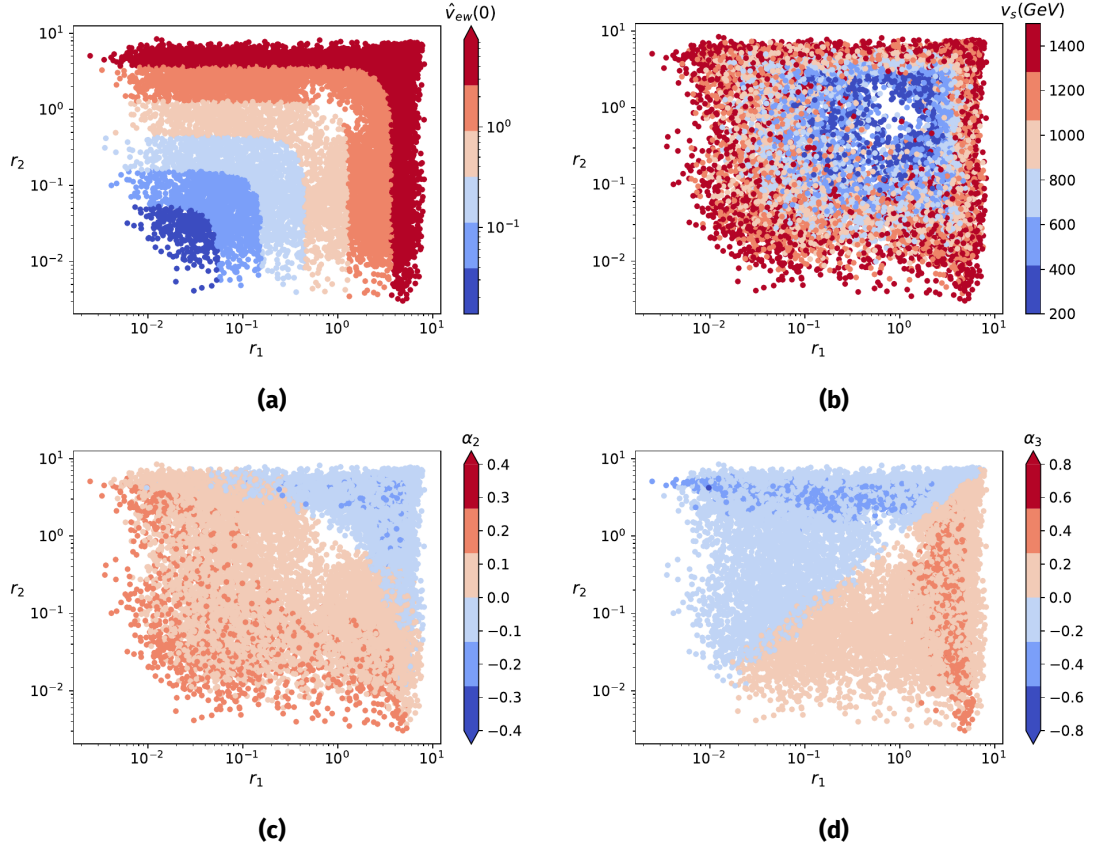


Figure 5.5: Result of the scan in terms of the ratios r_1 and r_2 . (a) Results for r_1 and r_2 as a function of the electroweak symmetry VEV $v_{ew}(0)$ inside the wall. (b) shows the correlations as a function of v_s . (c) shows the correlations as a function of α_2 . (d) shows the correlations as a function of α_3 .

We start with a general parameter scan of the N2HDM using a sample of 20000 parameter points (see Table 5.2). For this particular scan, we take $m_{12}^2 = 0$ and we only require Z'_2 symmetry restoration as we found that generating parameter points with `ScannersS` that also satisfy the constraint of EW symmetry restoration was much easier using non-zero values for m_{12} . Electroweak symmetry non-restoration at higher temperatures can constrain conventional models of electroweak baryogenesis since the non-restoration of the symmetry leads to the suppression of sphaleron transitions up to very high temperatures. However, the mechanism of electroweak baryogenesis using domain walls relies on the symmetry restoration (or on the partial symmetry restoration for intermediate values of $r_{1,2}$) only in the vicinity of the wall, where the sphaleron rate will be less suppressed than in the regions far from the wall and therefore EW symmetry non-restoration would not disfavour such a mechanism for baryogenesis.

The results of the scan are shown in Figure 5.5. The ratios $r_{1,2}$ inside the wall can achieve low values up to $r_{1,2} \approx 0.001$ but also very high values corresponding to a much higher VEV inside the wall. Notice that the requirement that the effective mass terms turn positive inside the wall is not enough to induce a total electroweak symmetry restoration inside the wall (even if the minimum of the potential is symmetric in that region). This is the case because the region in space with positive effective masses is not large enough for $v_{1,2}$ to converge to zero.

Due to the complexity of the model parameters, it is hard to obtain correlations between the physical variables of the model and the ratios r_1 and r_2 . For this particular scan of the

parameter points, we obtain some dependence between the values of the mixing angles α_2 , α_3 and the ratios r_1 and r_2 . As can be seen in Figure 5.5c, one can achieve both ratios being small only for positive α_2 , while for $\alpha_2 < 0$, the ratios are bigger than one. This happens because we obtain both negative λ_7 and λ_8 only when $\alpha_2 > 0$. Concerning the dependence on the singlet VEV v_s we find (see Figure 5.5b) that the smallest ratios $r_{1,2}$ are obtained for larger v_s .

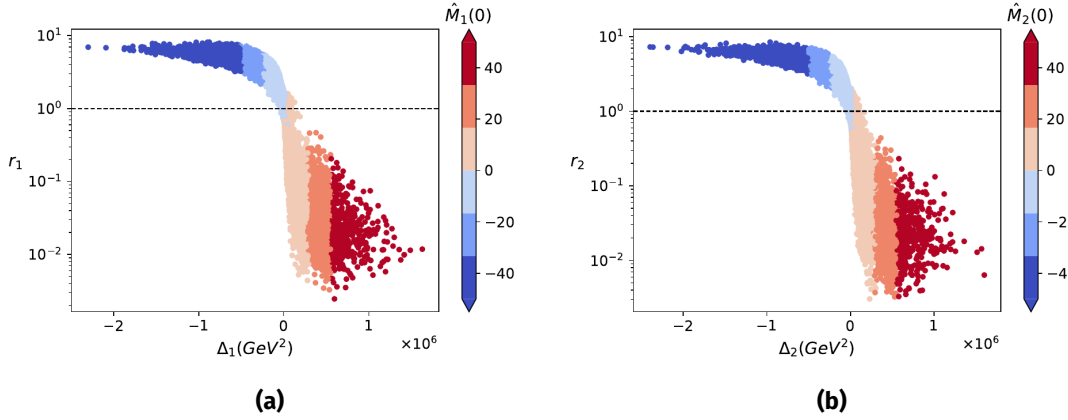


Figure 5.6: Correlations between the ratios $r_{1,2}$ and the difference in the effective mass inside and outside the wall $\Delta_{1,2}$.

In Figure 5.6, we verify the validity of our assumption concerning the correlations between the sign of $\Delta_{1,2}$ and the ratios $r_{1,2}$. The anticipated behavior that $r_{1,2} > 1$ for negative $\Delta_{1,2}$ and $r_{1,2} < 1$ for positive $\Delta_{1,2}$ holds for most of the parameter points. However, one can see that some parameter points can have ratios $r_{1,2} > 1$ even when $\Delta_{1,2} > 0$.

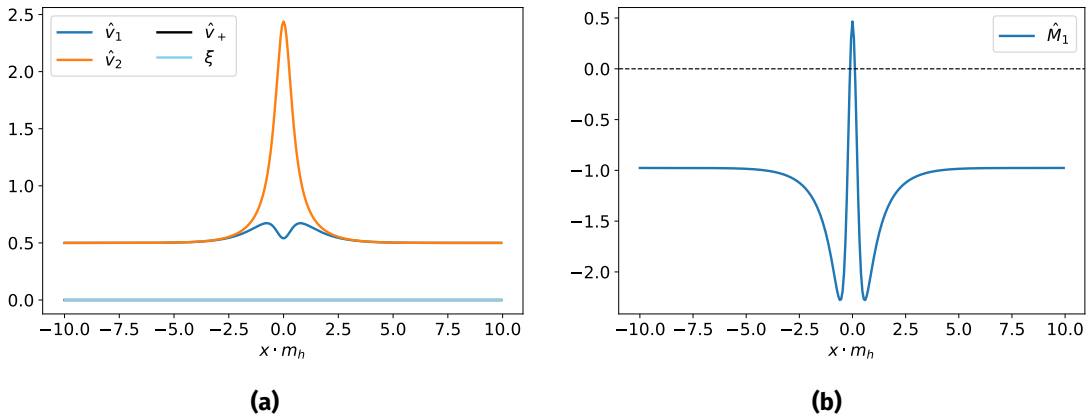


Figure 5.7: Anomalous behavior where a positive Δ_1 leads to $r_1 > 1$. (a) Electroweak field configuration for the parameter point P_3 (see Table 6.2). (b) Effective mass $\hat{M}_1(x)$ for the parameter point P_3 .

As an example for this anomalous behavior, consider the benchmark point P_3 (see Table 6.2). The domain wall solution for this parameter point is shown in Figure 5.7a. The profile of $v_1(x)$ initially grows as we approach the wall then gets a sharp drop near $x = 0$ with $v_1(0)$ still bigger than its value outside the wall leading to $r_1 > 1$. This behavior is explained by the profile of the effective mass (shown in Figure 5.7b). The effective mass M_1 is initially smaller (more negative) in the vicinity of the wall due to the term $\lambda_{345}v_2^2(x)$ in (5.26) being negative and sizable. This leads $v_1(x)$ to grow in that region. However, as we approach the core of the wall at $x = 0$, the large positive contribution from $\lambda_7v_s^2$ leads

the effective mass term to be bigger than its value outside the wall ($\Delta_1 > 0$). This sharp positive contribution is, however, only localized in a very small region around $x = 0$. It is therefore energetically more favorable for $v_1(x)$ to not decrease substantially in that small region and we end with $v_1(0) > v_1(\pm\infty)$. The same behavior can also happen for $r_2 > 1$ and $\Delta_2 > 0$. This scenario can occur for parameter points where λ_7 is negative, while λ_8 is positive and large, leading to $v_2(0)$ being large inside the wall which in turn leads to the contribution $\lambda_{345}v_2^2(x)$ inside the effective mass term M_1 to be sizable.

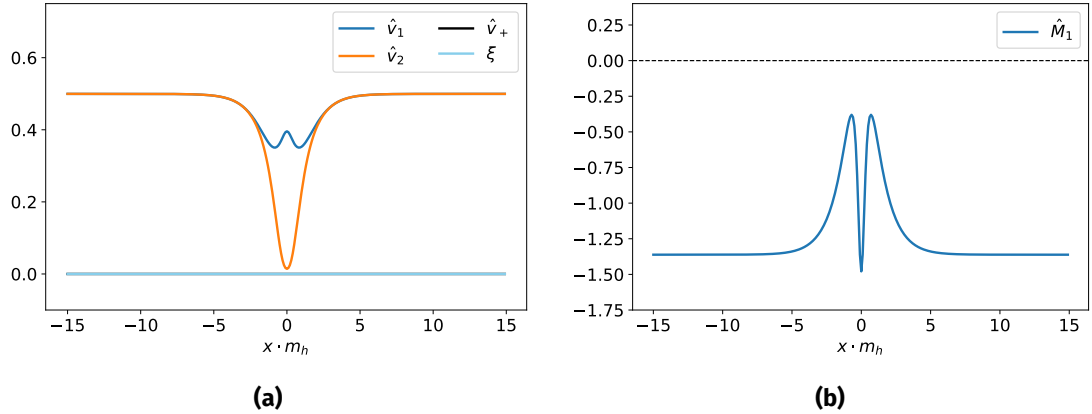


Figure 5.8: Anomalous behavior where a negative Δ_1 leads to $r_1 < 1$. (a) Electroweak vacuum configuration for the parameter point P_4 (see Table 6.2). (b) Effective mass $\hat{M}_1(x)$ for the parameter point P_4 .

We also find a few parameter points where r_1 is slightly smaller than 1 even for $\Delta_1 < 0$. As an example for this scenario, we take the benchmark point P_4 (see Table 6.2). The profile of the doublets is shown in Figure 5.8a, where we observe the opposite behavior of the previous anomalous scenario, namely that $v_1(x)$ initially decreases as we approach the wall and grows inside the core of the wall. This behavior is explained by the profile of the effective mass M_1 (see Figure 5.8b) which initially grows in the vicinity of the wall leading to smaller v_1 . However, due to λ_7 being positive, the effective mass obtains a sharp large negative contribution at $x = 0$ which makes $v_1(x)$ grow again inside the wall. This negative contribution is, however, only limited to a very small region in space which is not enough to make $v_1(0)$ grow higher than its asymptotic value. This scenario happens especially for parameter points where $\lambda_7 > 0$ while $\lambda_8 < 0$ and sizable, leading to v_2 being very small inside the wall and as a consequence, the term $\lambda_{345}v_2^2$ in (5.26) gives a large positive boost to M_1 (for $\lambda_{345} < 0$) in the vicinity of the wall.

5.2.2.2 Parameter scan with $m_{12}^2 \neq 0$

To see the effects of a non-zero m_{12}^2 term, we perform a parameter scan for 20000 points taking the same constraints used as in the previous scan (see Table 5.2) but with $0 < m_{12}^2 < 10^5 \text{ GeV}^2$. Notice that, in contrast to the previous case, even for positive values of the effective masses $M_{1,2}$ outside the wall, the potential can get a VEV due to the non-zero $-m_{12}^2\Phi_1\Phi_2$ -term that can lead to a dominant negative contribution to V_{N2HDM} . For this parameter scan, we impose the condition of symmetry restoration for both the Z_2' and the EW symmetry at high temperatures.

In contrast to the case with $m_{12}^2 = 0$, we do not observe the possibility of having one ratio r_i being very small while the other ratio r_j is big (see Figure 5.9a). Note that such

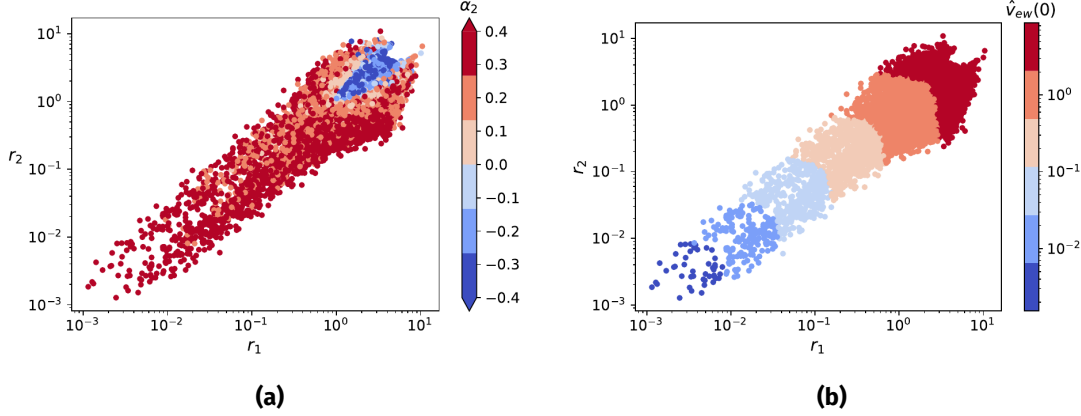


Figure 5.9: Results of the parameter scan for non-zero m_{12}^2 . It is possible to achieve smaller values for $r_{1,2}$ inside the wall compared to the previous parameter scan.

behavior in the previous case was obtained for parameter points that lead to one doublet field Φ_i having $M_i(0) > 0$ while $M_j(0) < 0$. Therefore, the potential inside the wall had its minimum at $(v_i = 0, v_j \neq 0)$. For the case $m_{12}^2 \neq 0$, and for parameter points where the two doublets have a different sign for their effective masses inside the wall, the term $-m_{12}^2 \Phi_1 \Phi_2$ shifts the minimum inside the wall to $(v_i \neq 0, v_j \neq 0)$ which reduces the difference between r_i and r_j .

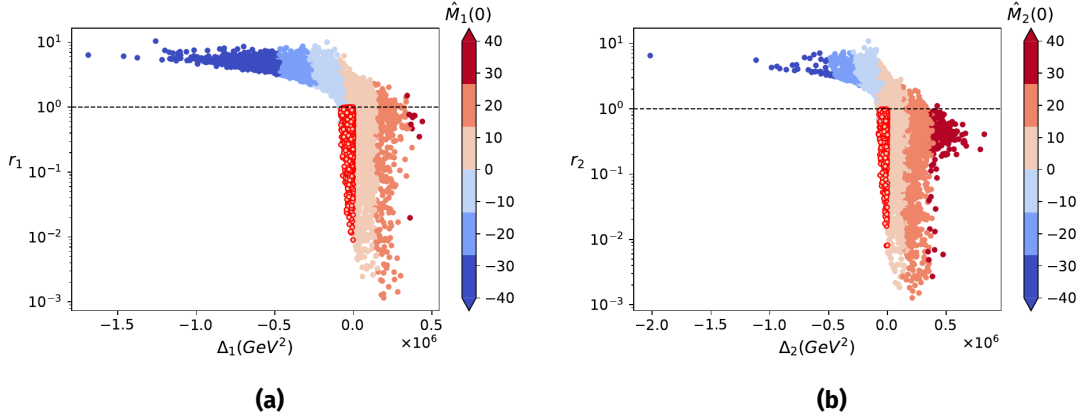


Figure 5.10: Correlations between the ratios $r_{1,2}$ and the difference in the effective mass inside and outside the wall $\Delta_{1,2}$ for the case when $m_{12} \neq 0$.

Another key difference is that we observe an anomaly for some parameter points satisfying $\Delta_{1,2} < 0$, but result in $r_{1,2} < 1$ (shown in bubbles with red edges in Figure 5.10). This happens for parameter points that have positive effective masses $M_{1,2}(x)$ everywhere in space and $\Delta_{1,2}$ being negative². For these parameter points, we found that the potential inside the domain wall can still have its minimum at $(v_1, v_2) = (0, 0)$ even if the effective mass terms get smaller (but are still positive). Therefore, the ratios $r_{1,2}$ will be small because the profile of $v_{1,2}(x)$ will converge to zero inside the wall. As an example for this scenario, we choose the benchmark point P_5 (see Table 6.2). The results for the profile of $v_{1,2}(x)$ and $M_1(x)$ are shown in Figure 5.11. For this parameter point, λ_8 is negative and M_2 grows substantially inside the wall. This leads the potential of the 2HDM in the direction v_2 to have its minimum at a small value near 0, making contributions from

² Recall that for the case $m_{12}^2 = 0$, such a scenario is not possible because the effective masses outside the wall are always negative.

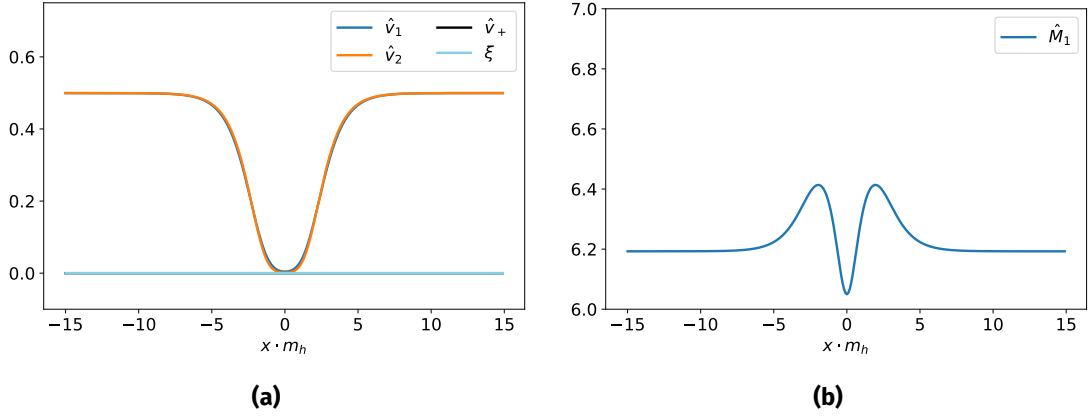


Figure 5.11: (a) Profiles of the doublet VEVs $v_{1,2}$ for parameter point P_5 . (b) Profile of the effective mass term M_1 for parameter point P_5 .

$-m_{12}v_1(0)v_2(0)$ vanishing or being small. For this parameter point, λ_7 is small and positive. Therefore $M_1(0)$ is smaller than outside the wall but stays positive. The minimum for v_1 inside the wall will then be 0, as the term $-m_{12}^2v_1v_2$ is negligible compared to the effective mass term M_1 .

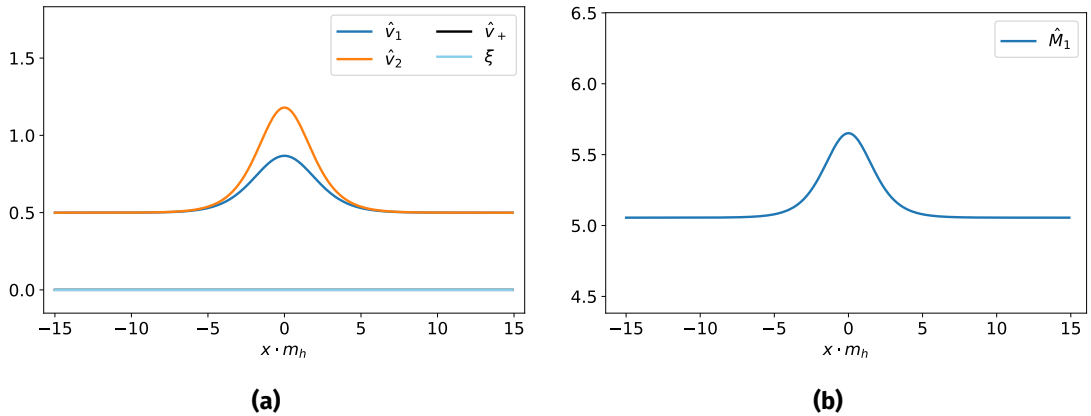


Figure 5.12: (a) Profiles of the doublet VEVs $v_{1,2}(x)$ for parameter point P_6 . (b) Profile of the effective mass term $M_1(x)$ for parameter point P_6 .

Even though we obtain mostly similar correlations between the ratios $r_{1,2}$ and the difference in the effective masses $\Delta_{1,2}$ for the case of $m_{12} \neq 0$, more parameter points can have $r_{1,2} > 1$ for $\Delta_{1,2} > 0$ (see Figure 5.10). This happens due to the minimum of the potential $V_{N2HDM}(v_1, v_2, 0)$ not being at the origin $(v_1, v_2) = (0, 0)$ but at a finite value for the VEVs and even for positive effective masses. This happens when contributions from the term $-m_{12}^2\Phi_1\Phi_2$ are substantial compared to the effective mass terms.

As an example of this behavior we take the benchmark parameter point P_6 (see Table 6.2). The profiles of $v_{1,2}(x)$ as well as $M_1(x)$ are shown in Figure 5.12. We find that $v_1(x)$ grows inside the wall even though the effective mass term $M_1(x)$ gets larger. For this parameter point, we obtain a large positive value for $\lambda_8 = 0.22$ compared to a negative $\lambda_7 = -0.04$. This has the effect that $M_2(x)$ sharply decreases inside the wall. This in turn "stretches" the 2HDM part of the potential in the v_2 direction, leading to a growing v_2 inside the wall. Because of the term $-m_{12}^2\Phi_1\Phi_2$, the minimum of the potential inside the wall in the direction of v_1 can be different than zero, even when the effective mass $M_1(0)$ is positive. Indeed, because $v_2(0)$ does not vanish inside the wall for this parameter point, a larger

non-zero $v_1(0)$ will minimize the potential since the overall contribution $-m_{12}^2 v_1(0)v_2(0)$ is negative.

5.2.2.3 Impact of the wall's width on the region of EWSR

One important consequence of electroweak symmetry restoration inside the wall is the enhancement of the sphaleron transitions compared to their rate in the region far from the wall. This can lead to the possibility of baryon number violating processes inside the wall that would be protected from being washed out once the wall moves away due to the sphaleron rate being highly suppressed in the broken phase. However, for such a mechanism to be efficient, the EW symmetry restoration region inside the wall should be large enough to fit a sphaleron. At high temperatures T , the radius of a sphaleron of the weak interactions is proportional to [66]:

$$R_{sph} \propto g^2 T^{-1},$$

where g denotes the coupling constant of $SU(2)_L$, while the sphaleron radius at $T = 0$ is on the order of the inverse of the W boson mass [159]. In this subsection, we discuss the dependence of the wall's width δ_s on the parameters of the model as well as how δ_s influences the size of the region where electroweak symmetry restoration of the Higgs doublets occurs.

In the case of a pure scalar singlet model with no interaction with other scalar fields (e.g. $\lambda_{7,8} = 0$), the width of the domain wall solution reduces to [13]:

$$\hat{\delta}_s = \left(\sqrt{\frac{\lambda_6}{4}} v_s \right)^{-1}. \quad (5.31)$$

Naively, one would expect that, for small values of λ_7 and λ_8 , the width of the singlet wall can be well approximated by (5.31), as the mixing between the singlet and the doublet would then be negligible. However, this is not correct in general, as the profiles of $v_1(x)$ and $v_2(x)$ can change considerably inside the wall for high values of v_s , which can lead to $\lambda_{7,8} \sim \mathcal{O}(10^{-4})$. Looking at the equation of motion governing the profile of $v_s(x)$:

$$\frac{\partial^2 v_s}{\partial x^2} = \frac{1}{2} \left(2m_S^2 + \lambda_7 v_1^2(x) + \lambda_8 v_2^2(x) \right) v_s(x) + \frac{\lambda_6}{4} v_s^3(x), \quad (5.32)$$

one then expects that a sizable change in the doublets contribution to the singlet effective mass $\lambda_7 v_1^2(x) + \lambda_8 v_2^2(x)$, which we define as:

$$\Sigma(x) = \lambda_7 (v_1^2(x) - v_1^2(\infty)) + \lambda_8 (v_2^2(x) - v_2^2(\infty)), \quad (5.33)$$

would lead to a considerable change in the width of the wall³. We verify this hypothesis using the parameter scan from the previous section (see Table 5.2). Figure 5.13a shows the numerical values of the wall's width δ_s^{num} compared with the width $\hat{\delta}_s$ obtained via (5.31) for each parameter point. The numerical value of the wall's width is obtained by calculating the full width at half the maximum of the field's profile.

Qualitatively, we find that parameter points with small $v_{ew}(0)$ and $\Sigma(0)$ lead to smaller ratios $r_\delta = \delta_s^{num}/\hat{\delta}_s$. In particular, we find that δ_s^{num} is well approximated by $\hat{\delta}_s$ for

³ A change in this quantity corresponds to the variation of the effective mass of the singlet field inside the wall. This will then lead to a change in the potential of the singlet inside the wall and therefore modify the path in field space that minimizes the energy of the field configuration.

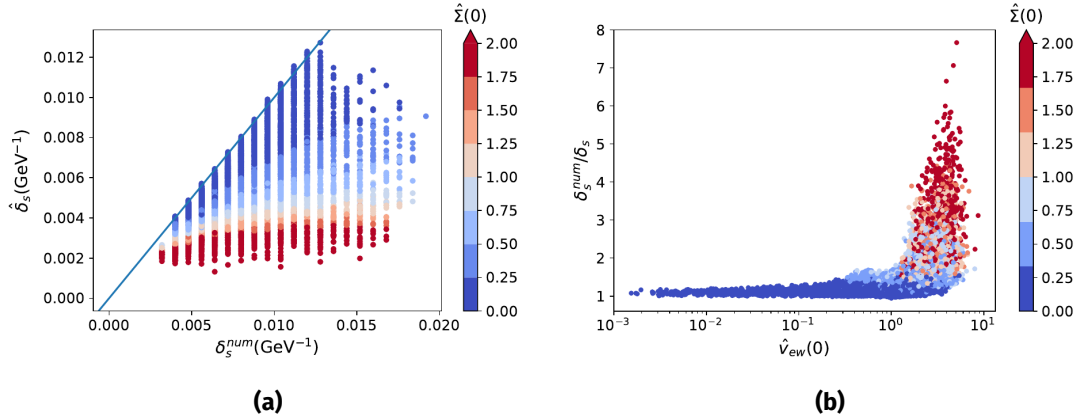


Figure 5.13: Correlations between the analytical formula for the domain wall width and the actual value calculated numerically for the parameter scan in Table 5.2 as a function of the normalized doublet vacuum expectation values inside the wall ($\hat{v}_{ew}(0)$) and the normalized quantity $\hat{\Sigma}(0)$. Note that a change in $\hat{\Sigma}(0)$ for fixed $\hat{v}_{ew}(0)$ corresponds to the variation of the couplings λ_7 and λ_8 . The blue line in (a) represents $\hat{\delta}_s = \delta_s^{num}$.

parameter points with very small $\Sigma(0)$. This is expected as the equation of motion for $v_s(x)$ (5.32) reduces to the pure singlet scalar equation of motion in the limit of vanishing $\Sigma(x)$. Some parameter points show a slightly smaller width than the analytical formula. This, however, is due to numerical precision and the result should be interpreted as 1 or slightly higher than 1. For high values of $v_{ew}(0)$ and $\Sigma(0)$, the calculated numerical width is much higher than δ_s . These general correlations can be intuitively understood by considering the change in the second derivative of $v_s(x)$ in (5.32). As the profiles of $v_{1,2}(x)$ change across the wall, the quantity $\Sigma(x)$ grows, decreasing $\frac{\partial^2 v_s}{\partial x^2}$ on the left side of the wall (where $v_s(x)$ is taken to have a negative sign). Therefore the kinetic energy of the solution gets smaller and the wall becomes thicker. Another intuitive way to look at this is interpreting the change in $\Sigma(x)$ as the change in the effective mass of the singlet. For all parameter points, $\Sigma(x)$ always grows in the vicinity of the wall. Therefore the effective mass of the singlet is higher, decreasing the barrier of the potential in the direction of the singlet field between the minima $-v_s$ and v_s . Consequently, the potential energy contribution to the domain wall solution gets smaller. According to the Bogomolnyi method for finding static kink solutions, the kinetic energy $(\frac{\partial \Phi_s}{\partial x})^2$ of the solution gets smaller and the wall gets thicker.

We now focus on the width of the region where the doublet scalar fields change their values, as this is a relevant quantity for electroweak baryogenesis mediated by domain walls. The change in the profile of $v_{1,2}(x)$ is related to the change in $v_s(x)$. Therefore, we expect that the width of the singlet domain wall influences the width of the region where $v_{1,2}(x)$ varies (which we define as δ_{ew}) and as such the width of electroweak symmetry restoration region for small values of $r_{1,2}$. Figure 5.14 shows the correlation between δ_{ew} , $v_{ew}(0)$ and δ_s^{num} . For parameter points where the EW VEV gets smaller inside the wall ($\hat{v}_{ew}(0) < 1$) we find that the width δ_{ew} can be much bigger than the width of the domain wall. We also find that the width δ_{ew} increases with decreasing $v_{ew}(0)$ and can be very sizable even for small δ_s^{num} .

For parameter points that have a higher EW VEV inside the wall ($\hat{v}_{ew}(0) > 1$), we also find that the width of the doublets increases with $\hat{\delta}_s^{num}$ as expected. Even though for this parameter scan one obtains higher values for δ_s^{num} when increasing $v_{ew}(0)$ (see Figure

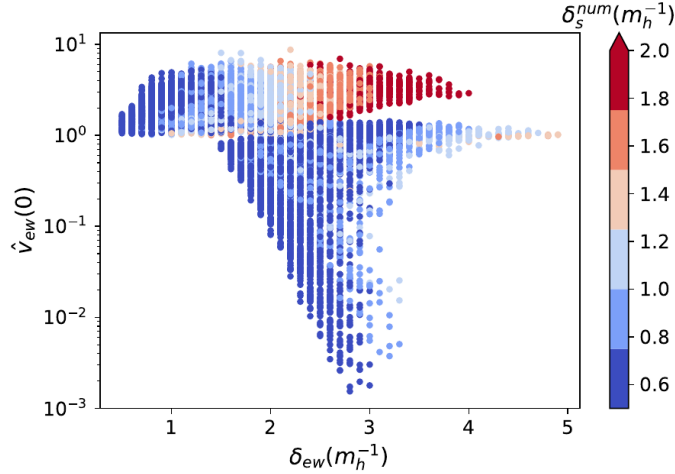


Figure 5.14: Correlations between δ_{ew} , the values of the electroweak vacuum inside the wall $v_{ew}(0)$ and the width of the singlet wall δ_s^{num} . We observe that δ_{ew} increases with smaller v_{ew} and larger δ_s^{num} .

5.13b), we observe that for a fixed value of δ_s^{num} and large $v_{ew}(0)$, the width δ_{ew} does not reach the high values observed for small values of $v_{ew}(0)$.

5.3 SCENARIOS WITH EWSR IN A LARGE REGION AROUND THE WALL

As we discussed in the last sections, the VEV ratios inside the wall are dependent on the change in the effective mass terms inside the wall. As we are mainly interested in electroweak symmetry restoration inside the domain wall, we shall focus in this section on some possible scenarios where $v_1(x)$ and $v_2(x)$ become small for a large region in the vicinity of the wall. We saw in the previous random parameter scans that the electroweak symmetry is not completely restored inside the wall. Instead, the electroweak VEV $v_{ew}(0)$ gets rather small values when the effective mass terms of the doublets grow higher (and positive) inside the wall, forcing the 2HDM part of the potential (the first two lines of (5.1)) to go into the symmetric phase. In order to make the profile of v_1 and v_2 vanish inside the wall, leading to complete electroweak symmetry restoration, we need the change in the effective masses $M_{1,2}$ to occur in a large region so that the doublet fields have enough space to converge to zero.

As was shown in the last section, parameter points leading to smaller $v_{ew}(0)$ typically have singlet wall widths δ_s^{num} that can be well approximated by (5.31) (see Figure 5.13b). As can be seen in Figure 5.14, for a fixed value of $v_{ew}(0)$ the width δ_{ew} increases with δ_s^{num} . Therefore, a larger region where the effective masses change is correlated with the quantity $\hat{\delta}_s = 2(\sqrt{\lambda_6}v_s)^{-1}$. Neglecting the contributions from λ_{345} , the change in the effective masses $M_{1,2}$ (see (5.30)) is proportional to $-\lambda_{7,8}v_s^2$. One can then define the ratios $B_{1,2} = \lambda_{7,8}/\lambda_6 \propto (\Delta_{1,2} \times (\hat{\delta}_s)^2)$ as dimensionless measures that provide a good correlation with parameter points leading to EWSR in a large region around the wall. This is the case namely when these ratios are big and negative. Therefore, one has to look for parameter points that lead to large values of $B_{1,2}$ with negative $\lambda_{7,8}$ (so that $\Delta_{1,2}$ are positive, leading to higher effective masses inside the wall).

Using the expressions (2.49) and (2.50) for λ_7 and λ_8 in the physical mass basis of the N2HDM, we can write $B_{1,2}$ as:

$$B_1 = \left(\frac{v_s}{v_1} \right) \left(\frac{R_{13}R_{11}m_{h_1}^2 + R_{23}R_{21}m_{h_2}^2 + R_{33}R_{31}m_{h_3}^2}{m_{h_1}^2 R_{13}^2 + m_{h_2}^2 R_{23}^2 + m_{h_3}^2 R_{33}^2} \right), \quad (5.34)$$

$$B_2 = \left(\frac{v_s}{v_2} \right) \left(\frac{R_{13}R_{12}m_{h_1}^2 + R_{23}R_{22}m_{h_2}^2 + R_{33}R_{32}m_{h_3}^2}{m_{h_1}^2 R_{13}^2 + m_{h_2}^2 R_{23}^2 + m_{h_3}^2 R_{33}^2} \right). \quad (5.35)$$

Therefore, finding parameter points with large negative values for $B_{1,2}$ involves a rather complex interplay between the masses of the CP-even Higgs scalars and the components of the diagonalization matrix R_{ij} , which are functions of the mixing angles $\alpha_{1,2,3}$.

In the following subsections, we discuss different scenarios for obtaining EWSR inside the wall. We generate parameter points using `ScannerS` satisfying all experimental and theoretical constraints discussed in the previous chapter. We also require that all parameter points restore the Z'_2 symmetry in the early universe to ensure the formation of the domain walls. Furthermore, for these sets of scenarios, we also require that the parameter points satisfy collider constraints (unless mentioned otherwise). This is done by using `HiggsBounds` [160, 161, 162, 163, 164, 124] and `HiggsSignals` [165, 125] implemented in `ScannerS`.

5.3.1 Scenario 1: Small CP-even Higgs masses

m_{h_a}	m_{h_b}	m_{h_c}	m_A	m_{H^\pm}	$\tan\beta$
125.09	[94, 98]	[200, 300]	[630, 750]	[650, 750]	[0.6, 10]
$C_{h_a t\bar{t}}^2$	$C_{h_a VV}^2$	R_{b3}	m_{12}^2	v_S	<i>type</i>
[0.6, 1.2]	[0.6, 1]	[-1, 1]	$[2 \times 10^4, 1.8 \times 10^5]$	[100, 10000]	1 – 4

Table 5.3: Set of input parameters for `ScannerS` scan of scenario 1. The masses and vacuum expectation values are given in GeV , while m_{12}^2 is given in GeV^2 . $C_{h_a t\bar{t}}$ and $C_{h_a VV}$ are defined respectively as the coupling factors of the CP-even Higgs boson h_a to the SM gauge bosons and the top quark and are defined as $C_{h_a VV} = \cos(\beta)R_{a1} + \sin(\beta)R_{a2}$ and $C_{h_a t\bar{t}} = R_{a2}/\sin(\beta)$ (see Table 2.2, and for more details [117]). For these parameter points the Z'_2 is unbroken at very high temperatures.

The simplest way to get large values for the ratios $B_{1,2}$ is to use parameter points with large v_s . The second factor in (5.34) and (5.35) are complicated functions of the masses and mixing angles (that enter into R_{ij}) between the CP-even Higgs scalars and, as such, we expect some interplay between the values of the masses and mixing angles that lead to large $B_{1,2}$. For this first scenario, we focus on parameter points with small masses for the CP-even Higgs particles with one scalar fixed to be the SM-like Higgs with mass $m_{h_2} = 125.09$ GeV. The lightest CP-even scalar is taken to be one with a mass in the vicinity of 95 GeV depicting a particle in the same mass range of some recent excesses observed in ATLAS [166] and CMS [167]. We vary the singlet VEV v_s between 100 GeV and 10 TeV as well as the mixing angles between the 3 CP-even Higgs states (see Table 5.3). The generated parameter points⁴ satisfying the theoretical and experimental constraints

⁴ Note that collider searches heavily constrain this particular scenario and therefore we start our discussion using a set of parameter points where these constraints were neglected. We later show the results for a parameter scan of 5000 points, where the collider constraints were considered.

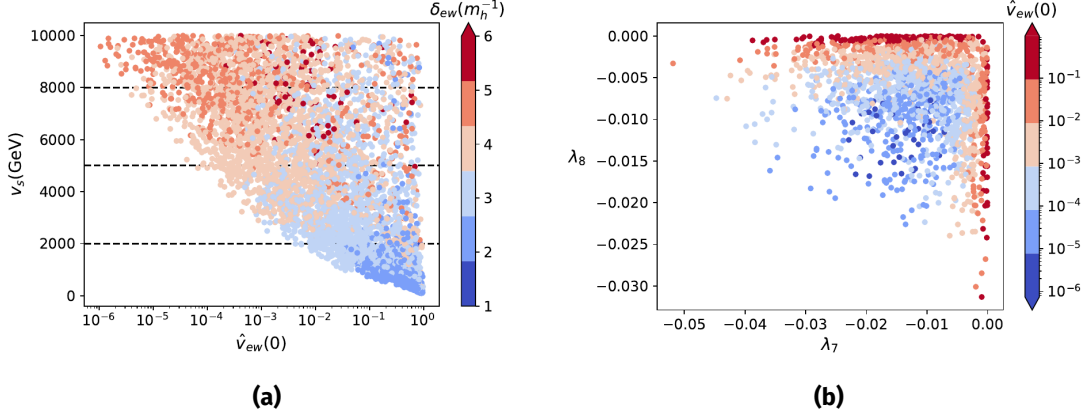


Figure 5.15: Results of the parameter scan for scenario 1. (a) The amount of EWSR inside the domain wall $\hat{v}_{ew}(0)$ as a function of the singlet VEV v_s and the width δ_{ew} of the symmetry restoration region $v_{ew}(x)$ around the wall. (b) The amount of EWSR inside the wall as a function of the couplings λ_7 and λ_8 for parameter points with $v_s > 6000$ GeV.

discussed in earlier chapters as well as the requirement of Z'_2 symmetry restoration is in the range shown in Table 5.3.

We start with a parameter scan where we do not require collider constraints in the parameter points search done by `ScannerS`. We later show the effects of these constraints by using a parameter scan where these constraints are imposed. This is done for pedagogical reasons in order to discuss how collider constraints affect the results.

The results of the scan in terms of the effective EW VEV inside the wall $v_{ew}(0)$ as a function of v_s and the width δ_{ew} are shown in Figure 5.15a. We find that for the lower range of $v_s < 2000$ GeV, the EW symmetry restoration measure $\hat{v}_{ew}(0)$ is at least above 0.01. We also find that for several parameter points with large $v_s > 6$ TeV, the doublet VEVs inside the wall are not suppressed. These parameter points correspond to the red and orange points in Figure 5.15b where one of the couplings between the singlet and doublet scalar fields λ_7 or λ_8 is small compared to the other one. This leads to one of the doublets having its VEV highly suppressed inside the wall, while the other doublet is only slightly affected by the domain wall, leading to an overall effect where $\hat{v}_{ew}(0)$ is slightly smaller than 1.

Concerning the width δ_{ew} , the observed indirect dependence on v_s is due to the change in $\hat{v}_{ew}(0)$ which decreases with higher v_s and leads to higher values for δ_{ew} . For the chosen interval in the masses of the CP-even Higgses (see Table 5.3), we verified that the width of the singlet wall δ_s^{num} is independent of v_s .

We now discuss the effects of the mixing angles α_i on the results. In order to do this, we look at the singlet admixture Σ_i of the CP-even Higgs states h_i defined as:

$$\Sigma_1 = R_{13}^2, \quad \Sigma_2 = R_{23}^2, \quad \Sigma_3 = R_{33}^2, \quad (5.36)$$

where R_{ij} corresponds to the entries of the diagonalizing matrix R defined in (2.41) and are functions of the mixing angles α_i . The correlations between Σ_i and the parameters $v_{ew}(0)$ and δ_{ew} are shown in Figure 5.16. We find that the smallest values for $v_{ew}(0)$ are obtained when the singlet admixture in the SM Higgs scalar h_2 is the highest. Such a correlation puts constraints on this parameter region, as a large singlet admixture in the SM Higgs scalar is not allowed experimentally.

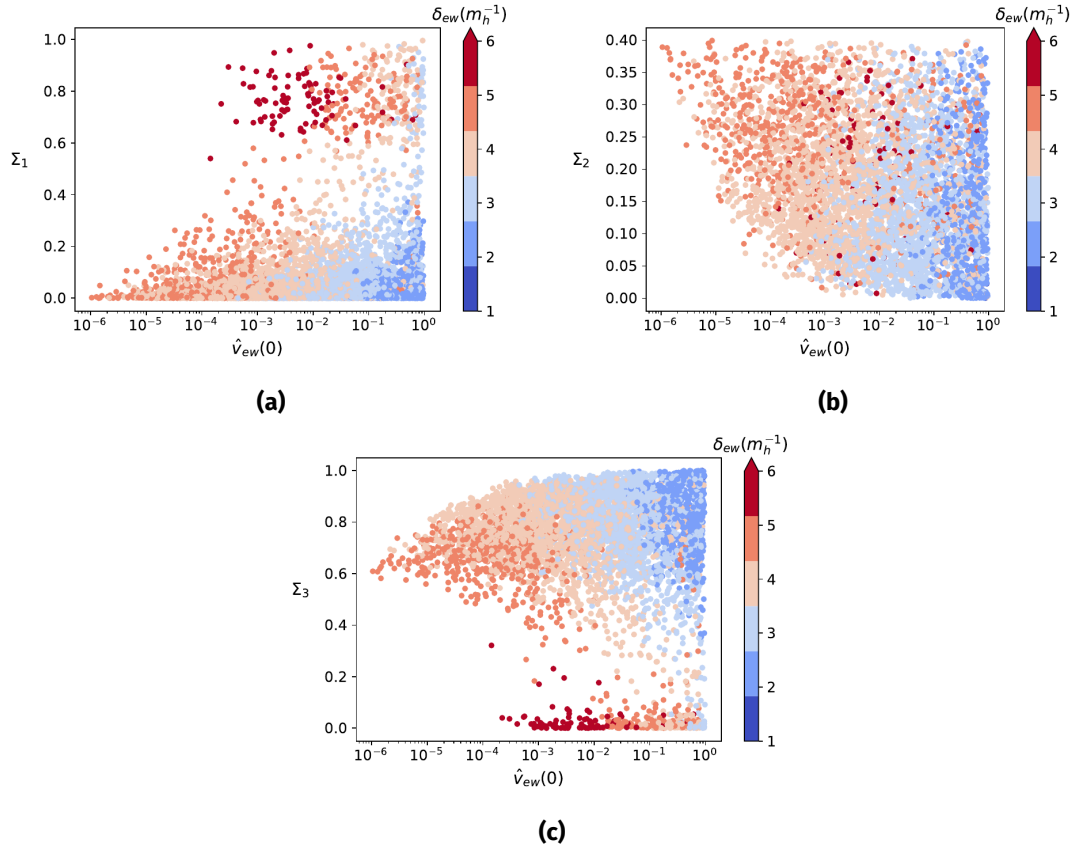


Figure 5.16: Singlet admixture Σ_i of the CP-even Higgs states h_i in the physical mass basis. For this particular parameter scan, Σ_2 corresponds to the singlet admixture in the SM Higgs state h_2 with mass $m_{h_2} = 125.09$ GeV, while Σ_1 corresponds to the singlet admixture of the CP-even Higgs boson with mass around 95 GeV.

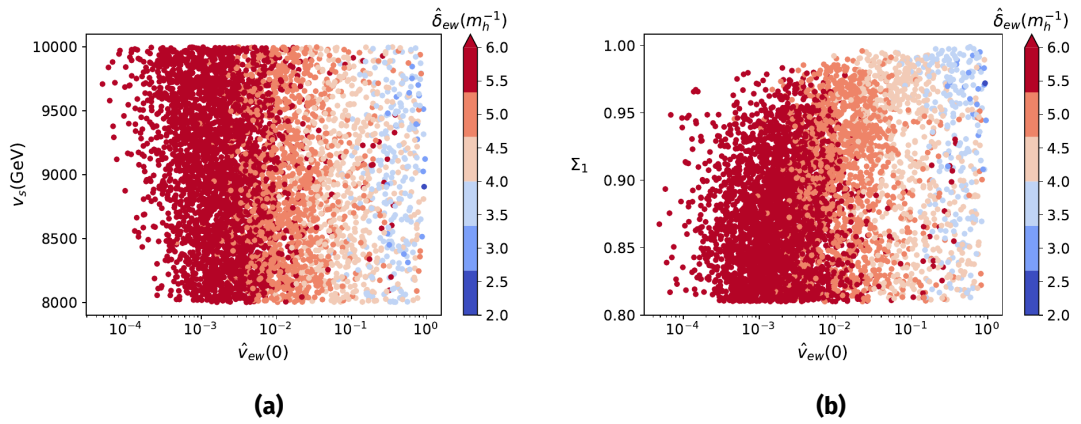


Figure 5.17: EW VEV inside the wall $v_{ew}(0)$ and the EW width δ_{ew} for the parameter scan where the singlet admixture of the lightest Higgs boson in scenario 1 is close to 1, while the singlet admixture of the SM Higgs boson is small, (a) dependent on v_s and (b) dependent on Σ_1 .

We also perform a parameter scan for 5000 points where the singlet admixture is dominant in the lightest Higgs scalar ($94 \text{ GeV} < m_{h_1} < 98 \text{ GeV}$) while it is negligible in the SM Higgs. We choose v_s to vary between 8 TeV and 10 TeV in order to get larger negative values for $B_{1,2}$ and therefore obtain parameter points that are more favorable to lead

to EWSR inside the wall. The results are shown in Figure 5.17. We find that, for this parameter scan, $v_{ew}(0)$ is lower than the values it can reach when the singlet admixture in the SM-like Higgs boson Σ_2 is higher. We therefore conclude that a larger effect of EWSR inside the wall correlates with parameter points that have higher singlet admixture Σ_2 in the SM-like Higgs boson. Such a scenario is, however, strongly constrained by collider results as we discuss next.

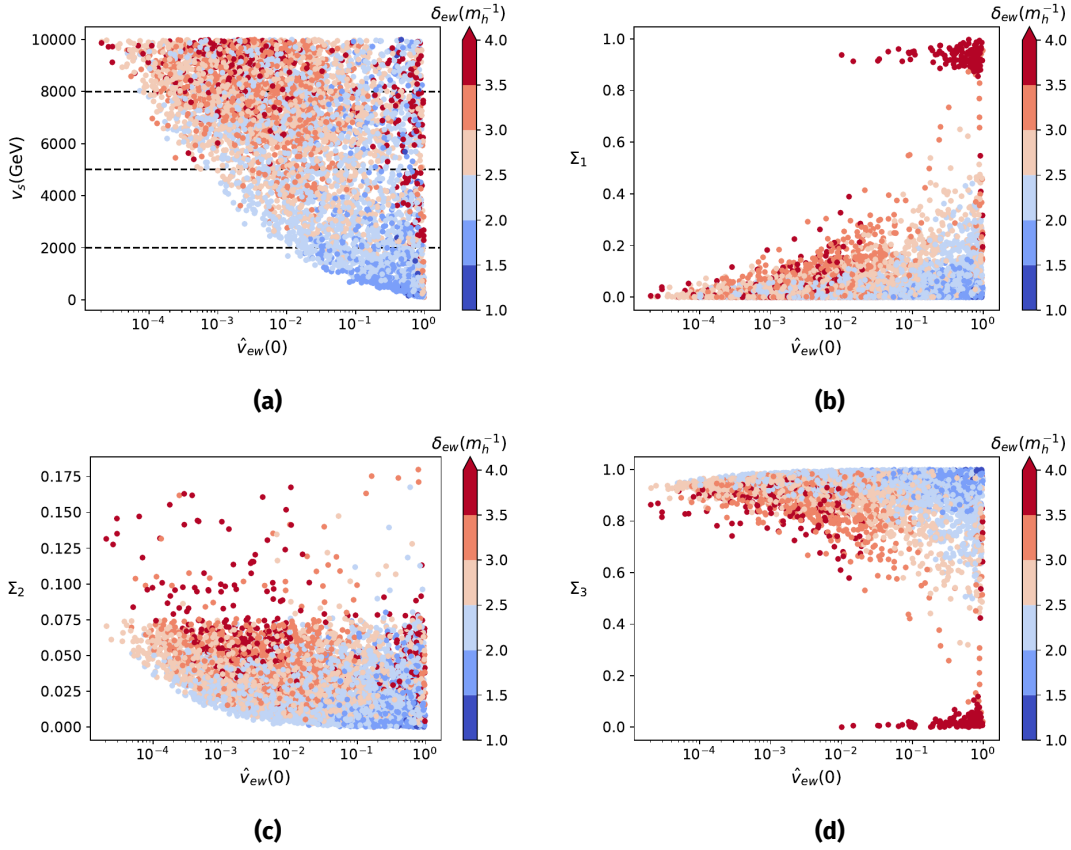


Figure 5.18: Results of the parameter scan satisfying all theoretical and experimental constraints including collider searches: (a) $\hat{v}_{ew}(0)$ as a function of v_s and the electroweak width; (b), (c) and (d) $\hat{v}_{ew}(0)$ as a function of the singlet admixtures in the CP-even Higgs bosons Σ_1 , Σ_2 and Σ_3 respectively. We find that collider constraints impose that the singlet admixture in the SM Higgs boson should be rather small, which leads to higher values for $\hat{v}_{ew}(0)$ than in the previous scan.

To demonstrate how collider constraints affect the results, we use `ScannerS` to generate a set of parameter points in the same range as the one shown in Table 5.3, but where also collider constraints are imposed. The results are shown in Figure 5.18. We find that imposing collider constraints reduces the maximum singlet admixture Σ_2 in the SM-like Higgs boson to values lower than 20%, which in turn increases the minimal values obtained for $v_{ew}(0)$ by approximately one order of magnitude. For most parameter points of this scan, we find that the heaviest CP-even Higgs boson is allowed to have the highest singlet admixture Σ_3 (see Figure 5.18d). For parameter points where the singlet admixture in the lightest CP-even Higgs boson with a mass around 95 GeV is close to one $\Sigma_1 \approx 1$ (see Figure 5.18b), we find that $v_{ew}(0)$ is large and therefore such a case will not yield electroweak symmetry restoration⁵.

⁵ Note that the values for v_s for the parameter points where $\Sigma_1 \approx 1$ varied between 100 GeV and 10 TeV. Therefore, the obtained high values for $v_{ew}(0)$ cannot be explained by a small v_s .

5.3.2 Scenario 2: Intermediate CP-even masses

m_{h_a}	m_{h_b}	m_{h_c}	m_A	m_{H^\pm}	$\tan\beta$
125.09	[300, 700]	[400, 700]	[500, 900]	[650, 900]	[0.5, 8]
$C_{h_a t\bar{t}}^2$	$C_{h_a VV}^2$	R_{b3}	m_{12}^2	v_s	$type$
[0.6, 1.2]	[0.6, 1]	[-1, 1]	$[2 \times 10^4, 2.2 \times 10^5]$	[100, 10000]	1 – 4

Table 5.4: Set of input parameters for ScannerS scan for scenario 2. The masses and vacuum expectation values are given in GeV , while m_{12}^2 is given in GeV^2 . $C_{h_a t\bar{t}}$ and $C_{h_a VV}$ are defined respectively as the coupling factors of the CP-even Higgs boson h_a to the SM gauge bosons and the top quark and are defined as $C_{h_a VV} = \cos(\beta)R_{a1} + \sin(\beta)R_{a2}$ and $C_{h_a t\bar{t}} = R_{a2}/\sin(\beta)$ (see Table 2.2, and for more details [117]).

In this case, we consider the scenario where the masses of the extra CP-even Higgs Bosons m_{h_2} and m_{h_3} are in the range $300 \text{ GeV} < m_{h_2} < 700 \text{ GeV}$ and $400 \text{ GeV} < m_{h_3} < 700 \text{ GeV}$, while m_{h_1} corresponds to the SM-like Higgs boson. For the singlet VEV v_s , the 15000 generated parameter points are again chosen in the range $100 \text{ GeV} < v_s < 10 \text{ TeV}$. All parameter points in this scan also satisfy collider constraints.

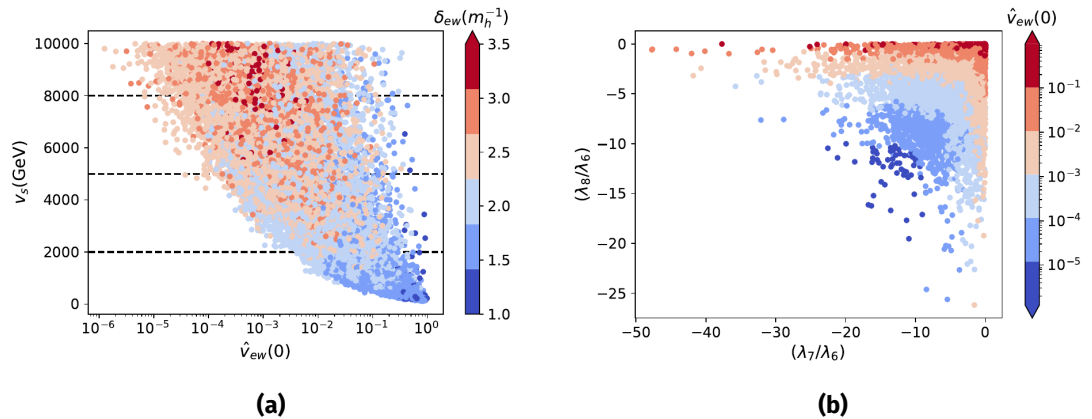


Figure 5.19: Results of the parameter scan for scenario 2. (a) The amount of EWSR inside the domain wall $\hat{v}_{ew}(0)$ as a function of the singlet VEV v_s and the width δ_{ew} of the symmetry restoration region $v_{ew}(x)$ around the wall. (b) The amount of EWSR inside the wall as a function of the couplings ratios (λ_7/λ_6) and (λ_8/λ_6) .

The results of this parameter scan are shown in Figure 5.19a. We find that fewer parameter points are leading to large values of $\hat{v}_{ew}(0)$ for large v_s compared to scenario 1 (see Figure 5.18a). We also find that δ_{ew} is overall smaller in this scenario. This is due to δ_s^{num} being smaller for higher masses $m_{h_{2,3}}$.

We show in Figure 5.19b the dependence of the EWSR measure $\hat{v}_{ew}(0)$ on the ratios $\lambda_{7,8}/\lambda_6$. In this case, we observe that the electroweak VEV inside the wall $\hat{v}_{ew}(0)$ decreases as the absolute value of these ratios increases. Again, this is interpreted as a larger change in the effective mass term alongside the wall occurring in a larger region in space. Therefore, the profiles of the doublet Higgs fields have enough space to reach their minimal values inside the wall. The correlations between the singlet admixtures Σ_i in Eq. (5.36) and the measures $v_{ew}(0)$ and δ_{ew} are similar to the previous scenario. We find that EWSR is preferred for a larger singlet admixture in the SM Higgs boson as can be seen in Figure 5.20. Note that the collider constraints are fulfilled in the whole range of parameter points.

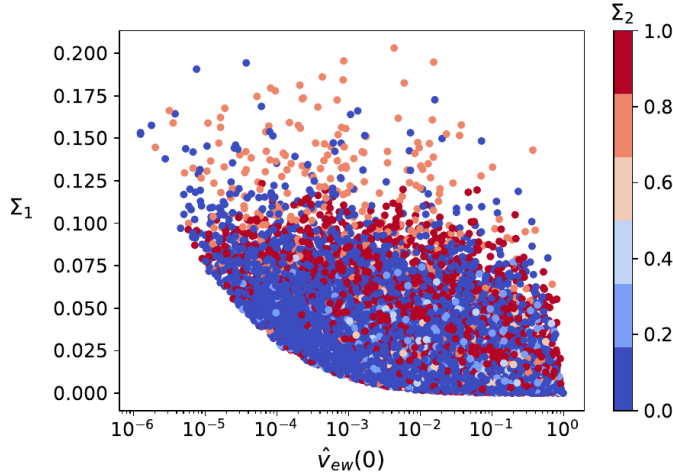


Figure 5.20: Electroweak symmetry restoration measure $\hat{v}_{ew}(0)$ as a function of the singlet admixture in the CP-even Higgs bosons for scenario 2. In this case, the SM Higgs boson is the lightest particle. We find, similar to the previous case, that the smallest $\hat{v}_{ew}(0)$ correlates with higher singlet admixture in the SM Higgs boson state.

5.3.3 Scenario 3: Heavy CP-even Higgs masses

In this scenario, we investigate the case where the extra CP-even Higgs bosons can be

m_{h_a}	m_{h_b}	m_{h_c}	m_A	m_{H^\pm}	$\tan\beta$
125.09	[700, 1200]	[700, 3000]	[500, 1000]	[650, 1200]	[0.5, 10]
$C_{h_a t\bar{t}}^2$	$C_{h_a VV}^2$	R_{b3}	m_{12}^2	v_s	type
[0.6, 1.2]	[0.6, 1]	[-1, 1]	$[5 \times 10^4, 5 \times 10^5]$	[100, 10000]	1 – 4

Table 5.5: Set of input parameters for ScannerS scan of scenario 3. The masses and vacuum expectation values are given in GeV , while m_{12}^2 is given in GeV^2 . $C_{h_a t\bar{t}}$ and $C_{h_a VV}$ are defined respectively as the coupling factors of the CP-even Higgs boson h_a to the SM gauge bosons and the top quark and are defined as $C_{h_a VV} = \cos(\beta)R_{a1} + \sin(\beta)R_{a2}$ and $C_{h_a t\bar{t}} = R_{a2}/\sin(\beta)$ (see Table 2.2, and for more details [117]).

very heavy. We fix the SM Higgs to be $m_{h_1} = 125.09$ GeV and vary the heavier masses $700 \text{ GeV} < m_{h_2} < 3000 \text{ GeV}$ and $700 \text{ GeV} < m_{h_3} < 3000 \text{ GeV}$. The value for the singlet VEV v_s varies again between 100 GeV and 10 TeV. The other parameter ranges are shown in Table 5.5.

The results for the electroweak VEV inside the wall (see Figure 5.21a) are overall similar to the previous case, i.e. smaller $v_{ew}(0)$ inside the wall correlate with a higher singlet VEV v_s . The major difference can be seen in the decrease in the value of the width δ_{ew} due to the increase in the masses of the CP-even Higgses leading to smaller δ_s^{num} and therefore, to an overall smaller δ_{ew} . We do not find a correlation between the values of the masses and the electroweak symmetry restoration measure $\hat{v}_{ew}(0)$ (see Figure 5.22a). The correlations are, however, dependent on the mixing angles and therefore the singlet admixtures Σ_i . These correlations are shown in Figure 5.22b, where the smallest values for $\hat{v}_{ew}(0)$ are obtained, again, for a higher singlet admixture Σ_1 in the SM-like Higgs boson state.

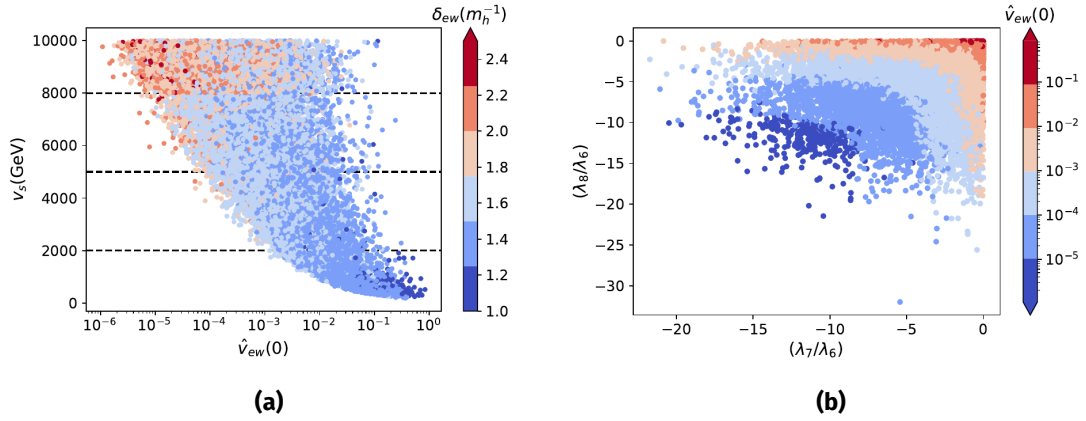


Figure 5.21: Results of the parameter scan for scenario 3. (a) The amount of EWSR inside the domain wall $\hat{v}_{ew}(0)$ as a function of the singlet VEV v_s and the width δ_{ew} of the symmetry restoration region $v_{ew}(x)$ around the wall. We find that this scenario leads to smaller minimal values for $v_{ew}(0)$ than the previous scenario. (b) The amount of EWSR inside the wall as a function of the ratios (λ_7/λ_6) and (λ_8/λ_6) . We find that the lowest values for $v_{ew}(0)$ are obtained when both ratios are large and negative.

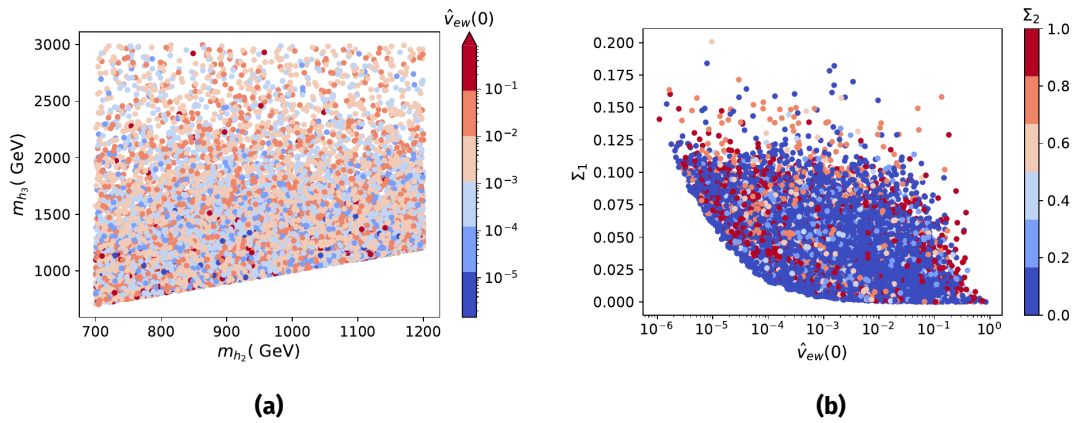


Figure 5.22: Results of parameter scan for scenario 3. (a) The amount of EWSR inside the domain wall $\hat{v}_{ew}(0)$ as a function of the masses m_{h_2} and m_{h_3} (b) The amount of EWSR inside the wall as a function of the singlet admixtures Σ_1 related to the SM-like Higgs boson h_1 and Σ_2 related to h_2 .

Concerning the width δ_{ew} , we plot the results that we get for different ranges of v_s as shown in Figure 5.23. We find that δ_{ew} is mostly independent of the range of v_s . The width is, however, largely dependent on the mass m_{h_3} and we obtain the largest values of δ_{ew} for smaller m_{h_3} .

As a summary of these three scenarios, we found that the singlet vev v_s is the most important parameter in determining the lowest values for the electroweak symmetry restoration measure $\hat{v}_{ew}(0)$ and that higher v_s leads to smaller $\hat{v}_{ew}(0)$. We found that the masses of the CP-even Higgs bosons influence the width δ_{ew} and that smaller masses lead, overall, to a higher δ_{ew} . The singlet admixture in the CP-even Higgs states also plays a major role: a higher singlet admixture in the SM Higgs boson leads to smaller values for $\hat{v}_{ew}(0)$. This correlation obviously puts rather strong experimental constraints on the feasibility of inducing electroweak symmetry restoration inside the singlet domain wall in the N2HDM.

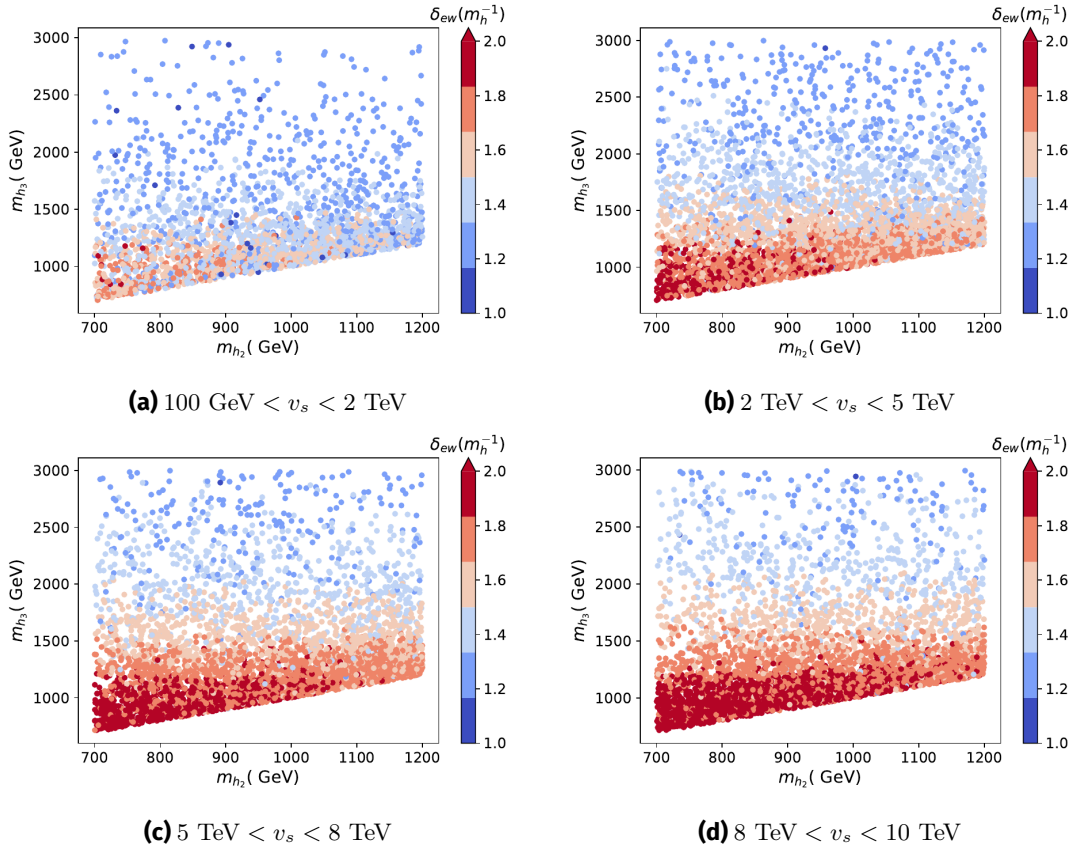


Figure 5.23: Width δ_{ew} of the Higgs doublet variation inside the wall for different ranges of v_s . We find that the behavior of δ_{ew} is independent of the range of v_s and is mostly determined by the mass of m_{h_3} .

5.3.4 Scans with fixed v_s

v_s (GeV)	m_{h_a} (GeV)	m_{h_b} (GeV)	m_{h_c} (GeV)	$\tan\beta$	m_{12}^2 (GeV ²)
800	125.09	200 – 1500	200 – 2000	0.5 – 10	0 – 10^6
2500	125.09	200 – 1500	200 – 2000	0.5 – 8	0 – 10^6
6000	125.09	200 – 1500	200 – 2000	0.5 – 7	0 – 10^6

Table 5.6: Range of the parameter points generated by Scanners for the different scenarios. For the variables $C_{h_a t\bar{t}}^2$, $C_{h_a VV}^2$ and R_{b3} relevant for determining the mixing angles, we use the same range as in the previous scans in Tables 5.3, 5.4 and 5.5.

In contrast to the previous scenarios where the singlet VEV v_s was the primary variable determining the amount of EWSR inside the wall for different mass hierarchies, we focus here on the effects of varying the CP-even Higgs masses h_2 and h_3 as well as their mixing angles while fixing v_s and the mass of h_1 to be the SM-like Higgs boson $m_{h_1} = 125.09$ GeV (see Table 5.6).

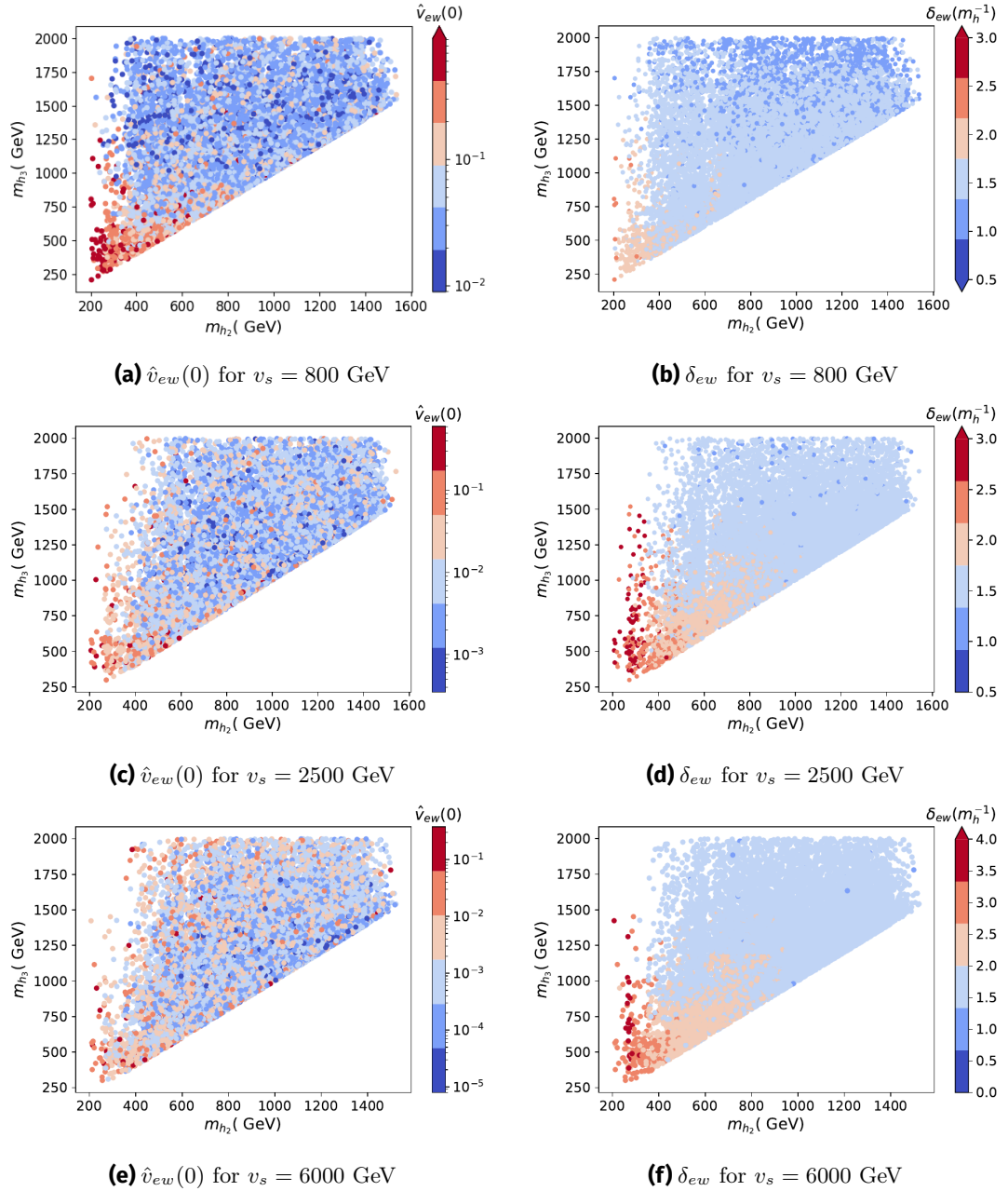


Figure 5.24: $\hat{v}_{ew}(0)$ and δ_{ew} for different fixed values for v_s (800, 2500 and 6000 GeV) as a function of the masses m_{h_2} and m_{h_3} and varying mixing angles. For all these scenarios, the SM-like Higgs boson h_1 has the mass $m_{h_1} = 125.09$ GeV. The generated parameter points satisfy all theoretical and experimental constraints, including collider constraints.

We show the results of the scans for different values of v_s (800, 2500 and 6000 GeV) in Figure 5.24. In terms of $\hat{v}_{ew}(0)$ and for the three different values of v_s , we observe that smaller $\hat{v}_{ew}(0)$ are obtained for mostly big and intermediate values of the masses m_{h_2} and m_{h_3} . However, those ranges of masses do not guarantee the possibility of having EWSR inside the wall, as they can also lead to high values for $\hat{v}_{ew}(0)$. We observe a large dependence of the minimal obtained values for \hat{v}_{ew} on v_s . As for the width δ_{ew} , we find a strong correlation between the masses and δ_{ew} . We observe that smaller masses lead, in general, to larger values as can be seen in Figures 5.24b, 5.24d, 5.24f. These results are in good agreement with the general behavior found in the previous scans of scenarios 1, 2, and 3.

For the case when $v_s = 800$ GeV, we obtain larger values for $\hat{v}_{ew}(0)$ compared to the scenarios with higher v_s . This is because the generated parameter points for low v_s (satisfying all theoretical and experimental constraints) lead mostly to small values for $\lambda_{7,8}/\lambda_6$. In order to further study this scenario of low v_s , we look for parameter points where the chosen masses and mixing angles lead to large negative $\lambda_{7,8}/\lambda_6$. We generated parameter points where we impose a limit on $\lambda_{7,8}/\lambda_6 < -8$ to obtain rather small $v_{ew}(0)$. We found that most parameter points of this scan have a large singlet admixture Σ_1 in the SM Higgs boson state $m_{h_1} = 125.09$ GeV. However, this set of parameter points is experimentally ruled out and is even incompatible with the constraint of perturbative unitarity. We therefore can conclude that, at zero or low temperatures, achieving electroweak symmetry restoration using domain walls with rather low v_s is ruled out.

5.4 DIFFERENT GOLDSTONE MODES AND CP-VIOLATION IN THE VICINITY OF THE WALL

Until now we focused on the trivial case when the vacua for the Higgs doublets have the same Goldstone modes in both domains. In a realistic electroweak phase transition, however, one expects causally disconnected domains of the universe to end up in vacua with different values for the Goldstone modes (2.34) given that they lead to degenerate minima of the potential. Recall that the VEVs of the Higgs doublets can be written in the general form (2.34):

$$\langle \Phi_1 \rangle = U \langle \tilde{\Phi}_1 \rangle = U \frac{1}{\sqrt{2}} \begin{pmatrix} 0 \\ v_1 \end{pmatrix}, \quad \langle \Phi_2 \rangle = U \langle \tilde{\Phi}_2 \rangle = U \frac{1}{\sqrt{2}} \begin{pmatrix} v_+ \\ v_2 e^{i\xi} \end{pmatrix}, \quad U = e^{i\theta} \exp\left(i \frac{\tilde{g}_i \sigma_i}{2v_{sm}}\right), \quad (5.37)$$

where U is an element of the $SU(2)_L \times U(1)_Y$ symmetry group. The possibility of having different Goldstone modes (θ, \tilde{g}_i) on different domains was found to have profound consequences on the solutions related to the Z_2 -symmetry domain walls in the 2HDM [76, 75, 1]. In general, one obtains several classes of domain wall solutions with different properties such as CP-violating or electric charge-breaking condensates localized inside or in the vicinity of the wall.

We now study these effects in the N2HDM. We consider two different cases of electroweak symmetry breaking. The first case is the breaking of the electroweak symmetry at the same time as the breaking of Z'_2 . This is a one-step phase transition according to:

$$(0, 0, 0) \rightarrow (v_1, v_2, \pm v_s).$$

In such a case the two domains related by the Z'_2 symmetry will also have different Goldstone modes. The second case is when the electroweak and the Z'_2 symmetries are broken at different times:

$$(0, 0, 0) \rightarrow (0, 0, \pm v'_s) \rightarrow (v_1, v_2, \pm v_s),$$

where v_s and v'_s can be equal or have different values. For this case, we assume that the Z'_2 symmetry is spontaneously broken before the electroweak symmetry in order to form the domain walls that will modify the doublet VEVs. Therefore, a domain with a given sign of v_s can include several smaller domains where the doublet VEVs have different Goldstone modes.

We start with the first case. This scenario requires that both the singlet and the doublets acquire their vacuum expectation values at the same time in the early universe. Checking whether such a one-step phase transition is the correct evolution in the early universe would require a substantial finite-temperature numerical analysis for every considered parameter point and is beyond the scope of the current analysis. Therefore, we assume for simplicity and pedagogical reasons that this requirement is fulfilled and restrict ourselves to the discussion of the extra domain walls properties that can occur in such a case. We postpone a complete discussion of this requirement for a future comprehensive work discussing the electroweak baryogenesis generated by the domain walls in the N2HDM.

We discuss the domain wall solution in the case when the Goldstone mode θ related to the $U(1)_Y$ symmetry is different in both domains. We show the results using two parametrization for the scalar fields: the non-linear parametrization where the field configuration is described in terms of v_1 , v_2 , θ and ξ as defined in (5.37) as well as the linear parametrization where the fields configuration for the scalar doublets is described using 8 degrees of freedom ϕ_i with $i \in \{1, \dots, 8\}$ ⁶:

$$\Phi_1 = \begin{pmatrix} \phi_1 + i\phi_2 \\ \phi_3 + i\phi_4 \end{pmatrix}, \quad \Phi_2 = \begin{pmatrix} \phi_5 + i\phi_6 \\ \phi_7 + i\phi_8 \end{pmatrix}. \quad (5.38)$$

One then re-constructs the fields $v_1(x)$, $v_2(x)$, $\theta(x)$ and $\xi(x)$ using:

$$v_1(x) = \frac{1}{\sqrt{2}} \sqrt{\phi_3^2(x) + \phi_4^2(x)}, \quad v_2(x) = \frac{1}{\sqrt{2}} \sqrt{\phi_7^2(x) + \phi_8^2(x)}, \quad (5.39)$$

$$\theta(x) = \arg(\phi_3 + i\phi_4), \quad \xi(x) = \arg(\phi_7 + i\phi_8) - \arg(\phi_3 + i\phi_4). \quad (5.40)$$

In order to get the domain wall solution of this scenario, we need to find the solution that minimizes the energy functional $\mathcal{E}_\theta(x)$ described, in the non-linear parametrization by:

$$\begin{aligned} \mathcal{E}_\theta(x) = & \frac{1}{2} \left(\frac{dv_1}{dx} \right)^2 + \frac{1}{2} \left(\frac{dv_2}{dx} \right)^2 + \frac{1}{2} \left(\frac{dv_+}{dx} \right)^2 + \frac{1}{2} v_2^2(x) \left(\frac{d\xi}{dx} \right)^2 + \frac{1}{2} v_1^2(x) \left(\frac{d\theta}{dx} \right)^2 \\ & + \frac{1}{2} v_2^2(x) \left[\left(\frac{d\theta}{dx} \right)^2 + 2 \frac{d\theta}{dx} \frac{d\xi}{dx} \right] + \frac{1}{2} v_+^2(x) \left(\frac{d\theta}{dx} \right)^2 + V_{N2HDM}(x), \end{aligned} \quad (5.41)$$

and, in the linear parametrization:

$$\mathcal{E}_\theta(x) = \left(\frac{d\phi_3}{dx} \right)^2 + \left(\frac{d\phi_4}{dx} \right)^2 + \left(\frac{d\phi_7}{dx} \right)^2 + \left(\frac{d\phi_8}{dx} \right)^2 + V_{N2HDM}(x). \quad (5.42)$$

The gradient flow equations of motion of the domain wall solution are given by:

$$\frac{dv_1}{dt} = \frac{d^2 v_1}{dx^2} - \frac{d\mathcal{E}_\theta}{dv_1}, \quad (5.43)$$

$$\frac{dv_2}{dt} = \frac{d^2 v_2}{dx^2} - \frac{d\mathcal{E}_\theta}{dv_2}, \quad (5.44)$$

$$\frac{dv_s}{dt} = \frac{d^2 v_s}{dx^2} - \frac{d\mathcal{E}_\theta}{dv_s}, \quad (5.45)$$

$$\frac{d\xi}{dt} = v_2^2(x) \left(\frac{d^2 \xi}{dx^2} + \frac{d^2 \theta}{dx^2} \right) + 2v_2(x) \frac{d\xi}{dx} \frac{dv_2}{dx} - \frac{d\mathcal{E}_\theta}{d\xi}, \quad (5.46)$$

⁶ Note that for the case where only the Goldstone mode θ varies, we only have to take into account 4 degrees of freedom ϕ_3 , ϕ_4 , ϕ_7 and ϕ_8 in the linear parametrization.

m_{h_1} (GeV)	m_{h_2} (GeV)	m_{h_3} (GeV)	v_s (GeV)	$\tan(\beta)$
125.09	483.50	567.65	1340	3.14
m_{12}^2 (GeV) ²	α_1	α_2	α_3	type
65316	1.29	0.51	0.33	1

Table 5.7: Parameter point used to calculate the CP-violating solution in Figure 5.25.

$$\begin{aligned} \frac{d\theta}{dt} &= 2 \frac{d\theta}{dx} \left(2v_1(x) \frac{dv_1}{dx} + 2v_2(x) \frac{dv_2}{dx} \right) + 2v_2(x) \frac{dv_2}{dx} \frac{d\xi}{dx} + \left(v_2^2(x) + v_1^2(x) \right) \frac{d^2\theta}{dx^2} \\ &+ v_2^2(x) \frac{d^2\xi}{dx^2}. \end{aligned} \quad (5.47)$$

In the linear parametrization, these are:

$$\frac{d\phi_3}{dt} = \frac{d^2\phi_3}{dx^2} - \frac{d\mathcal{E}_\theta}{d\phi_3}, \quad (5.48)$$

$$\frac{d\phi_4}{dt} = \frac{d^2\phi_4}{dx^2} - \frac{d\mathcal{E}_\theta}{d\phi_4}, \quad (5.49)$$

$$\frac{d\phi_7}{dt} = \frac{d^2\phi_7}{dx^2} - \frac{d\mathcal{E}_\theta}{d\phi_7}, \quad (5.50)$$

$$\frac{d\phi_8}{dt} = \frac{d^2\phi_8}{dx^2} - \frac{d\mathcal{E}_\theta}{d\phi_8}. \quad (5.51)$$

The advantage of using the non-linear parametrization is that one obtains the profiles of $v_{1,2}(x)$ and $\xi(x)$ directly. However, using the linear parametrization to solve the real-time evolution of the field configuration numerically is much simpler since the time dependant Klein Gordon equations in the case of the non-linear parametrization contain terms of the form $v_2^2(x, t) \frac{d^2\xi}{dt^2}$ which can lead to numerical instabilities when $v_2(x)$ is very small. We numerically solve this system of differential equations using a gradient flow algorithm [76, 75] and take the boundary conditions for the Goldstone mode θ to be 0 at $-\infty$ and $\pi/2$ at $+\infty$ using von Neumann boundary conditions. The chosen parameter point is given in table 5.7 and the results for the non-linear parametrization are shown in Figure 5.25a. We find that, in the vicinity of the wall, $\xi(x)$ is non-zero leading to a non-zero imaginary mass in the Yukawa sector and therefore to CP-violating phenomena [1]. This condensate vanishes in the core of the wall given that $v_2(0) = 0$ for this parameter point. We also obtain a kink-like profile for $\theta(x)$ interpolating between 0 and $\pi/2$. The profile of $\xi(x)$ can be explained using the equation of motion for the Goldstone mode θ . It was found in [76] that a change in θ across the wall will also induce a change in $\xi(x)$ according to the formula:

$$\frac{d\theta}{dx} = \frac{-v_2^2(x)}{v_1^2(x) + v_2^2(x) + v_+^2(x)} \frac{d\xi}{dx}. \quad (5.52)$$

To determine whether this solution is stable or not, we compute its energy $\sigma_\theta = \int dx \mathcal{E}_\theta(x)$ and compare it to the energy of the standard solution (where both domains have the same Goldstone modes and therefore $\xi(x) = 0$) as shown in Figure 5.25b. Numerically, we find that the CP-violating solution has a slightly higher energy causing such a solution to be unstable and to decay to the standard domain wall solution with $\xi(x) = 0$ everywhere. This decay process occurs due to $\theta(x)$ varying with time in such a way as to make both domains have the same Goldstone mode values ($\theta(-\infty) = \theta(+\infty)$).

In the case of electroweak symmetry restoration in a large region around the wall, we found that the decay of this CP-violating domain wall solution takes a longer iteration

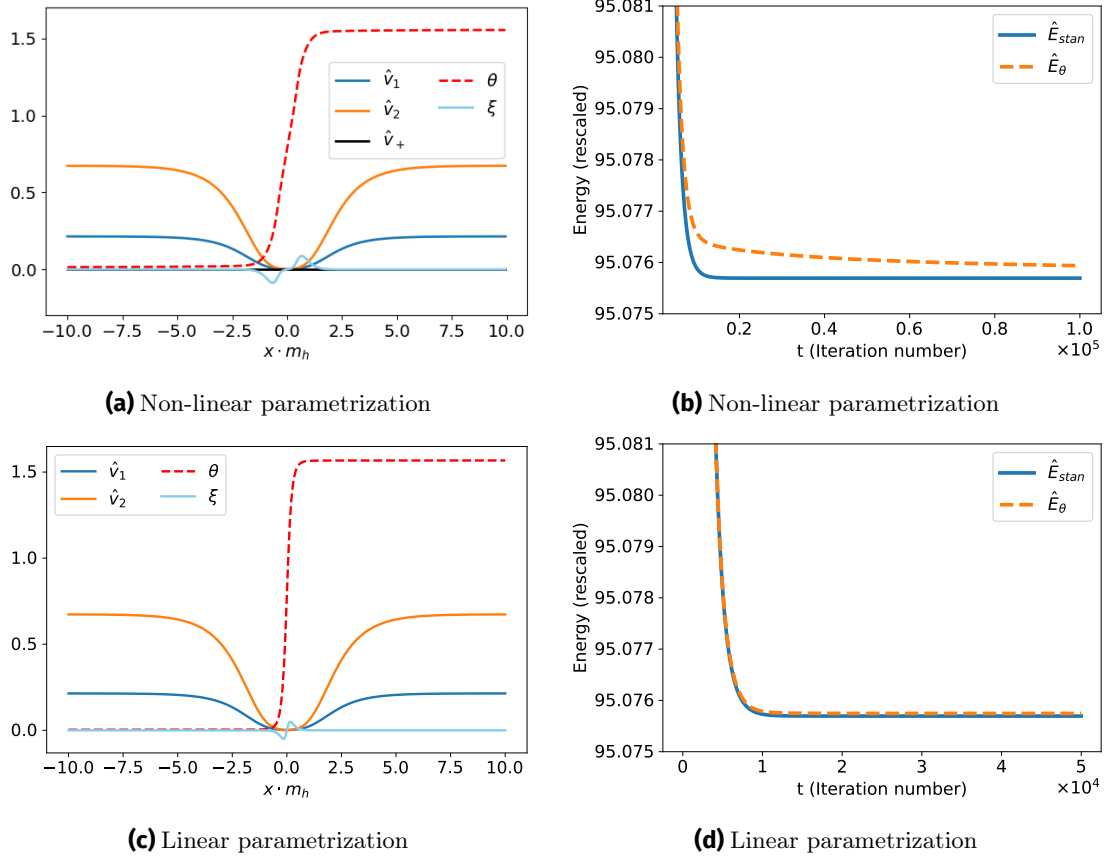


Figure 5.25: (a) Rescaled profile of the fields $\hat{v}_i = v_i/v_{sm}$ for a domain wall solution with different Goldstone modes θ in both domains. (b) The domain wall energy of the standard solution (blue) and the CP-violating solution (dashed orange). The used parameter point corresponds to the variables in Table 5.7. (c) and (d) same as (a) and (b) respectively using the linear parametrization.

time. Looking at $\mathcal{E}_\theta(x)$ (5.41), we see that all terms with a θ and ξ contributions are dependent on $v_1(x)$ and $v_2(x)$. In the case of a total electroweak symmetry restoration inside the wall, these terms vanish and therefore a CP-violating solution has almost the same energy as the stable standard domain wall field configuration, leading the CP-violating vacua around the wall to be long-lived. However, the imaginary mass proportional to $\text{Im}(v_2(x)e^{i\xi(x)}) = \sin(\xi(x))v_2(x)$ providing the CP-violation effects for fermions will, in such a case, be small.

The results for the linear parametrization are shown in Figure 5.25c (where we converted the profiles of $\phi_i(x)$ into their corresponding non-linear field profiles). The kink profile for $\theta(x)$ is sharply changing around $x = 0$, in contrast with the results obtained using the non-linear parametrization. The field configuration converges faster to its lowest energy solution and has an energy that is nearly equal to the standard solution. The slight discrepancy in the results is explained by the fact that the non-linear parameterization needs more time to converge to the profiles for $\theta(x)$ and $\xi(x)$ found using the linear parametrization. This can be seen in the gradient flow equations of $\xi(x)$ (5.46) and $\theta(x)$ (5.47), where the right-hand side of both equations is very small as soon as the values for $v_1(x)$ and $v_2(x)$ tend to zero inside the wall, leading to both $\frac{d\xi}{dt}$ and $\frac{d\theta}{dt}$ being small and therefore the relaxation of $\xi(x)$ and $\theta(x)$ to their stable profile will take significantly more iterations compared to the linear parametrization (where both the norm and phases of the fields change at the same time).

m_{h_1} (GeV)	m_{h_2} (GeV)	m_{h_3} (GeV)	v_s (GeV)	$\tan(\beta)$
125.09	589.5	697.5	9635	1.28
m_{12}^2 (GeV) ²	α_1	α_2	α_3	type
208249	0.94	0.25	-1.37	4

Table 5.8: Parameter point used to calculate the CP-violating solution in Figure 5.26.

We checked that both parameterizations quickly converge to the same results in the case when $v_1(x)$ and $v_2(x)$ are not small inside the wall.

We now look at the second scenario where the electroweak symmetry gets broken after the formation of the walls. In this case, one expects that a single domain of v_s can have multiple different values of Goldstone modes.

We model this scenario as follows. After EWSB, vacua with the same sign of $v_{1,2}$ start expanding in the region of the false vacuum $v_{1,2} = 0$. We then consider the case when a kink in the Goldstone modes is produced in the vicinity of the moving Z_2' domain wall due to the collision of regions with different Goldstone modes (see the initial vacuum field configuration in Figure 5.26a).

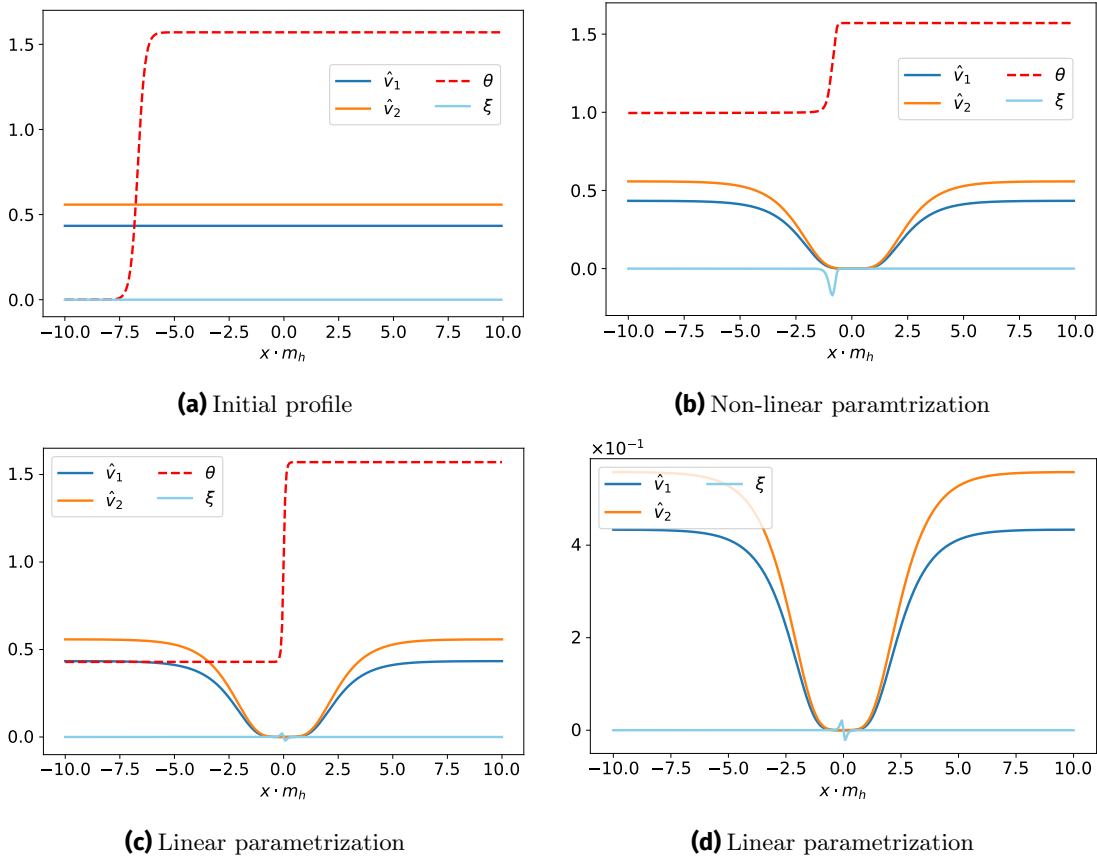


Figure 5.26: Scenario where the EWSB occurs after the formation of the walls. The domain wall solution for v_s is centered at $x = 0$. (a) Initial field configuration, where the value $\pi/2$ for θ is obtained for the domain $x > 0$ corresponding to $v_s > 0$ and part of the region $x < 0$ corresponding to $v_s < 0$, while the value $\theta = 0$ is obtained for the rest of the $x < 0$ domain. (b) Intermediate solution showing CP-violating vacua in the vicinity of the wall. The parameter point used for this scenario is shown in Table 5.8. (c) and (d) show the results obtained using the linear parametrization.

We solve the system of equations (5.43)-(5.47) as well as (5.48)-(5.51) using the initial boundary conditions and the initial guess solution shown in Figure 5.26a. Using the non-linear parametrization, we find that the kink-like solution for $\theta(x)$ evolves and moves to the vicinity of the wall, then slowly moves to the inner regions of the wall after some iteration time. This behavior is, however, only possible in the case of electroweak symmetry restoration in a large region around the wall: this is due to the extra contributions from a non-zero $\theta(x)$ and $\xi(x)$ to the energy $\mathcal{E}_\theta(x)$ (5.41) being vanishingly small for $v_{1,2}(x) \rightarrow 0$ as discussed earlier. Notice that in such a case, we obtain a CP-violating vacuum configuration only in the vicinity of the region where the Goldstone mode changes. This behavior was, however, not obtained when using the linear parametrization. In contrast to the non-linear parametrization, the kink profile for $\theta(x)$ is centered inside the wall at $x = 0$. This leads to a small non-zero $\xi(x)$ inside the wall. In the case of the non-linear parametrization at large iteration number in t , the kink profile in θ slowly moves to the center of the wall. Therefore, both results are equivalent in the long-time limit.

In order to study the real-time evolution of this field configuration in the context of a moving domain wall, we solve the time-dependent Klein-Gordon equations of motions for the scalar fields⁷ in the linear parametrization:

$$\frac{d^2\phi_i}{dt^2} = \frac{d^2\phi_i}{dx^2} - d\frac{d\phi_i}{dt} - \frac{dV_{N2HDM}}{d\phi_i}, \quad (5.53)$$

where d represents a friction term. The results for different times are shown in Figure 5.27. We find that as the domain wall moves to the left, the $\theta(x)$ (and consequently $\xi(x)$) field profiles get dragged by the wall instead of the domain wall simply moving through and leaving the kink profile of $\theta(x)$ behind.

For electroweak baryogenesis via domain walls to be effective, the CP-violating profile $\xi(x)$ should be non-zero on the outer edge of the wall to generate a non-zero imaginary mass that creates an axial asymmetry in the EWSR region inside the wall. This is not the case in our results, where a non-zero $\xi(x)$ is localized inside the wall, and leads to a rather negligible imaginary mass. However, one could also use the kink profile in $\theta(x)$ to produce an axial asymmetry inside the wall. In fact, the kink profile in $\theta(x)$ will lead to a pure gauge hypermagnetic field at the center of the wall:

$$B_\mu(x) = \frac{1}{g}\partial_\mu\theta(x), \quad (5.54)$$

where g is the hypermagnetic field gauge coupling. This hypermagnetic field interacts differently with left and right-handed fermions in the plasma and could eventually generate the needed axial asymmetry inside the region where the sphaleron rate is unsuppressed, leading to a successful creation of a matter-antimatter asymmetry. Investigating the role of hypermagnetic fields in generating the axial asymmetry needed for EWBG was already done in [168, 169, 170] in the context of standard bubble electroweak baryogenesis.

In the next section, we briefly discuss a simple calculation for the amount of baryogenesis created by these domain walls.

⁷ We take into account a friction term $\dot{\phi}_i$ that dissipates the energy of the fields configuration and leads to the relaxation of oscillations in the fields. This does not affect the observed phenomena and is only relevant to suppress the oscillations in the fields.

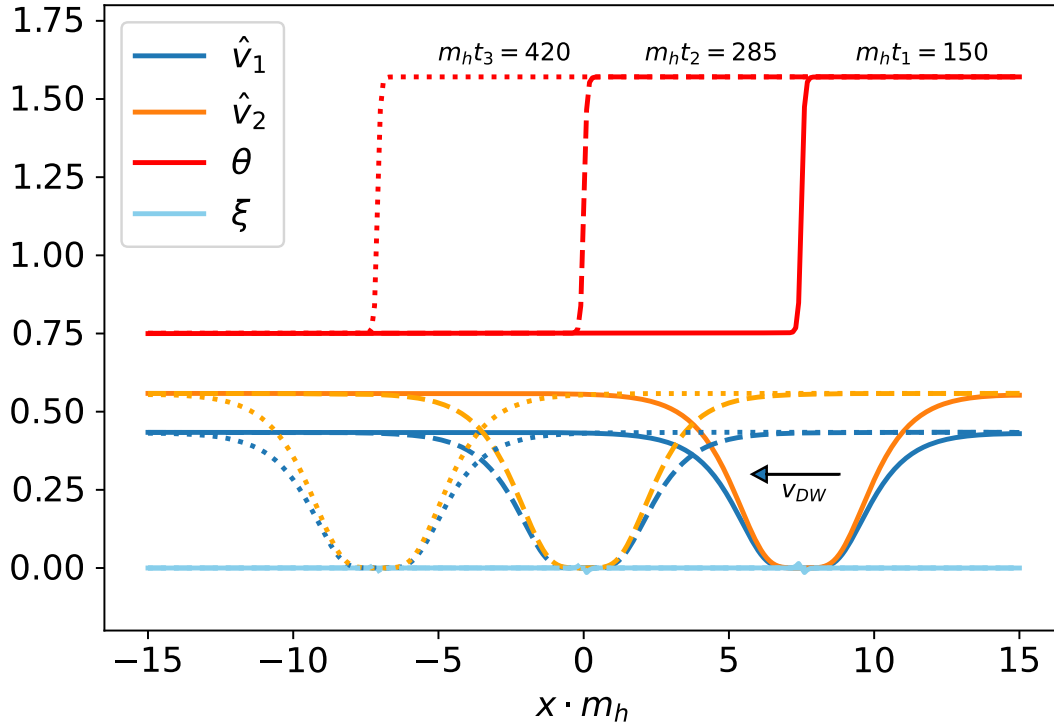


Figure 5.27: Time evolution of the scalar field configuration for a domain wall moving to the left with velocity v_{DW} . We show snapshots at different times $m_h t_1 = 150$ (solid lines), $m_h t_2 = 285$ (dashed lines) and $m_h t_3 = 420$ (dotted lines). The kink profile in $\theta(x)$ and the CP-violating phase $\xi(x)$ are both dragged with the domain wall as it moves to another region of space instead of being left behind.

5.5 ELECTROWEAK BARYOGENESIS VIA DOMAIN WALLS

Since the nineties, several mechanisms using topological defects such as cosmic strings and domain walls to source a matter-antimatter asymmetry were proposed [144, 145, 106, 146, 66, 47, 108, 171]. Their advantage compared with other well-known mechanisms such as the standard electroweak baryogenesis is that they don't rely on a first order phase transition, since topological defects can also form after second order phase transitions [9]. In the case of cosmic strings or magnetic monopoles, it is clear that any generated baryon asymmetry will be suppressed by the small volume that these defects occupy, which limits the amount of baryogenesis of any mechanism relying on them [66]. However, domain walls are two-dimensional and therefore will span a large volume of space during their evolution, which avoids this large volume suppression.

We discuss in this section the interesting idea that domain wall generate the matter-antimatter of the universe, which takes advantage of the results of the previous sections where we showed that domain walls in the N2HDM can lead to EWSR in a large region around the wall. We show that a hypercharge field centered around the wall can generate a chiral asymmetry, which is subsequently transformed into a baryon asymmetry by the sphalerons active inside the wall.

We start by briefly summarizing the standard electroweak baryogenesis mechanism, then provide a simplified calculation for the amount of baryogenesis induced by the domain wall electroweak baryogenesis mechanism.

5.5.1 Standard Electroweak Baryogenesis

Electroweak baryogenesis [89, 90, 172, 173, 174, 175, 68, 176, 177, 69] is an elegant mechanism to generate the matter-antimatter asymmetry of the universe. It relies on a first-order electroweak phase transition in order to satisfy the Sakharov condition of out-of-thermal equilibrium [71]. This is achieved by having bubbles of the true vacuum expanding in the surrounding region of unbroken EW symmetry, where the vacuum expectation value is zero. Since the sphaleron rate in the broken phase is exponentially suppressed, the bubble wall separates the regions where the sphalerons are active (outside the bubble) from the regions where they are inactive (inside the bubble). Note that a EW baryogenesis using a second-order EW phase transition is very inefficient [178] due to both the lack of departure from thermal equilibrium as well as the generated baryon asymmetry being washed out due to the expansion of the universe [178]. In fact, since the order parameter (the vacuum expectation value of the Higgs field) during a second order phase transition changes continuously and uniformly in space, there is no hard separation between regions where the sphaleron rate is unsuppressed from the regions where they are suppressed leading to the wash-out of any generated baryon asymmetry.

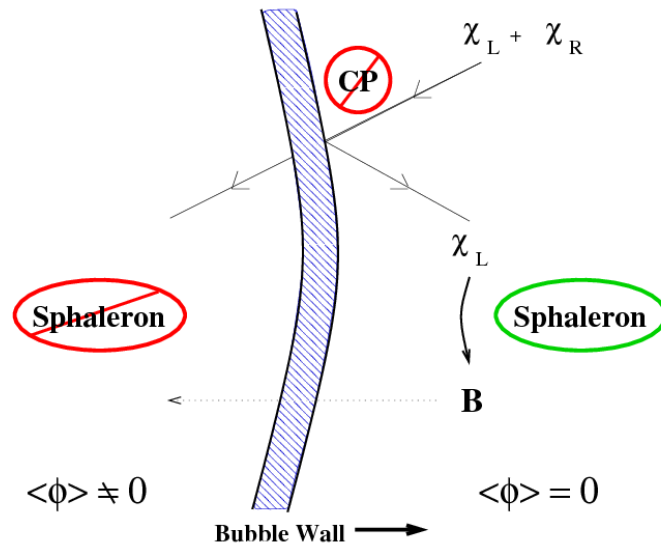


Figure 5.28: Mechanism for the standard electroweak baryogenesis. The bubble wall acts as a barrier between regions where baryon number violating processes are active and regions where they are suppressed. A CP-violating source on the wall leads to a chiral asymmetry which biases Sphalerons active outside the bubble into producing more matter than antimatter. The figure was taken from [68].

The standard realization of the electroweak baryogenesis mechanism, in which the baryon asymmetry is generated in the symmetric region near the wall (see Figure 5.28), relies on the following steps:

- Fermions in the thermal plasma scatter off the wall in a CP-violating way. This leads to a different reflection rate of left-handed particles compared to the reflection rate of right-handed antiparticles. We therefore obtain a chiral asymmetry in front of the wall.
- This chiral asymmetry diffuses in the symmetric region and is converted to a baryon asymmetry via sphaleron transitions with a rate $\Gamma_{sph} \sim \kappa \alpha_w^4 T^4$.

- As the bubble of the broken phase expands further, the generated baryon asymmetry is eventually caught inside the bubble. However, since the sphaleron rate inside the wall is exponentially suppressed $\Gamma_{sph} \sim e^{-E_{sph}/T}$ with $E_{sph} \propto v(T)$, this generated baryon asymmetry is frozen inside the bubble and is not washed-out.

Unfortunately, this elegant mechanism suffers from serious experimental constraints [179]. Besides the need for a first-order phase transition, the requirement of a source for CP-violation at the bubble wall is heavily constrained by electron dipole moment experiments [116]. The formation of domain walls does not require a first order phase transition. Since we showed in the previous section, that it is possible to obtain both a region of EW symmetry restoration and a CP-violating source localized inside the wall (and thus naturally circumventing any EDM constraints), using domain walls in the context of electroweak baryogenesis provides a new direction for mechanisms at the weak scales which can source a matter-antimatter asymmetry.

5.5.2 Domain Wall Electroweak Baryogenesis

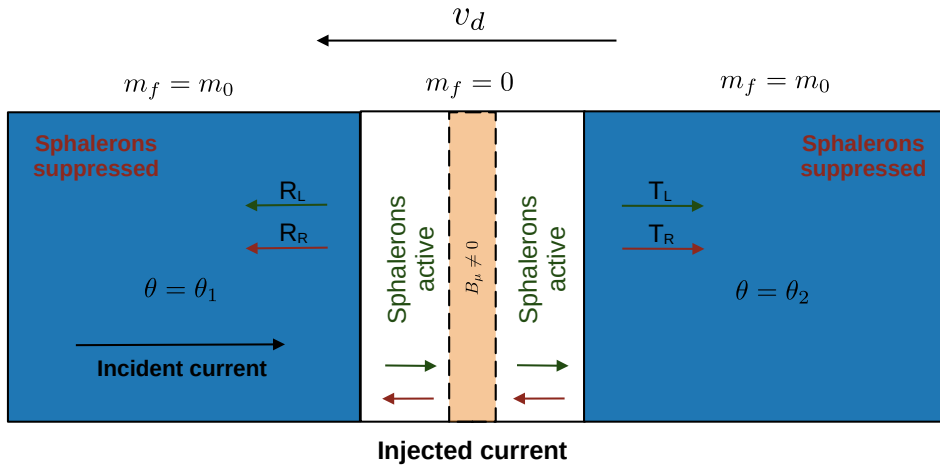


Figure 5.29: Mechanism for electroweak baryogenesis via domain walls.

We now briefly describe the general idea for electroweak baryogenesis via domain walls. In this case, the Sakharov conditions are fulfilled as follows:

- Baryon number violating processes: We keep using the sphaleron processes as a source for baryon number violation. The EW symmetry is restored (or at least the VEVs are very small) inside the wall. This leads to unsuppressed sphalerons inside the wall.
- CP-violating source: We rely in our case on the hypercharge gauge field localized inside the wall to source a chiral asymmetry inside the wall that biases sphalerons into producing more baryons than anti-baryons.
- Out-of-thermal-equilibrium condition: Since the EW symmetry restoration occurs only inside and in the vicinity of the wall, we naturally obtain a separation of regions where the sphaleron rate is active (inside the wall) from regions where the sphaleron rate is unsuppressed (outside the wall). A bias term in the potential will lead to the

annihilation of the domain wall network, making this mechanism only active for some time. This can be used in order not to wash out the created baryon asymmetry.

Having shown that the different Sakharov conditions are, in principle, fulfilled in our model, we now describe the dynamics of this mechanism. The idea is that as the domain walls move through the universe (due to their surface tension or pressure due to a bias term), the fermions in the thermal plasma enter the wall and scatter off the hypermagnetic field $B_\mu(x) = \frac{1}{g}\partial_\mu\theta(x)$ centered around the wall as shown in Figure 5.27. Due to interference from both edges of the wall, the wave functions of the left-handed fermions and right-handed antifermions will have different scattering rates. This generates a chiral asymmetry inside the wall, which subsequently gets transformed into a baryon asymmetry via the unsuppressed sphaleron rate in the symmetry-restored region. We show a simple sketch of the mechanism in Figure 5.29.

In the following, we find the net injected flux that participates in the baryogenesis mechanism. This is obtained by calculating the flux of left-handed particles minus the flux of their CP counterpart i.e. right-handed antiparticles. We find that this flux is equivalent to calculating the chiral asymmetry inside the wall, which we define as Δ_{LR} :

$$\Delta_{LR} = \mathcal{J}_L^{inside} - \mathcal{J}_R^{inside}, \quad (5.55)$$

where the currents $\mathcal{J}_{L,R}^{inside}$ denote the left and right-handed currents inside the wall. We solve the Dirac equation for a fermion incident from the left and moving towards the wall:

$$\partial_x u(x, t) = \left[-i\gamma_1\gamma_0\partial_t - i\partial_x\theta(x)(Y_L P_L + Y_R P_R) + i\gamma_1 m_R(x) - \gamma_1\gamma_5 m_I(x) \right] u(x, t), \quad (5.56)$$

where we used $B_\mu(x) = \frac{1}{g}\partial_\mu\theta(x)$ in the Lagrangian. We perform our calculations in the thin wall limit. In our case, the CP-violating phase ξ in the vicinity of the wall is negligible. Therefore, we have $m_I(x) = 0$. The profiles of the other fields and masses are given by:

$$m_R(x) = m_0 \mathcal{H}(-x) + m_0 \mathcal{H}(x - l_{dw}), \quad (5.57)$$

$$\partial_x\theta(x) = \Delta\theta \delta(x - \frac{l_{dw}}{2}), \quad (5.58)$$

where l_{dw} denotes the size of the symmetry restored region and \mathcal{H} denotes the Heaviside step-function.

We write down the plane wave solution in the different regions as:

$$u(t, x < 0) = e^{-iEt+ip_1x} u_{inc} + e^{-iEt-ip_1x} u_{ref}, \quad (5.59)$$

$$u(t, 0 < x < l_{dw}/2) = e^{-iEt+ip_2x} u_{t_2} + e^{-iEt-ip_2x} u_{r_2}, \quad (5.60)$$

$$u(t, l_{dw}/2 < x < l_{dw}) = e^{-iEt+ip_2x} u_{t_3} + e^{-iEt-ip_2x} u_{r_3}, \quad (5.61)$$

$$u(t, l_{dw} < x) = e^{-iEt+ip_1x} u_{tra}, \quad (5.62)$$

where E is the energy of the incident particle, p_1 its incident momentum in the broken phase, and p_2 its momentum in the symmetry restored region where the particle is massless. We solve the Dirac equation analogously to chapter 4 by using the continuity condition on the edges of the wall and the integration procedure at $x = l_{dw}/2$.

Before we deal with the relevant currents inside the wall that will lead to baryogenesis, we first discuss the reflection and transmission rates outside the wall, which show an interesting behavior compared with the usual scattering encountered in chapter 4.

The reflection and transmission coefficients are again given by:

$$T = \frac{\mathcal{J}_{tra}}{\mathcal{J}_{inc}} = \frac{\bar{u}_{tra}\gamma_1 P_L u_{tra}}{2p_1}, \quad R = -\frac{\mathcal{J}_{ref}}{\mathcal{J}_{inc}} = \frac{\bar{u}_{ref}\gamma_1 P_L u_{ref}}{2p_1}. \quad (5.63)$$

We first start with the case when no hypermagnetic field is present inside the wall. The

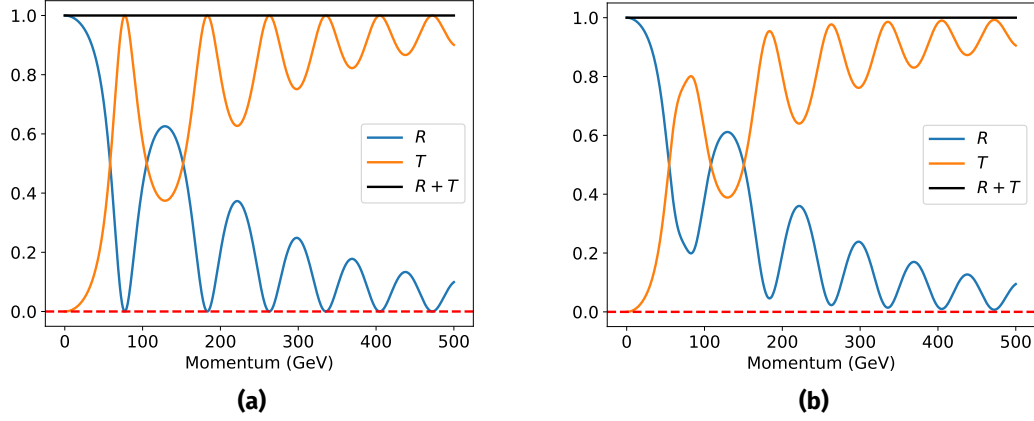


Figure 5.30: Scattering rates for a top quark incident on a symmetry restored region $l_{dw} = 5 \cdot m_h^{-1}$. (a) In the case when $\Delta\theta = 0$ and (b) when $\Delta\theta = 0.15\pi$.

results for reflection and transmission coefficients of a top quark scattering off a symmetry restored region of length $l_{dw} = 5 \cdot m_h^{-1}$ as a function of the incident top quark momentum is shown in Figure 5.30a, which correspond to a transmission and reflection coefficient given by:

$$T = \frac{2p_1^2}{m_f^2 + 2p_1^2 - m_f^2 \cos(2l_{dw}E)}, \quad R = 1 - \frac{2p_1^2}{m_f^2 + 2p_1^2 - m_f^2 \cos(2l_{dw}E)}. \quad (5.64)$$

We observe an oscillation in the reflection and transmission coefficients with particular values p_{rt} for the momentum where the particle is always transmitted with $T(p_{rt}) = 1$ when $2l_{dw}E = 2\pi n$ with n an integer number. These are given by $p_{rt} = (\frac{\pi^2 n^2}{4l_{dw}^2} - m_f^2)^{1/2}$. This behavior is known as the Ramsauer-Townsend effect. This effect was discovered in 1921 in the scattering of very low energy electrons on Xenon gas. These low-energy electrons showed a very small scattering rate and thus a high rate of transmission at particular energies. This effect was later explained in the framework of quantum mechanics by considering the scattering of the electron on the Xenon atom taken to represent an electrostatic potential well [180, 181, 182]. When $\Delta\theta \neq 0$, we still obtain oscillations in the scattering rates. However, the potential barrier in the form of the hypermagnetic field damps the transmission coefficient as shown in Figure 5.30b.

The relevant currents for electroweak baryogenesis via domain walls are the ones inside the wall:

$$\mathcal{J}_{inside,1}^L = \bar{u}_{t2}\gamma_1 P_L u_{t2} + \bar{u}_{r2}\gamma_1 P_L u_{r2}, \quad (5.65)$$

$$\mathcal{J}_{inside,1}^R = \bar{u}_{t2}\gamma_1 P_R u_{t2} + \bar{u}_{r2}\gamma_1 P_R u_{r2}, \quad (5.66)$$

$$\mathcal{J}_{inside,2}^L = \bar{u}_{t3}\gamma_1 P_L u_{t3} + \bar{u}_{r3}\gamma_1 P_L u_{r3}, \quad (5.67)$$

$$\mathcal{J}_{inside,2}^R = \bar{u}_{t3}\gamma_1 P_R u_{t3} + \bar{u}_{r3}\gamma_1 P_R u_{r3}. \quad (5.68)$$

We find that the currents $\mathcal{J}_1^{L,R}$ and $\mathcal{J}_2^{L,R}$ are the same on both regions separated by the hypermagnetic field. We plot in Figure 5.31 the difference Δ_{LR} (5.31) in the current

between the left-handed and right-handed particles. This difference in current can also give us the net left-handed particle current inside the wall since it is equivalent to calculating $\mathcal{J}_L - \mathcal{J}_{\bar{L}}$, the difference between the left-handed and its CP-conjugate current. We see that, for this particular value of $\Delta\theta = 0.15\pi$, Δ_{LR} first grows for low momenta, then subsequently oscillates around 0. Therefore, only relatively low momenta will significantly contribute to the generation of a baryon asymmetry.

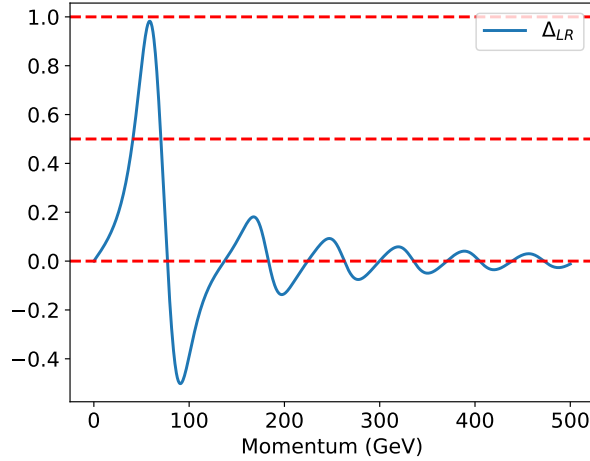


Figure 5.31: Difference between the left-handed and right-handed currents inside the wall.

Having obtained this chiral asymmetry inside the symmetry-restored region, we now need to calculate the generated baryon asymmetry. A detailed calculation would require taking into account several effects. These include, for example, diffusion effects inside the wall (when the symmetry restoration region is large), the consequences of any chiral asymmetry outside the wall, as well as the detailed evolution of the domain wall network, such as the velocity of the walls and their spatial distribution and annihilation time. We therefore only give a simplified "back-of-the-envelope" calculation to illustrate that this mechanism can indeed generate a significant amount of baryon asymmetry at the same order of magnitude as the experimentally observed values.

It is known that the production rate of baryons at a temperature T can be written as [107]:

$$\frac{dn_b}{dt} = -\frac{6N_F\Gamma_{sph}}{T^3}(3n_{q,L} + n_{l,L}), \quad (5.69)$$

where N_F denotes the number of particle families, $n_{q,L}$ the net number density of left handed quarks and $n_{l,L}$ the net number density of left-handed leptons. The net left-handed number density is calculated by:

$$n_{q,L} = \int \frac{d^3p}{(2\pi)^3} \Delta_{LR} f(p_x, p_\perp, T), \quad (5.70)$$

where:

$$f(p_x, p_\perp) = \frac{|p_x|}{E} \frac{1}{1 + \exp(\gamma/T(E - v_d\sqrt{p_x^2 - m_f^2}))}, \quad (5.71)$$

denotes the flux of particles moving with a velocity v_d at a temperature T with momentum p_x , p_\perp denoting the momentum in the direction perpendicular to the wall, and $\gamma = (1 - v_d^2)^{-1/2}$.

Using $\frac{dn_b}{dt} = -v_d \frac{dn_b}{dx}$, and for a domain wall which passes a volume fraction V_{dw} , the final amount of created baryogenesis normalized by the entropy is then given by:

$$\frac{n_b}{s} \approx \frac{45}{2\pi^2 g^* T^3} \frac{6N_F}{T^3} \frac{\Gamma_{sph}^{sym}}{v_d} n_{q,L} l_{dw} V_{dw}, \quad (5.72)$$

where $\Gamma_{sph}^{sym} = \kappa \alpha_w^4 T^4$ denotes the sphaleron rate per unit volume in the symmetric phase, and we used $s = \frac{2\pi^2}{45} g^* T^3$. Using this simplified formula for top quarks $m_t = 172$ GeV, $T = 50$ GeV, number of degrees of freedom $g^* = 100$, $l_{dw} = 5 \cdot m_h^{-1}$, $\Delta\theta = 0.15\pi$, $v_d = 0.3$, and $V_{dw} = 0.2$ we obtain a baryon asymmetry:

$$\frac{n_b}{s} \approx 1.41 \times 10^{-11},$$

which is not far from the experimentally measured value $\frac{n_b}{s} \approx 9 \times 10^{-11}$ [54, 183].

Therefore, this mechanism for baryogenesis via domain walls can be an effective way to explain the observed matter-antimatter asymmetry of the universe. However, as pointed out, this is a simplified calculation and several effects should be taken into account when calculating the actual baryon asymmetry, like the diffusion of the fermions inside the wall in case of large regions of symmetry restoration. One also needs to effectively calculate the time when domain walls form and annihilate, as well as the time when the electroweak symmetry gets broken, in order to determine the time interval during which this mechanism is active. We showed here that the chiral asymmetry is obtained by a value $\Delta\theta = 0.15\pi$. However, other values such as -0.15π will lead to an opposite antibaryon asymmetry, contributing to a wash-out effect in case when the same volume fraction is also spanned with that value of $\Delta\theta = -0.15\pi$.

These effects should be evaluated in the framework of a realistic simulation for an electroweak phase transition in the early universe, which is beyond the scope of this work. In case of washout, one can also look at other conventional ways to obtain the CP-violation, such as complex Yukawa couplings or a CP-violating phase in the early universe, such as the implementations in [107] and [108].

Note that this mechanism might also present a way to enhance or wash out a baryon asymmetry already generated by conventional electroweak baryogenesis during a first-order electroweak phase transition. This happens if the model includes the formation of domain walls that lead to symmetry restoration inside them, since sphaleron processes will be reactivated inside that region.

5.6 DISCUSSION

In this chapter, we investigated domain walls that are related to the singlet scalar field of the N2HDM, and arising after spontaneous symmetry breaking of the Z'_2 symmetry in the early universe. We numerically calculated the equations of motion of the scalar fields present in the N2HDM in order to determine the profiles of the doublet scalar fields in the background of the singlet domain wall. We found that the profile of the doublet fields can change considerably in the vicinity and inside the wall, making either the VEVs $v_{1,2}$ smaller or larger inside the wall. We focused, in particular, on the scenario where $v_{1,2}(x)$ becomes very small inside the wall, leading to electroweak symmetry restoration.

The presence of the domain wall solution effectively renders the 2HDM part of the scalar potential x -dependent. This has the effect that the 2HDM potential in the vicinity and

inside the wall can be in the symmetric phase where the minima of the potential are $v_{1,2} = 0$. We showed that this case is mostly related to the sign of the effective mass terms of the doublets $M_{1,2}$, which can turn positive inside the wall where the contribution $\lambda_{7,8}v_s^2(x)$ vanishes. We discussed in detail the different behaviors of the doublet fields inside the wall and showed that most parameter points where the effective mass terms become larger inside the wall lead to smaller values for the doublet VEVs inside and in the vicinity of the wall, while smaller (more negative) values for the effective mass term lead to higher values of $v_{1,2}(0)$. We also discussed the different possible anomalous behaviors for some particular parameter points.

We showed, in particular, that positive effective mass terms inside the wall are not sufficient to force the doublet VEVs to become zero, even though the potential of the Higgs doublets is in the symmetric phase inside the wall. To achieve EWSR, it was crucial to have a large change in the effective mass terms occurring in a large region of space in order for the doublet VEVs to converge to zero inside the wall. We found that parameter points that can satisfy this requirement have large and negative ratios $(\lambda_{7,8}/\lambda_6)$, and we found that they lead to very small $v_{1,2}$ in a large region around the wall.

To find parameter points with large $(\lambda_{7,8}/\lambda_6)$, we looked at different scenarios that satisfy all theoretical and experimental constraints including collider searches and showed that the vacuum expectation value of the singlet scalar as well as the masses of the CP-even Higgs bosons are the most important model parameters. In particular, we find that larger v_s mostly lead to smaller doublet VEVs inside the wall, while lower masses of the CP-even Higgs bosons mostly lead to a larger width for the EWSR region. Effects from the mixing angles between the different CP-even Higgs bosons also play an important role, since we observed that parameter points with higher singlet admixture in the SM-like Higgs boson state tend to have a higher electroweak symmetry restoration effect inside the wall. This, however, already puts constraints on the amount of EWSR that can be achieved inside the wall, given that collider constraints restrict the amount of singlet admixture in the SM-like Higgs boson state.

We also showed that it is possible to induce small CP-violating field configurations inside the wall in the case when different regions of the universe acquire different values for the Goldstone modes after EWSB. In contrast to the analogous case in the 2HDM [76, 1], we found that the energy difference between CP-violating solutions and standard domain wall solutions is very small, especially for parameter points that lead to EWSR in a large region around the wall. One would expect that the CP-violating domain wall in such scenarios would be long-lived. Determining the lifetime of these CP-violating solutions is crucial for the calculation of the matter-antimatter asymmetry generated by the motion of the domain walls in the N2HDM. Even though the obtained CP-violation is rather small, we find that the kink profile in $\theta(x)$ is long-lived and leads to the generation of a hypermagnetic field focused sharply inside the center of the wall. Since this hypermagnetic field interacts differently with left and right-handed fermions in the plasma, we anticipated that it could lead to the generation of the needed axial asymmetry inside the region of electroweak symmetry restoration.

We performed a simplified calculation for this baryon asymmetry generated by the domain walls. Even though we showed that this mechanism can generate an asymmetry which lies in the same order of magnitude as the one observed in nature, problematic washout effects can be relevant, and a precise calculation is necessary.

We performed in this study the first steps toward studying the viability of electroweak baryogenesis via domain walls in the N2HDM. This mechanism relies on the weak sphaleron

rate inside the wall being less suppressed than outside of it. The sphaleron rate in the broken electroweak phase and at a temperature T has an exponential suppression due to a non-zero doublets vacuum expectation value v_{ew} and is proportional to $\Gamma_{sphaleron} \propto e^{(-4\pi(v_{ew}/gT))}$ [68], where g is the weak coupling. Therefore, for small or vanishing values of v_{ew} , the sphaleron rate is not suppressed, and the rate of baryon-violating processes inside the wall will be significantly higher than that outside of it. Another important requirement is that the region of symmetry restoration needs to be large enough to fit a sphaleron. A significant amount of baryon asymmetry was shown to be generated using this mechanism in a simplified scenario. However, a complete and detailed calculation of the amount of baryogenesis generated via this mechanism in the case of an annihilating singlet domain wall network in the N2HDM is the subject of future work, where we incorporate thermal as well as diffusion effects for the fermions that scatter off the domain walls and most importantly, taking into account washout effects and the dynamics of the walls until their annihilation.

Another issue, which was also encountered in our analysis, is the possibility of negative transmission or reflection rates for the chiral states (left-handed or right-handed). Such an issue could be caused by a Klein Paradox in the CP-violating scattering of this mechanism. In this case, a treatment of the scattering process in the framework of quantum field theory might be required.

6

ELECTROWEAK VACUUM DECAY INDUCED BY DOMAIN WALLS

This chapter is based on the following work, prepared for publication:

- [3] M. Y. Sassi and G. Moortgat-Pick, “Electroweak Vacuum Decay in the N2HDM Induced by Domain Walls.” In preparation, to be published, 2025

6.1 MOTIVATION AND GENERAL IDEA

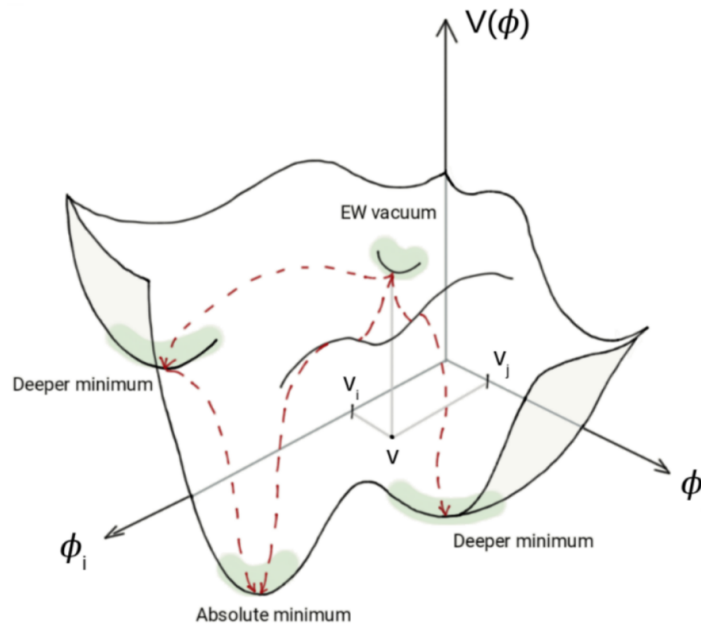


Figure 6.1: A generic illustration of the scalar potential in models with several Higgs bosons. The picture was created by Kateryna Radchenko [121].

In the Standard Model (SM) of particle physics, quarks, leptons, and gauge and scalar bosons acquire a mass via the Higgs mechanism, relying on the scalar field of the Higgs boson. After electroweak symmetry breaking in the early universe, the Higgs field acquires a vacuum expectation value corresponding to a minimum of the scalar potential. In the SM, this minimum corresponds to a VEV $v_{sm} \approx 246$ GeV. At tree-level, the SM electroweak (EW) minimum is stable. However, when higher-order corrections are included in the parameters of the SM Higgs potential, the potential can develop another deeper minimum at high scales, rendering the SM EW minimum to be a local minimum and thus metastable [118, 184]. Current experimental results for the top quark mass, strong coupling constant, and the W boson mass favor this scenario [185], and the electroweak (EW) vacuum in the SM could, therefore, be metastable but long-lived.

When considering an extended scalar sector, the addition of extra degrees of freedom can lead, already at tree-level, to the existence of several extra minima other than the EW minimum [27, 186, 112, 122, 187, 113, 188, 119]. The EW minimum is then stable if it is the global minimum of the potential, metastable when the tunneling rate between the EW minimum and the global minimum leads to an EW minimum with a lifetime larger than the age of the universe, and unstable when the lifetime of the EW minimum is smaller than the age of the universe. Obviously, an unstable EW minimum is ruled out, and the vacuum (meta)stability of the EW vacuum can be used as a strong constraint for the viability of models with an extended scalar sector [27, 186, 112, 122, 187, 113, 188, 119].

The vacuum stability of the Z'_2 symmetric N2HDM was extensively investigated [27], and a comparison with the $2HDM + S$ where S denotes a complex singlet scalar was done in [186]. It was found that large regions of parameter points in the N2HDM can be metastable, with the EW vacuum being very long-lived. In such a case, the potential barrier between the EW minimum and the global minimum can be very large, leading to an extremely small tunneling rate between the EW vacuum and the global one. However, these studies didn't take into account the possible presence of domain walls in the N2HDM. As was shown in the previous chapter, due to the coupling between the singlet and doublet scalar fields, the potential for the doublets in the background of the singlet domain wall will be dependent on the position with respect to the core of the domain wall. Inside the core of the defect, the VEV of the singlet field vanishes, and the effective quadratic terms for the doublet fields will be different. Because of this, the potential barrier to the global minimum of the potential can be different or even vanish, leading to the possible nucleation of the global minimum inside the wall. Due to the difference in the potential energy, the global minimum will then expand outside of the wall, and the universe is eventually populated with the global minimum instead of the EW minimum.

This chapter is organized as follows: we start with a brief discussion of the vacuum stability of the N2HDM. We later discuss how domain walls can lead to the decay of very long-lived EW minima via a classical rollover triggered in the core of the wall. Finally, we describe some phenomenological scenarios to demonstrate the possibility of using the mechanism of vacuum decay via domain walls in order to rule out large regions of the otherwise viable parameter points in the N2HDM.

6.2 VACUUM INSTABILITIES IN THE N2HDM

In this section, we briefly discuss the concept of vacuum instability and summarize the results obtained in [27], using the potential of the Z'_2 symmetric N2HDM in (5.1).

In our work we consider parameter points where the physical vacuum has an EW vacuum for the Higgs doublets $v_{ew} = \sqrt{v_1^2 + v_2^2} \approx 246$ GeV leading to the observed masses of the weak gauge fields as well as a non-zero VEV for the singlet scalar $v_s \neq 0$. We follow the notation in [27] and denote this minimum as $\mathcal{N}s$:

$$\langle \Phi_1 \rangle_{\mathcal{N}s} = \frac{1}{\sqrt{2}} \begin{pmatrix} 0 \\ v_1 \end{pmatrix}, \quad \langle \Phi_2 \rangle_{\mathcal{N}s} = \frac{1}{\sqrt{2}} \begin{pmatrix} 0 \\ v_2 \end{pmatrix}, \quad \langle \Phi_s \rangle_{\mathcal{N}s} = v_s. \quad (6.1)$$

It was found in [27] that for several parameter points of the model, the vacuum $\mathcal{N}s$ is not the global minimum, and different types of vacua can be deeper. This includes:

- Electric-charge breaking vacua \mathcal{CB} :

$$\langle \Phi_1 \rangle_{\mathcal{CB}} = \frac{1}{\sqrt{2}} \begin{pmatrix} 0 \\ c_1 \end{pmatrix}, \quad \langle \Phi_2 \rangle_{\mathcal{CB}} = \frac{1}{\sqrt{2}} \begin{pmatrix} c_+ \\ c_2 \end{pmatrix}, \quad \langle \Phi_s \rangle_{\mathcal{CB}} = 0. \quad (6.2)$$

- CP breaking vacua \mathcal{CP} :

$$\langle \Phi_1 \rangle_{\mathcal{CP}} = \frac{1}{\sqrt{2}} \begin{pmatrix} 0 \\ \bar{v}_1 \end{pmatrix}, \quad \langle \Phi_2 \rangle_{\mathcal{CP}} = \frac{1}{\sqrt{2}} \begin{pmatrix} 0 \\ \bar{v}_2 e^{i\xi} \end{pmatrix}, \quad \langle \Phi_s \rangle_{\mathcal{CP}} = 0. \quad (6.3)$$

- Deeper neutral EW breaking vacua leading to different gauge boson masses $v'_{ew} = \sqrt{v_1'^2 + v_2'^2} \neq 246$ GeV and a different v_s (denoted as \mathcal{N}' 's) or a vanishing $v_s = 0$ (denoted as \mathcal{N}'):

$$\langle \Phi_1 \rangle_{\mathcal{N}'} = \frac{1}{\sqrt{2}} \begin{pmatrix} 0 \\ v_1' \end{pmatrix}, \quad \langle \Phi_2 \rangle_{\mathcal{N}'} = \frac{1}{\sqrt{2}} \begin{pmatrix} 0 \\ v_2' \end{pmatrix}, \quad \langle \Phi_s \rangle_{\mathcal{N}'} = 0. \quad (6.4)$$

Electric charge and CP-breaking vacua with a non-zero VEV for v_s cannot be deeper than the \mathcal{N} 's (see [27] for a detailed discussion), and we therefore don't consider them in this work.

The existence of minima deeper than our EW minimum requires a careful study of the metastability of the vacuum. This requires the calculations of the tunneling rate from the EW vacuum to the deeper vacuum. This rate per unit volume is related to the bounce action B by [189]:

$$\Gamma = K e^{-B}, \quad (6.5)$$

where K is a dimensionful parameter that has subdominant effects on the value of the tunneling rate. The bounce action B for a scalar field configuration ϕ is obtained by finding the stationary point of the Euclidean action [189]:

$$B = 2\pi^2 \int_0^\infty \rho^3 \frac{d}{d\rho} \left[\frac{1}{2} \left(\frac{d}{d\rho} \phi_B(\rho) \right)^2 + V(\phi_B(\rho)) \right], \quad (6.6)$$

where $\rho = \sqrt{t^2 - x^2 - y^2 - z^2}$ denotes the spacetime variable, V is the scalar field potential, and $\phi_B(\rho)$ is the field bounce solution of the Euclidean equation of motion:

$$\frac{d^2 \phi}{d\rho^2} + \frac{3}{\rho} \frac{d\phi}{d\rho} = \frac{\partial V}{\partial \phi}, \quad (6.7)$$

which is solved using the boundary conditions:

$$\phi(\infty) = \phi_v \quad \text{and} \quad \left(\frac{d\phi}{d\rho} \right)_{\rho=0} = 0, \quad (6.8)$$

with ϕ_v denoting the metastable vacuum. Calculating this bounce action and determining the tunneling rate is usually done using numerical tools such as e.g. **EVADE** [189], which we use throughout our work. Since the tunneling rate (6.5) to the global minimum is exponentially suppressed with the value of B , the bounce action B predominantly determines the fate of the EW vacuum. By comparing the age of the universe to the value of Γ , one determines the intervals where the EW vacuum is unstable or metastable [189]. For parameter points with $B > 440$, the transition from the EW vacuum to the deeper vacuum takes longer than the age of the universe [189]. Therefore, our EW vacuum is then deemed metastable and

	m_{H_y}, m_{H_z}, m_A	m_{H^\pm}	$\tan \beta$	m_{12}^2	v_S
min	30 GeV	150 GeV	0.8	0 GeV ²	1 GeV
max	1.5 TeV	1.5 TeV	20	5×10^5 GeV ²	3 TeV

Table 6.1: Input parameters used for the scan with `ScannerS`. The mixing angles $\alpha_{1,2,3}$ were not constrained. The mass $m_{H_x} = 125.09$ GeV.

long-lived, and the parameter point is not ruled out. In case $390 < B < 440$, the fate of the EW vacuum is uncertain, and for $B < 390$, the EW vacuum is short-lived and unstable, rendering such parameter points unphysical [189].

This analysis of vacuum stability is valid for the regions of the universe that are far from the domain wall of the singlet scalar. As we saw in chapter 5, the vanishing of v_s inside the domain wall changes the effective quadratic terms in the potential of the doublet fields, making it necessary to check the tunneling rate to the deeper vacua inside the core of the domain walls.

Before discussing the role of domain walls in inducing the decay of long-lived EW vacua to deeper vacua, we briefly summarize some phenomenological aspects of the vacuum stability and instability and their influence on the allowed parameter space of the N2HDM. This is done following the numerical approach used in [27], and we refer the reader to that work for a comprehensive discussion. We perform a parameter scan of 10^5 parameter points of the N2HDM of type 1, which fulfill both theoretical constraints of perturbative unitarity and boundedness from below as well as the experimental constraints from precision electroweak variables, collider constraints from Higgs searches and Higgs measurements, as well as flavor constraints (see section 2). We also impose the condition of electroweak and Z'_2 symmetry restoration at high temperatures (see section 5.2.1) in order to ensure the formation of the singlet domain walls in the early universe. All these constraints were implemented in `ScannerS` [117], which generates random parameter points satisfying all these conditions. We follow the analysis in [27] and take the same range of model variables for the generated parameter points (see Table 6.1). For each parameter point, the stability of the EW vacuum is verified against the existence of deeper vacua using `EVADE`. We find that for this random parameter scan, 33% of the viable parameters exhibit a deeper vacuum than the EW one. These vacua can be of the \mathcal{N} , \mathcal{CB} and \mathcal{CP} types. Almost 25% of the viable parameter points have a long-lived EW vacuum that has a lifetime larger than the age of the universe, and 8% of the parameter points exhibit a short-lived EW vacuum that decays to the deeper vacuum and therefore is a dangerous minimum. The deeper vacua that were found in this scan had a vanishing v_s and therefore the rate of decay of the EW minimum will be enhanced in the vicinity and inside the singlet wall (where $v_s(0) = 0$), as will be shown later.

The presence of deeper minima than the EW one in this scan is random and does not exhibit strong correlations with the variables of the model. This was also found in [27] where it was shown that it is possible to obtain some constraints on the signal strength $\mu_{\gamma\gamma}$ for the decay of the h_{125} mass eigenstate to a pair of photons normalized to the rate of the SM Higgs decay to two photons, as a function of the charged Higgs mass m_{H^\pm} . The results are shown in Figure 6.2 where we differentiate between parameter points having a stable EW vacuum (blue), parameter points having a long-lived EW vacuum (orange), and parameter points having a short-lived unstable EW vacuum (black). The points with an unstable EW vacuum are plotted first, then stable points, and finally metastable ones on top.

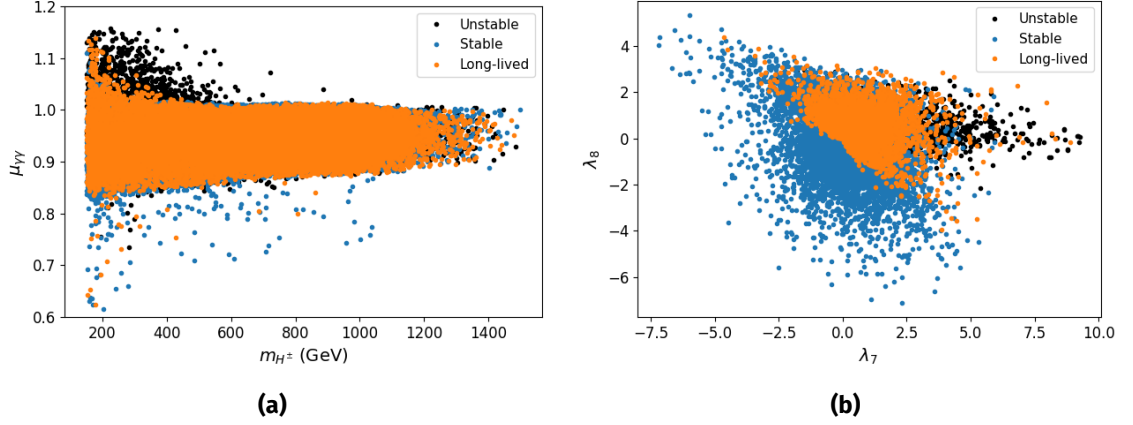


Figure 6.2: EW vacuum (in)stability for the random parameter scan. (a) The stability of the EW vacuum as a function of the signal ratio $\mu_{\gamma\gamma}$ and the charged Higgs mass m_{H^\pm} . (b) The stability of the vacuum as a function of the potential variables λ_7 and λ_8 .

We find that the regions of vacuum stability and instability mostly overlap. For small masses m_{H^\pm} between 300 GeV and 600 GeV and $\mu_{\gamma\gamma} > 1$, we find that the EW vacuum is short-lived and therefore one can exclude that region of the parameter space on vacuum stability arguments. We also observe (see Figure 6.2b) that the EW vacuum for negative λ_7 and λ_8 is always stable and the EW minimum is the global minimum in that scenario. The absence of a \mathcal{N} -type vacuum in this case can be explained by the fact that for $\lambda_{7,8} < 0$, the effective mass terms of the Higgs doublets receive a large positive contribution in the direction where $\phi_s \rightarrow 0$, due to $\lambda_7 |\Phi_1|^2 \phi_s^2 + \lambda_8 |\Phi_2|^2 \phi_s^2$ vanishing. In this case, the potential of the Higgs doublets approaches the local extremum $(v_1, v_2) = (0, 0)$, which always lies higher in the potential than the EW minimum.

Even though there is no strong correlation between short-lived EW vacua and model parameters, vacuum instability can be used to exclude a large number of parameter points of the model, which would otherwise be viable from a theoretical and experimental point of view. We also find that a large set of the parameter points of the random scan shows the presence of long-lived EW vacua. In principle, these metastable vacua are physically allowed since their lifetime is (much) larger than the age of the universe. However, we found that the deeper vacua of these parameter points have a vanishing $v_s = 0$. In the case of a homogeneous vacuum everywhere in the universe where every point in space falls into the EW vacuum \mathcal{N}_s , the metastability of the EW vacuum is ensured. However, the presence of domain walls makes the singlet VEV $v_s(x)$ space-dependent, with regions of the universe inside the domain wall having $v_s(0) = 0$. It is therefore important to check whether the presence of the walls will induce the decay into the deeper vacuum, making the long-lived EW vacuum unstable. In the next chapter, we solve the domain wall solutions in the N2HDM and check the fate of long-lived EW vacua inside and in the vicinity of the domain wall.

6.3 DOMAIN WALLS IN THE N2HDM INDUCING EW VACUUM DECAY

As discussed in chapter 5, the spontaneous breaking of the Z'_2 symmetry leads to the formation of cosmic domain walls in the early universe [8]. Due to the Z'_2 symmetry, the

two vacua v_s and $-v_s$ are degenerate¹ and therefore, have the same probability of occurring in the early universe. Different patches of the universe would then acquire different signs for v_s , and these domains will be separated by domain walls where $v_s = 0$. In order to obtain the field profile of the domain walls, one solves the equation of motion of the scalar fields ϕ_i with $i = 1, 2, +, s$ which will minimize the energy density of the vacuum configuration:

$$\frac{\partial^2 \phi_i}{\partial t^2} - \frac{\partial^2 \phi_i}{\partial x^2} + d \frac{\partial \phi_i}{\partial t} + \frac{\partial V_{N2HDM}}{\partial \phi_i} = 0, \quad (6.9)$$

where d is a friction term needed in order to relax the initial energy of the field configuration into the lowest energy solution. This friction term is related to both the expansion rate in the early universe as well as the friction induced by the interaction of the domain wall with the primordial thermal plasma. In our work, we do not explicitly estimate the value of d , and we use it in order to relax the field configuration into its lowest energy configuration. For $d = 0$, we obtain large gradients in the field configuration which disturb the numerical solution of this system of equations². The boundary conditions are taken to be $\phi_s = -v_s$ at $-\infty$ and $\phi_s = v_s$ at $+\infty$ for the singlet field and $\phi_{1,2} = v_{1,2}$ at $\pm\infty$ where $v_{1,2}$ denote the EW vacuum. The initial field profiles are taken to be a $\tanh(x)$ function for the singlet field and a constant $v_{1,2}$ for the doublets. We obtain the static field configuration by solving this differential equation numerically using the Euler method with spatial derivatives calculated using the three-point central difference formula.

We solve the coupled system of differential equations for the potential at $T = 0$. This is done for two reasons. First, in this work, we only consider the possibility of EW vacuum decay induced by the presence of domain walls in order to constrain the parameter points of the N2HDM, and therefore, we don't need to know exactly at which temperature after EW symmetry breaking, the decay to the deeper vacuum occurs. Since this decay will necessarily rule out the parameter point, determining the precise thermal evolution of such parameter points is not phenomenologically relevant. Second, performing large parameter scans and determining a precise thermal evolution of the finite-temperature potential of the N2HDM using available dedicated tools such as BSMPPT [150] is a rather time-consuming and computationally challenging task. For simplicity and speed of the calculation, we use the potential at $T = 0$. This approach is valid as long as the domain wall network does not annihilate before EW symmetry breaking or at a temperature T_{ann} slightly lower than T_{ew} . Since we assume that bias terms in the potential are very small, this assumption is valid, and the singlet domain wall network would only annihilate at a much later stage after EW symmetry breaking. Since the thermal potential at temperatures of order $\mathcal{O}(\text{GeV})$ would already approach the zero-temperature limit, this assumption gives reliable results for the calculated profiles of the scalar fields.

In the case when the bias terms are not negligible, one needs first to verify the formation of domain walls at some temperature T after the real singlet scalar field acquires a VEV. Then, we need to verify the existence of deeper vacua (since the presence of bias terms can significantly alter the potential) and also perform a precise study of the thermal evolution of the parameter points to determine whether the domain walls network annihilates before EW symmetry breaking making the domain walls harmless from the point of view of inducing the decay to deeper vacua. These aspects complicate the analysis significantly and are, therefore, not considered in this work.

¹ As mentioned before, we consider the Z'_2 soft breaking terms in the Lagrangian to be very small, making both vacua effectively degenerate.

² The value of d can be relevant in the case when the 2HDM potential inside the wall ($\phi_s = 0$) has multiple minima, as we will discuss later.

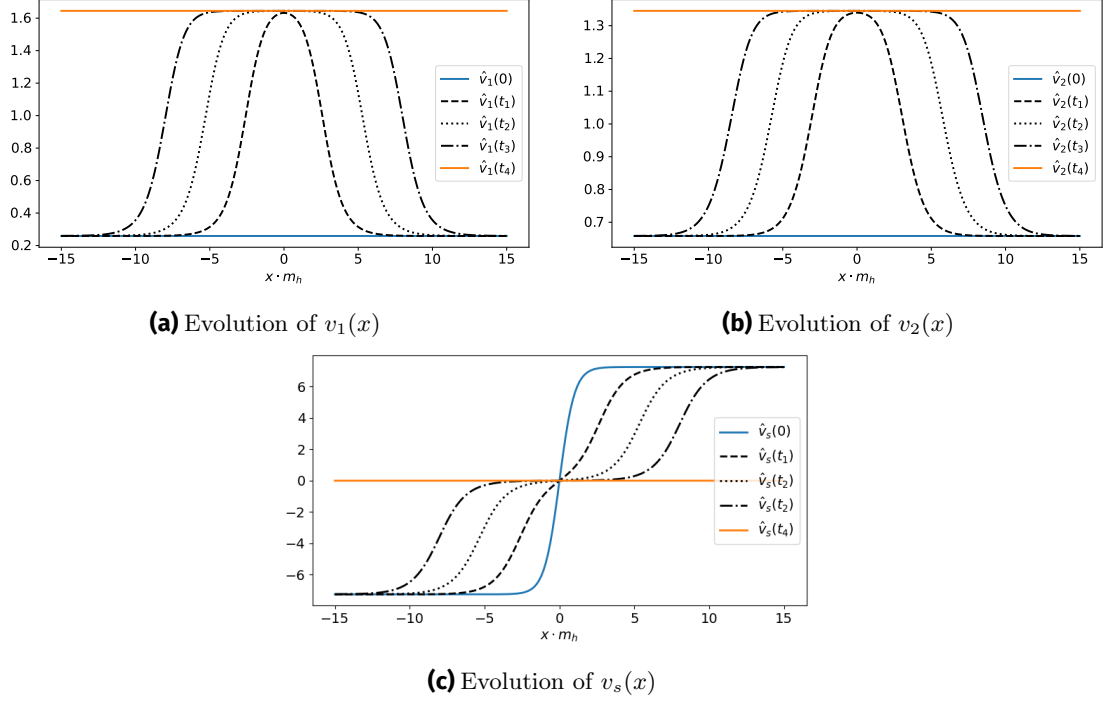


Figure 6.3: Evolution of the scalar fields inside the domain wall. We start with the doublet scalar fields in the EW vacuum and show the evolution to the deeper vacuum. The scalar fields roll over to the deeper vacuum, and the wall of true vacuum expands outside, leading to the decay of the EW vacuum everywhere. The region with $v_s = 0$ expands in space, leading to the eventual decay of the domain wall. The time steps are given by: $t_1 = 22.5m_h^{-1}$, $t_2 = 56.25m_h^{-1}$, $t_3 = 90m_h^{-1}$, and $t_4 = 191.25m_h^{-1}$.

We show the results for a parameter point P_1 (see Table 6.2) in Figure 6.3. This parameter point has a global minimum of type \mathcal{N} that is deeper than the EW vacuum. **EVADE** gives a bounce action of $B = 95368$ for the tunneling rate from the EW vacuum to the true vacuum of the potential. Therefore, the EW vacuum outside the wall is very long-lived and can be considered nearly stable since its decay rate is negligibly small. However, we see in Figure 6.3 that the Higgs doublets profiles inside the core of the domain wall rapidly change their values to correspond to the values of the deeper vacuum. This evolution occurs via a classical rollover from $(v_1, v_2, 0)$ to the true vacuum $(v'_1, v'_2, 0)$. Once this rollover is complete, the new vacuum nucleated inside the wall propagates outside of the wall since this expansion is energetically favorable and the gain in energy via the expansion is much larger than the domain wall's tension that would otherwise stabilize the profile of the fields inside the wall³. To explain this behavior, we consider the effective potential of the Higgs doublets in the background of the singlet domain wall solution:

$$\begin{aligned}
V_{2HDM}(\Phi_1, \Phi_2, \Phi_s(x)) &= \left(m_{11}^2 + \frac{\lambda_7}{2}\Phi_s^2(x)\right)\Phi_1^\dagger\Phi_1 + \left(m_{22}^2 + \frac{\lambda_8}{2}\Phi_s^2(x)\right)\Phi_2^\dagger\Phi_2 \\
&- m_{12}^2(\Phi_1^\dagger\Phi_2 + h.c.) + \frac{\lambda_1}{2}(\Phi_1^\dagger\Phi_1)^2 + \frac{\lambda_2}{2}(\Phi_2^\dagger\Phi_2)^2 + \lambda_3(\Phi_1^\dagger\Phi_1)(\Phi_2^\dagger\Phi_2) \\
&+ \lambda_4(\Phi_1^\dagger\Phi_2)(\Phi_2^\dagger\Phi_1) + \left[\frac{\lambda_5}{2}(\Phi_1^\dagger\Phi_2)^2 + h.c.\right] + \frac{m_S^2}{2}\Phi_s^2(x) + \frac{\lambda_6}{8}\Phi_s^4(x).
\end{aligned}$$

³ When considering thermal corrections, the transition and expansion of the deeper vacuum inside the region of the EW vacuum would only start when the gain in potential energy becomes larger than the domain wall's tension, this would then provide us with the temperature at which the decay occurs.

	m_{h_1}	m_{h_2}	m_{h_3}	m_A	m_{H^\pm}	$\tan(\beta)$	v_s	α_1	α_2	α_3	m_{12}
P_1	95	125	616	743	609	2.54	1786	-0.37	-1.49	0	359
P_2	125	410	733	481	368	2.11	4252	1.08	-0.19	-0.14	242
P_3	125	400	1200	400	470	1.88	1483	1.13	-0.32	-0.07	270
P_4	125	400	1200	279	429	2.93	2609	1.13	-0.16	-0.12	198

Table 6.2: Benchmark parameter points with metastable long-lived EW vacua. The mass parameters $m_{h_1}, m_{h_2}, m_{h_3}, m_A, m_{H^\pm}$ as well as v_s are given in GeV while m_{12} is given in GeV.

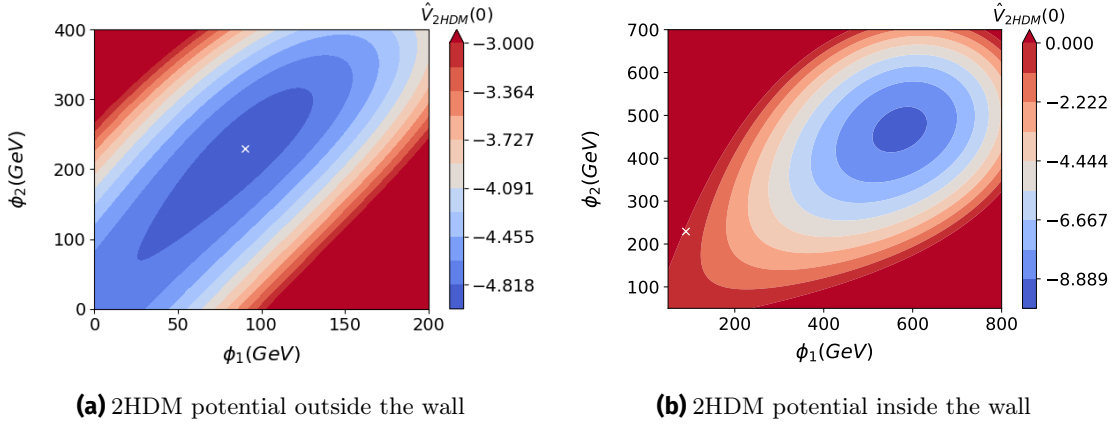


Figure 6.4: 2HDM potential in the background of the singlet domain wall $v_s(x)$. (a) 2HDM potential outside the wall, the EW vacuum is represented with a white cross and is protected from decaying to deeper vacua due to the presence of the potential barrier. (b) 2HDM potential inside the wall ($v_s = 0$). The EW vacuum is represented by a white cross. Inside the wall, the barrier between the EW vacuum and the deeper vacuum vanishes, and the scalar fields roll over from the EW vacuum to the deeper vacuum.

For P_1 we show in Figure 6.4 the potential of the Higgs doublets in the background of the domain wall, both outside (left) and inside the wall (right). The EW vacuum is represented by a white cross, and while it is protected by the potential barrier from tunneling to deeper vacua, the barrier disappears inside the wall, and the EW vacuum can roll over to the deeper vacuum. Notice that, inside the wall, $(v_1, v_2, 0)$ is not a stationary point of the potential and therefore the field will be unstable at that point.

The deeper vacuum can also be of electric charge breaking type \mathcal{CB} or type \mathcal{CP} (see P_2 and P_4 in Table 6.2). We verified that the rollover transition of the EW to such deeper vacua also occurs. In this case, small values of $v_+(0)$ start growing inside the wall, reach the values of a deeper vacuum, and then expand outside the wall.

Here again, the barrier between the EW vacuum and the global minimum disappears inside the domain wall, and the decay occurs via a classical rollover to the \mathcal{CB} vacuum as shown in Figure 6.5.

A similar behavior (see Figure 6.6) occurs for the decay of the EW metastable vacuum into a CP-violating global vacuum. The CP-violating phase $\xi(0)$ grows inside the wall, and once the global minimum is nucleated, it quickly expands outside.

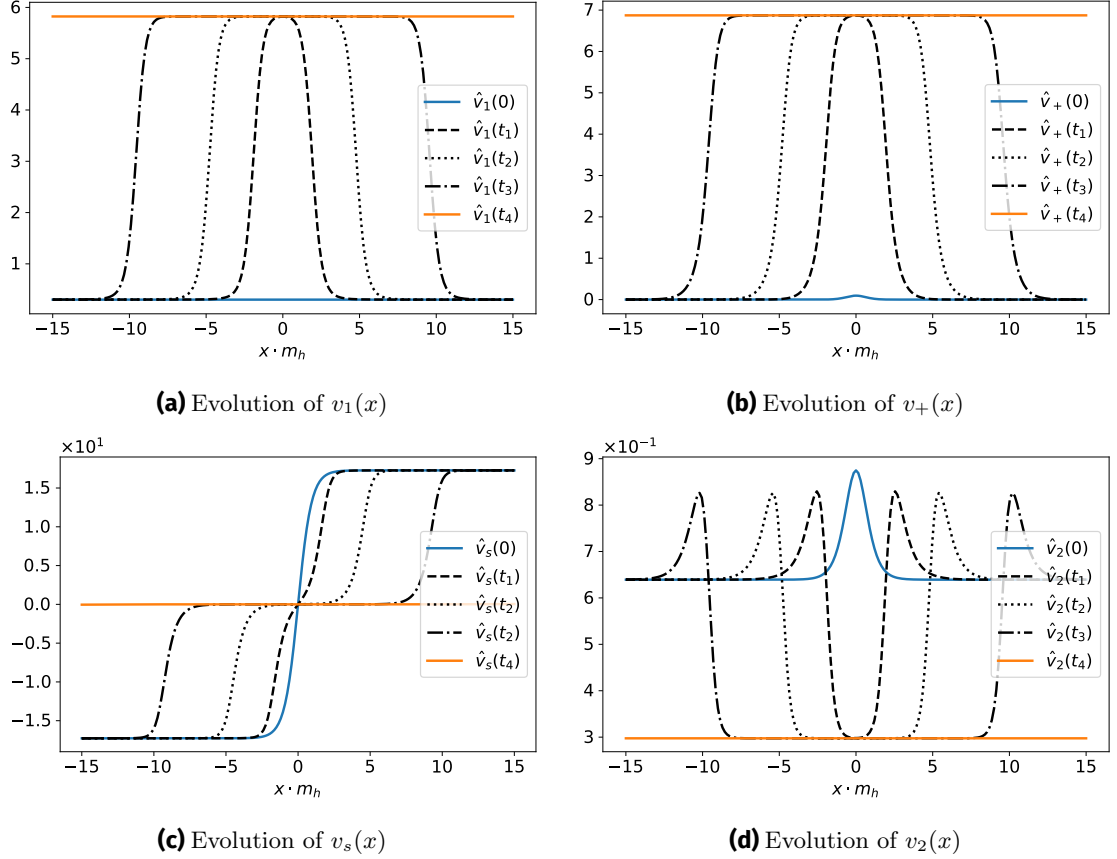


Figure 6.5: Evolution of the scalar fields inside the domain wall For the case when the deeper minimum is of \mathcal{CB} type. We start with the doublet scalar fields in the EW vacuum and show the evolution to the deeper vacuum. In this case, $v_+(0)$ acquires a VEV inside the wall, which then expands everywhere. The time steps are given by: $t_1 = 10.25m_h^{-1}$, $t_2 = 28.12m_h^{-1}$, $t_3 = 56.25m_h^{-1}$, and $t_4 = 90m_h^{-1}$.

6.3.1 Several extrema inside the wall

We observed that the decay of the EW vacuum inside the DW happens via a classical rollover into the true global vacuum of the potential. This happens due to the disappearance of the potential barrier between the initial field configuration $(v_1, v_2, 0)$ and the true minimum $(v_1^{true}, v_2^{true}, 0)$. Inside the wall, the 2HDM part of the EW vacuum $(v_1, v_2, 0)$ is not an extremum of the 2HDM potential at $x = 0$ (recall that inside the wall $v_s = 0$) since it does not, in general, satisfy the minimization conditions (2.12) and (2.13) of the potential in the ϕ_1 and ϕ_2 directions. We therefore have two possible scenarios:

- The 2HDM potential at $x = 0$ has only a single minimum that corresponds to the true global minimum. In this case, since $(v_1, v_2, 0)$ is not a stationary point of the potential, the EW vacuum experiences a rollover to the true vacuum, and we obtain a classical vacuum decay.
- The 2HDM potential at $x = 0$ has at least another intermediate minimum $(v_1^{int}, v_1^{int}, 0)$ between $(v_1, v_2, 0)$ and the true global minimum of the potential. In this case, the EW vacuum will either roll over to the intermediate vacuum and be trapped there, or roll over to the true global minimum, or roll over to the intermediate vacuum and later tunnel to the true vacuum. In case the intermediate minimum is lower than the EW minimum (v_1, v_2, v_s) , we will also experience a classical rollover vacuum decay via domain walls even if we don't

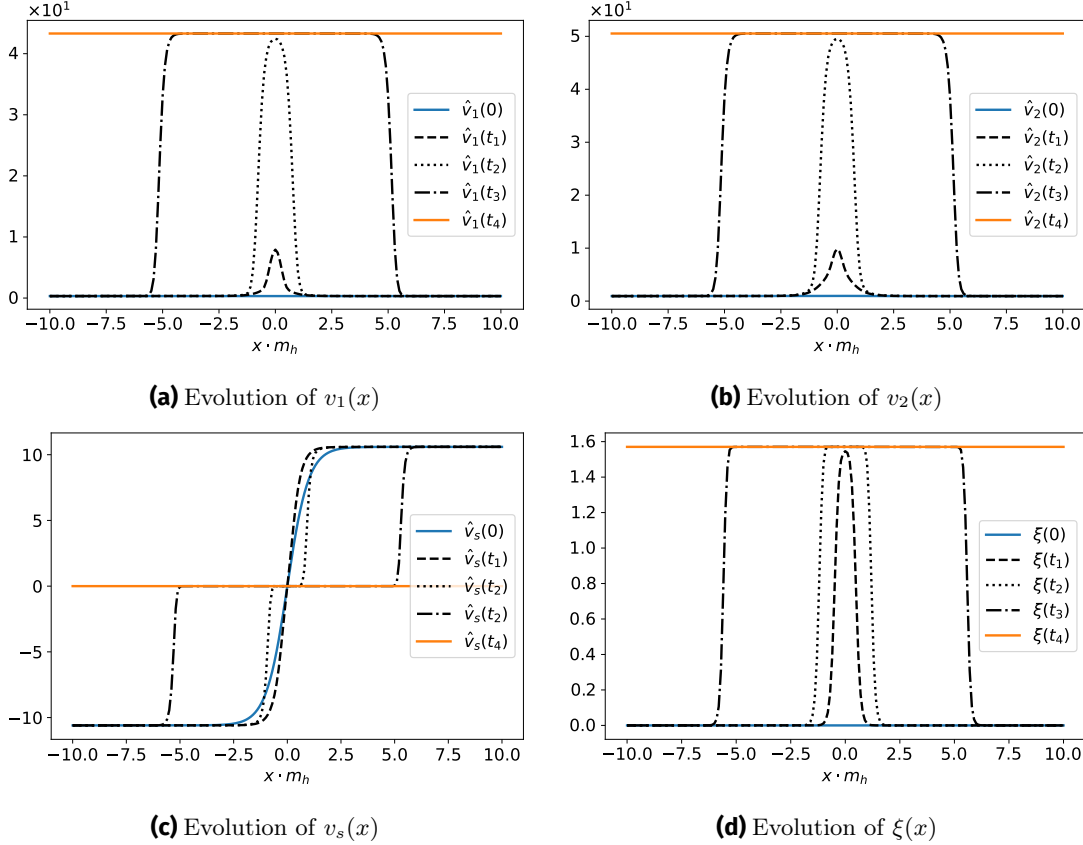


Figure 6.6: Evolution of the scalar fields inside the domain wall For the case when the deeper minimum is of \mathcal{CP} type. We start with the doublet scalar fields in the EW vacuum and show the evolution to the deeper vacuum. In this case, $\xi(x=0)$ acquires a non-vanishing value inside the wall, which then expands everywhere. The time steps are given by: $t_1 = 10m_h^{-1}$, $t_2 = 20m_h^{-1}$, $t_3 = 50m_h^{-1}$, and $t_4 = 100m_h^{-1}$.

reach the true global minimum of the potential. The possibility of tunneling inside the DW from the intermediate vacuum into the true global vacuum requires a detailed study of the temperature evolution of the effective potential as well as the annihilation time of the domain wall network, and is beyond the scope of our work. We therefore reserve its investigation for a future study⁴.

The existence of several distinct minima for the 2HDM potential inside the wall can complicate the analysis of the fate of the EW metastable minimum. When intermediate minima exist (see e.g. the potential in Figure 6.7a), one needs to verify if the EW vacuum decays or not by following the time evolution of the scalar fields inside and outside the wall. This also depends heavily on the magnitude of the friction term d in (6.9) since the field configuration would oscillate around the intermediate minimum and can eventually move over the potential barrier to the global minimum. If, however, the true global vacuum is the only minimum of the 2HDM potential inside the DW, then the EW vacuum will necessarily decay to the true vacuum via a classical rollover, and no DW simulation is needed.

It is possible in the 2HDM to determine analytically if the potential has several coexisting stationary points [187, 122]. In those publications, the authors discuss the necessary

⁴ In all the parameter scans that will be discussed later, we didn't find a parameter point where the fields are trapped in an intermediate minimum when taking the friction term to be small.

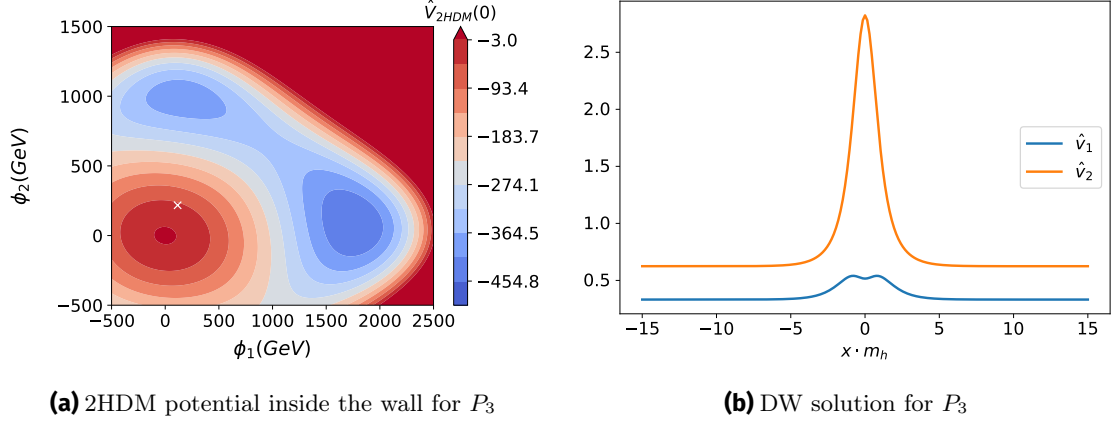


Figure 6.7: 2HDM potential inside the domain wall and DW solutions of parameter points P_3 with $\hat{d} = \frac{d}{m_h} = 1$.

conditions⁵ needed so that the 2HDM potential can have two coexisting neutral minima: the EW one and another one dubbed the panic vacuum, which could lie lower in the potential and lead to different masses of the gauge bosons and SM fermions. The two conditions for the possibility of the presence of two neutral minima in the potential are:

$$m_{22}^2 + k^2 m_{22}^2 < 0, \quad (6.10)$$

$$\sqrt[3]{x^2} + \sqrt[3]{y^2} \leq 1, \quad (6.11)$$

where:

$$x = \frac{4km_{12}^2}{m_{11}^2 + k^2 m_{22}^2} \frac{\sqrt{\lambda_1 \lambda_2}}{\lambda_{345} - \sqrt{\lambda_1 \lambda_2}}, \quad (6.12)$$

$$y = \frac{m_{11}^2 - k^2 m_{22}^2}{m_{11}^2 + k^2 m_{22}^2} \frac{\lambda_{345} + \sqrt{\lambda_1 \lambda_2}}{\sqrt{\lambda_1 \lambda_2} - \lambda_{345}}, \quad (6.13)$$

$$k = \sqrt[4]{\frac{\lambda_1}{\lambda_2}}. \quad (6.14)$$

If these conditions are not met, the 2HDM potential only admits a single minimum, and we conclude that the DW will necessarily induce the rollover transition of the EW vacuum. However, if these conditions are met, we verify the existence of intermediate minima in the 2HDM potential at $x = 0$ using **EVADE**. For parameter points where the extra stationary points are either maxima or saddle points, the EW vacuum decays via a classical rollover to the deeper vacuum. However, if the extra stationary points are local minima, in that case, one should numerically verify the real-time evolution of the scalar field configurations inside the DW in order to determine the fate of the EW metastable vacuum. We consider P_3 (see Table 6.2) as an example for a parameter point where the 2HDM potential inside the wall has at least another minimum alongside the deepest global minimum. The local minimum at $(v_{1,i}, v_{2,i}) = (172 \text{ GeV}, 991 \text{ GeV})$ lies higher in the potential than the EW vacuum (outside the wall). Notice that there is no barrier between the starting field values (corresponding to the EW vacuum) and the two minima, while there is a potential barrier between both minima.

In this case, the fate of the electroweak vacuum is dependent on the value of the friction term d in (6.9). For $\hat{d} = \frac{d}{m_h} = 1$, where \hat{d} is the dimensionless friction term⁶, the EW

⁵ These are necessary and sufficient conditions for the existence of 4 stationary points, but are not sufficient conditions to ensure that 2 of these stationary points are indeed minima.

⁶ Recall that we make all quantities in the equation of motion (6.9) dimensionless when solving it numerically.

vacuum rolls over to the intermediate minimum of the 2HDM potential inside the wall, briefly oscillates around that minimum, and gets trapped there since the kinetic energy in the scalar field is not enough to cross the barrier to the global minimum. This leads the EW vacuum to remain metastable (since the EW vacuum outside the wall lies lower in the N2HDM potential than this intermediate minimum). However, since the potential barrier between the intermediate minimum inside the wall and the global minimum can be smaller than the potential barrier between the metastable EW minimum and the global minimum, one should consider the possibility of quantum tunneling inside the wall. These scenarios were studied in detail in the case of the real singlet scalar extension of the SM, see e.g. [24, 21], where the authors use the domain walls as impurities to seed the EW phase transition inside the wall and rescue parameter points from vacuum trapping. We reserve the discussion of the quantum tunneling stimulated by domain walls leading to the EW vacuum decay to future work.

For the case when the friction term is smaller e.g. $\hat{d} = 0.05$, we observe the classical rollover to the intermediate minimum, the field oscillates around that minimum, and then crosses the barrier to the global minimum. Once the global minimum is nucleated inside the wall, we obtain the same behavior observed for the usual EW vacuum decay via domain walls.

Since we are working in the zero temperature limit at the radiation domination era, the Hubble parameter $\mathcal{H} \propto T^2/M_{pl}$ [190], which would act as a component in the friction term d , is very suppressed. Another, a priori, more sizable contribution might come from the interaction of the scalar fields with the thermal plasma, leading to the damping of the kinetic energy that the doublet fields start with. The evaluation of this contribution depends heavily on the thermal evolution and the coupling between the scalars and fermions.

Another very important issue is determining whether this intermediate minimum is also present just after EW phase transition, or if this minimum only develops after some time. In the case when the global minimum is the only minimum present in the doublet potential inside the wall at high temperatures after EW phase transition, the classical rollover will occur to the global minimum leading to the decay of the EW vacuum.

However, in case the intermediate minimum is also present in the potential at high temperatures just after EW phase transition, it is then possible that, after the EW phase transition, the intermediate vacuum is trapped inside the wall. This happens because the doublet fields lose their kinetic energy during their roll over. As the universe cools down, the friction term gets smaller, and as the singlet domain wall moves to other regions of the universe, the doublet fields experience less friction and those regions might undergo a domain walls induced EW vacuum decay.

We saw that there is no barrier between the initial doublet field configuration inside the wall $(v_1, v_2, 0)$, and the two minima (the global minimum and the intermediate minimum) inside the wall. Thermal or quantum fluctuations can also play an important role in determining into which direction the doublet fields start rolling over.

All these aspects require a careful study of the thermal history of particular parameter points and we leave their discussion for a future study.

	m_{H^\pm}	m_A	v_s	$C_{h_2VV}^2$	$C_{h_2t\bar{t}}^2$	R_{23}	m_{12}^2
1	[200, 1500]	[200, 1500]	[1, 10^4]	[0.6, 1]	[0.6, 1]	[-1, 1]	[0, $5 \cdot 10^4$]
	m_{H^\pm}	m_A	v_s	$C_{h_1VV}^2$	$C_{h_1t\bar{t}}^2$	R_{13}	m_{12}^2
2	[200, 1500]	[200, 1500]	[1, 10^4]	[0.6, 1]	[0.6, 1]	[-1, 1]	[0, $5 \cdot 10^4$]

Table 6.3: Set of input parameters for our `ScannerS` scans with all parameters in GeV unit. For Scenario 1, the masses of the CP-even Higgs particles are: $m_{h_1} \in [94, 96]$ GeV, $m_{h_2} = 125.09$ GeV and $m_{h_3} \in [200, 1500]$ GeV. For Scenario 2, the masses of the CP-even Higgs particles are: $m_{h_1} = 125.09$ GeV, $m_{h_2} = 400$ GeV and $m_{h_3} \in \{600, 800, 1200\}$ GeV. For both scans, the range of v_s is between 1 and 10^4 GeV, while $\tan(\beta) \in [0.5, 3]$. The scans were conducted over all types 1-4.

6.4 PHENOMENOLOGICAL SCENARIOS FOR METASTABILITY

In this section, we discuss some phenomenological scenarios leading to the separation of parameter regions with metastable and stable EW vacua. We saw in the previous section that a free parameter scan did not provide a correlation between parameter variables and the nature of the EW vacuum. We now study some specific scenarios where we fix some parameter variables of the model.

For the parameter scans generated using `ScannerS`, we impose the theoretical constraints of boundedness from below and perturbative unitarity. We also make sure that the generated parameter points cannot be unstable i.e. all generated parameter points are either stable or have a bounce action $B > 390$. We don't directly impose the requirement of Z'_2 and electroweak symmetry restoration in the early universe based on the analytical conditions derived in [23] and summarized in 5.2.1. We later check if those conditions are fulfilled by the generated set of parameter points. These conditions are based on the Arnold-Espinosa Daisy resummation method. It was argued in [155] that other resummation methods do not show symmetry non-restoration in the 2HDM. Since this might also be the case in the N2HDM, we also include, in our analysis, parameter points that feature the possibility of symmetry non-restoration. This is done in order not to overlook other possible metastable parameter points that would be ruled out by vacuum decay via domain walls and, more importantly, not to overlook parameter points that have a stable EW vacuum but feature symmetry non-restoration. If, however, symmetry non-restoration actually occurs (up to ultra-high energies in the early universe) and is not an artifact of the resummation method, then showing these parameter points is important to keep in mind that these parameter points could still be rescued from vacuum decay via domain walls. In any case, a careful determination of the thermal evolution at high temperatures using different resummation schemes would be crucial.

In case when parameter points with symmetry-restored metastable EW vacua overlap with symmetry non-restored metastable parameter points in the whole scan range, we plot both types in orange. Metastable parameter points with symmetry non-restoration are only shown explicitly if they can be separated from regions with only symmetry restoration. Therefore, unless otherwise specified, parameter regions in orange include both types of metastable vacua.

We start our discussion with scans where the experimental constraints of electroweak precision observables, as well as flavor and Higgs searches are not imposed. This is done in order to avoid those constraints "incidentally" ruling out some regions that contain stable EW minima, and therefore leading to the generation of regions with only metastable

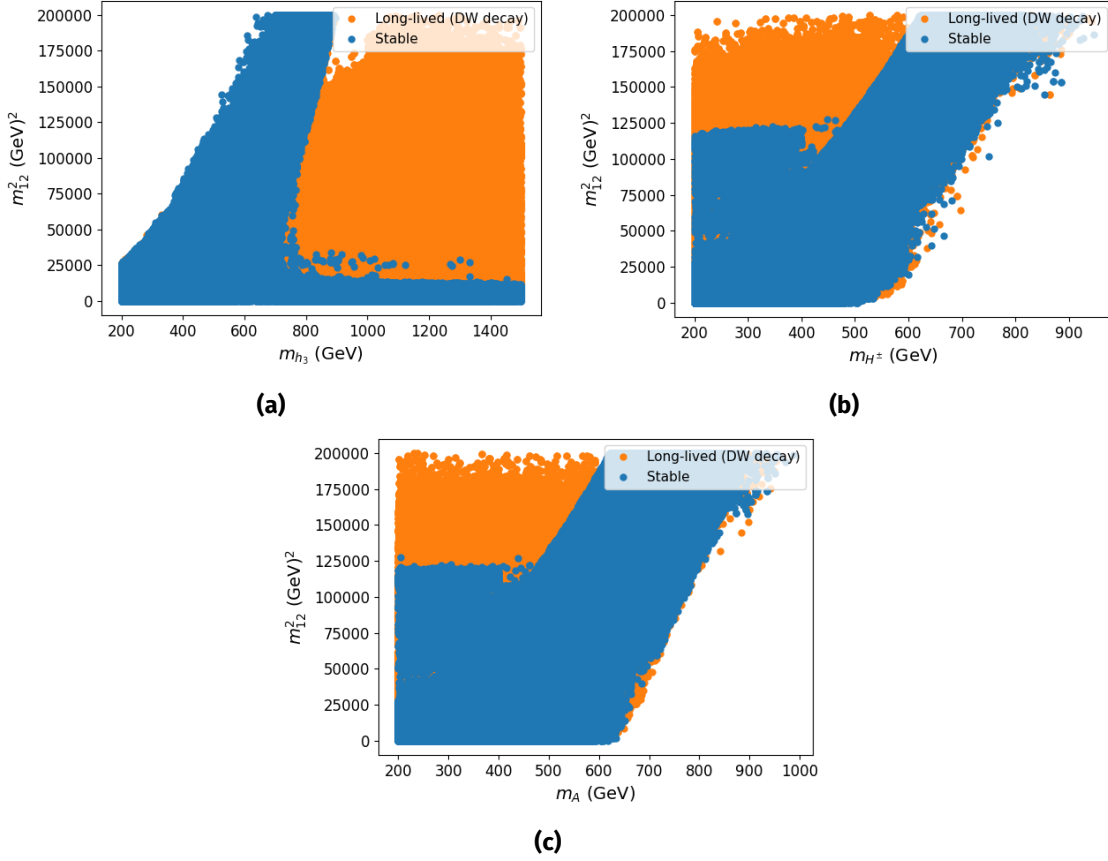


Figure 6.8: Results of Scan 1 showing the possibility to separate the metastable-only region from the regions of parameter space which include both stable and metastable vacua.

minima. Since we want to emphasize the possibility of our mechanism in inducing the EW vacuum decay via domain walls as a new important constraint on its own, it is important to make sure that experimental constraints don't filter parameter points with stable EW vacua from regions that also have metastable vacua. We later discuss a scan where all experimental constraints were also imposed and show that the mechanism of EW vacuum decay via domain walls can rule out parameter regions that are otherwise still viable.

6.4.1 Scenario 1: a 95 GeV CP-even Higgs particle

We first start with a general parameter scan of 850×10^3 points where we take the lightest CP-even Higgs boson to have a mass between 94 GeV and 96 GeV, which is motivated by the excesses observed by the CMS [167] and ATLAS collaborations [191]. We fix the mass of the CP-even Higgs particle h_2 to $m_{h_2} = 125.09$ GeV, corresponding to the SM Higgs boson and allow the mass of h_3 to vary between 200 GeV and 1500 GeV. We vary the masses of the charged and CP-odd Higgs bosons as well as the parameters m_{12}^2 , $\tan \beta$, v_s , and the mixing angles (see Table 6.3). This first scan is done in order to obtain the most general correlations in the parameters that lead to the separation of stable and metastable regions of the parameter space.

The parameter points with a stable electroweak minimum are shown in blue, while the parameter points with a metastable EW minimum and a global minimum with $v_s = 0$ are shown in orange.

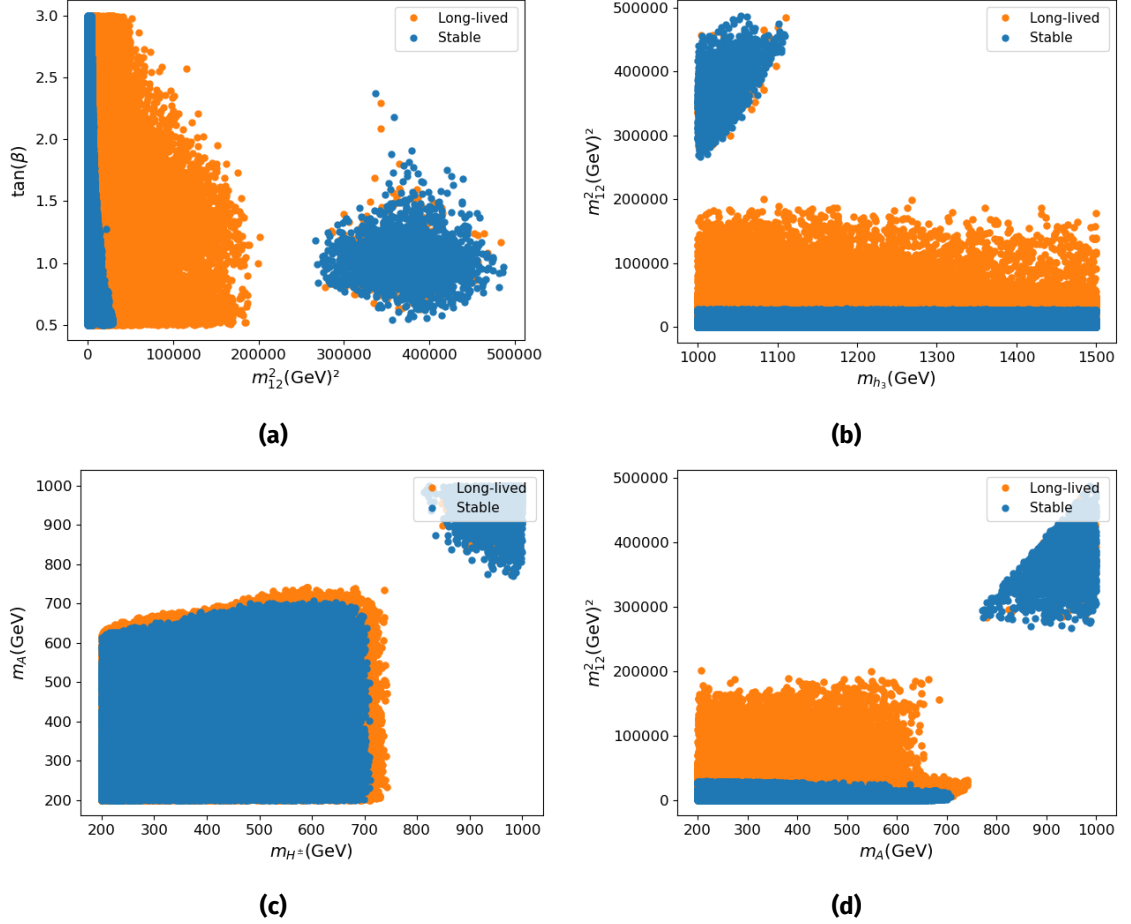


Figure 6.9: Results of Scan 1 showing the possibility to separate the metastable-only region from the regions of parameter space which include both stable and metastable vacua.

The results are shown in Figure 6.8. We observe a clear separation between stable and metastable regions only in the $m_{h_3} - m_{12}^2$ as well as the $m_A - m_{12}^2$, and the $m_{H^\pm} - m_{12}^2$ planes as shown in Figure 6.8. This metastable-only region is obtained for $m_{h_3} > 900$ GeV and $m_{12}^2 > 30000$ GeV. The obtained results do not show any dependence on v_s . The dependence on the mixing angles is modeled in our case by the singlet admixture $\Sigma_i = R_{i3}^2$ as well as the coupling of the SM-like Higgs boson to gauge bosons (c_{2V}^2) and top quarks (c_{2tt}^2). Both stable and metastable minima overlap over the scanned parameter regions for the mixing angles. Note that the symmetry non-restoration metastable points overlap with the ones where we obtain symmetry restoration. Therefore, one can exclude those regions based on DW induced vacuum decay only if symmetry non-restoration is an artifact of the Arnold-Espinosa daisy resummation scheme.

Motivated by these results, we perform several specific parameter scans:

1. Scan of the region $1000 \text{ GeV} < m_{h_3} < 1500 \text{ GeV}$ and $(2.5 \cdot 10^4 < m_{12}^2 < 5 \cdot 10^4) \text{ GeV}^2$.
2. Scan with fixed $m_{12}^2 = 2 \cdot 10^4 \text{ GeV}^2$ and variable m_{h_3} , $\tan(\beta)$, m_A , and m_{H^\pm} .
3. Scan with fixed $m_{h_3} = 600 \text{ GeV}$ and variable m_{H^\pm} , m_A , $\tan(\beta)$, and m_{12}^2 .
4. Scan with fixed $m_{h_3} = 1000 \text{ GeV}$ and variable m_{H^\pm} , m_A , $\tan(\beta)$, and m_{12}^2 .
5. Scan with fixed $m_{h_3} = 1000 \text{ GeV}$ and variable m_{H^\pm} , m_A , and m_{12}^2 but in the alignment limit.

The results for scan 1 are shown in Figure 6.9. We find that the region of metastability depends heavily on m_{12}^2 , and, to a lesser extent, on $\tan(\beta)$. The region of vacuum stability is concentrated at $m_{12}^2 < 3 \cdot 10^4 \text{ GeV}^2$ for $\tan(\beta) < 1$. For higher values of $\tan(\beta)$ the region of vacuum stability falls to $m_{12}^2 < 10^4 \text{ GeV}^2$. For this scan, we find that all parameter points between $(3 \cdot 10^4 < m_{12}^2 < 2 \cdot 10^5) \text{ GeV}^2$ are metastable. Note that for much higher values of $2.5 \cdot 10^5 \text{ GeV}^2 < m_{12}^2$, we also find a region where vacuum stability and metastability coexist.

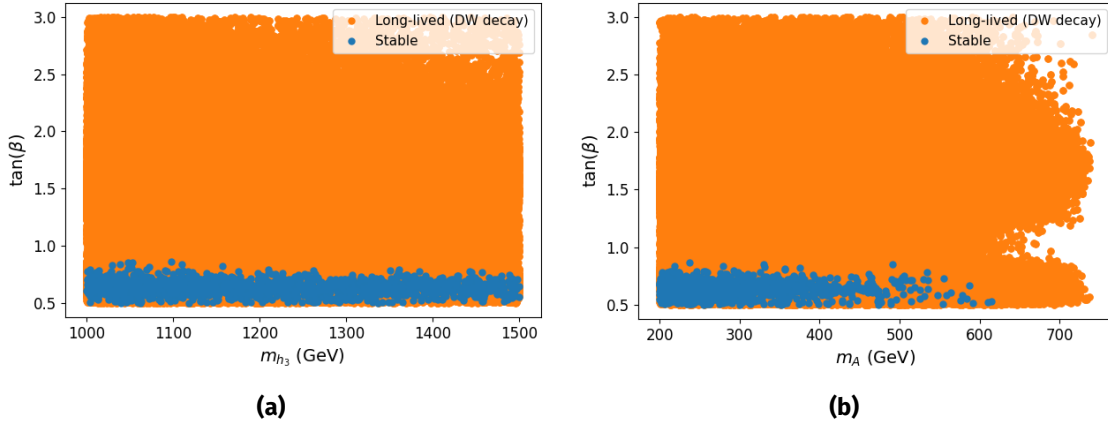


Figure 6.10: Results of Scan 2 showing the possibility to separate the metastable-only region from the regions of parameter space which include both stable and metastable vacua. We find that parameter points with stable EW vacua are concentrated at low $\tan(\beta)$.

For the second scan, we find that the parameter points with stable minima are concentrated around small $\tan(\beta) < 0.9$ values (see Figure 6.10). Note that when we performed a scan for parameter points with $m_{h_3} > 1000 \text{ GeV}$ and fixed $m_{12}^2 = 3 \cdot 10^4 \text{ GeV}^2$, the region of parameter points with stable vacua reduces to $\tan(\beta) < 0.7$. This is in agreement with the observation that, as we increase m_{12}^2 , the region with stable vacua disappears for all $\tan(\beta)$.

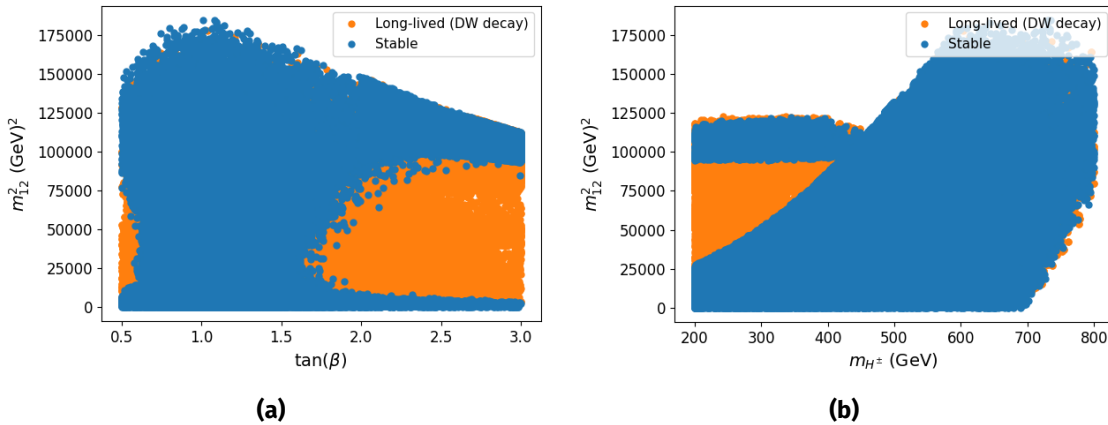


Figure 6.11: Results of Scan 3 showing the possibility to separate the metastable-only region from the regions of parameter space which include both stable and metastable vacua.

For the third scan, we fix $m_{h_3} = 600 \text{ GeV}$ and vary the other parameters. As shown in Figure 6.11, we find that parameter region with only metastable vacua is concentrated in the region of low m_{H^\pm} and m_A and $(2.5 \cdot 10^4 < m_{12}^2 < 9 \cdot 10^4) \text{ GeV}^2$. This region also corresponds to values $2 < \tan(\beta) < 3$.

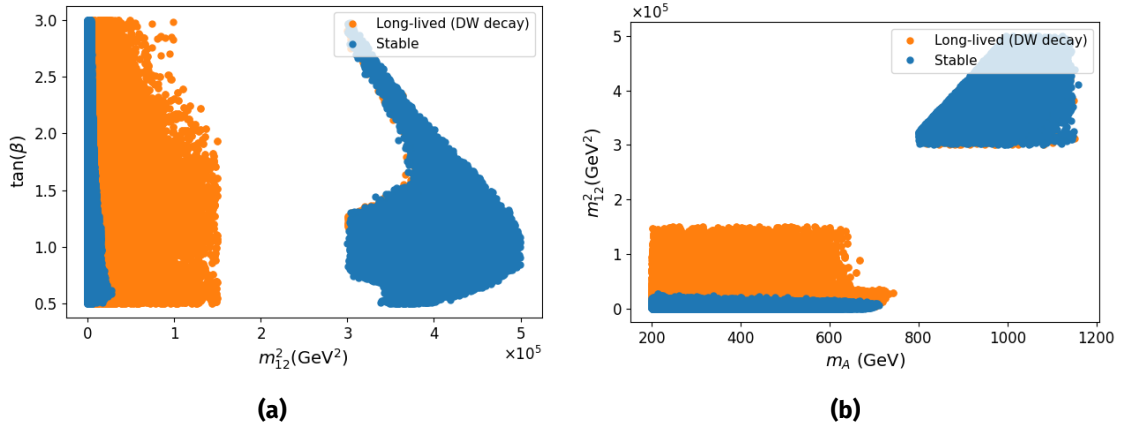


Figure 6.12: Results of Scan 4 showing the possibility to separate the metastable-only region from the regions of parameter space which include both stable and metastable vacua.

As for the fourth scan, we find that the results depend on m_{12} and $\tan\beta$. In this scan, parameter points with $(3 \times 10^4 < m_{12}^2 < 2 \cdot 10^5) \text{ GeV}^2$ and low $\tan\beta < 1$ were always metastable, while parameter points with higher $\tan\beta < 3$ showed metastable region already at smaller $(10^4 < m_{12}^2 < 10^5) \text{ GeV}^2$ (See Figure 6.12a). When extending the scan to higher values of m_{12}^2 , we also find a region where stable and metastable vacua coexist which is characterized by masses m_A and m_{H^\pm} of the order $\mathcal{O}(1 \text{ TeV})$.

For the final scan with the same range but at the alignment limit where $c_{2VV}^2 = c_{2tt}^2 \approx 1$. We find, for this scan, that regions of stability and metastability overlap with each other for all variables and therefore, we cannot use this mechanism to rule out parameter point regions and the DW decay mechanism can only be used to rule out individual parameter points.

To summarize our results, we find that for this particular scenario, the variable m_{12}^2 and to a lesser extent $\tan(\beta)$ play a crucial role in determining regions of parameter space that are only metastable. However, we found that for these regions, symmetry restored parameter points as well as parameter points with possible symmetry non-restoration (according to the Arnold-Espinosa resummation scheme) overlap. In order to be able to conclusively rule out those parameter regions using DW induced vacuum decay, this possibility of symmetry non-restoration needs to be addressed in detail, which is beyond the scope of this work.

6.4.2 Scan including experimental constraints

We now generate parameter points with `ScannerS`, taking also into account experimental constraints such as collider searches, flavor constraints, and electroweak precision measurements. We focus on a parameter scan with $m_{h_3} = 600 \text{ GeV}$.

We find that the region where only metastable vacua are obtained is independent on v_s . Again, one can use the variable m_{12}^2 to differentiate between stable and metastable regions. We find that lower values lead to regions with mostly metastable EW minima, while parameter points with higher values of m_{12}^2 lead to both stable and metastable EW minima. However, for very small $m_{12}^2 < 15 \cdot 10^3 \text{ GeV}^2$, we can also obtain parameter points with stable EW vacua, and we show these parameter points as black circles. Therefore, one can use the mechanism of vacuum decay via domain walls to exclude lower values of m_{12}^2 in this scenario up to $m_{12}^2 = 15 \cdot 10^3 \text{ GeV}^2$.

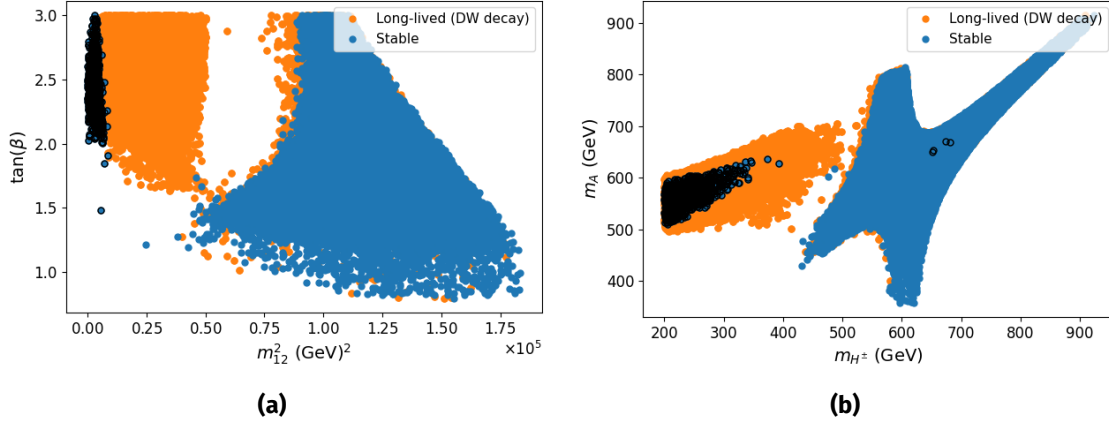


Figure 6.13: Parameter scan for $m_{h_3} = 600$ GeV after applying all experimental constraints. The parameter points shown in black circles have a stable EW vacuum but with very low values of $m_{12}^2 < 15 \cdot 10^3$ GeV².

We also find a correlation between the masses of H^\pm and A and the regions featuring mostly metastable EW minima as shown in Figure 6.13b. This is the case for mostly lower values for H^\pm , and A and $m_{12}^2 > 15 \cdot 10^3$ GeV².

Finally, one can use the singlet admixture $\Sigma_i = R_{i3}^2$ in order to differentiate between regions of EW minimum metastability and stability. We find that parameter points where the singlet admixture in h_3 is higher lead to regions with metastable EW vacua only.

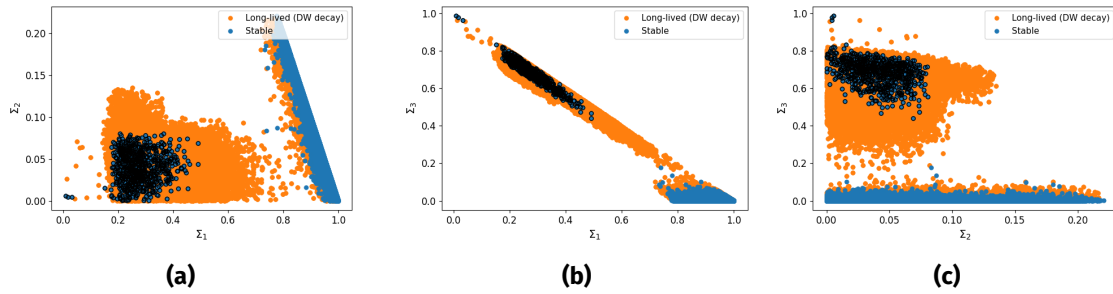


Figure 6.14: Scenario 1: Stability of the EW minimum for different parameter scans as a function of Σ_i , the singlet admixture in the CP-even Higgs bosons. The parameter points shown in black circles have a stable EW vacuum but with very low values of $m_{12}^2 < 15 \cdot 10^3$ GeV².

6.4.3 Scenario 2: SM Higgs as the lightest CP-even Higgs boson

We now consider the case when the SM Higgs is the lightest CP-even Higgs boson. We fix the second CP-even Higgs mass to $m_{h_2} = 400$ GeV, and allow the mass of h_3 to take the values $m_{h_3} \in \{600, 800, 1200\}$ GeV. We keep the same scan range for all the other model parameters as shown in Table 6.3.

The results of the scan are shown in Figures 6.15 and 6.16. For this scan, the distinction between parameter point regions with solely metastable minima and regions with both stable and metastable minima is not possible, and one cannot use the decay of the EW vacuum induced by the domain walls in order to systematically rule out specific parameter regions like in scenario 1.

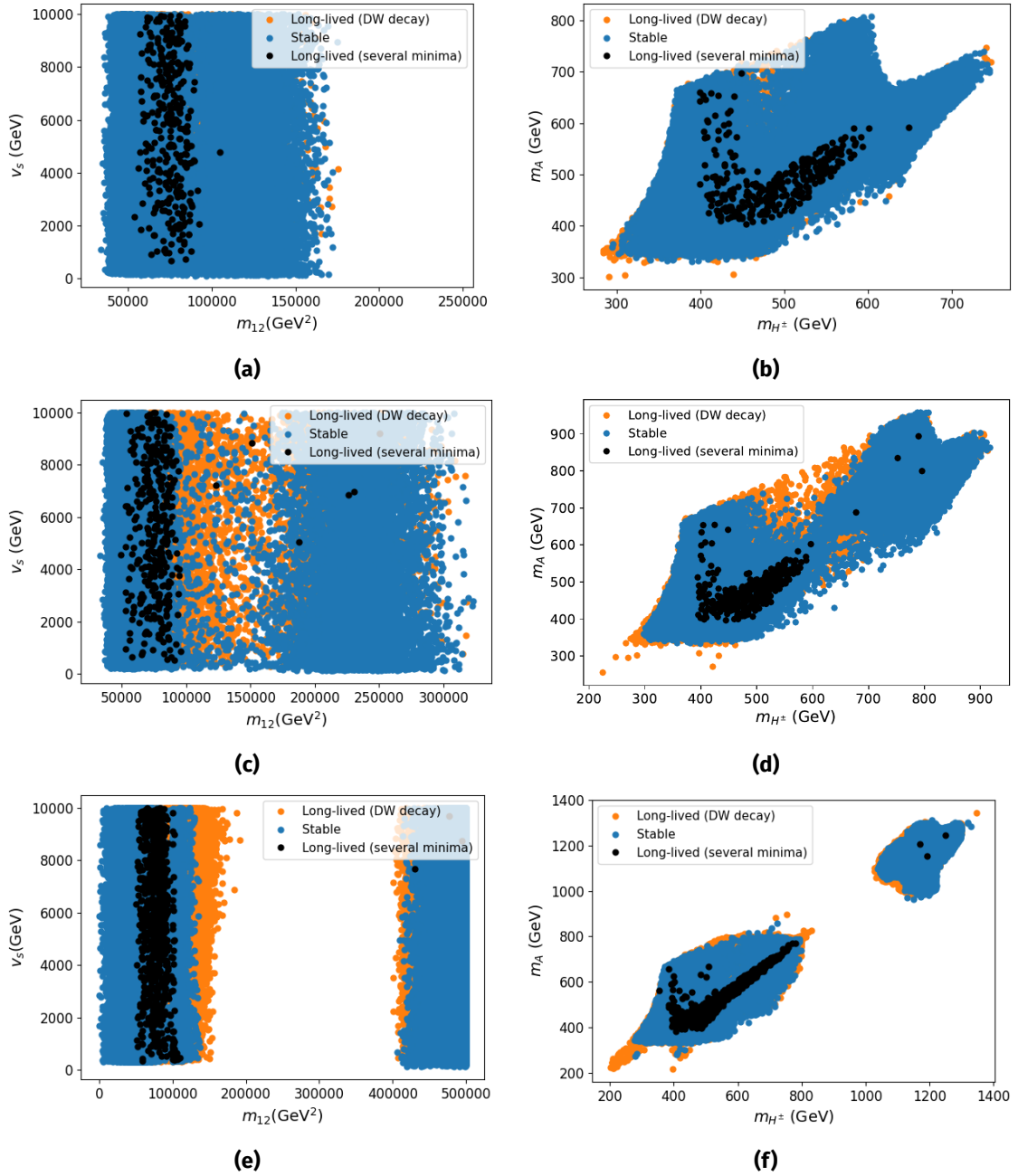


Figure 6.15: Scenario 2: Stability of the EW minimum for different parameter scans as a function of the singlet VEV v_s and Z_2 breaking term m_{12} . (a) and (b) correspond to a mass $m_{h_3} = 600$ GeV, (c) and (d) correspond to a mass $m_{h_3} = 800$ GeV, and (e) and (f) correspond to a mass $m_{h_3} = 1200$ GeV.

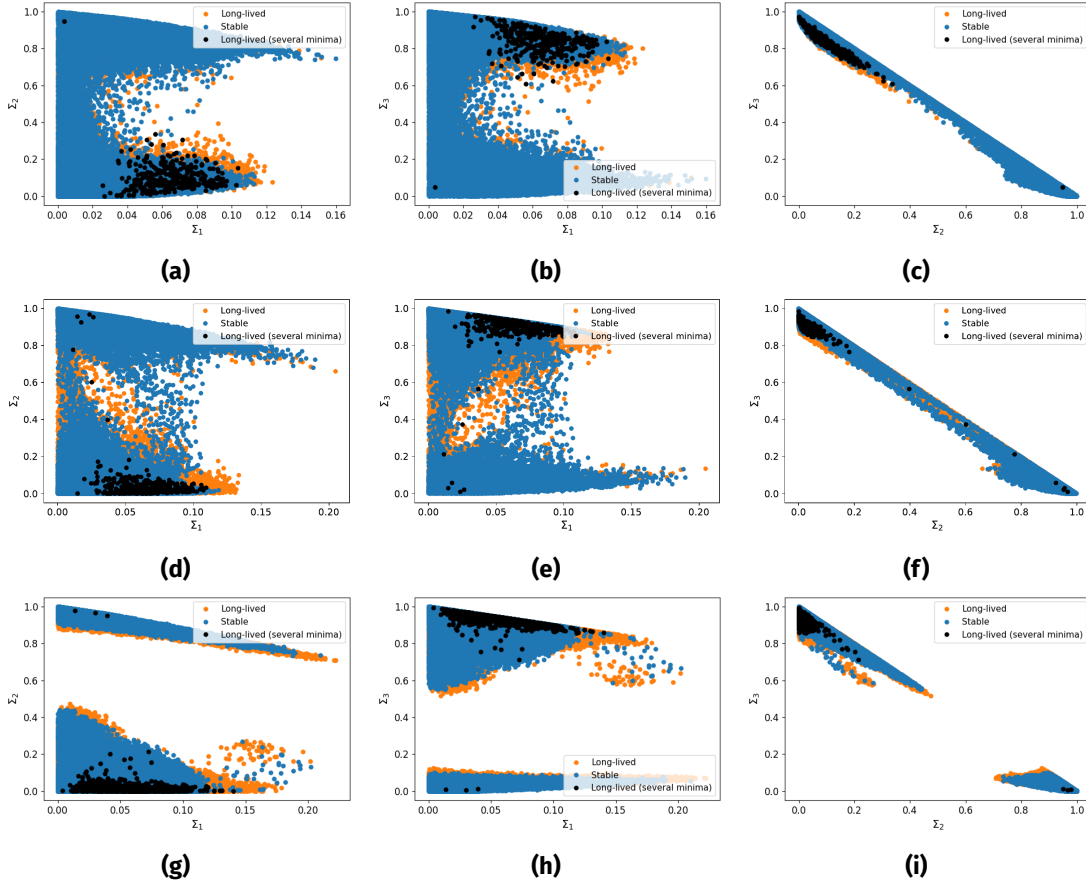


Figure 6.16: Scenario 2: Stability of the EW minimum for different parameter scans as a function of Σ_i the singlet admixture in the CP-even Higgs bosons. Upper row corresponds to the scan with $m_{h_3} = 600$ GeV, middle row corresponds to $m_{h_3} = 800$ GeV, and lower row to $m_{h_3} = 1200$ GeV.

We obtain several parameter points featuring at least two minima for the potential at $v_s = 0$ GeV. In all three scans, these points were concentrated around ($5 \cdot 10^4 < m_{12}^2 < 10^5$) GeV^2 , $\tan(\beta) > 1.5$, as well as around the same range of the masses for $m_{H^\pm, A}$ and the singlet admixture, which shows that this effect is more pronounced for parameter points with a large singlet admixture in the heavier CP-even Higgs. Note here that the singlet admixture in the SM-like Higgs boson h_1 is quite low in these scans since larger values are already ruled out by Higgs measurement and searches at the LHC [124, 125, 164].

This leads to the possibility that the global minimum is not nucleated inside the domain wall and instead, the scalar fields converge to the intermediate minimum. For those parameter points (shown in black). We explicitly calculate the real-time evolution (6.9) of the DW solution to determine the fate of the metastable EW minimum using $\dot{d} \approx 0$. We find that all these parameter points roll over to the global minimum, leading to the decay of the long-lived EW vacuum. One cannot, however, conclude that any parameter point with multiple minima will necessarily experience vacuum decay via domain wall, and the possibility that the field configuration gets trapped inside the intermediate vacuum for some other parameter points is still possible. In such a case, one would then need to calculate the tunneling rate between the trapped field configuration and a field configuration where the global vacuum is nucleated inside the wall. We leave the investigation of this possibility to a future work.

6.5 DISCUSSION

In this chapter, we investigated the decay of the long-lived metastable EW vacuum induced by the domain walls in the N2HDM. This mechanism of vacuum decay can be used in order to rule out a large number of (otherwise viable) parameter points in several scenarios. In the standard N2HDM, where the model is invariant under the Z'_2 symmetry, the formation of domain walls related to the scalar singlet leads to the possibility that the scalar doublet potential inside the wall can be very different in comparison to the potential outside the wall. For parameter points where the global minimum has a vanishing singlet VEV, the field configuration inside the domain wall can roll over to the global minimum. Since the potential of the global minimum is lower than the EW metastable minimum outside the wall, the global vacuum gets nucleated inside the wall and then quickly expands outside, leading to the total decay of the EW vacuum. Those parameter points are thus not allowed since the masses of all particles will have very different values.

We checked that the mechanism of vacuum decay occurs for all types of vacua in the N2HDM: neutral, electrically charged as well as CP-violating vacua. We also showed that one can use this mechanism in certain scenarios to rule out some regions of parameter points. In particular, we found that in case of a possible 95-GeV Higgs boson, the region of metastability depends heavily on the values of m_{h_3} , m_{12}^2 , and $\tan(\beta)$.

One important aspect that we found in our work was the possibility that, inside the wall, several minima in the doublets potential can coexist alongside the global minimum. This observation makes it not possible to directly rule out a parameter point of the model based only on the metastability of the EW vacuum. In such cases, one needs to explicitly compute the real-time evolution of the scalar field configuration inside the domain wall to determine whether the global vacuum will be nucleated inside the wall. Even though several parameter points featured this case of multiple minima, we didn't find a parameter point in our large scans where the field configuration inside the wall is trapped in the intermediate vacuum. If a parameter point leads to such behavior, one then needs to calculate the tunneling rate between the trapped field configuration and the field configuration where the global vacuum is nucleated inside the wall. These calculations are non-trivial and numerically time-consuming. We therefore leave the discussion of quantum tunneling induced by the domain wall field configuration to a future work.

We showed that many parameter points of the Z'_2 symmetric N2HDM would be ruled out due to domain wall EW vacuum decay. This mechanism provides strong constraints for this model by ruling out parameter points that lead to long-lived metastable EW vacua. There are, however, possible ways to circumvent this constraint. First, one could break the Z'_2 symmetry by introducing large symmetry-breaking terms in order to avoid the formation of domain walls altogether. This, however, can considerably alter the phenomenology of the N2HDM. Another way is to only choose parameter points where the Z'_2 symmetry is not spontaneously broken and $v_s = 0$. One could also use parameter points that feature Z'_2 symmetry non-restoration, which avoids the formation of the domain walls in the early universe. This final solution requires, however, a detailed and careful use of the daisy resummation methods in order to obtain reliable results.

7 | SUMMARY AND OUTLOOK

In this manuscript, we studied domain wall solutions in several extended Higgs sectors. Traditionally, domain walls in the early universe are particularly discussed in the context of their gravitational wave signal emitted during their annihilation, a topic that gained a lot of renewed interest in the wake of the recent PTA results [18, 19, 14, 15]. However, we showed that domain walls can also be relevant for many other applications in the early universe, such as generating chiral asymmetries, providing electric charge violating field configurations, leading to EW symmetry restoration, creating a matter-antimatter asymmetry, and leading to the decay of long-lived metastable EW minima.

In particular, we showed in chapter 3 that domain wall solutions in the 2HDM can be classified into several classes with each having different properties. This is due to the simultaneous spontaneous breaking of the discrete symmetry alongside the EW symmetry, leading to a vacuum manifold made of two disconnected 3-spheres. Since, in this case, there are several choices for the boundary conditions at spatial infinity compared with the standard Z_2 case, scalar field configurations with new features localized on the wall can occur, such as CP and electric charge violating field configurations.

In the case of the electric charge violating field configurations, the $U(1)_{em}$ symmetry of electromagnetism was broken inside the wall, making photons massive and leading to electric charge violating interactions with SM particles. This behavior was related to having different Goldstone modes at the boundaries, and we showed that such domain wall solutions can even have smaller energy than the standard domain wall solutions where the Goldstone modes are the same on the boundaries. We also showed in this case that standard domain wall solutions eventually evolve to the electric charge-breaking field configuration. From a theoretical point of view the breaking of $U(1)_{em}$ can be understood in terms of the "clash-of-symmetries" mechanism which states that, due to having different Goldstone modes on the boundaries, we obtain different embeddings of $U(1)_{em}$ in $SU(2)_L \times U(1)_Y$ on both domains, reducing the symmetry group inside the wall to the trivial identity I .

One possible future extension could be investigating this behavior in other extended Higgs models, such as the 3HDM or Grand Unified Theories. Another possibility is to study the stability of these scalar field configurations by determining in a detailed way their relaxation to the lowest energy domain wall solutions. One could also check the stability of domain wall solutions in the 2HDM where the gauge fields are non-zero, due e.g. for the presence of primordial magnetic or electric fields in the early universe.

Having obtained these scalar field configurations, we later looked, in chapter 4, at their interactions with SM particles such as top and bottom quarks (which have the largest Yukawa couplings to the Higgs sector). We solved the Dirac equation for scattering states in the background of the different types of scalar field configurations. We showed in the case of CP-violating scalar field configurations that left and right-handed particles scatter off the wall at different rates, leading to a chiral asymmetry in front and behind the wall. In the case of the electric charge violating field configurations, we showed that, e.g., top quarks can be reflected or transmitted through the wall as bottom quarks and that the rate

of this transformation is higher for particles with higher incoming momenta. One important issue that needs further investigation is the appearance of negative transmission coefficients for the chiral states (left or right-handed components). This behavior is similar to the case of a Klein-Paradox in QED [142], where electrons with high enough momenta can lead to particle-antiparticle pair creation when hitting a step-like potential of an electric field. Looking at this issue in more detail, including a quantum field theory treatment, is a possible future direction of this work. Another idea is to look at a new production mechanism for keV scale sterile neutrinos in the presence of electric charge breaking scalar field configurations in the early universe. These field configurations generate a non-zero mixing for the sterile neutrinos with SM leptons, leading to the possible transformation of SM leptons into sterile neutrinos upon hitting the walls.

Motivated by the observation of this chiral asymmetry caused by the interaction of SM fermions with the DW in the 2HDM, we wanted to investigate, in chapter 5, the possibility of using domain walls in order to generate the observed matter-antimatter asymmetry of the universe. This idea of having electroweak baryogenesis using topological defects was already introduced in the 90s [144, 145, 106, 146, 192] and it was shown that it can't produce a large enough asymmetry in the case of one-dimensional defects like cosmic strings. The case of domain walls, a two-dimensional defect, is certainly more appealing.

In contrast with conventional electroweak baryogenesis, where a first-order phase transition is mandatory to produce bubbles that separate the region where sphalerons are active from the regions where they are suppressed, domain walls electroweak baryogenesis can be achieved irrespective of the type of the phase transition that caused the formation of the walls. Its main idea is relying on a domain wall scalar field configuration that couples with the electroweak Higgs doublet(s), since such a singlet scalar field will vanish inside the core of the DW, the effective mass term of the Higgs doublet(s) can turn positive inside and in the vicinity of the wall leading to EW symmetry restoration in some region around the wall. In our work, we achieved this for the case of the real singlet scalar domain walls in the N2HDM and demonstrated the possibility of restoring the EW symmetry in a region large enough to contain a sphaleron.

The second ingredient for electroweak baryogenesis is a CP-violating source that causes a chiral asymmetry in the EW symmetry restored region. Since electron dipole moment experiments put a huge constraint on the possibility of having CP-violation at the electroweak scale [116], a novel way to generate the needed chiral asymmetry is needed, which evades these stringent constraints. For these reasons, we looked at the possibility of having a CP-violating scalar field configuration in the case when the DW moves into regions with different Goldstone modes, a scenario that naturally occurs after EW symmetry breaking. Since the CP violation would only occur in the vicinity of the wall, EDM constraints will be naturally circumvented. Our simulations for 1D field configurations showed that this CP-violating phase ξ in the field configuration is concentrated on the wall and is negligibly small. However, we found that the change in the Goldstone mode, related to e.g. the hypercharge symmetry, is also concentrated in the center of the wall, which induces a hypermagnetic field centered in the core of the wall. Such a pure gauge hypermagnetic field can lead to a chiral asymmetry.

We proposed in that chapter the needed ingredients for a successful electroweak baryogenesis via domain walls. We later performed a simplified calculation in a simplified scenario to obtain an order of magnitude value for the amount of baryon asymmetry that can be possible to generate via this mechanism. We showed that the pure-gauge hypercharge field leads to a chiral asymmetry inside the wall, which, alongside the unsuppressed sphaleron rate inside the wall, successfully generated a matter-antimatter asymmetry comparable to

the amount given by experimental observations. The detailed calculation of the precise amount of baryon asymmetry generated by this mechanism requires a detailed analysis of the domain wall dynamics including a careful treatment of the issue of negative transmission coefficients that could be caused by a Klein-Paradox and a discussion of the annihilation time of the domain wall network that can be achieved e.g. by introducing a bias term in the potential, which breaks the Z'_2 symmetry. Another important details include the possibility of having wash-out effects that depletes any generated baryon asymmetry.

In our final project, discussed in chapter 6, we looked at the intriguing possibility of domain walls inducing the decay of metastable EW vacua in the N2HDM. The conventional vacuum stability analysis of extended Higgs sectors only looked at the decay of metastable EW vacua in a homogeneous field configuration, calculating the tunneling rate from the EW minimum to the global minimum and comparing it to the age of the universe. However, in the presence of domain walls that couple to the doublet scalar fields, the effective potential of the 2HDM will be different from the potential far away from the wall, where a large potential barrier protects the EW minimum from decaying to the global minimum. In case the global minimum of the potential has a vanishing singlet vacuum expectation value, we showed that the field configuration classically rolls over inside the wall to the global minimum, once the global minimum is nucleated inside the wall, it rapidly expands outside and the new vacuum of the universe is then at the global minimum. This has catastrophic consequences, since the global minimum would give different masses to the SM particles than the ones we observe. We showed that this mechanism puts a very strong constraint on the viable parameter space of the N2HDM. In the case when the global minimum is the only minimum with a vanishing v_s , a classical rollover to the global minimum is guaranteed. However, when multiple minima with $v_s = 0$ exist, one then needs to check the time-dependent evolution of the scalar fields to determine the fate of the metastable EW minimum, as well as perform a careful study of the thermal evolution of the scalar field sector.

This mechanism illustrates the need for a careful study of domain walls when dealing with the standard N2HDM, where the Z'_2 symmetry is either exact or softly broken by very small bias terms. One usually invokes the argument that a domain wall network will quickly annihilate in the case of a very small bias term for the Z'_2 symmetry in order to use the simpler phenomenology of the standard N2HDM. However, we showed that even if the presence of small bias terms would solve the domain wall energy domination problem, we still need to make sure that domain walls do not lead to the EW vacuum decay. One can therefore conclude that the use of such a model is safe when the EW minimum is the global minimum, making it stable, or when the Z'_2 symmetry is never restored in the early universe in order to avoid the formation of domain walls.

In some BSM Higgs models, such as the real singlet extension [21] or the N2HDM [23], the electroweak phase transition is not guaranteed even if the potential develops the EW minimum as a global minimum. In such a case, we have *vacuum trapping* and the universe stays in the symmetric phase even at zero temperature [21, 23, 22]. This happens because there is a large enough barrier between a minimum in the potential at the origin of the field space and the EW minimum, making the tunneling rate to the broken phase extremely low. One possible future direction for this work is to look at the possibility of domain walls rescuing these parameter points from vacuum trapping by inducing the vacuum decay of the symmetric minimum to the EW minimum. Such a cure for vacuum trapping was already effective in the real singlet extension [21, 22], and extending it to more complicated models such as the N2HDM is subject to future work.

We discuss the interaction of the electroweak gauge field degrees of freedom with the Higgs scalar degrees of freedom and show that any contribution from the gauge fields is pure gauge or will lead to the DW solution having a higher energy, and therefore, the ground state solution is the one where the gauge fields vanish.

The energy functional for the scalar and gauge sector is given by:

$$\mathcal{E}(x) = |D_\mu \Phi_1|^2 + |D_\mu \Phi_2|^2 + \frac{1}{4} B^{\mu\nu} B_{\mu\nu} + \frac{1}{4} W^{a\mu\nu} W_{\mu\nu}^a + V_{\text{HDM}}(\Phi_1, \Phi_2), \quad (\text{A.1})$$

with:

$$D_\mu = \partial_\mu + igW_\mu^a \sigma^a + \frac{ig_y}{2} B_\mu. \quad (\text{A.2})$$

The third and fourth terms denote the kinetic energy of the $B_\mu(x)$ and W_μ^a gauge fields and are positive definite. In order to investigate the possibility that the first two terms could decrease the energy of the field configuration when having a non-vanishing gauge field solution, we expand these terms using A.2:

$$\begin{aligned} |D_\mu \Phi_i|^2 &= |\partial_\mu \Phi_i|^2 + igW_\mu^a [(\partial_\mu \Phi_i)^\dagger \sigma_a \Phi_i - \Phi_i^\dagger \sigma_a (\partial_\mu \Phi_i)] + i\frac{g'}{2} B^\mu [(\partial_\mu \Phi_i)^\dagger \Phi_i - \Phi_i^\dagger (\partial_\mu \Phi_i)] \\ &\quad + g^2 W_\mu^a (W^a)^\mu |\Phi_i|^2 + gg' W_\mu^a B^\mu (\Phi_i^\dagger \sigma_a \Phi_i) + \frac{g'^2}{4} B^\mu B_\mu |\Phi_i|^2, \end{aligned} \quad (\text{A.3})$$

where i denotes the sum over the two Higgs doublets. Using $A_\mu = \frac{1}{\sqrt{g^2 + g'^2}} (gW_\mu^3 + \frac{g'}{2} B_\mu)$ and $Z_\mu = \frac{1}{\sqrt{g^2 + g'^2}} (-gW_\mu^3 + \frac{g'}{2} B_\mu)$, we can re-write the last 3 terms of A.3 as:

$$\begin{aligned} (g^2 W_\mu^+ (W^-)^\mu + (g^2 + g'^2) Z_\mu Z^\mu) (v_1^2 + v_2^2) + ((g^2 + g'^2) A_\mu A^\mu + g^2 W_\mu^+ (W^-)^\mu) v_2^2 \\ + 2v_2 v_+ g \sqrt{g^2 + g'^2} (A_\mu + Z_\mu) (W_1^\mu \cos(\xi) + W_2^\mu \sin(\xi)). \end{aligned} \quad (\text{A.4})$$

The last term could lead to a negative contribution to the energy functional. However, inside the wall, $v_2 \rightarrow 0$ which makes this term small for our domain wall solutions.

We now focus on the second and third terms in A.3. In the special case of one-dimensional static field configurations (as is the case for a domain wall in the scaling regime), $\partial_\mu \Phi_i = 0$ for $\mu \neq 1$, therefore, these terms vanish for $\mu = 0, 2, 3$ corresponding to time and the y and z directions. Only along the x-axis we get non-vanishing contributions.

One can find expressions for $[(\partial_\mu \Phi_i)^\dagger \sigma_a \Phi_i - \Phi_i^\dagger \sigma_a (\partial_\mu \Phi_i)]$ and $[(\partial_\mu \Phi_i)^\dagger \Phi_i - \Phi_i^\dagger (\partial_\mu \Phi_i)]$ by using the equations of motion for the scalar and gauge fields:

$$D_\mu D^\mu \Phi_i = -\frac{\partial V}{\partial \Phi_i^\dagger}, \quad (\text{A.5})$$

$$J^{\nu,a}(x) = \partial_\mu W^{a,\mu\nu} + g\epsilon^{abc} W_\mu^b W^{c,\mu\nu} = \frac{ig}{2} \left[\Phi_i^\dagger \sigma^a D^\nu \Phi_i - (D^\nu \Phi_i)^\dagger \sigma^a \Phi_i \right], \quad (\text{A.6})$$

$$J_B^\nu(x) = \partial_\mu B^{\mu\nu} = \frac{ig'}{2} \left[\Phi_i^\dagger D^\nu \Phi_i - (D^\nu \Phi_i)^\dagger \Phi_i \right], \quad (\text{A.7})$$

where $j^{\nu,a}$ and j_B^ν denote the gauge field currents. As we want to obtain static one-dimensional spatial solutions on the x -axis, we use the temporal gauge $B^0(x) = 0$ and $W_a^0(x) = 0$. The equations of motion for $B^1(x)$ and $W_a^1(x)$ reduce to:

$$B^1(x) = \frac{1}{2ig'|\Phi_i|^2} \left[\Phi_i^\dagger (\partial_x \Phi_i) - (\partial_x \Phi_i^\dagger) \Phi_i - 2igW_a^1 \Phi_i^\dagger \sigma_a \Phi_i \right], \quad (\text{A.8})$$

$$W_a^1(x) = \frac{1}{2ig|\Phi_i|^2} \left[\Phi_i^\dagger \sigma_a (\partial_x \Phi_i) - (\partial_x \Phi_i^\dagger) \sigma_a \Phi_i - 2ig' B^1(x) \Phi_i^\dagger \sigma_a \Phi_i \right]. \quad (\text{A.9})$$

Using these two equations, one can rewrite the second and third terms of A.3 as:

$$\begin{aligned} & igW_a^\mu [(\partial_\mu \Phi_i)^\dagger \sigma_a \Phi_i - \Phi_i^\dagger \sigma_a (\partial_\mu \Phi_i)] + i\frac{g'}{2} B^\mu [(\partial_\mu \Phi_i)^\dagger \Phi_i - \Phi_i^\dagger (\partial_\mu \Phi_i)] \\ &= \frac{g'}{2} |\Phi_i|^2 B^1(x) B_1(x) + 2g'gW_a^1(x) B_1(x) \Phi_i^\dagger \sigma_a \Phi_i + 2g^2 |\Phi_i|^2 W_a^1(x) W_{a,1}(x), \end{aligned} \quad (\text{A.10})$$

which, as shown earlier (in A.4), leads to a positive contribution to the energy density of the field configuration. As for the $\mu = 2$ and $\mu = 3$ components of the gauge fields, we see from (A.4) that their contributions to the energy density is always positive. Therefore, the least energy solution is the one with $B^j(x) = 0$ and $W_a^j(x) = 0$. Note, however, that a non-zero gauge field will lead to a positive contribution to the effective mass term of the Higgs doublets.

In the case of non-vanishing gauge fields on the wall (e.g due to primordial gauge fields), we would then expect that the backreaction between the Higgs and gauge fields leads to a bigger region where the Higgs VEVs become smaller or zero. This is due to the term $g'^2 |B|^2 |\Phi_i|^2 + g^2 |W|^2 |\Phi_i|^2$ giving a positive contribution to the effective mass of the Higgs doublets. In such a case, a perturbation analysis of such a field configuration has been made in order to study the stability of such a solution.

BIBLIOGRAPHY

- [1] M. Y. Sassi and G. Moortgat-Pick, *Domain walls in the Two-Higgs-Doublet Model and their charge and CP-violating interactions with Standard Model fermions*, *JHEP* **04** (2024) 101, [[2309.12398](#)].
- [2] M. Y. Sassi and G. Moortgat-Pick, *Electroweak Symmetry Restoration in the N2HDM via Domain Walls*, [[2407.14468](#)].
- [3] M. Y. Sassi and G. Moortgat-Pick, “Electroweak Vacuum Decay in the N2HDM Induced by Domain Walls.” In preparation, to be published, 2025.
- [4] J. Harz, M. Klasen, M. Y. Sassi, and L. P. Wiggering, *Dipole formalism for massive initial-state particles and its application to dark matter calculations*, *Phys. Rev. D* **107** (2023), no. 5 056020, [[2210.03409](#)].
- [5] P. W. Higgs, *Broken symmetries and the masses of gauge bosons*, *Phys. Rev. Lett.* **13** (Oct, 1964) 508–509.
- [6] R. A. Battye, G. D. Brawn, and A. Pilaftsis, *Vacuum Topology of the Two Higgs Doublet Model*, *JHEP* **08** (2011) 020, [[1106.3482](#)].
- [7] G. Brawn, *Symmetries and Topological Defects of the Two Higgs Doublet Model*. PhD thesis, Manchester U., 2012.
- [8] T. W. B. Kibble, *Topology of Cosmic Domains and Strings*, *J. Phys. A* **9** (1976) 1387–1398.
- [9] A. Vilenkin, *Cosmic strings and domain walls*, *Physics Reports* **121** (1985), no. 5 263–315.
- [10] Y. Gouttenoire, *Beyond the Standard Model Cocktail*. Springer Theses. Springer, Cham, 2022.
- [11] K. Saikawa, *A review of gravitational waves from cosmic domain walls*, *Universe* **3** (2017), no. 2 40, [[1703.02576](#)].
- [12] Y. B. Zeldovich, I. Y. Kobzarev, and L. B. Okun, *Cosmological Consequences of the Spontaneous Breakdown of Discrete Symmetry*, *Zh. Eksp. Teor. Fiz.* **67** (1974) 3–11.
- [13] T. Vachaspati, *Kinks and Domain Walls: An Introduction to Classical and Quantum Solitons*. Cambridge University Press, 2023.
- [14] Y. Gouttenoire and E. Vitagliano, *Domain wall interpretation of the PTA signal confronting black hole overproduction*, *Phys. Rev. D* **110** (2024), no. 6 L061306, [[2306.17841](#)].
- [15] Y. Gouttenoire, S. F. King, R. Roshan, X. Wang, G. White, et al., *Cosmological Consequences of Domain Walls Biased by Quantum Gravity*, [[2501.16414](#)].
- [16] R. Z. Ferreira, A. Notari, O. Pujolàs, and F. Rompineve, *Collapsing domain wall networks: impact on pulsar timing arrays and primordial black holes*, *JCAP* **06** (2024) 020, [[2401.14331](#)].

- [17] X.-F. Li, *Probing the high temperature symmetry breaking with gravitational waves from domain walls*, [2307.03163].
- [18] **NANOGrav Collaboration**, G. Agazie et al., *The NANOGrav 15 yr Data Set: Evidence for a Gravitational-wave Background*, *Astrophys. J. Lett.* **951** (2023), no. 1 L8, [2306.16213].
- [19] **NANOGrav Collaboration**, A. Afzal et al., *The NANOGrav 15 yr Data Set: Search for Signals from New Physics*, *Astrophys. J. Lett.* **951** (2023), no. 1 L11, [2306.16219]. [Erratum: *Astrophys.J.Lett.* 971, L27 (2024), Erratum: *Astrophys.J.* 971, L27 (2024)].
- [20] S. Blasi, R. Jinno, T. Konstandin, H. Rubira, and I. Stomberg, *Gravitational waves from defect-driven phase transitions: domain walls*, *JCAP* **10** (2023) 051, [2302.06952].
- [21] S. Blasi and A. Mariotti, *Domain Walls Seeding the Electroweak Phase Transition*, *Phys. Rev. Lett.* **129** (2022), no. 26 261303, [2203.16450].
- [22] D. Wei, H. Chen, Q. Fan, and Y. Jiang, *Cosmological first-order phase transitions without bubbles*, [2401.08801].
- [23] T. Biekötter, S. Heinemeyer, J. M. No, M. O. Olea, and G. Weiglein, *Fate of electroweak symmetry in the early Universe: Non-restoration and trapped vacua in the N2HDM*, *JCAP* **06** (2021) 018, [2103.12707].
- [24] P. Agrawal, S. Blasi, A. Mariotti, and M. Nee, *Electroweak phase transition with a double well done doubly well*, *JHEP* **06** (2024) 089, [2312.06749].
- [25] G. C. Branco, P. M. Ferreira, L. Lavoura, M. N. Rebelo, M. Sher, et al., *Theory and phenomenology of two-Higgs-doublet models*, *Phys. Rept.* **516** (2012) 1–102, [1106.0034].
- [26] M. Muhlleitner, M. O. P. Sampaio, R. Santos, and J. Wittbrodt, *The N2HDM under Theoretical and Experimental Scrutiny*, *JHEP* **03** (2017) 094, [1612.01309].
- [27] P. M. Ferreira, M. Mühlleitner, R. Santos, G. Weiglein, and J. Wittbrodt, *Vacuum Instabilities in the N2HDM*, *JHEP* **09** (2019) 006, [1905.10234].
- [28] I. Engeln, P. Ferreira, M. M. Mühlleitner, R. Santos, and J. Wittbrodt, *The Dark Phases of the N2HDM*, *JHEP* **08** (2020) 085, [2004.05382].
- [29] **Particle Data Group Collaboration Collaboration**, S. Navas, C. Amsler, T. Gutsche, C. Hanhart, J. J. Hernández-Rey, et al., *Review of particle physics*, *Phys. Rev. D* **110** (Aug, 2024) 030001.
- [30] Wikipedia, “Standard Model — Wikipedia, the free encyclopedia.” <http://en.wikipedia.org/w/index.php?title=Standard%20Model&oldid=1279111824>, 2025. [Online; accessed 05-May-2025].
- [31] **ATLAS Collaboration**, G. Aad et al., *Observation of a new particle in the search for the Standard Model Higgs boson with the ATLAS detector at the LHC*, *Phys. Lett. B* **716** (2012) 1–29, [1207.7214].
- [32] **CMS Collaboration**, S. Chatrchyan et al., *Observation of a New Boson at a Mass of 125 GeV with the CMS Experiment at the LHC*, *Phys. Lett. B* **716** (2012) 30–61, [1207.7235].

- [33] J. F. Gunion, H. E. Haber, G. L. Kane, and S. Dawson, *The Higgs Hunter's Guide*, vol. 80. 2000.
- [34] C. T. Hill and E. H. Simmons, *Strong Dynamics and Electroweak Symmetry Breaking*, *Phys. Rept.* **381** (2003) 235–402, [[hep-ph/0203079](#)]. [Erratum: *Phys.Rept.* 390, 553–554 (2004)].
- [35] O. Witzel, *Review on Composite Higgs Models*, *PoS LATTICE2018* (2019) 006, [[1901.08216](#)].
- [36] S. Carlip, *Quantum gravity: A Progress report*, *Rept. Prog. Phys.* **64** (2001) 885, [[gr-qc/0108040](#)].
- [37] R. Sundrum, *Unfolding Particle Physics Hierarchies with Supersymmetry and Extra Dimensions*, *PoS TASI2022* (2024) 010, [[2306.07173](#)].
- [38] S. Koren, *New Approaches to the Hierarchy Problem and their Signatures from Microscopic to Cosmic Scales*. PhD thesis, UC, Santa Barbara (main), 2020. [[2009.11870](#)].
- [39] M. E. Peskin, *What is the Hierarchy Problem?*, 5, 2025. [[2505.00694](#)].
- [40] C. Csáki, S. Lombardo, and O. Telem, *TASI lectures on non-supersymmetric BSM models.*, in *Theoretical Advanced Study Institute in Elementary Particle Physics: Anticipating the Next Discoveries in Particle Physics*, pp. 501–570, WSP, 2018. [[1811.04279](#)].
- [41] A. Hook, *TASI Lectures on the Strong CP Problem and Axions*, *PoS TASI2018* (2019) 004, [[1812.02669](#)].
- [42] A. Ringwald, *Review on Axions*, 4, 2024. [[2404.09036](#)].
- [43] J. Martin, *Everything You Always Wanted To Know About The Cosmological Constant Problem (But Were Afraid To Ask)*, *Comptes Rendus Physique* **13** (2012) 566–665, [[1205.3365](#)].
- [44] R. Bousso, *TASI Lectures on the Cosmological Constant*, *Gen. Rel. Grav.* **40** (2008) 607–637, [[0708.4231](#)].
- [45] **SNO Collaboration**, Q. R. Ahmad et al., *Direct evidence for neutrino flavor transformation from neutral current interactions in the Sudbury Neutrino Observatory*, *Phys. Rev. Lett.* **89** (2002) 011301, [[nucl-ex/0204008](#)].
- [46] **Super-Kamiokande Collaboration**, Y. Fukuda et al., *Evidence for oscillation of atmospheric neutrinos*, *Phys. Rev. Lett.* **81** (1998) 1562–1567, [[hep-ex/9807003](#)].
- [47] J. Schechter and J. W. F. Valle, *Neutrino Masses in $SU(2) \times U(1)$ Theories*, *Phys. Rev. D* **22** (1980) 2227.
- [48] E. Ma, *Verifiable radiative seesaw mechanism of neutrino mass and dark matter*, *Phys. Rev. D* **73** (2006) 077301, [[hep-ph/0601225](#)].
- [49] R. Foot, H. Lew, X. G. He, and G. C. Joshi, *Seesaw Neutrino Masses Induced by a Triplet of Leptons*, *Z. Phys. C* **44** (1989) 441.
- [50] Y. Cai, J. Herrero-García, M. A. Schmidt, A. Vicente, and R. R. Volkas, *From the trees to the forest: a review of radiative neutrino mass models*, *Front. in Phys.* **5** (2017) 63, [[1706.08524](#)].

- [51] V. C. Rubin and W. K. Ford, Jr., *Rotation of the Andromeda Nebula from a Spectroscopic Survey of Emission Regions*, *Astrophys. J.* **159** (1970) 379–403.
- [52] F. Zwicky, *Die Rotverschiebung von extragalaktischen Nebeln*, *Helv. Phys. Acta* **6** (1933) 110–127.
- [53] D. Clowe, M. Bradac, A. H. Gonzalez, M. Markevitch, S. W. Randall, et al., *A direct empirical proof of the existence of dark matter*, *Astrophys. J. Lett.* **648** (2006) L109–L113, [[astro-ph/0608407](#)].
- [54] **Planck Collaboration**, N. Aghanim et al., *Planck 2018 results. VI. Cosmological parameters*, *Astron. Astrophys.* **641** (2020) A6, [[1807.06209](#)]. [Erratum: *Astron. Astrophys.* 652, C4 (2021)].
- [55] **WMAP Collaboration**, E. Komatsu et al., *Five-Year Wilkinson Microwave Anisotropy Probe (WMAP) Observations: Cosmological Interpretation*, *Astrophys. J. Suppl.* **180** (2009) 330–376, [[0803.0547](#)].
- [56] **SDSS Collaboration**, D. J. Eisenstein et al., *Detection of the Baryon Acoustic Peak in the Large-Scale Correlation Function of SDSS Luminous Red Galaxies*, *Astrophys. J.* **633** (2005) 560–574, [[astro-ph/0501171](#)].
- [57] I. Labbe et al., *A population of red candidate massive galaxies ~ 600 Myr after the Big Bang*, *Nature* **616** (2023), no. 7956 266–269, [[2207.12446](#)].
- [58] K. Chworowsky, S. L. Finkelstein, M. Boylan-Kolchin, E. J. McGrath, K. G. Iyer, et al., *Evidence for a shallow evolution in the volume densities of massive galaxies at $z = 4-8$ from ceers*, *The Astronomical Journal* **168** (aug, 2024) 113.
- [59] S. Tremaine and J. E. Gunn, *Dynamical Role of Light Neutral Leptons in Cosmology*, *Phys. Rev. Lett.* **42** (1979) 407–410.
- [60] L. Hui, *Wave Dark Matter*, *Ann. Rev. Astron. Astrophys.* **59** (2021) 247–289, [[2101.11735](#)].
- [61] P. J. Fox, *TASI Lectures on WIMPs and Supersymmetry*, *PoS TASI2018* (2019) 005.
- [62] J. L. Feng, *The WIMP paradigm: Theme and variations*, *SciPost Phys. Lect. Notes* **71** (2023) 1, [[2212.02479](#)].
- [63] J. M. Cline, *TASI Lectures on Early Universe Cosmology: Inflation, Baryogenesis and Dark Matter*, *PoS TASI2018* (2019) 001, [[1807.08749](#)].
- [64] D. Chowdhury and S. Show, *SIMP dark matter during reheating*, *JCAP* **01** (2025) 101, [[2410.02871](#)].
- [65] L. J. Hall, K. Jedamzik, J. March-Russell, and S. M. West, *Freeze-In Production of FIMP Dark Matter*, *JHEP* **03** (2010) 080, [[0911.1120](#)].
- [66] J. M. Cline, J. R. Espinosa, G. D. Moore, and A. Riotto, *String mediated electroweak baryogenesis: A Critical analysis*, *Phys. Rev. D* **59** (1999) 065014, [[hep-ph/9810261](#)].
- [67] J. M. Cline, *Baryogenesis*, in *Les Houches Summer School - Session 86: Particle Physics and Cosmology: The Fabric of Spacetime*, 9, 2006. [[hep-ph/0609145](#)].

- [68] D. E. Morrissey and M. J. Ramsey-Musolf, *Electroweak baryogenesis*, *New J. Phys.* **14** (2012) 125003, [[1206.2942](#)].
- [69] D. Croon, *TASI lectures on Phase Transitions, Baryogenesis, and Gravitational Waves*, *PoS TASI2022* (2024) 003, [[2307.00068](#)].
- [70] R. H. Cyburt, *Primordial nucleosynthesis for the new cosmology: Determining uncertainties and examining concordance*, *Phys. Rev. D* **70** (2004) 023505, [[astro-ph/0401091](#)].
- [71] A. D. Sakharov, *Violation of CP Invariance, C asymmetry, and baryon asymmetry of the universe*, *Pisma Zh. Eksp. Teor. Fiz.* **5** (1967) 32–35.
- [72] J. Riebesell and S. Bringuier, *Collection of scientific diagrams*, 2020. 10.5281/zenodo.7486911 - <https://github.com/janosh/diagrams>.
- [73] T. Vachaspati, *Kinks and Domain Walls : An Introduction to Classical and Quantum Solitons*. Oxford University Press, 2007.
- [74] C. Ringeval, *Cosmic strings and their induced non-Gaussianities in the cosmic microwave background*, *Adv. Astron.* **2010** (2010) 380507, [[1005.4842](#)].
- [75] D. Viatic, *Simulations and Phenomenology of Topological Defects in Two Higgs Doublet Models*. PhD thesis, Manchester U., Manchester U., 2020.
- [76] K. H. Law and A. Pilaftsis, *Charged and CP-violating kink solutions in the two-Higgs-doublet model*, *Phys. Rev. D* **105** (2022), no. 5 056007, [[2110.12550](#)].
- [77] T. Vachaspati, *A Class of kinks in $SU(N) \times Z(2)$* , *Phys. Rev. D* **63** (2001) 105010, [[hep-th/0102047](#)].
- [78] E. M. Shin and R. R. Volkas, *$O(10)$ kinks: Clash of symmetries on the brane and the gauge hierarchy problem*, *Phys. Rev. D* **69** (2004) 045010, [[hep-ph/0309008](#)].
- [79] L. Pogosian and T. Vachaspati, *Domain walls in $su(5)$* , *Phys. Rev. D* **62** (Nov, 2000) 123506.
- [80] S. R. Coleman and E. J. Weinberg, *Radiative Corrections as the Origin of Spontaneous Symmetry Breaking*, *Phys. Rev. D* **7** (1973) 1888–1910.
- [81] M. Quiros, *Finite temperature field theory and phase transitions*, in *ICTP Summer School in High-Energy Physics and Cosmology*, pp. 187–259, 1, 1999. [[hep-ph/9901312](#)].
- [82] W. H. Press, B. S. Ryden, and D. N. Spergel, *Dynamical Evolution of Domain Walls in an Expanding Universe*, *Astrophys. J.* **347** (1989) 590–604.
- [83] K. S. Babu, T. Kobayashi, and J. Kubo, *Finite theories and the SUSY flavor problem*, *Phys. Rev. D* **67** (2003) 075018, [[hep-ph/0212350](#)].
- [84] G. R. Dvali and G. Senjanovic, *Is there a domain wall problem?*, *Phys. Rev. Lett.* **74** (1995) 5178–5181, [[hep-ph/9501387](#)].
- [85] O. Pujolas and G. Zahariade, *Domain wall annihilation: A QFT perspective*, *Phys. Rev. D* **107** (2023), no. 12 123527, [[2212.11204](#)].
- [86] F. Quevedo, S. Krippendorff, and O. Schlotterer, *Cambridge Lectures on Supersymmetry and Extra Dimensions*, [[1011.1491](#)].

- [87] M. D. Schwartz, *Quantum Field Theory and the Standard Model*. Cambridge University Press, 2013.
- [88] P. W. Graham, D. E. Kaplan, and S. Rajendran, *Cosmological Relaxation of the Electroweak Scale*, *Phys. Rev. Lett.* **115** (2015), no. 22 221801, [[1504.07551](#)].
- [89] M. E. Shaposhnikov, *Possible Appearance of the Baryon Asymmetry of the Universe in an Electroweak Theory*, *JETP Lett.* **44** (1986) 465–468.
- [90] M. Trodden, *Electroweak baryogenesis*, *Rev. Mod. Phys.* **71** (1999) 1463–1500, [[hep-ph/9803479](#)].
- [91] J. R. Espinosa, T. Konstandin, and F. Riva, *Strong Electroweak Phase Transitions in the Standard Model with a Singlet*, *Nucl. Phys. B* **854** (2012) 592–630, [[1107.5441](#)].
- [92] J. Bernon, L. Bian, and Y. Jiang, *A new insight into the phase transition in the early Universe with two Higgs doublets*, *JHEP* **05** (2018) 151, [[1712.08430](#)].
- [93] M. Mühlleitner, J. Müller, S. L. Williamson, and J. Wittbrodt, *The CN2HDM*, [[2110.06680](#)].
- [94] K. Funakubo, *CP violation and baryogenesis at the electroweak phase transition*, *Prog. Theor. Phys.* **96** (1996) 475–520, [[hep-ph/9608358](#)].
- [95] W. Khater and P. Osland, *CP violation in top quark production at the LHC and two Higgs doublet models*, *Nucl. Phys. B* **661** (2003) 209–234, [[hep-ph/0302004](#)].
- [96] A. W. El Kaffas, P. Osland, and O. M. Ogreid, *CP violation, stability and unitarity of the two Higgs doublet model*, *Nonlin. Phenom. Complex Syst.* **10** (2007) 347–357, [[hep-ph/0702097](#)].
- [97] L. Biermann, M. Mühlleitner, and J. Müller, *Electroweak phase transition in a dark sector with CP violation*, *Eur. Phys. J. C* **83** (2023), no. 5 439, [[2204.13425](#)].
- [98] W.-L. Guo and Y.-L. Wu, *The Real singlet scalar dark matter model*, *JHEP* **10** (2010) 083, [[1006.2518](#)].
- [99] M. Gustafsson, *The Inert Doublet Model and Its Phenomenology*, *PoS CHARGED2010* (2010) 030, [[1106.1719](#)].
- [100] J. Dutta, G. Moortgat-Pick, and M. Schreiber, *Phenomenology of the dark matter sector in the 2HDM extended with complex scalar singlet*, *Eur. Phys. J. Plus* **140** (2025), no. 1 87, [[2203.05509](#)].
- [101] J. Dutta, J. Lahiri, C. Li, G. Moortgat-Pick, S. F. Tabira, et al., *Dark Matter Phenomenology in 2HDMS in light of the 95 GeV excess*, [[2308.05653](#)].
- [102] J. Dutta, M. Matlis, G. Moortgat-Pick, and A. Ringwald, *Inflation and Higgs Phenomenology in a Model Unifying the DFSZ Axion with the Majoron*, [[2309.10857](#)].
- [103] J. Dutta, J. Lahiri, C. Li, G. Moortgat-Pick, S. F. Tabira, et al., *Search for Dark Matter in 2HDMS at LHC and future Lepton Colliders*, [[2504.14529](#)].
- [104] J. A. Ziegler, J. Dutta, J. Lahiri, C. Li, G. Moortgat-Pick, et al., *Dark matter phenomenology in Z'2 broken singlet extended 2HDM*, *PoS EPS-HEP2023* (2024) 111, [[2310.19962](#)].

- [105] **LHC Dark Matter Working Group Collaboration**, T. Abe et al., *LHC Dark Matter Working Group: Next-generation spin-0 dark matter models*, *Phys. Dark Univ.* **27** (2020) 100351, [[1810.09420](#)].
- [106] R. H. Brandenberger, A.-C. Davis, and M. Trodden, *Cosmic strings and electroweak baryogenesis*, *Phys. Lett. B* **335** (1994) 123–130, [[hep-ph/9403215](#)].
- [107] T. Schröder and R. Brandenberger, *Embedded Domain Walls and Electroweak Baryogenesis*, [[2404.13035](#)].
- [108] J. Azzola, O. Matsedonskyi, and A. Weiler, *Minimal Electroweak Baryogenesis via Domain Walls*, [[2412.10495](#)].
- [109] A. Mariotti, X. Nagels, A. Rase, and M. Vanvlasselaer, *DW-genesis: baryon number from domain wall network collapse*, *JHEP* **03** (2025) 199, [[2411.13494](#)].
- [110] R. A. Battye, A. Pilaftsis, and D. G. Viatic, *Simulations of Domain Walls in Two Higgs Doublet Models*, *JHEP* **01** (2021) 105, [[2006.13273](#)].
- [111] A. B. Lahanas, V. C. Spanos, and V. Zarikas, *Charge asymmetry in two-Higgs doublet model*, *Phys. Lett. B* **472** (2000) 119, [[hep-ph/9812535](#)].
- [112] A. Barroso, P. M. Ferreira, and R. Santos, *Charge and CP symmetry breaking in two Higgs doublet models*, *Phys. Lett. B* **632** (2006) 684–687, [[hep-ph/0507224](#)].
- [113] I. P. Ivanov, *Minkowski space structure of the Higgs potential in 2HDM*, *Phys. Rev. D* **75** (2007) 035001, [[hep-ph/0609018](#)]. [Erratum: *Phys.Rev.D* 76, 039902 (2007)].
- [114] M. Mühlleitner, M. O. P. Sampaio, R. Santos, and J. Wittbrodt, *Phenomenological Comparison of Models with Extended Higgs Sectors*, *JHEP* **08** (2017) 132, [[1703.07750](#)].
- [115] C.-Y. Chen, M. Freid, and M. Sher, *Next-to-minimal two Higgs doublet model*, *Phys. Rev. D* **89** (2014), no. 7 075009, [[1312.3949](#)].
- [116] T. S. Roussy et al., *An improved bound on the electron’s electric dipole moment*, *Science* **381** (2023), no. 6653 adg4084, [[2212.11841](#)].
- [117] M. Mühlleitner, M. O. P. Sampaio, R. Santos, and J. Wittbrodt, *ScannerS: parameter scans in extended scalar sectors*, *Eur. Phys. J. C* **82** (2022), no. 3 198, [[2007.02985](#)].
- [118] G. Hiller, T. Höhne, D. F. Litim, and T. Steudtner, *Vacuum stability in the Standard Model and beyond*, *Phys. Rev. D* **110** (2024), no. 11 115017, [[2401.08811](#)].
- [119] I. P. Ivanov, *Minkowski space structure of the Higgs potential in 2HDM. II. Minima, symmetries, and topology*, *Phys. Rev. D* **77** (2008) 015017, [[0710.3490](#)].
- [120] P. M. Ferreira, R. Santos, and A. Barroso, *Stability of the tree-level vacuum in two Higgs doublet models against charge or CP spontaneous violation*, *Phys. Lett. B* **603** (2004) 219–229, [[hep-ph/0406231](#)]. [Erratum: *Phys.Lett.B* 629, 114–114 (2005)].
- [121] K. Radchenko, “Unlocking the Higgs Potential: from Colliders to the Cosmos..” PhD Thesis, 2025.
- [122] A. Barroso, P. M. Ferreira, I. P. Ivanov, R. Santos, and J. P. Silva, *Evading death by vacuum*, *Eur. Phys. J. C* **73** (2013) 2537, [[1211.6119](#)].

- [123] S. Coleman, *Fate of the false vacuum: Semiclassical theory*, *Phys. Rev. D* **15** (May, 1977) 2929–2936.
- [124] P. Bechtle, D. Dercks, S. Heinemeyer, T. Klingl, T. Stefaniak, et al., *HiggsBounds-5: Testing Higgs Sectors in the LHC 13 TeV Era*, *Eur. Phys. J. C* **80** (2020), no. 12 1211, [[2006.06007](#)].
- [125] P. Bechtle, S. Heinemeyer, T. Klingl, T. Stefaniak, G. Weiglein, et al., *HiggsSignals-2: Probing new physics with precision Higgs measurements in the LHC 13 TeV era*, *Eur. Phys. J. C* **81** (2021), no. 2 145, [[2012.09197](#)].
- [126] J. Haller, A. Hoecker, R. Kogler, K. Mönig, T. Peiffer, et al., *Update of the global electroweak fit and constraints on two-Higgs-doublet models*, *Eur. Phys. J. C* **78** (2018), no. 8 675, [[1803.01853](#)].
- [127] W. Grimus, L. Lavoura, O. M. Ogreid, and P. Osland, *A Precision constraint on multi-Higgs-doublet models*, *J. Phys. G* **35** (2008) 075001, [[0711.4022](#)].
- [128] L. Pogosian and T. Vachaspati, *Domain walls in $SU(5)$* , *Phys. Rev. D* **62** (2000) 123506, [[hep-ph/0007045](#)].
- [129] A. Davidson, D. P. George, A. Kobakhidze, R. R. Volkas, and K. C. Wali, *$SU(5)$ grand unification on a domain-wall brane from an $E(6)$ -invariant action*, *Phys. Rev. D* **77** (2008) 085031, [[0710.3432](#)].
- [130] A. Davidson, B. F. Toner, R. R. Volkas, and K. C. Wali, *Clash of symmetries on the brane*, *Phys. Rev. D* **65** (2002) 125013, [[hep-th/0202042](#)].
- [131] D. A. Steer and T. Vachaspati, *Domain walls and fermion scattering in grand unified models*, *Phys. Rev. D* **73** (2006) 105021, [[hep-th/0602130](#)].
- [132] R. A. Battye and D. G. Viatic, *Photon interactions with superconducting topological defects*, *Phys. Lett. B* **823** (2021) 136730, [[2110.13668](#)].
- [133] L. Pogosian and T. Vachaspati, *Space of kink solutions in $SU(N) * Z(2)$* , *Phys. Rev. D* **64** (2001) 105023, [[hep-th/0105128](#)].
- [134] A. Ghoshal and Y. Hamada, *Gravitational Wave Mountains: current-carrying domain walls*, [[2501.01542](#)].
- [135] L. Campanelli, *Scattering of Dirac and Majorana fermions off domain walls*, *Phys. Rev. D* **70** (2004) 116008, [[hep-ph/0408078](#)].
- [136] V. Klimashonok, I. Perapechka, and Y. Shnir, *Fermions on kinks revisited*, *Phys. Rev. D* **100** (2019), no. 10 105003, [[1909.12736](#)].
- [137] M. Joyce, T. Prokopec, and N. Turok, *Nonlocal electroweak baryogenesis. Part 1: Thin wall regime*, *Phys. Rev. D* **53** (1996) 2930–2957, [[hep-ph/9410281](#)].
- [138] D. Griffiths and S. Walborn, *Dirac deltas and discontinuous functions*, *American Journal of Physics* **67** (05, 1999) 446–447, [https://pubs.aip.org/aapt/ajp/article-pdf/67/5/446/10115861/446_1_online.pdf].
- [139] M. G. Calkin, D. Kiang, and Y. Nogami, *Proper treatment of the delta function potential in the one-dimensional Dirac equation*, *American Journal of Physics* **55** (Aug., 1987) 737–739.

- [140] B. Sutherland and D. C. Mattis, *Ambiguities with the relativistic δ -function potential*, *Phys. Rev. A* **24** (Sep, 1981) 1194–1197.
- [141] C. L. Roy, *Boundary conditions across a δ -function potential in the one-dimensional dirac equation*, *Phys. Rev. A* **47** (Apr, 1993) 3417–3419.
- [142] O. Klein, *Die Reflexion von Elektronen an einem Potentialsprung nach der relativistischen Dynamik von Dirac*, *Z. Phys.* **53** (1929) 157.
- [143] C. Caprini, S. Biller, and P. G. Ferreira, *Constraints on the electrical charge asymmetry of the universe*, *JCAP* **02** (2005) 006, [[hep-ph/0310066](#)].
- [144] R. H. Brandenberger, A.-C. Davis, and M. Hindmarsh, *Baryogenesis from collapsing topological defects*, *Phys. Lett. B* **263** (1991) 239–244.
- [145] R. H. Brandenberger and A.-C. Davis, *Electroweak baryogenesis with electroweak strings*, *Phys. Lett. B* **308** (1993) 79–84, [[astro-ph/9206001](#)].
- [146] R. H. Brandenberger, A.-C. Davis, T. Prokopec, and M. Trodden, *Local and nonlocal defect mediated electroweak baryogenesis*, *Phys. Rev. D* **53** (1996) 4257–4266, [[hep-ph/9409281](#)].
- [147] I. Dasgupta, *Baryogenesis from cosmic strings at the electroweak scale*, *Phys. Rev. D* **55** (1997) 3318–3329, [[hep-ph/9604356](#)].
- [148] A.-C. Davis and M. A. Earnshaw, *Baryogenesis from collapsing cosmic string loops*, *Nucl. Phys. B* **394** (1993) 21–34.
- [149] M. O. Olea Romacho, *Higgs physics as a window to the electroweak epoch*. PhD thesis, U. Hamburg (main), Hamburg U., 2022.
- [150] P. Basler, L. Biermann, M. Mühlleitner, J. Müller, R. Santos, et al., *BSMPT v3 A Tool for Phase Transitions and Primordial Gravitational Waves in Extended Higgs Sectors*, [[2404.19037](#)].
- [151] P. Basler and M. Mühlleitner, *BSMPT (Beyond the Standard Model Phase Transitions): A tool for the electroweak phase transition in extended Higgs sectors*, *Comput. Phys. Commun.* **237** (2019) 62–85, [[1803.02846](#)].
- [152] M. Le Bellac, *Thermal Field Theory*. Cambridge Monographs on Mathematical Physics. Cambridge University Press, 1996.
- [153] P. B. Arnold and O. Espinosa, *The Effective potential and first order phase transitions: Beyond leading-order*, *Phys. Rev. D* **47** (1993) 3546, [[hep-ph/9212235](#)]. [Erratum: *Phys.Rev.D* 50, 6662 (1994)].
- [154] R. R. Parwani, *Resummation in a hot scalar field theory*, *Phys. Rev. D* **45** (1992) 4695, [[hep-ph/9204216](#)]. [Erratum: *Phys.Rev.D* 48, 5965 (1993)].
- [155] P. Bittar, S. Roy, and C. E. M. Wagner, *Self Consistent Thermal Resummation: A Case Study of the Phase Transition in 2HDM*, [[2504.02024](#)].
- [156] R. Coimbra, M. O. P. Sampaio, and R. Santos, *ScannerS: Constraining the phase diagram of a complex scalar singlet at the LHC*, *Eur. Phys. J. C* **73** (2013) 2428, [[1301.2599](#)].
- [157] P. M. Ferreira, R. Guedes, M. O. P. Sampaio, and R. Santos, *Wrong sign and symmetric limits and non-decoupling in 2HDMs*, *JHEP* **12** (2014) 067, [[1409.6723](#)].

- [158] R. Costa, M. Mühlleitner, M. O. P. Sampaio, and R. Santos, *Singlet Extensions of the Standard Model at LHC Run 2: Benchmarks and Comparison with the NMSSM*, *JHEP* **06** (2016) 034, [[1512.05355](#)].
- [159] Y. Brihaye and J. Kunz, *Electroweak bubbles and sphalerons*, *Phys. Rev. D* **48** (1993) 3884–3890, [[hep-ph/9304256](#)].
- [160] P. Bechtle, O. Brein, S. Heinemeyer, G. Weiglein, and K. E. Williams, *HiggsBounds: Confronting Arbitrary Higgs Sectors with Exclusion Bounds from LEP and the Tevatron*, *Comput. Phys. Commun.* **181** (2010) 138–167, [[0811.4169](#)].
- [161] P. Bechtle, O. Brein, S. Heinemeyer, G. Weiglein, and K. E. Williams, *HiggsBounds 2.0.0: Confronting Neutral and Charged Higgs Sector Predictions with Exclusion Bounds from LEP and the Tevatron*, *Comput. Phys. Commun.* **182** (2011) 2605–2631, [[1102.1898](#)].
- [162] P. Bechtle, O. Brein, S. Heinemeyer, O. Stal, T. Stefaniak, et al., *Recent Developments in HiggsBounds and a Preview of HiggsSignals*, *PoS CHARGED2012* (2012) 024, [[1301.2345](#)].
- [163] P. Bechtle, O. Brein, S. Heinemeyer, O. Stål, T. Stefaniak, et al., *HiggsBounds – 4: Improved Tests of Extended Higgs Sectors against Exclusion Bounds from LEP, the Tevatron and the LHC*, *Eur. Phys. J. C* **74** (2014), no. 3 2693, [[1311.0055](#)].
- [164] P. Bechtle, S. Heinemeyer, O. Stal, T. Stefaniak, and G. Weiglein, *Applying Exclusion Likelihoods from LHC Searches to Extended Higgs Sectors*, *Eur. Phys. J. C* **75** (2015), no. 9 421, [[1507.06706](#)].
- [165] P. Bechtle, S. Heinemeyer, O. Stål, T. Stefaniak, and G. Weiglein, *HiggsSignals: Confronting arbitrary Higgs sectors with measurements at the Tevatron and the LHC*, *Eur. Phys. J. C* **74** (2014), no. 2 2711, [[1305.1933](#)].
- [166] L. Dominguez, *Search for low and high mass resonances with $\gamma\gamma/\gamma Z$ final states with the atlas detector*, p. 389, 02, 2024.
- [167] **CMS Collaboration**, A. Hayrapetyan et al., *Search for a standard model-like Higgs boson in the mass range between 70 and 110 GeV in the diphoton final state in proton-proton collisions at $\sqrt{s} = 13$ TeV*, [[2405.18149](#)].
- [168] A. Ayala and G. Pallares, *Electroweak baryogenesis in the standard model with strong hypermagnetic fields*, [[hep-ph/0008142](#)].
- [169] G. Piccinelli and A. Ayala, *Electroweak baryogenesis and primordial hypermagnetic fields*, *Lect. Notes Phys.* **646** (2004) 293–308, [[hep-ph/0404033](#)].
- [170] A. Ayala, J. Besprosvany, G. Pallares, and G. Piccinelli, *Axially asymmetric fermion scattering off electroweak phase transition bubble walls with hypermagnetic fields*, *Phys. Rev. D* **64** (2001) 123529, [[hep-ph/0107072](#)].
- [171] M. Vanvlasselaer, *DW-genesis: generating the baryon number from domain walls*, *PoS DISCRETE2024* (2025) 012, [[2501.00491](#)].
- [172] A. G. Cohen, D. B. Kaplan, and A. E. Nelson, *Progress in electroweak baryogenesis*, *Ann. Rev. Nucl. Part. Sci.* **43** (1993) 27–70, [[hep-ph/9302210](#)].
- [173] V. A. Kuzmin, V. A. Rubakov, and M. E. Shaposhnikov, *On the Anomalous Electroweak Baryon Number Nonconservation in the Early Universe*, *Phys. Lett. B*

155 (1985) 36.

- [174] S. Bruggisser, T. Konstandin, and G. Servant, *CP-violation for Electroweak Baryogenesis from Dynamical CKM Matrix*, *JCAP* **11** (2017) 034, [[1706.08534](#)].
- [175] S. J. Huber, T. Konstandin, T. Prokopec, and M. G. Schmidt, *Electroweak Phase Transition and Baryogenesis in the n MSSM*, *Nucl. Phys. B* **757** (2006) 172–196, [[hep-ph/0606298](#)].
- [176] I. Baldes and G. Servant, *High scale electroweak phase transition: baryogenesis & symmetry non-restoration*, *JHEP* **10** (2018) 053, [[1807.08770](#)].
- [177] E. Fernández-Martínez, J. López-Pavón, J. M. No, T. Ota, and S. Rosauero-Alcaraz, *ν Electroweak baryogenesis: the scalar singlet strikes back*, *Eur. Phys. J. C* **83** (2023), no. 8 715, [[2210.16279](#)].
- [178] T. Prokopec, R. H. Brandenberger, and A.-C. Davis, *The Impossibility of baryogenesis at a second order electroweak phase transition*, [[hep-ph/9601327](#)].
- [179] J. M. Cline, *Is electroweak baryogenesis dead?*, [[1704.08911](#)].
- [180] H. Faxén and J. Holtsmark, *Beitrag zur theorie des durchganges langsamer elektronen durch gase*, *Zeitschrift für Physik* **45** (1927) 307–324.
- [181] J. Townsend and V. B. and, *Xcvii. the motion of electrons in gases*, *The London, Edinburgh, and Dublin Philosophical Magazine and Journal of Science* **42** (1921), no. 252 873–891, [<https://doi.org/10.1080/14786442108633831>].
- [182] C. Ramsauer, *Über den wirkungsquerschnitt der gasmoleküle gegenüber langsamen elektronen*, *Annalen der Physik* **369** (1921), no. 6 513–540, [<https://onlinelibrary.wiley.com/doi/pdf/10.1002/andp.19213690603>].
- [183] **Planck Collaboration**, N. Aghanim et al., *Planck 2018 results. I. Overview and the cosmological legacy of Planck*, *Astron. Astrophys.* **641** (2020) A1, [[1807.06205](#)].
- [184] A. V. Bednyakov, B. A. Kniehl, A. F. Pikelner, and O. L. Veretin, *Stability of the Electroweak Vacuum: Gauge Independence and Advanced Precision*, *Phys. Rev. Lett.* **115** (2015), no. 20 201802, [[1507.08833](#)].
- [185] **CMS Collaboration**, A. M. Sirunyan et al., *Measurement of $t\bar{t}$ normalised multi-differential cross sections in pp collisions at $\sqrt{s} = 13$ TeV, and simultaneous determination of the strong coupling strength, top quark pole mass, and parton distribution functions*, *Eur. Phys. J. C* **80** (2020), no. 7 658, [[1904.05237](#)].
- [186] J. Lahiri and G. Moortgat-Pick, *Vacuum (in)stability in 2HDMS vs N2HDM*, [[2408.13592](#)].
- [187] A. Barroso, P. M. Ferreira, I. P. Ivanov, and R. Santos, *Metastability bounds on the two Higgs doublet model*, *JHEP* **06** (2013) 045, [[1303.5098](#)].
- [188] V. Branchina, F. Contino, and P. M. Ferreira, *Electroweak vacuum lifetime in two Higgs doublet models*, *JHEP* **11** (2018) 107, [[1807.10802](#)].
- [189] W. G. Hollik, G. Weiglein, and J. Wittbrodt, *Impact of Vacuum Stability Constraints on the Phenomenology of Supersymmetric Models*, *JHEP* **03** (2019) 109, [[1812.04644](#)].

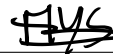
- [190] E. W. Kolb and M. S. Turner, *The Early Universe*, vol. 69. Taylor and Francis, 5, 2019.
- [191] **ATLAS Collaboration**, G. Aad et al., *ATLAS searches for additional scalars and exotic Higgs boson decays with the LHC Run 2 dataset*, [[2405.04914](#)].
- [192] J. R. Espinosa, *Electroweak baryogenesis with cosmic strings?*, in *3rd International Conference on Strong and Electroweak Matter*, pp. 304–308, 1, 1999. [[hep-ph/9901310](#)].

EIDESSTATTLICHE VERSICHERUNG

Hiermit versichere ich an Eides statt, die vorliegende Dissertationsschrift selbst verfasst und keine anderen als die angegebenen Hilfsmittel und Quellen benutzt zu haben.

Sofern im Zuge der Erstellung der vorliegenden Dissertationsschrift generative Künstliche Intelligenz (gKI) basierte elektronische Hilfsmittel verwendet wurden, versichere ich, dass meine eigene Leistung im Vordergrund stand und dass eine vollständige Dokumentation aller verwendeten Hilfsmittel gemäß der Guten wissenschaftlichen Praxis vorliegt. Ich trage die Verantwortung für eventuell durch die gKI generierte fehlerhafte oder verzerrte Inhalte, fehlerhafte Referenzen, Verstöße gegen das Datenschutz- und Urheberrecht oder Plagiate.

Hamburg, den 16. Mai 2025



Mohamed Younes Sassi